

Department of Electrical and Computer Engineering

Improved Design of Wireless Electrical Energy Transfer System
for Various Power Applications

Do Won Kim

This thesis is presented for the Degree of
Doctor of Philosophy
of
Curtin University

October 2020

Declaration

To the best of my knowledge and belief, this thesis contains no material previously published by any other person except where due acknowledgment has been made. This thesis contains no material which has been accepted for the award of any other degree or diploma in any university.

Author: Do Won Kim

Date: 05/10/2020

Acknowledgments

I sincerely express gratitude to my supervisor, Associate Professor Dr. Ahmed Abu-Siada, for his professional research guidance and passionate support. It was a great honour to explore the beautiful academic world with him. I extend my thanks to my co-supervisor, Dr. Adrian Sutinjo, for encouraging me continuously and expanding my knowledge.

I acknowledge the Australian Government and Curtin University for offering me a great opportunity and scholarship. Also, I appreciate the support of the technical and administrative staff and other postgraduate students at Curtin University.

Last but not least, I thank my love and family for their faith and devotion.

Abstract

Nikola Tesla, a scientist pursuing power delivery in free space, suggested a huge amount of power can be transferred through the earth, while Guglielmo Marconi concentrated on inventing wireless communication systems over the ocean a hundred years ago. While telecommunication technology has been successfully developed, the development of a wireless power transfer (WPT) system stagnated for decades, as large devices were required to create the resonant oscillation in a safe manner, and the system exhibited low efficiency. Due to the subsequent development of power devices and the day-by-day increase in mobile products, electric vehicles, and wireless sensors in smart grids, WPT technology is expected to undergo substantial advancement and significant power systems applications in the near future.

This thesis introduces a state-of-the-art review of existing WPT technologies with a detailed comparison, and presents the limitations of the inductive power transfer system through simulation and practical analyses. The thesis subsequently provides recommendations and future perspectives for overcoming these limitations through four main themes: design, efficiency, stability, and safety.

Furthermore, this thesis presents a comprehensive analysis of the design of the WPT system with a numerical simulation tool. The electromagnetic field solver known as FEldberechnung für Körper mit beliebiger Oberfläche (FEKO) is mainly used for studying high-frequency devices. However, this computational tool is not only applicable in the analysis of the electromagnetic characteristics but also in the identification of the electrical parameters in the WPT system operating in the near field. In this study, the self and mutual inductance of the wireless transfer windings over the various airgaps were inferred from the simulated scattering parameters. Then, the formation of the magnetic coupling and the distribution of the magnetic fields between the coils in the series-parallel compensation model were examined through near-field analysis for recognising the

efficient performance of the WPT system. It was then clarified that the FEKO simulation results showed good agreement with the practical measurements.

Besides, the reliability of an extensive WPT system can also be evaluated using a frequency response analyser (FRA) measurement. A FRA plays a vital role in the assessment of mechanical integrity, and hence the reliability of high-voltage power transformers. The WPT system, based on Faraday's law of electromagnetic induction, is similar to a conventional power transformer. When the WPT system is constructed, the electrical components and the desired transfer distance need to be ascertained accurately. Furthermore, the structure of the winding and the electrical characteristics of the components in WPT systems may vary due to ageing or fault events.

A FRA measurement can examine the discrepancy between the WPT system parameters and the reference fingerprint data to provide a cost-effective condition monitoring-based maintenance scheme for WPT systems. This thesis presents a detailed circuit analysis of a two-coil inductively-coupled WPT model in different compensating topologies to accomplish efficient energy transfer. Then, a FRA measurement is used to detect the variation in the amplitude and the phase angle of the developed circuit input impedance in a wide frequency range. In addition, displacements due to the placement of ferrite material and the variation of the transfer distance between the transmitter and receiver units are investigated through practical measurements.

In summary, the electrical parameters of WPT systems in different structures or mediums can be extracted through the scattering parameter results of the FEKO simulation. The electromagnetic field solver provides the strength of the magnetic coupling, transferred power, and efficiency between the transmitter and receiver. Also, the FRA measurements verify the actual resonance frequency, input impedance, and phase angle of WPT systems in different conditions. As the integrity of WPT systems can be assessed based on the initial frequency response signature, a FRA provides a valuable maintenance method. The accuracy of FEKO and practicality of a FRA in improving the design of WPT systems are demonstrated with the various experiments in this thesis.

Statement of contribution to publications

This thesis includes the technical materials and the results of the experiments that have been published in international journals and conferences. These publications are listed below.

- **International Peer Review Journal Publications.**

1. Dowon Kim, Ahmed Abu-Siada, and Adrian Sutinjo, "**State-of-the-art literature review of WPT: Current limitations and solutions on IPT**," *Electric Power Systems Research*, vol. 154, pp. 493-502, 2018, doi: <https://doi.org/10.1016/j.epsr.2017.09.018>.
2. Dowon Kim, Ahmed Abu-Siada, and Adrian Sutinjo, "**Application of FRA to Improve the Design and Maintenance of Wireless Power Transfer Systems**," *IEEE Transactions on Instrumentation and Measurement*, pp. 1-13, 2019, doi: 10.1109/TIM.2018.2889360.
3. Dowon Kim, Adrian Sutinjo, and Ahmed Abu-Siada, "**Near-Field Analysis and Design of Inductively-Coupled Wireless Power Transfer System in FEKO**," *Applied Computational Electromagnetics Society*, vol. 35, pp. 82-93, 2020.
 - *The main contribution of the candidate to journal papers 1–3:*
Originating novel ideas, researching previous studies, performing software simulations, designing a prototype, conducting practical experiments, writing a manuscript, and replying to reviewer's comments.
 - *The main contribution of the co-authors to the journal paper 1-3:*
Verifying the contribution of the new idea, assessing the quality of the experimental performance, reviewing and rectifying the manuscript, instructing the academic writing.

- **Conference Publications.**

4. Dowon Kim, Ahmed Abu-Siada, and Adrian Sutinjo, "**A novel application of frequency response analysis for wireless power transfer system,**" in *2017 Australasian Universities Power Engineering Conference (AUPEC)*, 19-22 Nov. 2017, pp. 1-6, doi: 10.1109/AUPEC.2017.8282474.
 5. Dowon Kim, "**Literature Review of Wireless Power Transfer Technology for Electric Vehicle Battery Charging,**" in *2017 One Curtin International Postgraduate Conference*, 10-12 Dec. 2017.
 6. Dowon Kim, Ahmed Abu-Siada, and Stuart Higgins, "**An Inductively-coupled Wireless Power Transfer Application for Autonomous Underwater Vehicles,**" in *2019 11th Autonomous Underwater Technology, technical conference & exhibition*, 23 Oct. 2019.
 7. Dowon Kim and Ahmed Abu-Siada, "**A new role of SFRA for reliable performance in wireless power transfer system,**" in *2020 International Conference of Doble Clients*, 8-13 Mar. 2020.
- *The main contribution of the candidate to papers 4–7:*
Originating novel ideas, researching previous studies, performing software simulations, designing a prototype, conducting practical experiments, writing a manuscript, replying to reviewer’s comments, and preparing the presentation.
 - *The main contribution of the co-authors to paper 4-7:*
Verifying the contribution of the new idea, assessing the quality of the experimental performance, reviewing and rectifying the manuscript, instructing the academic writing.

Keywords

Wireless Power Transfer

Inductive power transfer

Magnetic coupling

RLC resonance

FEKO simulation

Near-field analysis

Frequency response analyser

Compensation topology

Impedance Analysis

Wireless Power Transfer Design and Maintenance

List of Figures

Figure 1.1. Tesla’s Colorado Springs experiment in 1899	2
Figure 1.2. Tesla’s Wardencliffe experiment in 1914	2
Figure 1.3. Brief schematic of a modern WPT system.....	3
Figure 2.1. Overview of WPT technology	8
Figure 2.2. Inductive power transfer with compensating capacitors in series.....	10
Figure 2.3. Capacitive Power Transfer	11
Figure 2.4. Microwave method for Space Solar Power.....	12
Figure 2.5. MPT (radiative).....	15
Figure 2.6. Circuit diagram of a 2-coil series-series WPT system	18
Figure 2.7. Comparison of electromagnetic field limit for public exposure: (a) electric field, and (b) magnetic field.....	27
Figure 3.1. Inductively-coupled WPT system	30
Figure 3.2. Megawatt range WPT application examples: (a) high-speed train, and (b) large-scale vessel	32
Figure 3.3. Helical-coil WPT design: (a) actual single copper coils, and (b) values of relevant simulation parameters	35
Figure 3.4. Observation of the magnetic field over: (a) a distance of 100 mm, and (b) a distance of 180 mm.....	37

Figure 3.5 Traditional transformer model	38
Figure 3.6. S_{21} over distance and frequency: (a) S_{21} on 2D, and (b) S_{21} on 3-D.....	40
Figure 3.7. Comparison of S_{21} results over distance: (a) 40 mm, (b) 113 mm (critical point), (c) 150 mm, and (d) S_{21} measurement set-up	42
Figure 3.8. Configuration for the FRA measurement: (a) circuit diagram, and (b) FRA test leads connection.....	44
Figure 3.9. VTR of SS circuit: (a) VTR over distance and frequency, and (b) Aerial view of (a).....	45
Figure 3.10. FRA measurement: (a) FRA setup on WPT, and (b) FRA connection on Tx unit.....	47
Figure 3.11. FRA results of VTR magnitude under critical distance: (a) at the wide-range frequencies, and (b) at the resonance frequency.....	48
Figure 3.12. FRA results of impedance value under the critical distance: (a) at the wide-range frequencies, and (b) at the resonance frequency.....	49
Figure 3.13. FRA results of VTR magnitude over the critical distance: (a) at the wide-range frequencies, and (b) at the resonance frequency.....	50
Figure 3.14. FRA results of impedance value over the critical distance: (a) at the wide-range frequencies, and (b) at the resonance frequency.....	51
Figure 3.15. Equivalent circuit of WPT interwinding FRA measurement.....	52
Figure 3.16. Intentional misalignment of Rx winding at 60 mm distance	53
Figure 3.17. FRA measurements under the condition of misalignments	53
Figure 3.18. Transfer impedance comparison	54

Figure 3.19. WPT system model for calculating the self and mutual inductance of coils	56
Figure 3.20. Example of S-parameter result at a 100-mm air gap: (a) absolute, and (b) phase angle.....	57
Figure 3.21. Compensating topologies based on C_1 location: (a) SS, (b) SP, (c) PS, and (d) PP	60
Figure 3.22. Magnetic coupling and field distribution in SP topology using different air gaps ($C_1=180$ nF) at 20 kHz: (a) 10 mm, $C_1=779$ nF, (b) 55mm, $C_1=240$ nF, (c) 100 mm, $C_1=200$ nF, and (d) 150 mm, $C_1=187$ nF.....	64
Figure 3.23. Transferring power and magnetic field distribution in SP topology at 55 mm: (a) supplied power and transferred power across the load, and (b) magnetic coupling at the frequency of 16 kHz.....	65
Figure 3.24. Experimental measurement setup: (a) 1650-filament Litz coils of Tx and Rx with compensating capacitors, and (b) Full-bridge switching device and pulse (gate) signals	67
Figure 3.25. FEKO results of the near field in the SP system at a 100 mm air gap at 20 kHz: (a) electric field, and (b) magnetic field.....	68
Figure 3.26. FEKO results for the electrical parameters of an SP WPT system at 100 mm: (a) in/output voltage, (b) in/output current, (c) input impedance, and (d) in/output power	70
Figure 3.27. Practical measurement of an SP system at 100 mm air gap: (a) Input power, and (b) Output power.....	72
Figure 4.1. Compensating scheme of inductively-coupled WPT system.....	75
Figure 4.2. Simplified IPT Equivalent Circuit: (a) SS or SP topology, (b) PS or PP topology, and (c) equivalent total input impedance.....	77

Figure 4.3. Planar Litz-wire spiral coils design and installation	81
Figure 4.4. Hardware setup along with FRA.....	82
Figure 4.5. FRA measurement schematic.....	82
Figure 4.6. The phase of the input impedance (θ°) using FRA measurement for various compensating topologies: (a) SS, (b) SP, (c) PS, and (d) PP	88
Figure 4.7. VTR patterns at various transfer distances for: (a) SS, (b) SP, (c) PS, and (d) PP topologies	91
Figure 4.8. Input impedance patterns at various transfer distances for: (a) SS, (b) SP, (c) PS, and (d) PP topologies	93
Figure 4.9. Input impedance amplitude of PP topology at an air gap of 55 mm.....	94
Figure 4.10. The layout of the prototype WPT: (a) cross-sectional diagram, and (b) actual implementation.....	95
Figure 4.11. Placement of the ferrite bar: (a) initial position, (b) moderate movement, and (c) significant movement	96
Figure 4.12. Efficiency measurement of the WPT system	96
Figure 4.13. FRA plots at air gap of 55 mm for various placements of the ferrite rods: (a) VTR, and (b) Phase angle δ° of the transfer function $H(j\omega)$	97
Figure 4.14. Flowchart of FRA application on WPT system	98
Figure 4.15. The voltage and current waveforms on RL	100
Figure 5.1. Underwater WPT system model	104
Figure 5.2. Self and mutual inductance of the coils with ferrite materials: (a) self-inductance over the air gap, and (b) coupling coefficient over the air gap.	105

Figure 5.3. Simulation of the magnetic coupling over the distances of: (a) 10 mm, (b) 50 mm, and (c) 100 mm.....	107
Figure 5.4. Prototype of the AUT WPT system	108
Figure 5.5. Prototype and experiment: (a) hardware setup, and (b) control devices....	109
Figure 5.6. Waveform of Tx and Rx in air at 50 mm: (a) Tx measurement, and (b) Rx measurement	111
Figure 5.7. Waveform of Tx and Rx in seawater at 50 mm: (a) Tx measurement, and (b) Rx measurement	112
Figure 5.8. Transfer efficiency comparison.....	113
Figure 5.9. DC–DC efficiency comparison	113
Figure 5.10. FRA measurement of WPT system in seawater.....	115
Figure 5.11. Voltage gain results in air and seawater.....	115
Figure 5.12. Input impedance of AUV WPT system in air and seawater: (a) amplitude, and (b) phase angle	116
Figure 5.13. Demonstration of the WPT Prototype.....	117
Figure 5.14. Two-Coil inductively-coupled SSP WPT system and FRA application..	118
Figure 5.15. Example of FRA connected to WPT system	118
Figure 5.16. Electromagnetic study of two-coil WPT at 85kHz	119
Figure 5.17. Coil misalignments	120
Figure 5.18. FRA measurement at different air gaps	121
Figure 5.19. FRA measurement under different facing conditions	123
Figure 5.20. Example of a WPT system with tilted Rx unit.....	124

Figure 5.21. FRA measurement for different angles	125
Figure 5.22. FRA measurements under different values for compensating capacitor C2	127
Figure 5.23. FRA measurements under different values for compensating capacitor Cm	128
Figure 5.24. FRA measurement under different positioning of ferrite bars	130
Figure 5.25. Phase angle graph: (a) FRA measurement, and (b) calculated angle of the WPT system.....	131
Figure 5.26. Various Waveforms: (a) Sine Wave, (b) Square Wave, and (c) Adjustable Square Wave.....	132

List of Tables

Table 2.1. Classification of WPT methods.....	8
Table 2.2. State of WPT EV charging technology	14
Table 2.3. State of WPT AUV charging technology	17
Table 2.4. Classification and current matters in WPT.....	21
Table 2.5. State of IPT-based WPT technologies in various applications	26
Table 3.1. Detail of winding design	36
Table 3.2. Comparison of the results.....	43
Table 3.3. Properties of the practical coils	56
Table 3.4. S-parameter at 20 kHz.....	58
Table 3.5. Comparison of inductance value between FEKO results and practical measurements	59
Table 3.6. Comparison of the FEKO results and the experimental measurement for an SP WPT model at a 100 mm air gap.....	71
Table 4.1. Compensating Capacitor Value at the Tx side	76
Table 4.2. Parameters of Tx and Rx coils.....	81
Table 4.3. Input impedance and phase angle results using FRA.....	86
Table 4.4. Parameters of the WPT system with ferrite material.....	95
Table 4.5. Overall efficiency of the developed prototype	100
Table 4.6. Comparison of compensation topologies	100

Table 5.1. Underwater WPT system design parameters.....	104
Table 5.2. Electrical parameters of the WPT system	106
Table 5.3. Electromagnetic constant of air and water	108
Table 5.4. Transfer and DC–DC efficiency over different distances	110
Table 5.5. Parameters of WPT System in air	119
Table 5.6. WPT parameters for various distances	122
Table 5.7. WPT parameters for different facing areas	122
Table 5.8. WPT parameters for each angle variation	124
Table 5.9. WPT parameters of C_2 variations	126
Table 5.10. WPT parameters of C_m variations	126
Table 5.11. WPT parameters from variations in the positioning of L_2 ferrite bars	129

List of Abbreviations:

WPT	Wireless Power Transfer
IPT	Inductive Power Transfer
CPT	Capacitive Power Transfer
MPT	Microwave Power Transfer
Tx	Transmitting
Rx	Receiving
HF	High Frequency
RF	Radio Frequency
EVs	Electric Vehicles
AUVs	Autonomous Underwater Vehicles
USD	United States Dollar
HVDC	High Voltage Direct Current
3-D	Three-dimensional
EMI	Electromagnetic Interference
SS	Series-Series
SP	Series-Parallel
PS	Parallel-Series
PP	Parallel-Parallel
SSP	Series/Series-Parallel
SSPS	Space Solar Power System
S-parameter	Scattering Parameter
FEKO	FEldberechnung für Körper mit beliebiger Oberfläche
FRA	Frequency Response Analyser
LVI	Low Voltage Impulse
VTR	Voltage Transfer Ratio

Table of Contents

Acknowledgments

Abstract	i
Statement of contribution to publications	iii
Keywords.....	v
List of Figures	vi
List of Tables.....	xii
List of Abbreviations:.....	xiv
Chapter 1 Introduction	1
1.1. Motivation and objective of the research.....	3
1.2. Contribution of the research	4
1.3. Structure of the thesis	5
Chapter 2 Literature Review	7
2.1. Classification of WPT systems	7
2.1.1. Inductive Power Transfer (IPT).....	9
2.1.2. Capacitive Power Transfer (CPT)	10
2.1.3. Microwave method.....	11

2.2.	WPT technology for EV battery charging	12
2.2.1.	EV charging methods	13
2.2.2.	Standstill WPT charging.....	15
2.2.3.	Dynamic WPT charging	16
2.2.4.	Autonomous Underwater Vehicle Charging	16
2.3.	IPT circuit analysis for problem deduction.....	17
2.4.	Current constraints and solutions.....	21
2.4.1.	Design.....	22
2.4.2.	Efficiency.....	23
2.4.3.	Stability.....	24
2.4.4.	Safety	24
2.4.5.	Summary and expectations	25
2.5.	Summary.....	28
Chapter 3 WPT System Design in FEKO and FRA.....		29
3.1.	Electromagnetic field solver for WPT design.....	29
3.2.	Frequency Analysis Tool for a WPT design.....	31
3.3.	1 MHz Helical-coil WPT design	33
3.3.1.	Coil design.....	34
3.3.2.	S-parameter analysis	38

3.3.3.	FRA Application on WPT	44
3.3.4.	Experimental FRA measurement with different airgaps	46
3.4.	20 kHz Spiral-coil WPT design	55
3.4.1.	Self and mutual inductance of coils.....	55
3.4.2.	Compensation for resonance	59
3.4.3.	Magnetic coupling and field distribution in near field	62
3.4.4.	Power transferred and practical verification.....	66
3.5.	Summary	74
Chapter 4 Design and Maintenance of WPT Systems in Different Compensating Topologies Using FRA.....		75
4.1.	Circuit analysis and input impedance	75
4.2.	Prototype design for FRA measurement.....	80
4.3.	Experimental FRA measurement in various topologies	81
4.4.	VTR patterns over different transfer distances	89
4.5.	LCL topology and ferrite material on the coils.....	94
4.6.	Practical demonstration of WPT system and discussion	99
4.7.	Summary	101
Chapter 5 Performance of WPT System Under Various Operating Conditions .		103
5.1.	FRA for an Autonomous Under Water Vehicle	103

5.1.1.	AUT WPT system design	103
5.1.2.	Magnetic coupling study and practical experiment	106
5.1.3.	FRA measurement of AUT WPT system	114
5.2.	FRA using Various Misalignments of the Coils	117
5.2.1.	Distance Variation	120
5.2.2.	Facing area Variation.....	122
5.2.3.	Angle Variation	124
5.2.4.	Electrical parameter C2 Variation.....	126
5.2.5.	Magnetic parameter variation: ferrite bar movements	129
5.3.	Discussion	131
5.4.	Summary	133
Chapter 6 Conclusion and Future Work.....		135
6.1.	Conclusion	135
6.2.	Future Work.....	137
References.....		139

Chapter 1

Introduction

Since electromagnetism was defined through the combined work of M. Faraday and J. C. Maxwell in the nineteenth century [1], it has been clarified that electromagnetic radiation behaves like light, and hence it was proposed that electric energy is able to be transmitted without wires [2]. Nikola Tesla proposed energy transmission through the air in 1899 and 1914, as shown in Figure 1.1 and Figure 1.2 [3, 4]. He elevated AC voltage up to 100 MV at the top of a transmitting sphere, where a 300 kW power at 150 kHz resonant frequency was radiated to the far end of the coil [5]. He believed that power energy could be transmitted and collected at any place through the ground by an oscillating standing wave. However, practical measurements indicated a low level of efficiency, as the research was conducted on a large scale with the application of a relatively low frequency [6]. In addition, this research was suspended due to a lack of financial support. Consequently, the research on wireless electric energy transmission was shelved for decades [7]. With the rapid advancement in mobile devices, electric vehicles (EVs), and the global trend to adopt smart grids that call for millions of low power-based sensors, wireless technology has re-entered the picture. Unlike information and communication technology (ICT), which utilises a small amount of power to carry valid data, a wireless power transfer (WPT) system aims to send a large amount of electric energy over a particular distance safely. In recent decades, the use of battery-powered devices such as mobile phones, EVs, and medical implants has significantly increased worldwide, and WPT can find significant applications in these devices. WPT can also be implemented in various industrial and robotic applications, such as conveying electric power through a bent joint without physical contact [7] and robotic devices that perform duties such as disaster relief in non-accessible or dangerous areas [8]. For these reasons, it is important to develop more efficient and safe designs for WPT technology.

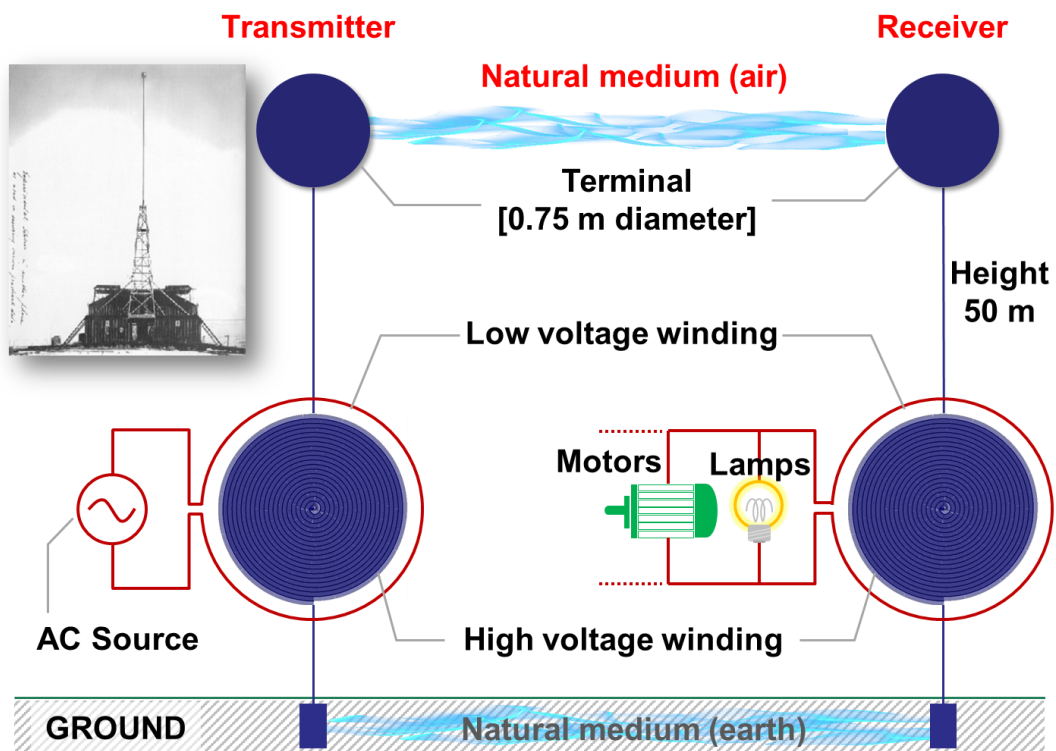


Figure 1.1. Tesla's Colorado Springs experiment in 1899

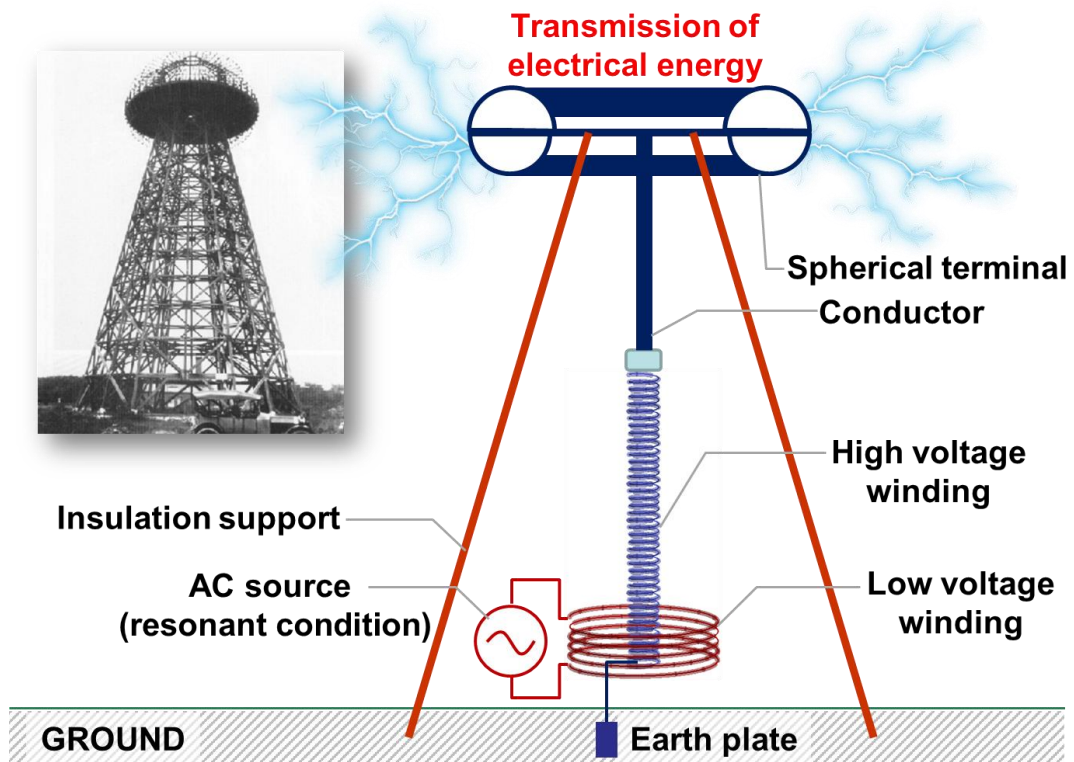


Figure 1.2. Tesla's Wardenclyffe experiment in 1914

1.1. Motivation and objective of the research

The principle of a WPT system was introduced by Nikola Tesla a century ago. At that time, he already understood that electrical energy could be transmitted when the resonance frequency is accurately tuned between the transmitting (Tx) and receiving (Rx) device. Tesla eliminated the magnetic iron core between primary and secondary windings in power transformers like an air-core transformer, then he put capacitors in the windings to compensate for the high reactive component due to the absence of the iron core and tuned the resonance frequency. His century-old practical demonstration presented in [9] is similar to modern WPT systems, as shown in Figure 1.3.

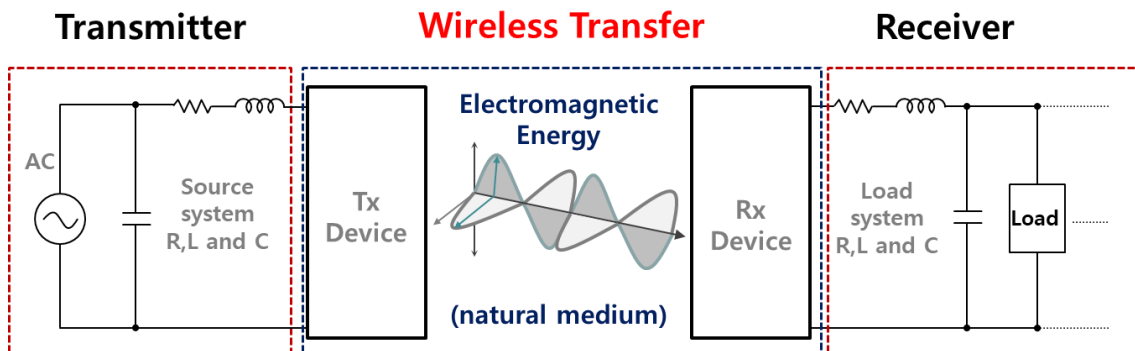


Figure 1.3. Brief schematic of a modern WPT system

As the use of mobile devices and EVs has been increasing over the last decade, WPT applications have been broadly adopted. It is estimated that the wireless charging market for EVs will grow from 16 million US dollars in 2020 to \$234 million in 2027, according to MarketsandMarkets [10]. Currently, WPT systems in the megawatt range are being adopted for public transportation [11-13]. Madawala, U et al. of the University of Auckland also proposed a modular-based WPT system to tap power in the high-voltage direct current (HVDC) system in 2014 [14]. It has not been practically implemented in an existing HVDC system, but they conducted simulations using a 533 kV of 1.8 MW series tap in the system of 1.8 kA HVDC transmission line. It is, therefore, clear that the rated power and size of WPT applications are increasing.

Therefore, it is essential to develop reliable and high-performance WPT applications, and the key objectives of this thesis can be summarised as follows:

- reviewing current studies and trends in WPT applications and design;
- analysing the electric circuit of an inductively-coupled WPT system in various compensations;
- analysing the magnetic coupling characteristics between the Tx and Rx unit of an inductively-coupled WPT system with a 3-D finite element simulation tool;
- developing a practical design for an inductively-coupled WPT system with different materials and mediums;
- suggesting a novel method for the improved design and maintenance performance of the WPT system.

1.2. Contribution of the research

The contribution of this research is summarised below:

- providing a review of the-state-of-the-art IPT, CPT, and microwave current technologies along with a brief comparison of these techniques;
- providing recommendations and future perspectives to overcome current WPT limitations in four main areas: design, efficiency, stability, and safety;
- presenting a case study for an IPT system through analytical calculations, and experimental measurements;
- providing a precise analysis for the formation and distribution of the magnetic coupling between a Tx and Rx unit using the finite element simulation tool known as FEldberechnung für Körper mit beliebiger Oberfläche (FEKO). FEKO is mainly used for studying high-frequency devices. However, the computational tool is not only applicable for the analysis of the electromagnetic characteristic but also identifying the electrical parameters in a WPT system operating in the near field;
- verifying the effectiveness of the electromagnetic solver application for the design and performance analysis of an inductively-coupled WPT system through a practical experiment;
- analysing the input impedance and phase of a two-coil WPT system to tune the resonance frequency. Although the primary purpose of the frequency

response analyser (FRA) is to assess the mechanical integrity of power transformers, the input impedance of WPT systems can be extracted accurately using FRA measurement;

- presenting different patterns of the voltage transfer ratio (VTR) over the transfer distance. When there is any variation in the air gap between the Tx and Rx coils, the performance of the WPT system is critically affected. FRA is used to identify a precise alignment and a valid calibration;
- presenting the discrepancy in the FRA measurements when the magnetic coupling or the geometry of the WPT system changes. When the WPT system is implemented on-site, any mismatch between the designed parameters and the installation should be identified. In addition, monitoring the changes in the electrical components of the WPT system over time is required. FRA measurement is a useful application to diagnose the reliability of WPT systems;
- verifying the efficiency of the WPT systems based on the FEKO simulation results and FRA measurements;
- analysing the frequency responses on the WPT system in different mediums, and various conditions of misalignments between Tx and Rx units.

1.3. Structure of the thesis

This thesis consists of six chapters.

Chapter two introduces a detailed classification and comparison of current WPT technologies. The various applications of different types of transportations are also presented. Then, the limitations of the IPT system are presented through circuit analysis. Recommendations on the basis of four categories – efficiency, design, stability, and safety – for enhancing the performance of WPT technology are then highlighted.

Chapter three presents the utilisation of the 3-D finite element electromagnetism simulation tool known as FEKO and the novel application of FRA for WPT designs. The prototype of a 1.16 MHz spiral-coil shape WPT is designed on the basis of FEKO. Then,

the performance of the prototype WPT system at a frequency of 1.16 MHz is observed over a distance. The results of the experiments indicate that the maximum power transfer distance and the frequency bifurcation can be identified through analysing the WPT voltage transfer ratio and transfer impedance using FRA.

Also, the strength of the magnetic coupling, electrical parameter, and performance of the 20 kHz spiral-coil shaped WPT system is explored. The detailed process for designing the WPT system using FEKO is described, and FRA is used to validate the electrical parameters based on the simulation results. Subsequently, practical measurements to examine the transferred power, output voltage, and other electrical parameters of the WPT prototype are conducted, and the results are compared with the FEKO results.

Chapter four introduces the design and maintenance application of the frequency response analyser for WPT systems in various compensations. A two-coil 20 kHz WPT circuit in different topologies and the equivalent input impedance are observed. Then, FRA measurement is utilised to identify the variation of the resonance frequency, and the value of input impedance in a wide range of frequencies. The experiment results confirm that the FRA measurements are advantageous for detecting any displacements in the magnetic coupling and the geometric change of the WPT components.

Chapter five provides several case studies using FRA measurements on WPT systems. The FRA results show the difference with the initial fingerprint trace when the Tx and Rx coils are misaligned in three-dimensional coordinates, and the electromagnetic parameters were altered due to deterioration over time or in different mediums between the coils.

Lastly, an entire summary of this thesis and future works are proposed in Chapter six.

Chapter 2

Literature Review

WPT applications are broadly adopted for charging batteries and supplying electric power to various devices [15-19]. Since WPT technology was introduced a century ago by Nikola Tesla, who dreamed of delivering free electric energy everywhere through the earth, his idea was frozen until the 1990s due to a lack of funds and technology support [6, 20]. However, wireless communication technology commercialised by Guglielmo Marconi has been successfully developed because it requires a small amount of electric energy to transmit information over long distances effectively [21]. WPT technology resurfaced as a result of increasing demand from EVs, mobile devices, and sensors. The modern design and application of the wireless charging system for EVs was presented by J. T. Boys in 1994 [22]. In 2007, the Massachusetts Institute of Technology demonstrated a transfer of electric power of 60 W at a distance of 2 m with 15% efficiency [23]. The Korea Advanced Institute of Science Technology introduced a WPT system that can send a few hundred watts over a distance of 5 m in 2015 [24]. The efficiency in the demonstration by the Harbin Institute of Technology in China to transmit electric power of 2.86 kW over a distance of 150 mm reached approximately 90% [25].

2.1. Classification of WPT systems

WPT can be mainly categorised into near-field and far-field applications, which are also called non-radiative and radiative applications, respectively. Near-field WPT can be feasible using inductive power transfer (IPT) and capacitive power transfer (CPT), as shown in Figure 2.1. Although the performance of CPT is improving fast, IPT applications are broadly adopted for high-power and mid-range distance charging applications [26].

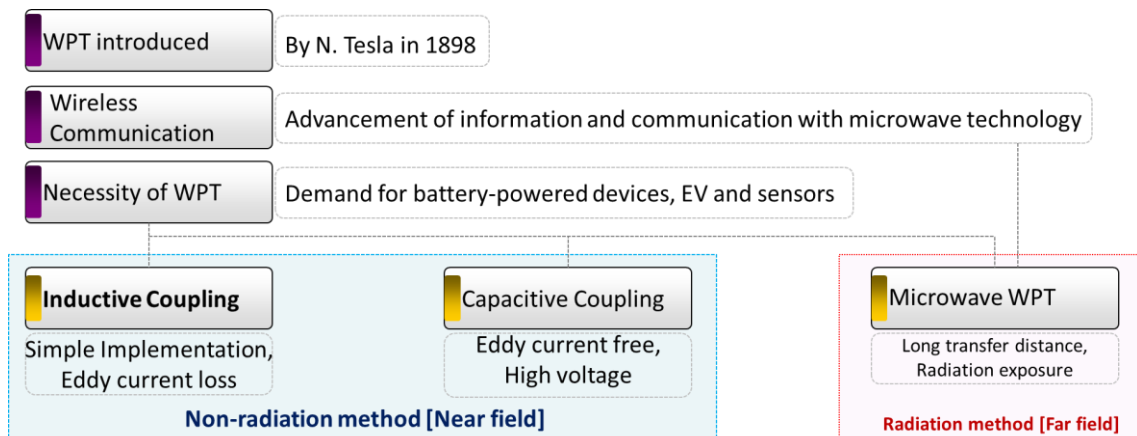


Figure 2.1. Overview of WPT technology

Table 2.1. Classification of WPT methods

Classification Category	Non-radiative		Radiative
	Inductive Power Transfer (IPT)	Capacitive Power Transfer (CPT)	Microwave Power Transfer (MPT)
Composition	Inductive coupling system, Intermediator (if necessary)	Capacitive coupling system, Intermediator (if necessary)	Microwave source, Waveguide, Tx, Rx Antenna, Rectifying System
Transfer Capacity	mW – kW	mW – 3 kW	μW, mW-kW
Frequency Range	kHz – MHz	kHz – MHz	GHz
Transfer Distance	≈ 10 times of coil diameter	< 360 mm [27]	m – km
Features	Non-radiated characteristics	Non-radiated characteristics	Radiated characteristics
Difficulty of Design	Moderate	Moderate	High
Advantages	Non-radiative (uncertain safety)	Eddy current loss free	High energy, Long-distance
Drawbacks	Sensitive to misalignment and driving frequency	High voltage	Electromagnetic wave exposure
Applications	Home appliances, Railway vehicles, EVs	Railway Vehicles, EVs, Medical devices	SSPS, Wireless sensor, Home appliances

WPT has been found to be feasible under two main categories: radiative and non-radiative methods, as shown in Table 2.1. The non-radiative application is classified into two approaches: inductive power transfer (IPT) and capacitive power transfer (CPT). An innovative IPT-CPT combined system transferring electric power of 2.84 kW at 1 MHz frequency with 94.5% efficiency over a distance of 150 mm was demonstrated in 2016 [28]. Also, the inductive and capacitive hybrid system indicated a constant output power of 655 W with 85.82% DC-DC efficiency over various ranges of coupler misalignments between 0 mm and 270 mm in 2019 [29].

2.1.1. Inductive Power Transfer (IPT)

The first demonstration of WPT, which is analogous to the present IPT topology, was performed by Tesla in 1898 [30]. He clarified that the resonant system allows for the electromagnetic coupling between transmitter and receiver in near field. Afterward, further research was continued to enhance the technology of IPT in the field of biological engineering [31-33]. The development of Litz wire, consisting of several stranded-wires, to reduce skin and proximity effect losses at high-frequency (HF), and the advancement of HF power electronic switches, contributed to the enhancement of IPT in the mid-19th century. A commercial inductively-coupled WPT was introduced by J. Boys in 1994 [34], and an intermediate coil at the Tx device to increase the transfer distance was proposed in 1998 [35]. The intermediate coil, also known as a relay coil, can enhance the efficiency over the transfer distance. However, this requires further considerations, such as cost-effectiveness and the difficulty of tuning the frequency due to the additional unit [36]. The magnetic resonant coupling (MRC) system introduced by the Massachusetts Institute of Technology (MIT) in 2007 proposed auxiliary coils with compensating capacitors at both transmitter and receiver [23]. The transfer distance of this four-coil system was enhanced by inserting additional sending and Rx coils [37]. This system could achieve 60 W of WPT over a 2 m distance. While system efficiency between the transmitter and the receiver was only 15% at 10 MHz, this achievement has motivated researchers to advance the WPT for mid-range distances.

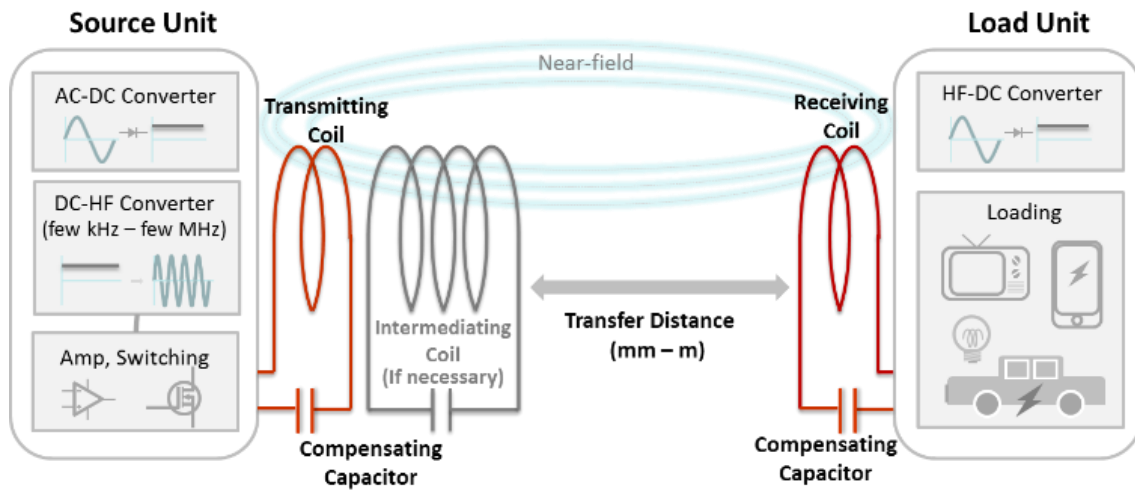


Figure 2.2. Inductive power transfer with compensating capacitors in series

It is convenient to think of inductively-coupled power transfer as an air-core transformer. When the current is flowing in the source coil, it produces magnetic flux that links within the load coil and induces electric energy into it based on Faraday's law, as shown in Figure 2.2. When the compensating capacitor cancels out the leakage inductance of the winding, energy conversion takes place between the two coils wirelessly without significant radiation. The mechanism of both IPT and MRC systems is based on the same principle [36]. Although with four-coils the system can achieve a larger distance than the two-coil system [38], it was pointed out that the system efficiency and amount of power delivered are mainly affected by the volume of copper (or the number of turns), not by the number of coils [39].

2.1.2. Capacitive Power Transfer (CPT)

Power energy can also be transferred using capacitive coupling between the transmitter and the receiver, as shown in Figure 2.3. It was considered that the CPT system is suitable for sending low power over a gap of a few millimetres until 2015 [26, 40-43]. However, a system that can transfer 700 W of electric power over 17 mm to charge the battery pack of a railway vehicle with 300V DC output voltage with 91% efficiency at 2 MHz switching frequency was introduced in 2016 [44]. Furthermore, recent research in 2017 indicated that 1.97 kW of power could be transferred over a gap of 150 mm by a six-plate capacitive coupler with system efficiency (or DC-DC efficiency)

of 91.6 % [45]. The demonstration in 2017 showed that a transfer distance of 360 mm was possible with input power of 150 W and DC-DC efficiency of 66.9 %; however, the repeater was implemented between the Tx and Rx unit to extend the transfer distance [46]. This system requires consideration of the electromagnetic interference (EMI) effect and extreme caution due to the high voltage on the capacitive coupling plates [45]. However, unlike IPT, CPT is free from eddy current loss due to the high-frequency current [47].

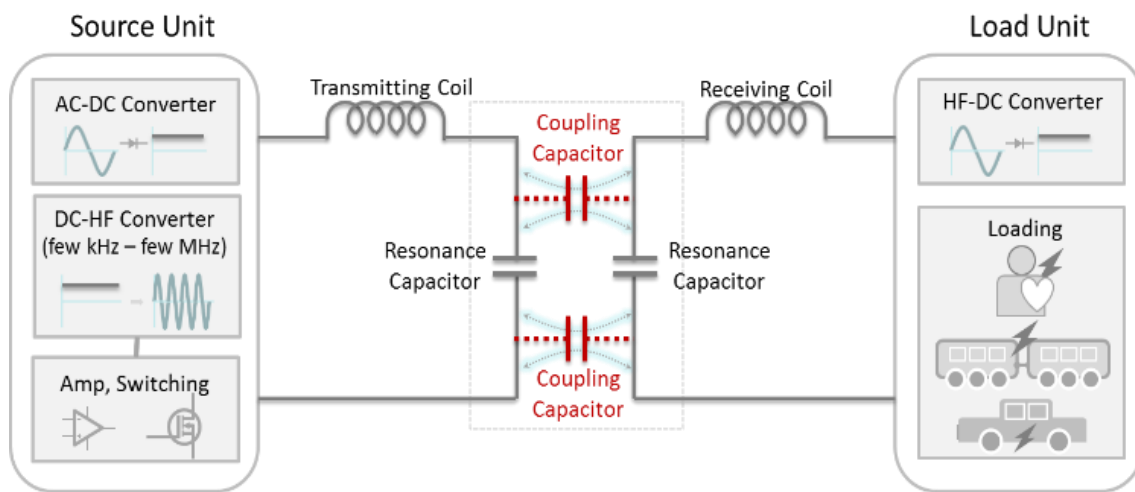


Figure 2.3. Capacitive Power Transfer

2.1.3. Microwave method

In the case of microwave power transfer (MPT), the radiative energy transfer occurs at far-field. In 1968, W. C. Brown demonstrated a free-flying helicopter powered by MPT [5]. He then improved the DC-RF-transfer-RF-DC system at a frequency of 2.45 GHz with a DC-DC efficiency of 26.5%. The first ground-to-ground MPT was demonstrated in 1975 [5]. In the experiment, 470 kW of electric energy was radiated on a transmitter with a diameter of 26 m, and 30 kW of power was received via the rectenna arrays of 3.4×7.2 m over a distance of 1 mile.

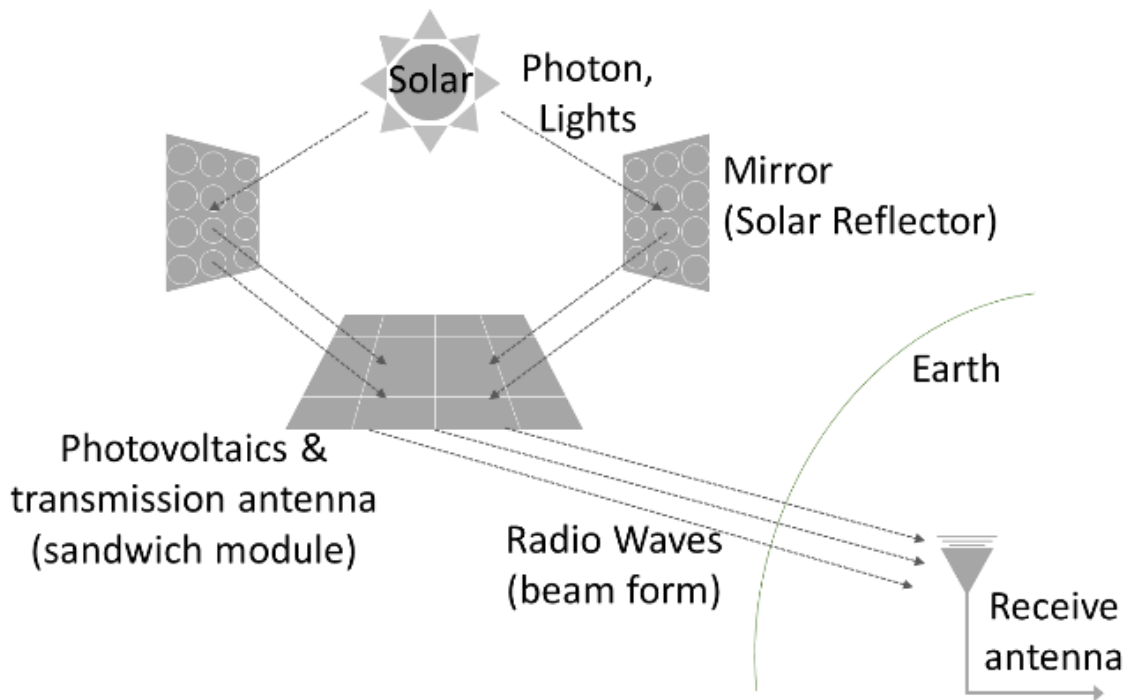


Figure 2.4. Microwave method for Space Solar Power

The rectifying efficiency was 82.5 % at 2.388 GHz transmitting frequency. The US Department of Energy and the National Aeronautics and Space Administration (NASA) suggested a free energy transmission from space solar power system (SSPA) in the 1970s [48]. The expected transmitting power was from 50 MW to 250 MW at middle earth orbits over a distance between 6,000 and 12,000 km, as shown in Figure 2.4 [49].

The overall efficiency of SSPA is generally under 17% at a frequency range of 2.45 GHz to 5.8 GHz. Energy harvesting can be accomplished when a rectifying antenna is installed near transmitters to collect unused power. In general, the collectable power is only from μW to a few mW [50]. Although the amount of energy is little and the implementation of the rectenna is complex, MPT provides a great solution for charging wireless micro-sensors or medical devices in remote areas [51].

2.2. WPT technology for EV battery charging

In 2016, over 2.3 million charging systems for EVs were used around the world, and it was expected that the global EV stock will surpass 20 million in 2020 [52]. WPT

technology facilitates removing the electrical plugs between a charging device and EVs. Furthermore, the volume of the batteries equipped in the EVs can be significantly reduced when using such a dynamic charging system. Therefore, it is predicted that the application of WPT charging systems for charging EV batteries will lead the global growth of EV markets [53]. Due to the rapid increase in demand for EVs, and the advancement of power electronics, the application of the WPT system is currently being considered a convenient and efficient solution for battery charging. The transfer distance between the charger on the ground (or wall) and a vehicle can be enhanced by implementing relay coils between the Tx and Rx units. However, the maximum efficiency of the four-coil system in [23] is restricted to 50% as the highest coupling coefficient between the coils can be accomplished when the source impedance equals the circuit input impedance according to the mathematical circuit model.

Furthermore, the additional coils of the WPT system result in the difficulty of the frequency tuning [36]. The WPT system, consisting of a Tx and Rx unit, can charge an EV battery at the distance of the road-to-body with high efficiency. Therefore, a two-coil IPT or CPT topology is considered as a commercial EV charging system.

2.2.1. EV charging methods

The various applications of WPT technologies for supplying electric energy to all forms of transportation on land, at sea and in the air have been suggested. In 1968, W. C. Brown demonstrated a microwave-powered helicopter weighing 2.27 kg in flight at an altitude of 15.24 m [54]. He then proposed an innovative helicopter flying at 15 km altitude powered by 600 kW at 2.45 GHz transferred from the ground. The laboratory verification for high-power WPT marine applications have also been completed in Norway. It was expected that a ferry with an IPT battery charging device exceeding 1 MW of power be put into service in 2017 [11]. On land, WPT technologies are mainly used for charging the battery in four-wheel vehicles. The efficiency, method type, transfer distance, and other details for the EV charging technologies are summarised in Table 2.2.

Table 2.2. State of WPT EV charging technology

Ref.	Year	Method	Topology	freq.	Power	Efficiency	Air Gap	Location	Application	Objective
[55]	2013	IPT	<i>PP</i> (Double D)	20 kHz	2kW	-	200 mm	New Zealand	EV (Prototype)	Battery Charging
[56]	2013	IPT	<i>SS</i>	20 kHz	100kW	85%	170 mm (track:12km)	Korea	Commercial Public Bus	Battery Charging
[13]	2015	IPT	<i>SS</i>	61.5 kHz	818kW	82.7%	50 mm (track:128m)	Korea	High-Speed Train	Real-Time Use
[57]	2017	IPT	<i>SS</i>	50 kHz, 68.5 kHz	1.5kW	94.5%	100 mm	Hong Kong	EV	Battery Charging
[25]	2017	IPT	<i>SS</i>	85.5 kHz	2.86kW	88.1%	150 mm	China	Sightseeing EV	Battery Charging
[11]	2017	IPT	<i>SS</i>	2-8 kHz	1MW	97% (expected)	200-500 mm	Norway	Vessel (Pilot stage)	Battery Charging
[58]	2018	IPT	<i>LCC</i>	85kHz	3.09kW	95.49%	150mm	USA	EV	Battery Charging
[59]	2019	IPT with solenoid	<i>SS</i>	85kHz	3.5kW	> 90%	132 mm	New Zealand	EV	Battery Charging
[60]	2019	IPT	<i>LCL</i> Three phases Bi-directional	85kHz	1.3kW	91%-96%	106 mm	New Zealand	EV	Battery Charging
[61]	2020	IPT	<i>SS</i> Bi-directional	85kHz	5kW	90.1%	50 mm	Canada	EV rear side Tx and Rx	Battery Charging
[62]	2020	IPT	<i>LCC</i>	18.9kHz	27.8kW	93%	150 mm	China	Light Rail Train	Hybrid Storage charging
[63]	2015	CPT	<i>LCLC</i>	1 MHz	2.4kW 1.6kW	90.8% 89.7%	150 mm 300 mm	USA	EV (Prototype)	Battery Charging
[40]	2016	CPT	<i>LCLC</i>	530 kHz	1kW	88%	0.1mm	USA	EV	Battery Charging
[44]	2016	CPT	<i>LCLC</i>	2 MHz	700W	91.3%	17 mm (track:1.5m)	China	Railway (Prototype)	Dynamic Charging
[45]	2017	CPT	<i>LCL</i>	1 MHz	1.97kW	91.6%	150 mm	USA	EV (Prototype)	Battery Charging
[64]	2020	CPT	<i>LCL-L</i>	1 MHz	1.5kW	85.5%	150mm	UK	EV	Battery Charging
[28]	2016	IPT + CPT	<i>LC</i> Two-coupler	1 MHz	2.84kW	94.5%	150 mm	USA	EV	Battery Charging
[65]	2017	IPT + CPT	<i>LCL</i> Integrated coupler	1 MHz	100W	73.6%	180 mm	USA	EV	Battery Charging
[66]	2020	IPT + CPT	<i>Double LC</i>	1 MHz	653 W	87.7%	60 mm	China	Railway	Battery Charging
[54]	1968	MPT	Tx antenna on ground	2.45 GHz	270W	<26.5%	15.2 m	USA	Helicopter	Real-Time Use
[67]	2009	MPT	road-to-body	2.45 GHz	1kW	38%	125 mm	Japan	EV	Battery Charging
[68]	2012	MPT	top-to-roof	2.45 GHz	10kW	80% (RF-DC)	1.200 m	Japan	Heavy EV	Battery Charging
[69]	2016	MPT	top-to-roof	5.8 GHz	100kW	62%	0.1-06 m	Japan	Heavy EV (suggested)	Battery Charging

2.2.2. Standstill WPT charging

The charging device in a stationary WPT charging system can be more simplified than that used by plug-in EVs due to the absence of the power cable between the charging station and the EV. The efficiency of the current IPT systems for standstill charging is over 90% [57]. The CPT and MPT technologies can also be adopted if the potential hazards – high-voltage electric shock in CPT, and radiation exposure in MPT – are eliminated. To construct an efficient and simple system, the CPT conformal bumper charging system was suggested [40]. However, the charging station on the wall and the car bumper should be in contact as the allowable air gap is very small. The research team at Kyoto University in Japan suggests two types of MPT EV charging systems, as shown in Figure 2.5 [68]. For light vehicles, the road-to-body topology, similar to the conventional IPT charging system, was demonstrated in 2008. The transmission efficiency in the first demonstration was 67%, then it was improved to 76% by modifying the rectenna and using enhancing RF devices. Then, they found that poor efficiency is observed at a short distance. Hence, the mid-distance MPT charging system was introduced. The battery in heavy EVs, such as trucks and buses, is chargeable in top-to-roof systems to maintain the right charging gap between the transmitting antenna and the rectenna on the roof of the vehicle.

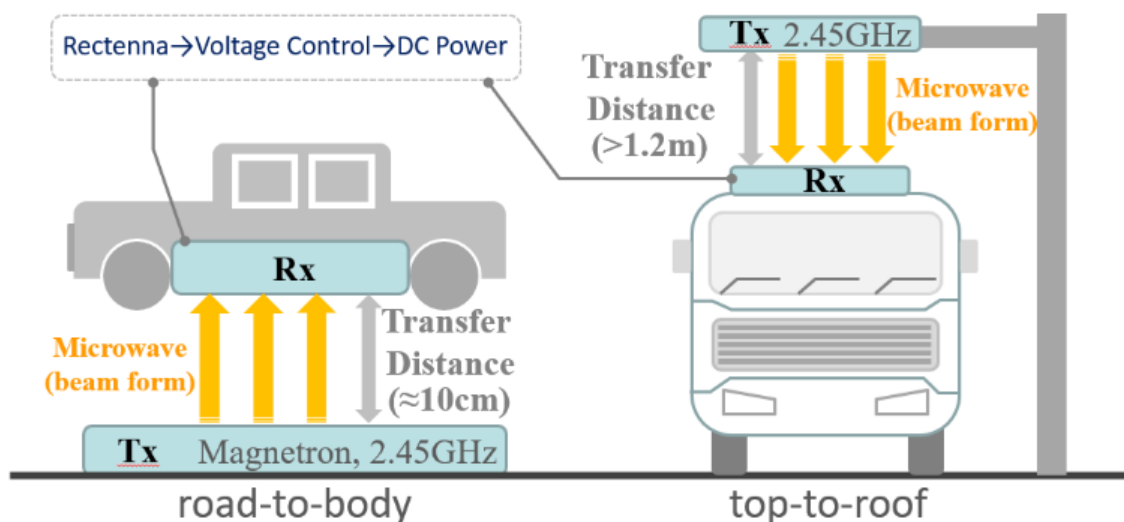


Figure 2.5. MPT (radiative)

2.2.3. Dynamic WPT charging

As large EV vehicles save more fossil fuel, make more profit, and require more significant battery volume than light vehicles, a dynamic charging solution can contribute to the expansion of the large EV market. In the city of Gumi in the south-east region of Korea, an electric passenger bus has been operated on a 12-km shuttle route since 2014 [56]. The transmitting cable is buried under the road and is magnetically coupled with the pick-up on the underbody of the bus. A wireless-powered high-speed train was also successfully demonstrated in Korea in 2017 [13]. The train received 818 kW electric energy at a frequency of 85.5 kHz with a 5cm air gap between the rails and the underbody of the train with an efficiency rate of 82.7%. For light EVs, it is also essential to reduce the volume of the battery. A Li-Ion cell is widely used for rechargeable EV batteries, and a 10 kWh cell costs approximately 7,000 USD. Moreover, it is estimated that the weight of the mounted battery is a third of the total weight of the EV [70]. Therefore, both the fully-dynamic, like the examples mentioned above, and semi-dynamic applications, where the battery of the EV is recharged at road junctions or designated stopping areas on the road, are being considered.

2.2.4. Autonomous Underwater Vehicle Charging

Autonomous underwater vehicles (AUVs) are used for surveying marine resources and monitoring the condition of the properties underwater. AUVs are operated unmanned, and rechargeable batteries provide the power. To charge or replace the battery pack on the AUV, it is necessary to approach the ship, and this results in increased cost and inefficient performance [71]. A plug-in system with a connector between the charging station and the AUV can also be unsafe, and it is difficult to maintain in the water. Hence, a WPT charging application could be a valid solution. The charging system on AUVs mainly adopts an inductively-coupled WPT system, and the expected efficiency is over 94% when the output power is 500 W at 1,000 m deep in the sea [72]. The details of the WPT application on AUVs are presented in Table 2.3.

Table 2.3. State of WPT AUV charging technology

Ref.	Year	Power	Efficiency	Airgap	Frequency	Location	Application
[73]	2007	240 W	70%	2 mm	50 kHz	USA	Underwater Vehicle Charging
[74]	2010	400 W	90%	2 mm	94.3 kHz	China	4000-m Deep sea
[72]	2014	45 W	84%	2 mm	167 kHz	China	Underwater Vehicle Charging
[75]	2016	25 W	65%	100 mm	200 kHz	Japan	Underwater Vehicle Charging (floating charging station)
[76]	2017	10 W	<47% [Z matching]	82 mm	90 kHz	China	Frequency bifurcation study
[77]	2018	1 kW	92.41 %	21 mm	465 kHz	USA	3phase Underwater Vehicle Charging
[78]	2019	200 W	<90 %	66 mm	60-600 kHz	China	Underwater Vehicle Charging
[79]	2020	630 W	89.7 %	8 mm	50 kHz	China	Underwater Vehicle Charging (dipole coil)

The WPT system for AUVs has a similar design procedure and circuit topology to that of EVs on the road. However, it should be considered that AUVs indicate increased eddy current loss when the resonance frequency rises [78]. Unlike WPT systems in the air, the literature [80] has highlighted additional considerations: the correlation between the electrical parameters of the WPT circuit and the highly conductive seawater, the radiation in the seawater, and the optimisation of the resonance frequency in the dynamic nature of the ocean.

2.3. IPT circuit analysis for problem deduction

As WPT systems generally require a high frequency and a compensating component to comply with a resonant condition, some difficulties are inevitable. To understand the mechanism of power transfer under magnetic coupling and to illustrate the implementation difficulties, a two-coil inductively-coupled WPT system is presented below.

A two-coil WPT circuit with compensating capacitors in series on both sides is depicted in Figure 2.6. The efficiency of this series-series (SS) system can be enhanced by installing an intermediate coil. However, this will require accurate frequency tuning [39]. The circuit input and output currents are expressed in the matrix form in (2.1) where, r_1 , r_2 , L_1 , L_2 , C_1 and C_2 represent the parasitic resistance, self-inductance and compensating capacitance of the Tx and Rx units, respectively.

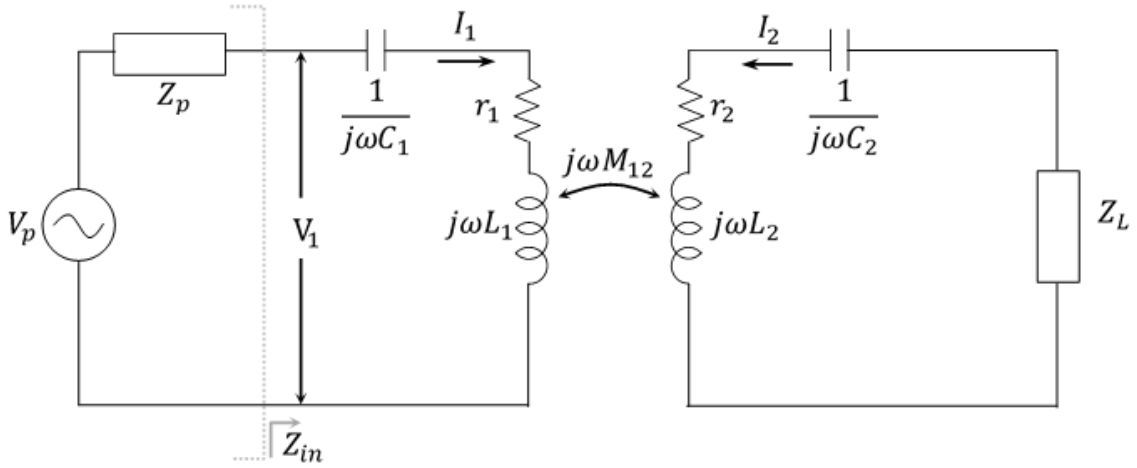


Figure 2.6. Circuit diagram of a 2-coil series-series WPT system

$$\begin{bmatrix} I_1 \\ I_2 \end{bmatrix} = \frac{1}{Z_{det}} \begin{bmatrix} Z_2 + Z_L & -j\omega M_{12} \\ -j\omega M_{12} & Z_p + Z_1 \end{bmatrix} \begin{bmatrix} V_p \\ 0 \end{bmatrix} \quad (2.1)$$

The impedances in (2.1) can be derived as $Z_1 = r_1 + j\omega L_1 + 1/j\omega C_1$, $Z_2 = r_2 + j\omega L_2 + 1/j\omega C_2$ and $Z_{det} = (Z_p + Z_1)(Z_2 + Z_L) + \omega^2 M_{12}^2$. To simplify the analysis, the Tx and Rx units are assumed to be reciprocal (i.e. $L_1 = L_2$, $C_1 = C_2$), from which resonant frequency can be calculated as $\omega_0^2 = 1/L_1 C_1 = 1/L_2 C_2$. Additionally, it is assumed that source impedance Z_p and load impedance Z_L are purely resistive – $Z_L = R_L$, $Z_p = R_p$. The efficiency is defined as the ratio of the power transferred to the load to the total input power as in (2.2), where $R_{lump} = 2R_L R_p r_2 + r_2^2 R_p + R_L^2 r_1 + 2R_L r_1 r_2 + r_1 r_2^2$ and k_{12} is the coupling coefficient (defined in (2.3)). As can be seen in (2.2), efficiency can be increased through controlling several parameters: the resonance frequency ω_0 and self-

inductance of the two coils need to be as high as possible, whereas the parasitic resistances r_1 and r_2 should be minimized. These parameters are strongly correlated with the resonance circuit quality factor $Q = \frac{\omega_0 L}{r}$, which represents the proportion of the stored energy within the reactive components and the dissipated energy in the resistive components.

$$\begin{aligned} \eta &= \frac{\omega_0^2 M_{12}^2 R_L}{(R_p + r_1)(R_L + r_2)^2 + \omega_0^2 M_{12}^2 (R_L + r_2)} \\ &= \frac{R_L}{\left(\frac{R_p R_L^2 + R_{lump}}{\omega_0^2 k_{12}^2 L_1 L_2} \right) + (R_L + r_2)} \end{aligned} \quad (2.2)$$

A high level of Q results in a large amount of power conversion; however, this requires a precise adjustment to the resonance frequency. For this reason, a magnetic resonance WPT with multiple intermediating coils is less practical than a two-coil system, although the transfer distance is superior in the former. The efficiency can also be enhanced by adjusting either the source resistance R_p or the load resistance R_L . The efficiency also depends on the coupling coefficient k_{12} between the Tx coil and the Rx coil given in (2.3) [81]. k_{12} is sensitive to the distance between the coils and it sharply declines when the distance increases. In the coupling coefficient formula, N_1, N_2, a_1, a_2, L_1 and L_2 are the number of turns, radius of the coil loop, self-inductance at the Tx and the Rx sides, respectively, while D is the distance between the coils.

$$k_{12} = \frac{\mu_0 \pi N_1 N_2 (a_1 a_2)^2}{2(a_1^2 + D^2)^{3/2} \sqrt{L_1 L_2}} \quad (2.3)$$

In the resonance condition, the receiving power P_L is defined as in (2.4). To accomplish maximum power transfer, the load resistance is extracted by differentiating (2.4) with respect to R_L , which will lead to optimum load resistance $R_{L,max}$ given in (2.5).

$$P_L = I_2^2 R_L = \frac{\omega_0^2 M_{12}^2 V_p^2}{\left((R_p + r_1)(R_L + r_2) + \omega_0^2 M_{12}^2 \right)^2} R_L \quad (2.4)$$

$$R_{L,max} = \sqrt{\frac{(\omega_0^2 M_{12}^2 + R_p r_2 + r_1 r_2)^2}{R_p^2 + r_1^2}} \quad (2.5)$$

Assuming the values of parasitic resistances r_1 and r_2 are very small with respect to the load resistance R_L , (2.5) can be simplified to

$$R_{L,max} = \frac{\omega_0^2 M_{12}^2}{R_p} \quad (2.6)$$

With $R_{L,max}$, the maximum receiving power can be expressed as below

$$P_{L,max} = \frac{\omega_0^2 M_{12}^2 R_{L,max}}{(R_p R_{L,max} + \omega_0^2 M_{12}^2)^2} V_p^2 \quad (2.7)$$

2.4. Current constraints and solutions

From the above review and circuit analysis, one can identify four main issues within WPT technology that need further research, as summarised in Table 2.4 and briefly explained below.

Table 2.4. Classification and current matters in WPT

Classification	Indication of problems	Reference
Design	How can the resistance of the coils be reduced to enhance the Q factor?	[82], [83], [84]
	What type of coil is most suitable for the system? (e.g., spiral, helical or others)	[85], [86], [58]
	How should inductive coupling over distance be compensated?	[8], [24]
Efficiency	What type of amplifier provides the best performance?	[87], [88]
	How should the impedance matching between Tx and Rx be performed correctly?	[89], [90], [91]
	How does the efficiency increase below the critical distance?	[92], [93], [94], [95]
	How should high efficiency be kept constant, with multiple coils or loads?	[96], [97],
Stability	How should the system be protected from abnormal conditions?	[98]
	What kind of LC combination is applied to the resonant circuit? (e.g., SS, SP, PS or PP)	[99], [100], [101], [102]
	How should the power transfer in multiple devices be optimised?	[103]
Safety	How should the radiation in the magnetic coupling system be measured precisely?	[104], [105], [106], [107]
	What kind of standard is applied to the radiation exposure measurement?	[106]

2.4.1. Design

From (2.2), it was clarified that a high Q factor enhances energy conversion in the near field. By increasing the coupling coefficient, self-inductance, resonance frequency, or reducing the parasitic resistance of the coil, a high level of Q factor can be achieved. To reduce the power loss on the windings, two types of coils: solid-ferrite-material-based and prefractured-material-based, are introduced in [82]. The solid-ferrite-material-based coil is beneficial when system efficiency is more important than the difficulty of the implantation. On the other hand, a prefractured-material-based coil is suitable for portable device applications. For the suppression of the skin and proximity effect on the conductor in the high-frequency range, a stranded Litz wire is used [83]. Superconductor winding can also be used to improve efficiency by 40% compared to conventional copper wound coil [84]. However, the implementation of superconductors is still impractical and expensive. The parasitic resistance of the coil can be mitigated by rewinding the coil with a thick wire or utilising a conductor made of advanced material, but the convenience of the implementation and the cost need to be examined. Besides, in the system with a single transmitter and receiver, the interaction between the two coils only occurs in a single coordinate plane. To resolve this, a three-dimensional transmitter was introduced in [85]. In such a 3-D system, the strength of the mutual inductance can be compensated using the multidirectional couplings, and the power is transferred through the skew path with the domino coils [86]. A prototype WPT at 60Hz was demonstrated in [8]. To overcome the lack of Q factor, a silicon steel magnetic core was used to reinforce the coupling coefficient. However, the number of turns is much larger than a high frequency-based system, and the efficiency sharply declined over a 100 mm distance. In 2015, Korea Advanced Institute of Science and Technology (KAIST) implemented a new topology of WPT that can send a few hundred watts of energy up to a 5-m distance. The expansion of the transfer distance was accomplished by inserting a dipole antenna made of a magnetic core into the Tx and Rx windings [24].

2.4.2. Efficiency

For the best performance of a WPT system, primarily, an efficient HF power supply is essential. The power supply for WPT generally falls into three topologies: resonant half, full-bridge converter or resonant push-pull converter, and class-E amplifier [47]. As reported in [87], the class-E amplifier with independent gate drive achieved end-to-end efficiency of 75.7% for a 295 W power transfer at 134 kHz. The current-mode and voltage-mode class-E amplifier, providing an advanced performance over the load variation, was presented in [88]. It was recorded that an efficiency of 83%, with an approximately 25 W power transfer at 6.78 MHz. More power can be transferred with the impedance matching technique [89]. However, this calls for a trade-off between the amount of power transfer and transfer efficiency. The accomplishment of impedance matching is not easy in WPT, as various conditions in a complex conjugate (i.e., reflections, dynamic range, and signal to noise ratio) need to be considered [90]. A frequency bifurcation is physically unclear [108], and it is unavoidable at close distances between coils in the inductive power transfer system. To enhance the efficiency in the magnetically over-coupled region, two non-identical Tx and Rx coils are proposed [93]. It was also verified that the low efficiency at near distance could also be enhanced by adjusting the angle of the resonance coil to reduce the mutual inductance M_{12} , as the rapid increase of M_{12} at the over-coupled region results in the frequency bifurcation [92]. Alternatively, efficiency over short distances is improved by shifting the resonance frequency [94]. In [95], an algorithm to optimise the load resistance for maximum transfer efficiency is presented. The transfer efficiency was improved from 53% to 71% with this optimisation technique. Distinct patterns of the frequency bifurcation are observed against the variation of the frequency and the coupling coefficient between Tx and Rx [109]. In general, the inductively-coupled system indicates a V-pattern similar to the one in Figure 3.6. However, different patterns such as I-type or W-type can also be shown when multiple relay (or intermediating, repeating) coils are placed between the transmitter and the receiver. The additional coil strengthens the magnetic coupling and improves the efficiency [96]. However, the system becomes more sensitive to the frequency bifurcation and it requires precise frequency tuning [97].

2.4.3. Stability

The WPT system can be damaged when a malfunction occurs in amplifying units or in any of the electrical components or due to the high voltage induction in the energisation without load condition. The circuits of WPT systems can be classified based on the compensating capacitance for series-series (SS), series-parallel (SP), parallel-parallel (PP), and parallel-series (PS) [99]. In [100], a SS composition with a constant current source is reported as the most reliable configuration in terms of five criteria: maximum efficiency, maximum power transfer, load-independent output voltage and current, magnetic coupling co-efficient (k_{12}) independence, and allowance for no magnetic coupling ($k_{12} = 0$). As previously stated in section 2.3.1, the efficiency of an SS system significantly declines with increased source resistance. The load detection system without a supplementary communication device was introduced in [98]. Three different conditions – safe, no-load, and fault – are determined by the voltage on the transmitter coil and the source current. In addition, the optimal load resistance is handled to achieve maximum power efficiency or maximum power delivery in a multiple-receiver system [103].

2.4.4. Safety

The human exposure to electric and magnetic fields in the transfer space must be considered in any WPT topology. The level of the electric field exceeds the guideline of 83 V/m recommended by the International Commission on Non-Ionising Radiation Protection (ICNIRP) [110], when two coils are closer than 5 cm in a WPT system of 1 W input power and 10 MHz frequency. On the other hand, the level of the magnetic field of the above-mentioned system complies with the standard level of 21 A/m [104]. Although the inductive coupling method is categorised as a non-radiative mechanism, residual electromagnetic power still arises in the vicinity of the WPT system. In this regard, James C. Lin stated that WPT energy could be absorbed into human bodies or biological organisms [105].

2.4.5. Summary and expectations

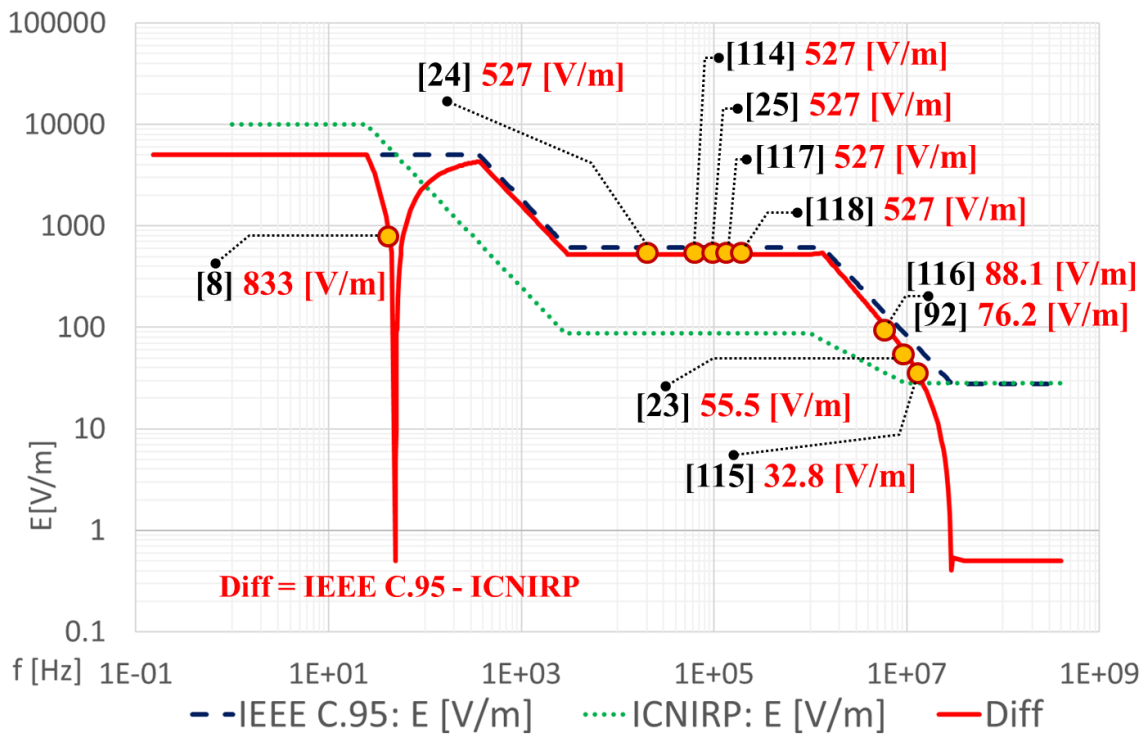
Since the technology of the middle-range power transfer was introduced, the efficiency and the transfer distance have been improved over the last decade, as summarised in Table 2.5. The critical challenge in developing a reliable WPT system is to maximise the amount of safely transferred energy while maintaining efficiency over the distance. For instance, if the resonance frequency merely rises to enhance the Q factor, the parasitic resistance on the coil might increase due to the skin effect, and it is difficult to tune the sensitive elements at the exact frequency. In an advanced WPT design, new materials such as superconductors or supercapacitors are applied. It was also clarified that the additional magnetic elements such as dipole magnetic cores in the coils or the extra transmitters in 3-D planes could enhance the performance of WPT. However, optimisation analysis with a cost-benefit study is essential for the implementation of these solutions. As shown in Table 2.5, the efficiency of the recently developed systems reaches 90% due to the high-performance power devices used in the implementation. However, this high efficiency presents only at near transfer distance while poor efficiency still occurs in the region of the weak magnetic coupling.

It is expected that the demands of more high-powered and more reliable WPT systems in various environments increase significantly in the very near future. It is also expected that the demand for a higher amount of power transfer and simultaneous use of multiple WPT devices in a room will increase [111]. It is noted that transfer efficiency does not consider the source impedance, unlike with end-to-end efficiency. As the general WPT system consists of various units – power source, amplifier (or converter), transmitter and receiver, rectifier, voltage regulator and load units – definitions of efficiencies need to be clarified to avoid the confusion of terminology. To preserve the stability of future WPT systems, the procedure of measuring electromagnetic interference (EMI) in near field and the limit of EMI should be clarified. The safety concerning human exposure to the designated frequency must also be considered. In the comparison between the ICNIRP guidelines and the IEEE standard, it is necessary to clarify the gap in the exposure limits [106]. The public exposure limits suggested by the IEEE C95.1-2014 standard [112] and the ICNIRP guidelines [113] along with the difference between the two limits in a wide

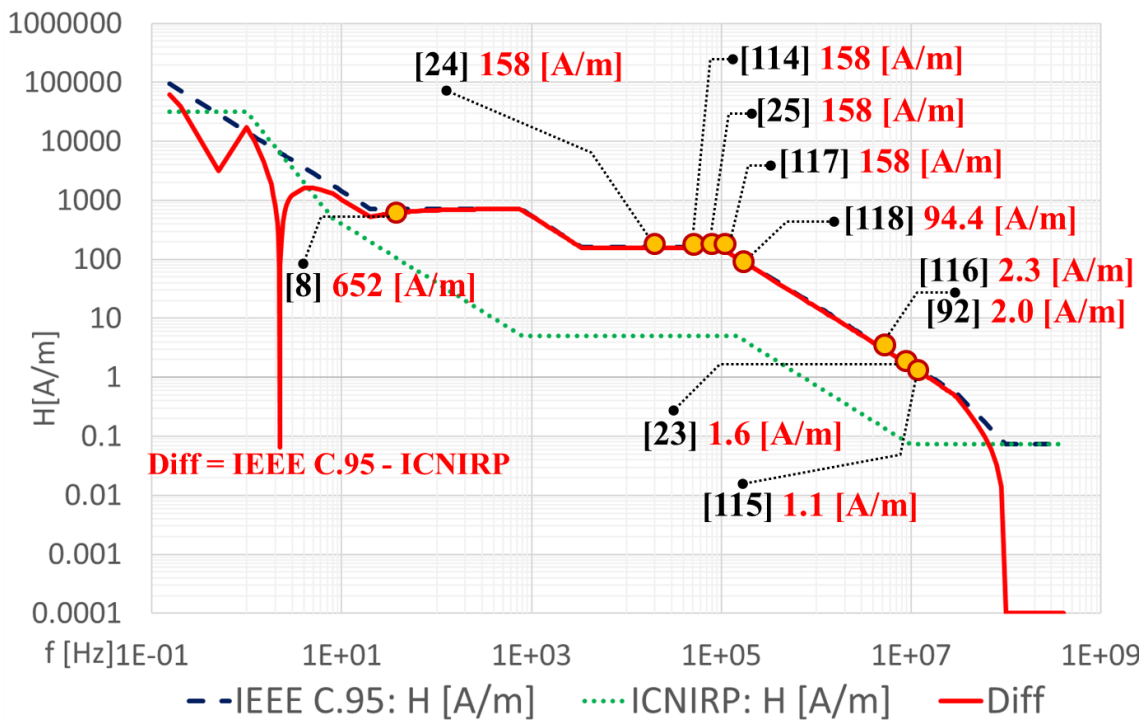
frequency range are illustrated in Figure 2.7. In this figure, various WPT applications listed in Table 2.5 are shown by their reference number at a specific frequency range. The significant discrepancies of the electric field and the magnetic field exposure limits over a hundred V/m and A/m, respectively, are observed in the frequency range 60 Hz to 10 MHz. Comparable values for the exposure limits of the two guidelines are observed at a frequency range above 10 MHz.

Table 2.5. State of IPT-based WPT technologies in various applications

Ref.	Year	No. of Coils	Frequency	Power	Distance	end-to-end Efficient	Transfer Efficiency	Application (Charging)
[23]	2007	4	9.9 MHz	60 W	2 m	15%	40%	-
[92]	2011	4	7.65 MHz	12 W	0.7 m	-	50%	Laptop
[114]	2014	2	60 kHz	180 kW	70 mm	-	86%	Railway Vehicle
[8]	2015	2	60 Hz	314 W 165 W	50 mm 100 mm	-	86.5% 78.3%	Rescue robot In Nuclear Station
[24]	2015	2	20 kHz	1403 W 471 W 209 W	3 m 4 m 5 m	29% 16% 8%	-	Back-up power for sensor charging in nuclear Station
[115]	2015	2	13.56 MHz	60 mW	30 mm	50%	92.6%	Medical Implant
[116]	2016	2	6.78 MHz	5 W	30 mm	51%	81%	Mobile phone
[25]	2017	2	85.5 kHz	2860 W	150 mm	88.05%	-	Electric Vehicle
[117]	2020	2	162 kHz	66 W	40 mm	-	62.44%	Unmanned Aerial Vehicle
[118]	2020	2	100 kHz	30-50 W	5 mm	>75%	>90%	Rotary machine



(a)



(b)

Figure 2.7. Comparison of electromagnetic field limit for public exposure: (a) electric field, and (b) magnetic field

2.5. Summary

As the demand for battery charging on mobile applications and remote sensors increases, WPT based on various methods – inductive coupling, capacitive coupling, and microwave – is regarded as a convenient solution for remote charging of these devices. This chapter presents a state-of-the-art review of the aforementioned WPT mechanisms. The validity of enhancing the Q factor and strengthening mutual inductance between a transmitter and a receiver to improve the efficiency of a two-coil IPT circuit has been described by analytical calculation. The limitations of the current WPT system were extracted with solutions in four areas: design, efficiency, stability, and safety. Although the amount of energy, transfer distance, and efficiency have been enhanced over recent decades by advances in power materials and the improvement of topologies, Tesla's desire has not yet been accomplished. To achieve the conveyance of a significant amount of electric energy over a large distance with high efficiency, the four themes need to be considered without partiality based on optimum analysis and reasonable procedures.

Chapter 3

WPT System Design in FEKO and FRA

For the improved design of a WPT device, it is essential to analyse both electromagnetic phenomena (i.e., magnetic field and coupling between the coils) and electrical components (i.e., inductance and transferred power) prior to a practical implementation. In this study, both simulation and hardware tools have been utilised to enhance the process of WPT design. This chapter introduces the expanded use of the high-frequency analysis tool known as FEldberechnung für Körper mit beliebiger Oberfläche (FEKO) for the 3-D simulation of the WPT system. The novel application of a frequency response analyser (FRA) is also presented with practical demonstrations.

3.1. Electromagnetic field solver for WPT design

FEKO is an electromagnetic field solver [119], and it is mainly employed for analysing radio frequency components, antennas, and radiations [120-122]. The previous research presented that FEKO is employed to examine the power transfer efficiency of near-field WPT systems using different materials between the antennas [123]. The application of FEKO was introduced for analysing scattering parameter (S -parameter), input impedance, and wire structure in the frequency range of 10–11.5 MHz [124]. However, the magnetic coupling study was not presented. The numerical value of the magnetic field between the Tx and Rx of the WPT system was also examined over variations of transfer distance [125, 126]. However, it did not cover the application of the design or analysis of WPT performance, and a simulation tool was utilised for the partial inspection of WPT performance. This chapter introduces the comprehensive implementation of WPT systems using FEKO.

The performance of wireless power transfer models can be analysed by several EM software or high-frequency antenna design tools. These tools offer various solvers

known as Finite-Difference Time-Domain (FDTD), Finite Elements Method (FEM), Method of Moments (MoM), and ElectroMagnetic Ray Tracing (EMRT) [127]. FEKO mainly uses MoM and exhibits hybrid solvers that result in high efficiency and accuracy of simulation progress by using multilevel fast multipole method (MLFMM) surface equivalence principle (SEP) [128]. FEKO can be easily used in personal computers to mimic the WPT prototypes investigated in this thesis, which comprise complex geometries of wiring conductors ferrite bars, and insulation materials. The single EM simulation for analysing electromagnetic coupling between coils is generally executed within a few minutes, and the simulation outcomes are comparable to the practical results. Besides, FEKO provides sub-tools for efficient performance [129]. The topology of the WPT system was built, and the parameters were defined through CADFEKO, then the results of the electromagnetic coupling strength and efficiency were analysed and processed in POSTFEKO using 3D view and Cartesian coordinates. Also, multiple simulations in different parameters or environment are available in EDITFEKO.

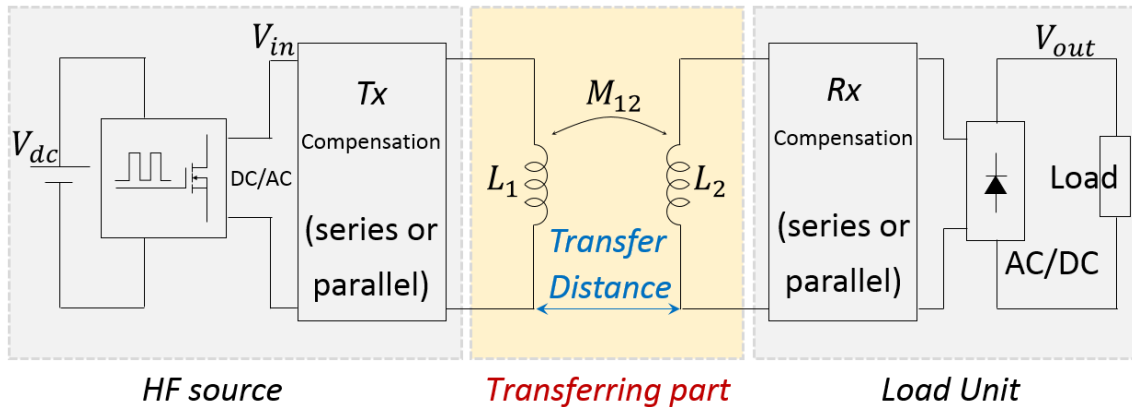


Figure 3.1. Inductively-coupled WPT system

A WPT system is mainly composed of a high-frequency (HF) source, Tx and Rx coils, and a load unit, as shown in Figure 3.1. In the practical WPT device, the HF source is generated by a switching device such as a half or full-bridge inverter, and the load unit has a rectifying device to obtain DC power from the transferred HF source. To analyse the switching process in the DC/AC or AC/DC circuit accurately, specialised simulation tools are required. However, the HF source and load unit in FEKO can be described on the wire ports, and the inductive coupling behaviour in the transferring part can be

simulated in numerical simulation software. Furthermore, the self and mutual inductance of the WPT coils can be extracted from the results of the S -parameter, and the transferred power using different loads and airgaps is predictable. Accordingly, FEKO provides a precise analysis for the formation and distribution of magnetic coupling between the coils. It also provides the electrical parameters of the simplified WPT circuit in the wire ports, as shown in Figure 3.1.

3.2. Frequency Analysis Tool for a WPT design

The principle of WPT is based on Faraday's law of electromagnetic induction, similar to a power transformer. An IPT system is mainly composed of a Tx coil and Rx coil representing a primary and secondary winding of a power transformer. The difference between a WPT system and a traditional power transformer is that a WPT device has compensating capacitors at the Tx and Rx sides to reduce the leakage inductance. The Tx and Rx coils are also loosely coupled without any magnetic core, as the coupling coefficient factor k of a WPT device is about 0.2 – 0.3, whereas the iron core transformer has almost unity k . When the WPT coils are coupled at the resonance frequency, electric power can be transferred efficiently through free space [130]. The typical transfer distance, also known as the air gap, of the current WPT systems is in the range of a few millimetres to several centimetres [36, 131, 132]. As public transport vehicles (e.g., high-speed trains and large ferries) have adopted a wireless charging application, WPT systems in the megawatt range have been recently introduced, as shown in Figure 3.2 [11, 13]. Hence, it is expected that the size and capacity of WPT systems will increase rapidly in the near future. To avoid the confusion of terminology, WPT in this chapter is used to refer to IPT.

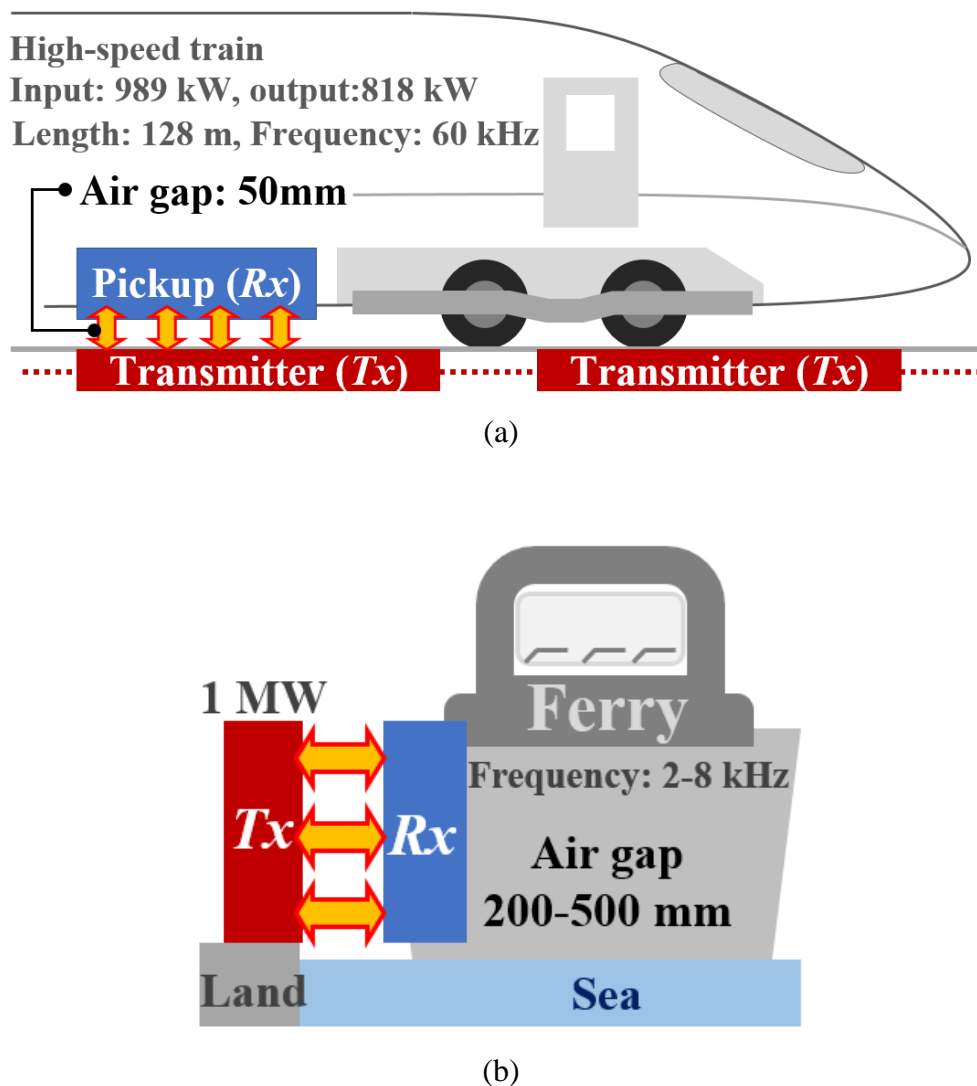


Figure 3.2. Megawatt range WPT application examples: (a) high-speed train, and (b) large-scale vessel

FRA has played a significant role in detecting mechanical deformation and certifying the reliability of power transformers in recent decades [133-135]. To observe the malfunction of the windings in power transformers, the application of a low-voltage impulse (LVI) was adopted as a reliable field test in the 1960s [136]. However, LVI analysis required precise instrumentation systems for repeatable works. Furthermore, the test results fluctuated sensitively due to external interference and calibrations in different conditions. Therefore, FRA was presented to precisely detect the winding deformation or insulation degradation in the interior of the transformer in 1978 [137]. Unlike the impulse-test, which is dependent on the reliability of the impulse generator and the form of the

test-voltage, a transfer function technique using FRA is independent of the shapes of the test-voltage impulse. It provides constant results by deconvoluting the test-voltage and the neutral-current in the frequency domain [138]. Fast Fourier transform (FFT) with advancements in digital signal processing technology facilitated the accurate use of FRA in 1992 [136]. Since then, FRA has played a significant role in assessing the condition of power transformers [139, 140].

The principle concept of FRA is based on two-port network theory [141], and it is more user-friendly, cost-effective, and robust than a vector network analyser for power industry applications [142]. To detect changes in the electrical parameters in the interior of a power transformer, a new measurement of the voltage gain waveforms over a wide range of frequencies is compared with a reference signature known as a baseline measurement or fingerprint signature [143]. The source unit of FRA injects sinusoidal voltage over a wide range of frequencies into one end of a winding, then the output voltage with a displacement of the phase angle is measured at another winding. A power transformer can be described as the distributed electrical components RLC reacting against each level of the frequencies differently, and the resonance frequencies are observed when the resistive component R is only maintained when reactive components L and C are cancelled. To verify a WPT installation accurately on-site, and for maintenance purposes in the future, FRA can perform another critical role in the WPT industry. FRA can be adopted to clarify the characteristics of the voltage transfer ratio (VTR) and the transfer function of WPT systems [125]. The optimum distance corresponding to the maximum power transfer and the optimum resonance frequency could also be correctly identified in various compensations of WPT systems using FRA.

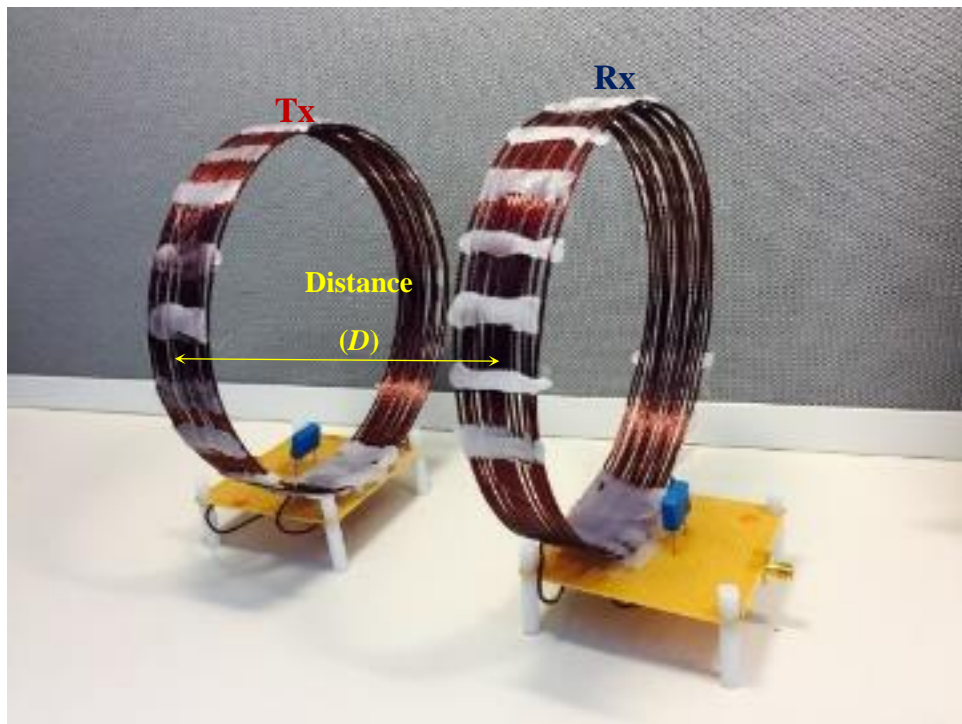
3.3. 1 MHz Helical-coil WPT design

To analyse the maximum power delivery between the coils, a 1 MHz SS WPT system with a helical-shaped coil was built. The maximum power transfer can be discovered at the critical distance between the coils. When the transfer distance is over or under the critical distance, the performance of the WPT system degrades. FEKO and FRA can examine the performance in different environments. The resonance frequency of the

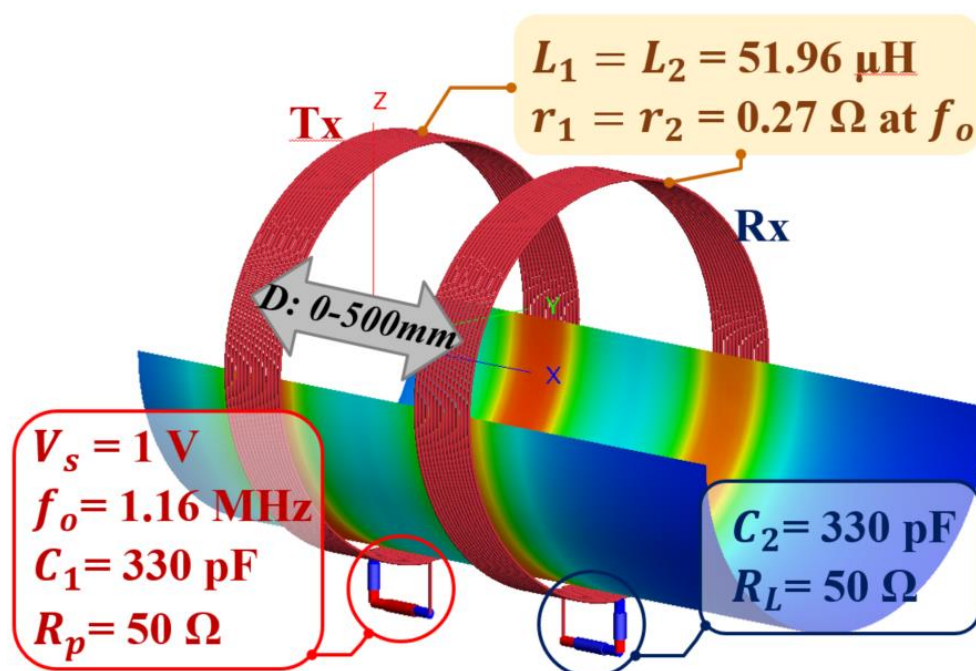
experimental SS WPT system in this chapter is set at 1 MHz for three reasons. First, some CPT or IPT-CPT hybrid applications for transferring a few kilo-watts of power are also feasible at a resonant frequency of 1 MHz [28, 45]. The FRA measurement at a frequency level of tens of kHz can be conducted by adjusting the user-defined frequency range setting. Second, to observe the variation of the VTR between the windings clearly, a megahertz frequency was adopted. The maximum power transfer and the frequency bifurcation occurring under the critical distance fluctuate more sensitively at a frequency of 1 megahertz than in the range of a few kilohertz. Lastly, the measurable frequency range of the commercialised FRA equipment is between 10 Hz and 25 MHz [144]. Like an analysis of the frequency response for a power transformer in distinctive VRT signatures with respect to different frequencies (e.g., excitation region and winding property region), the complex WPT system with additional magnetic materials (i.e., ferrite bars or magnetic iron dipoles) can also be examined at the different frequency ranges.

3.3.1. Coil design

Two identical coils were built to demonstrate the feasibility of the WPT system in Figure 2.6, as shown in Figure 3.3 (a). The Tx and Rx coils are identical. The wire radius, the loop radius, and the number of turns are 0.675 mm, 80 mm, and 15 turns, respectively. A self-inductance L of 56.96 μH and parasitic resistance r of 0.27 Ω at the resonance frequency $f_o = 1.16$ MHz were extracted using FEKO [145]. During the simulation, the source and the load resistors are assumed to be 50 Ω , and the compensating capacitor is set to 330 pF, as presented in Table 3.3.



(a)



(b)

Figure 3.3. Helical-coil WPT design: (a) actual single copper coils, and (b) values of relevant simulation parameters

Table 3.1. Detail of winding design

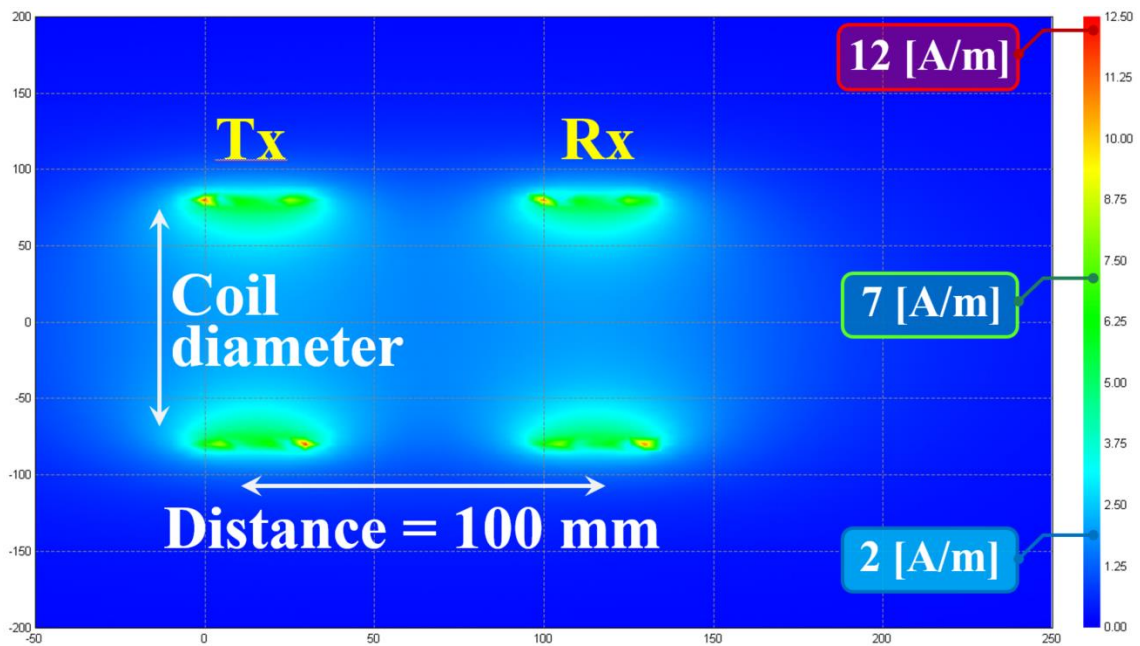
Parameters	Values
copper wire radius, a	0.675 mm
loop radius, l_d	80 mm
number of turns, N	15
self-inductance L_1 and L_2	56.958 μ H
resonance frequency, f_o	1.16 MHz
paramedic resistance of winding at f_o	0.27 Ω
source resistance R_o and load resistance R_L	50 Ω

A sinusoidal voltage of 1 V at the calculated resonance frequency of 1.16 MHz is connected to the Tx unit, and the strength of the magnetic field between the two coils is observed over distances ranging from 0 mm to 500 mm as shown in Figure 3.3 (b). The distribution of the magnetic field on the cross-sectional view around the Rx and Tx coils is observed at a distance of 100 mm and 180 mm. A magnetic field level of approximately 7 A/m is presented evenly at both the Tx and Rx coils when the separation distance is 100 mm, whereas the magnetic field linkage with the Rx coil decreases till it vanishes at a particular distance between the two coils as shown in Figure 3.4 (a) and (b), respectively.

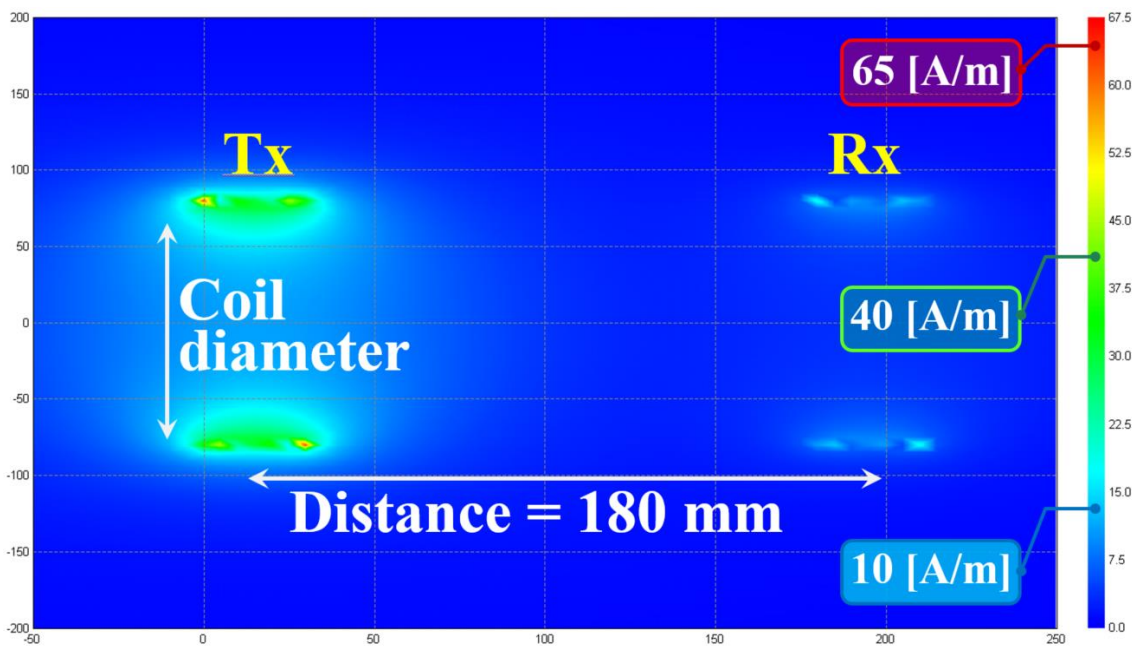
The mutual inductance corresponding to maximum power transfer, $M_{12,max}$ is extracted by differentiating the receiving power in (2.4) with respect to M_{12} ($\partial P_L / \partial M_{12} = 0$), which will lead to:

$$M_{12,max} = \frac{\sqrt{R_p R_L}}{\omega_0} \quad (3.1)$$

$$M_{12,max} = k_{12} \sqrt{L_1 L_2} = \frac{\sqrt{R_p R_L}}{\omega_0} = \frac{\mu_o \pi N_1 N_2 (a_1 a_2)^2}{2(a_1^2 + D^2)^{\frac{3}{2}}} \quad (3.2)$$



(a)



(b)

Figure 3.4. Observation of the magnetic field over: (a) a distance of 100 mm, and (b) a distance of 180 mm

The result indicates that mutual inductance as a critical parameter for WPT is determined by the resistances R_p and R_L and the resonance frequency ω_0 . It can be seen also that maximum power transfer can take place at the critical distance D_c given in (3.3).

$$D_c = \pm \sqrt{\left(\frac{\mu_0 \pi N^2 a^4 \omega_0}{2\sqrt{R_p R_L}}\right)^{\frac{2}{3}} - a^2} \quad (3.3)$$

3.3.2. S-parameter analysis

The traditional transformer can be described as a two-port network, as indicated in Figure 3.5, and the impedance parameter (Z-parameter) in the network is convertible to an S-parameter [146]. Therefore, self-inductance (L_1 and L_2) and mutual-inductance M_{12} as constructed in the simulation tool can be inferred from the S-parameters. When the voltage source V_{in} with resistance R_o excites the two-port networks in the Tx, the impedance matrix is expressed in (3.4)), and the self and mutual impedance of the coils are determined through (3.5) and (3.6).

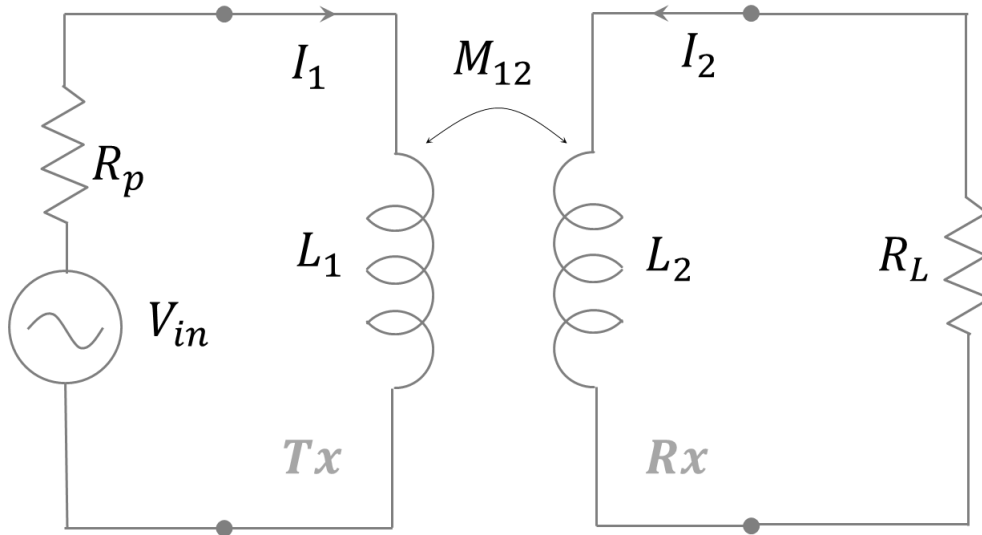


Figure 3.5 Traditional transformer model

$$\begin{bmatrix} V_{in} \\ 0 \end{bmatrix} = \begin{bmatrix} R_p + j\omega L_1 & j\omega M_{12} \\ j\omega M_{12} & R_L + j\omega L_2 \end{bmatrix} \begin{bmatrix} I_1 \\ I_2 \end{bmatrix} = \begin{bmatrix} R_p + Z_{11} & Z_{12} \\ Z_{21} & R_L + Z_{22} \end{bmatrix} \begin{bmatrix} I_1 \\ I_2 \end{bmatrix} \quad (3.4)$$

$$Z_{11} = Z_{22} = \frac{(R_p + S_{11}R_p)(1 - S_{22}) + S_{12}S_{21}R_p}{(1 - S_{11})(1 - S_{22}) - S_{12}S_{21}} \quad (3.5)$$

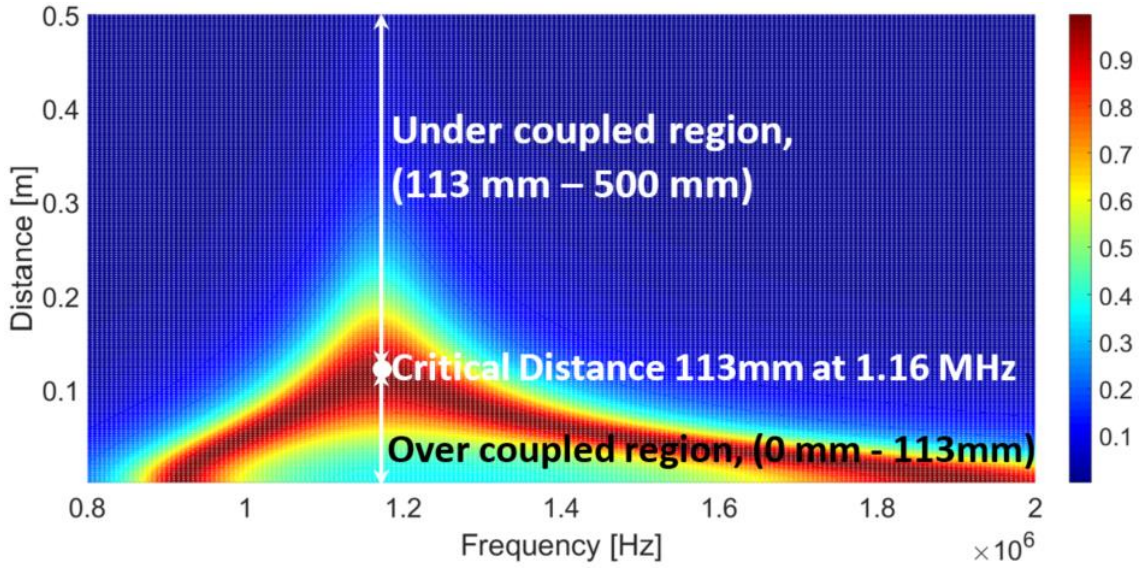
$$Z_{12} = Z_{21} = \frac{2S_{21}(R_p R_L)^{1/2}}{(1 - S_{11})(1 - S_{22}) - S_{12}S_{21}} \quad (3.6)$$

Furthermore, the S -parameter indicates the level of the transmitting and the reflecting coefficients in the frequency domain, and this is convertible to the Z -parameter. The two-coil system in Figure 2.6 is considered a two-port network. The transmitting coefficient S_{21} represents the transfer efficiency and is given in (3.7) in which V_L is the voltage across the load resistance R_L .

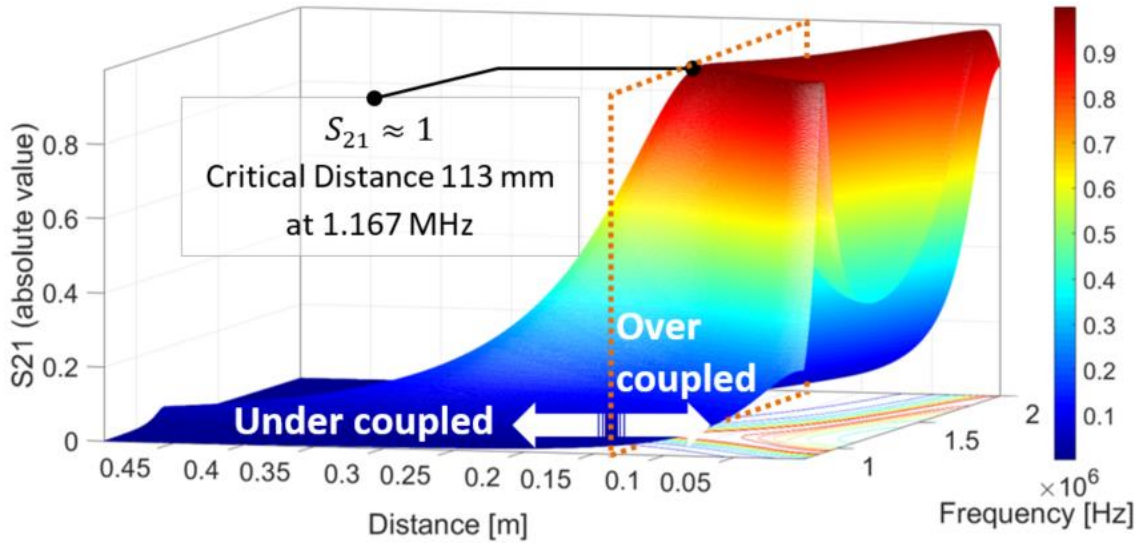
$$S_{21} = 2 \sqrt{\frac{R_p}{R_L}} \frac{V_L}{V_p} = \frac{2j\omega M_{12} \sqrt{R_p R_L}}{(R_p + Z_1)(Z_2 + R_L) + \omega^2 M_{12}^2} \quad (3.7)$$

S_{21} can be at its maximum level when the circuit is at resonance condition, and the mutual inductance satisfies the condition of the maximum power transfer given in (3.1) [93]. The correlation between the absolute value of S_{21} , the distance, and the frequency is displayed in Figure 3.6. In this computation, the height of the helical coil is 0.03 m and the distance is measured between the centres of the coils. The highest level of S_{21} is achieved at a distance of 0.113 m at a resonance frequency of 1.167 MHz. The practical results of S_{21} measured by the network analyser (Agilent Technology FieldFox N9915A) is compared to the calculated value and the value obtained through the FEKO simulation at the near, critical, and far distance, as shown in Figure 3.7. The expected critical distance is extracted as 113 mm from (3.3), and the transferred power

corresponding to this critical distance is shown in Figure 3.7 (b) which shows the highest level of S_{21} (0.915) at a frequency of 1.123 MHz.

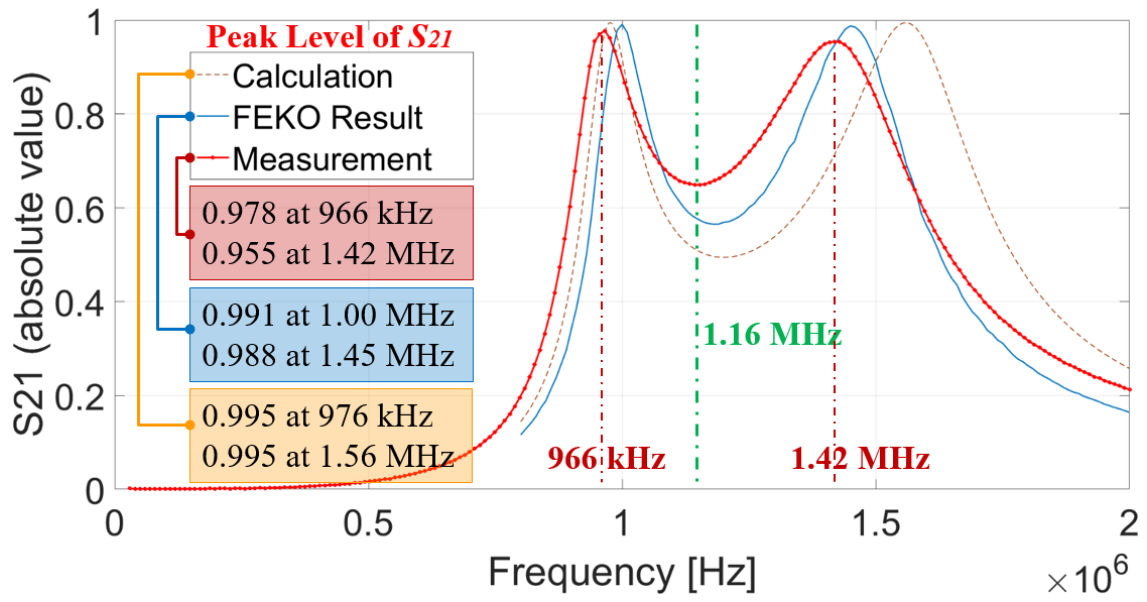


(a)

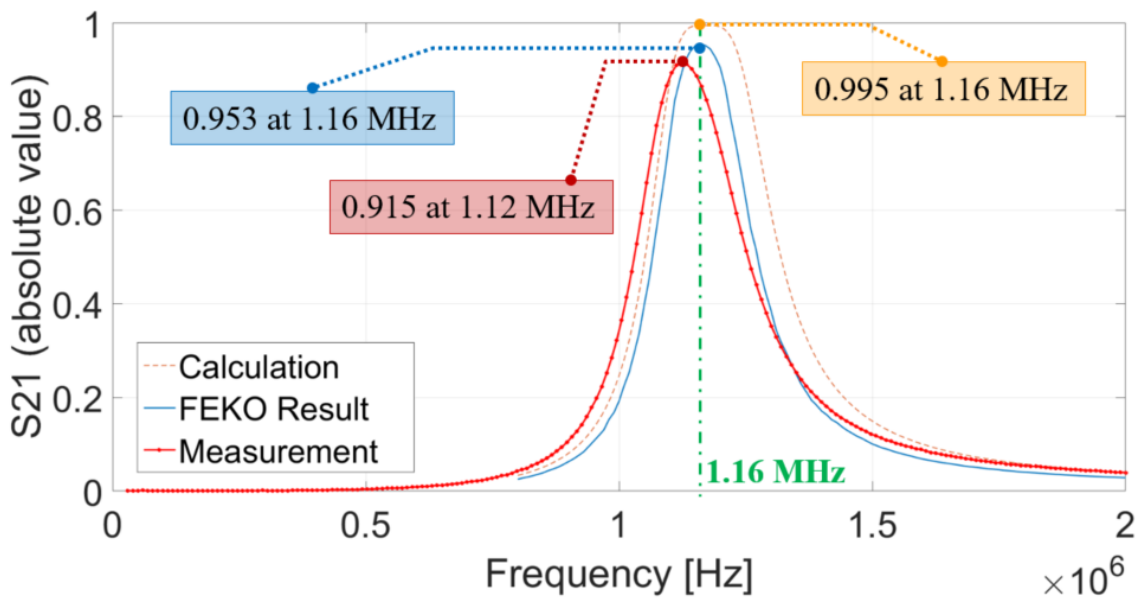


(b)

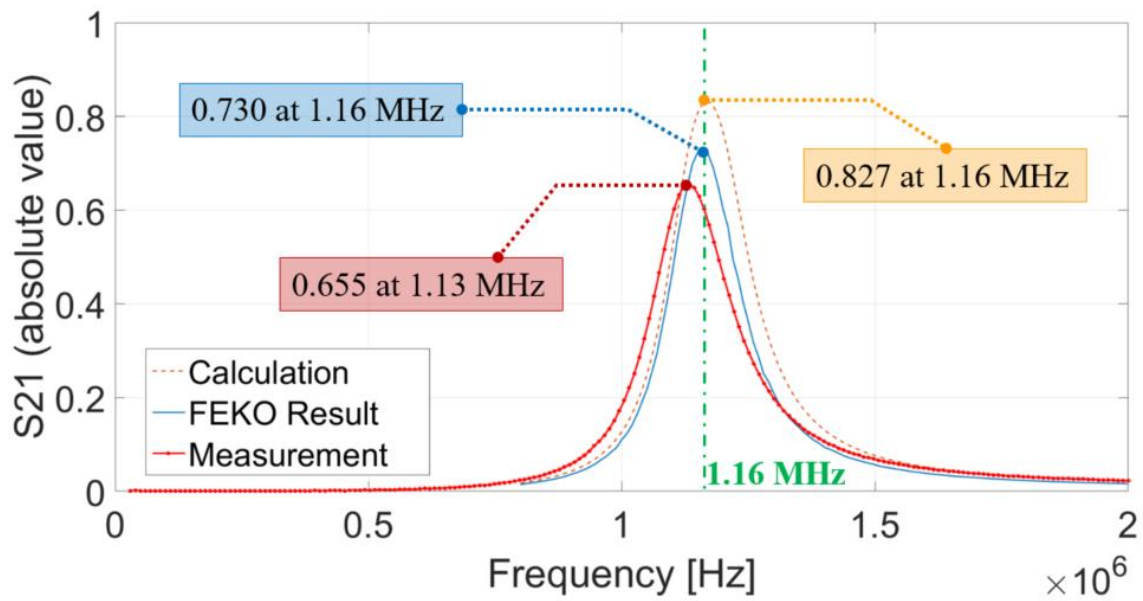
Figure 3.6. S_{21} over distance and frequency: (a) S_{21} on 2D, and (b) S_{21} on 3-D



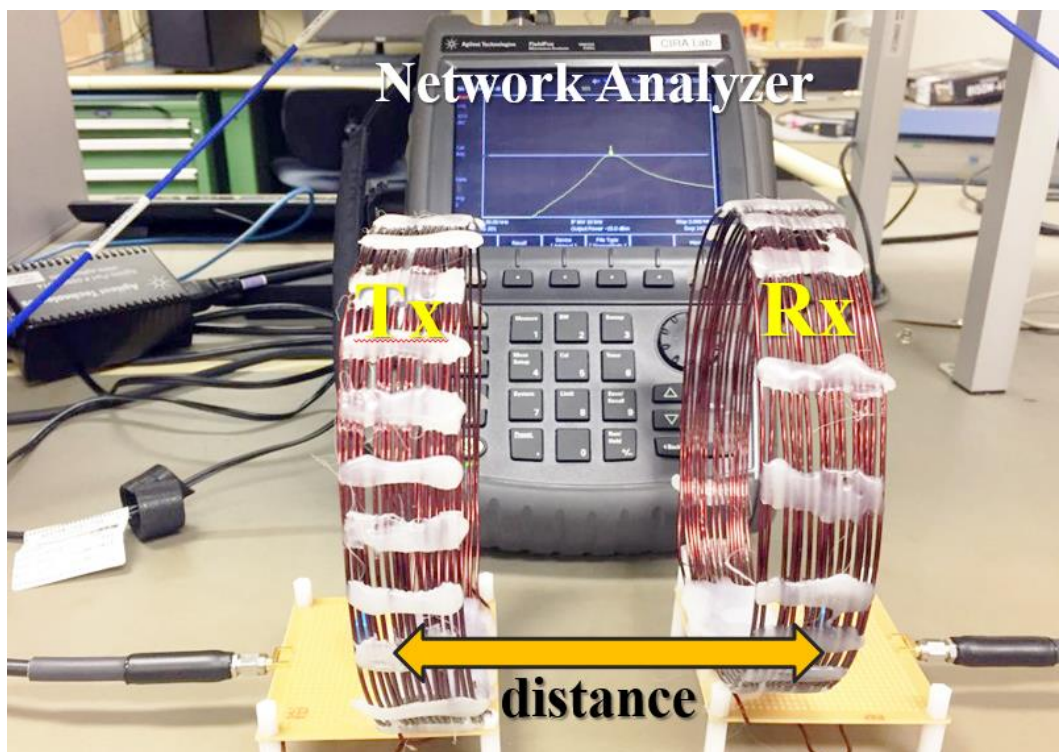
(a)



(b)



(c)



(d)

Figure 3.7. Comparison of S_{21} results over distance: (a) 40 mm, (b) 113 mm (critical point), (c) 150 mm, and (d) S_{21} measurement set-up

When the two coils are in an under-coupled region, as the distance between the Rx unit and the Tx unit is more than the critical distance, the transferred power declined sharply, as can be seen in Figure 3.7 (c), while multiple resonances can be observed when the distance between the two coils is less than the critical distance, as shown in Figure 3.7 (a). These results indicate that the power is not transferred efficiently at the original resonance frequency in an over-coupled region.

Table 3.2 shows a comparison of the results obtained through experimental measurements, simulation, and analytical calculation. The percentage error of the simulation and analytical analyses is calculated with respect to the value obtained through experimental measurement. Table 3.2 reveals that the error in the simulation and calculated results is relatively small when the transfer distance is less than the critical distance (113 mm), and the error increases outside this distance. Also, it can be observed that the error in the calculation is higher than in the simulation, which is attributed to the assumption that the skin and proximity effects are neglected in the calculation analysis.

Table 3.2. Comparison of the results

Measurement Result		% Error	
		FEKO	Calculation
40 mm distance	$S_{21} = 0.978$	1.31%	1.71%
	$f_o = 966$ kHz	3.40%	1.02%
113 mm distance	$S_{21} = 0.955$	3.34%	4.02%
	$f_o = 1.42$ MHz	2.07%	8.97%
150 mm distance	$S_{21} = 0.915$	3.99%	8.04%
	$f_o = 1.12$ MHz	3.45%	3.45%
150 mm distance	$S_{21} = 0.655$	10.27%	20.80%
	$f_o = 1.13$ MHz	2.59%	2.59%

3.3.3. FRA Application on WPT

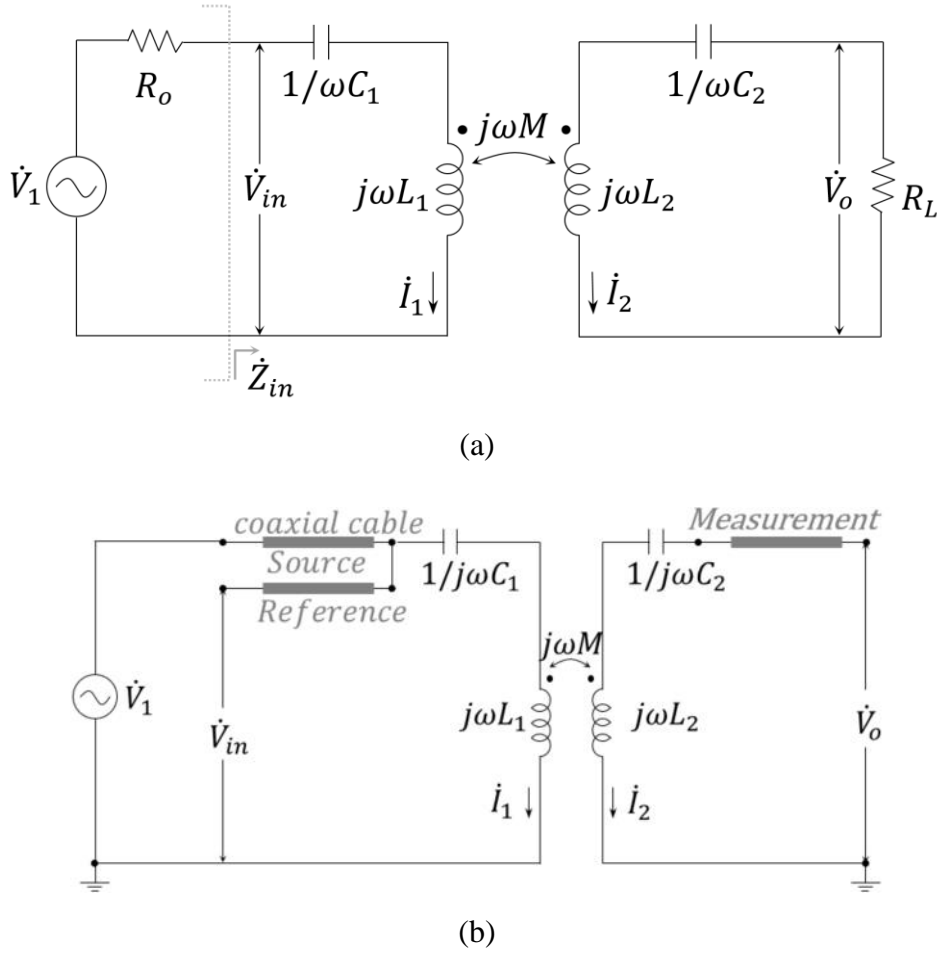


Figure 3.8. Configuration for the FRA measurement: (a) circuit diagram, and (b) FRA test leads connection.

The absolute value of the VTR between V_{in} and V_o , as shown in Figure 3.8 (a), can be described in (3.8).

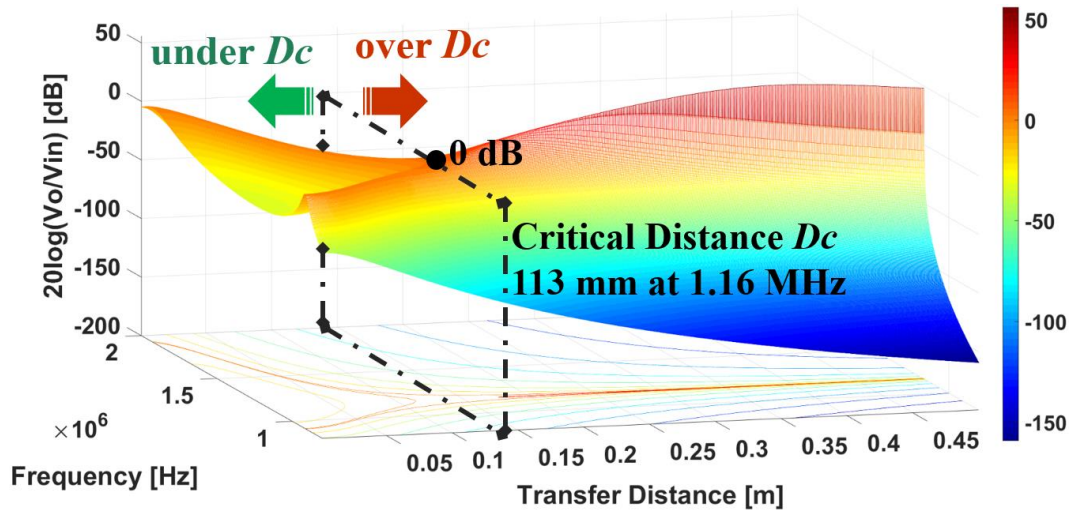
$$VTR = \left| \frac{V_o}{V_{in}} \right| = \left| \frac{-j\omega MR_L}{jX_1(R_L + jX_2) + \omega^2 M^2} \right| \quad (3.8)$$

When the frequency reaches ω_o and assuming that R_o equals R_L , the VTR in (3.8) is simplified to:

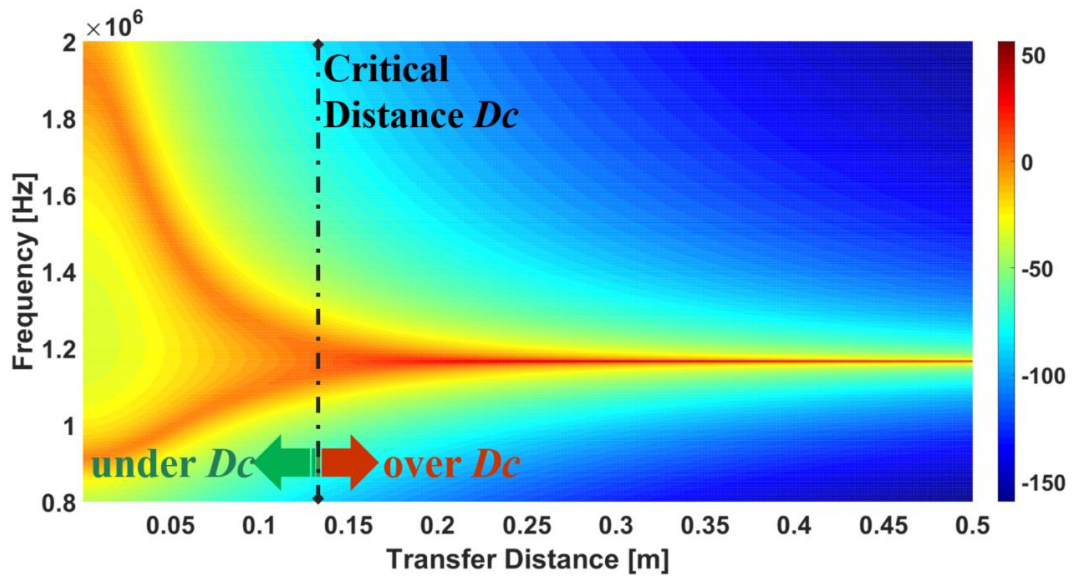
$$MAG_{(\omega_o)} = 20 \log \left| \frac{R_L}{\omega_o M} \right| \quad (3.9)$$

As shown in Figure 3.9, the VTR is calculated in the frequency range from 800 kHz to 2 MHz at a distance of up to 0.5 m. From (3.8), it can be known that the VTR reaches unity value when the critical value of the mutual inductance is as below.

$$M_c = \frac{R_L}{\omega_o} \tag{3.10}$$



(a)



(b)

Figure 3.9. VTR of SS circuit: (a) VTR over distance and frequency, and (b) Aerial view of (a)

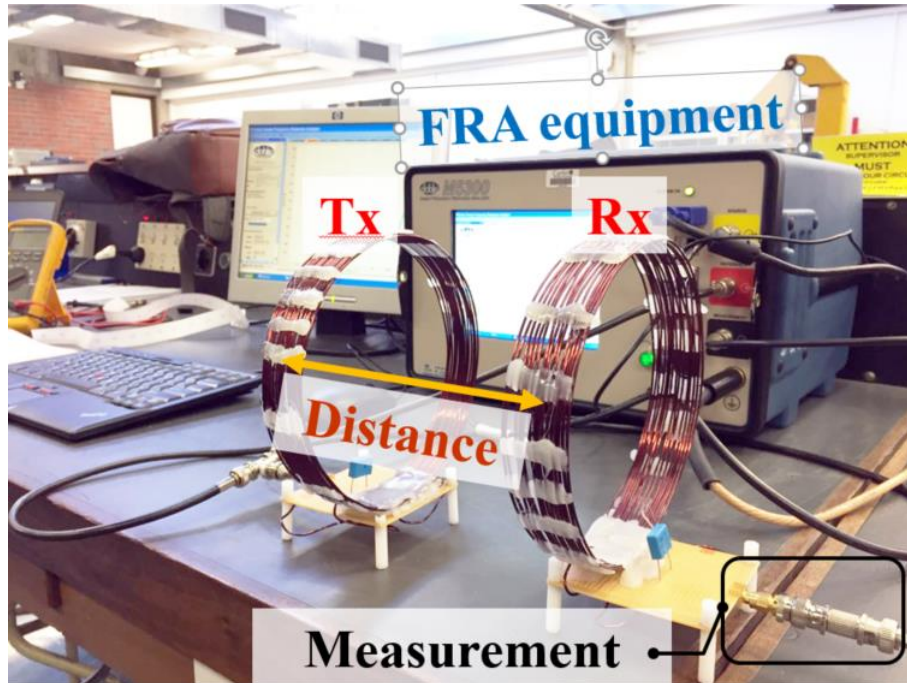
The critical distance can be defined where the VTR reaches unity at the resonance frequency. The critical distance of the experimental system is found at a distance of 113 mm, as shown in Figure 3.9. The VTR exceeds the unity level as the input voltage V_{in} is proportional to M^2 where V_o is proportional to M in (3.8) at the resonance frequency. In the circuit model, the VTR increases above the critical distance. Then it reduces again, as this circuit is not perfectly tuned at the frequency of 1.16 MHz, as shown in Figure 3.9. In other words, the higher output voltage V_o across load resistance R_L is induced than the applied input voltage V_{in} across the input impedance Z_{in} as shown in Figure 3.8 (a) when the magnetic coupling is below the critical level.

3.3.4. Experimental FRA measurement with different airgaps

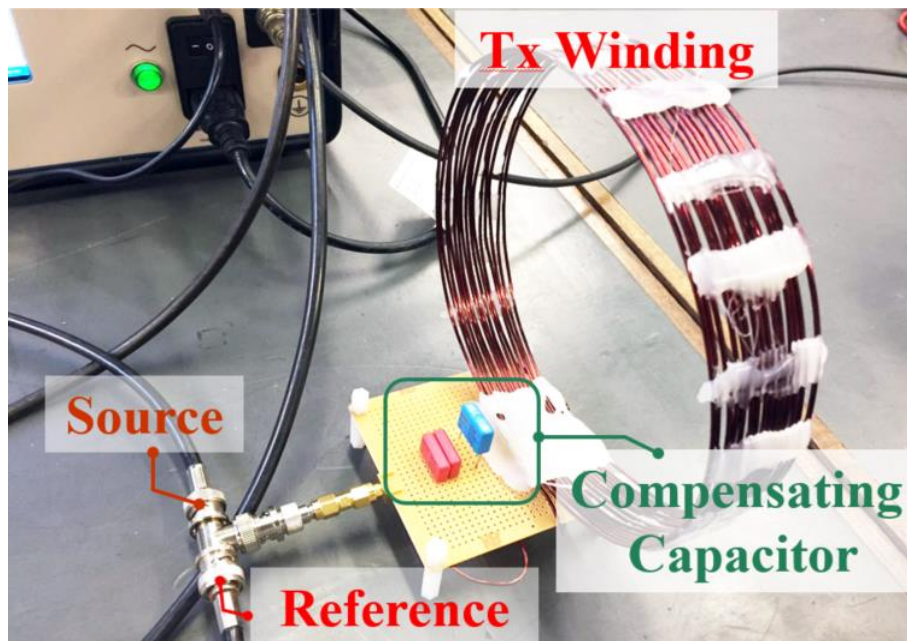
To conduct a FRA measurement on a two-winding WPT system, the Tx and Rx winding were isolated from the power source and the load unit similar to a FRA measurement on a power transformer. From the external voltage source V_1 , as described in Figure 3.8, the FRA device injected $20 V_{p-p}$ with 50 ohms source resistance into the Tx winding in a user-defined frequency range between 20 kHz and 10 MHz. Commercial FRA equipment (DOBLE M5300) was used [144], and the windings with the capacitors at both ends were terminated by the subminiature version A (SMA) connectors as depicted in Figure 3.10 (a) and (b). The injecting voltage V_{in} across the input impedance was recorded through the reference terminal then the transferred voltage V_o across the Rx winding was measured at the measurement terminal.

Based on (3.10), the critical mutual inductance can be extracted as 6.864 μH , and the critical distance D_c can be calculated by transposing the equation of the coupling coefficient between the helical windings in (3.3). The efficiency of this system significantly declines if the Rx winding is in the vicinity of the Tx or is placed far from the critical distance. As shown in Figure 3.11 and Figure 3.13, the unity VTR was practically found when the Rx winding approaches a distance of 105 mm at a frequency of 1.06 MHz. This result is comparable to the expected distance at the frequency of 1.16 MHz, as depicted in Figure 3.9. Furthermore, the transfer impedance between the magnetically coupled windings can be observed according to the FRA results. The lowest

level of impedance 8.8 ohms was recorded at the distance of 105mm at the resonance frequency in the red trace of Figure 3.12 and Figure 3.14.

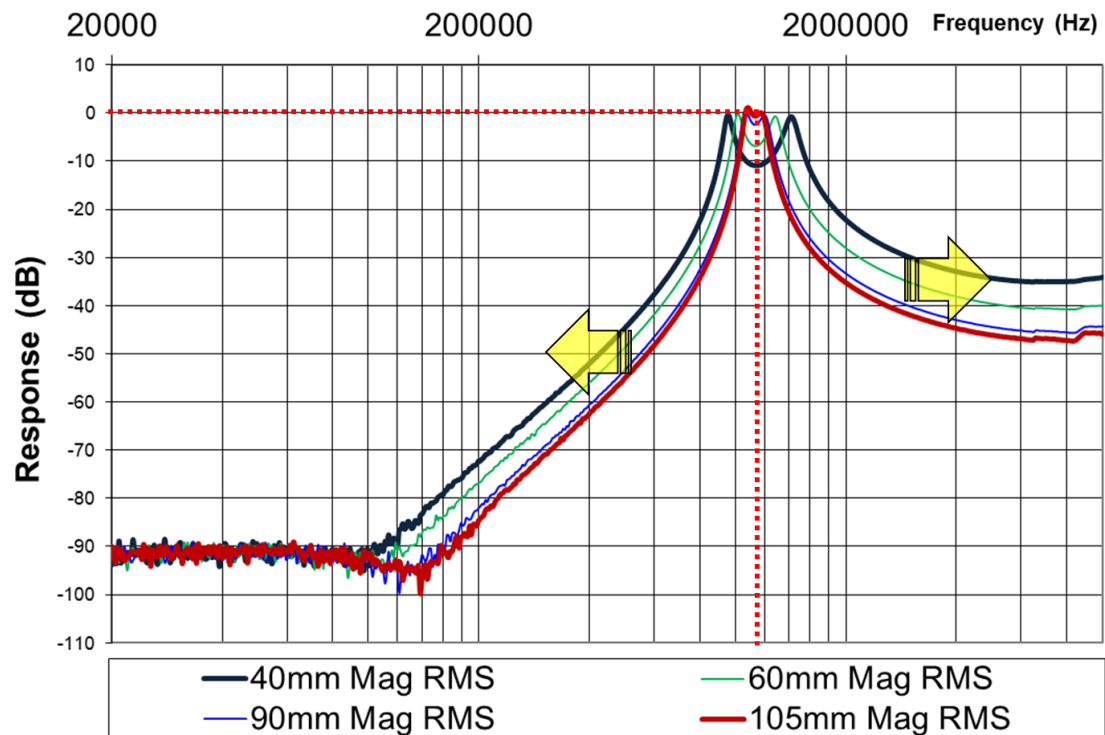


(a)

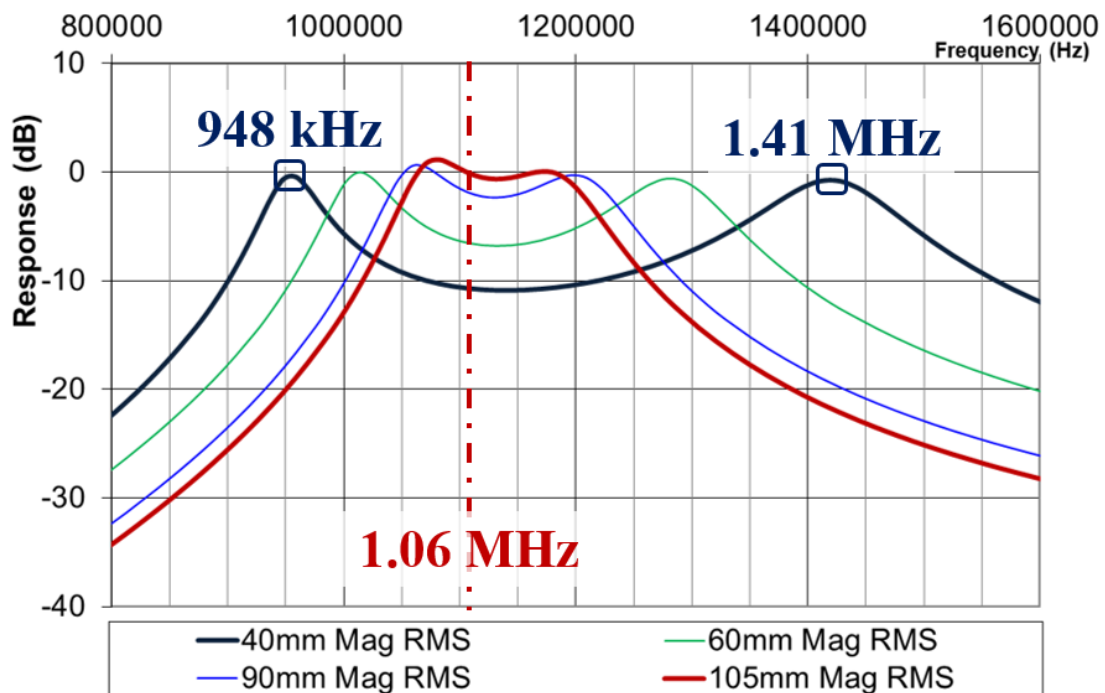


(b)

Figure 3.10. FRA measurement: (a) FRA setup on WPT, and (b) FRA connection on Tx unit

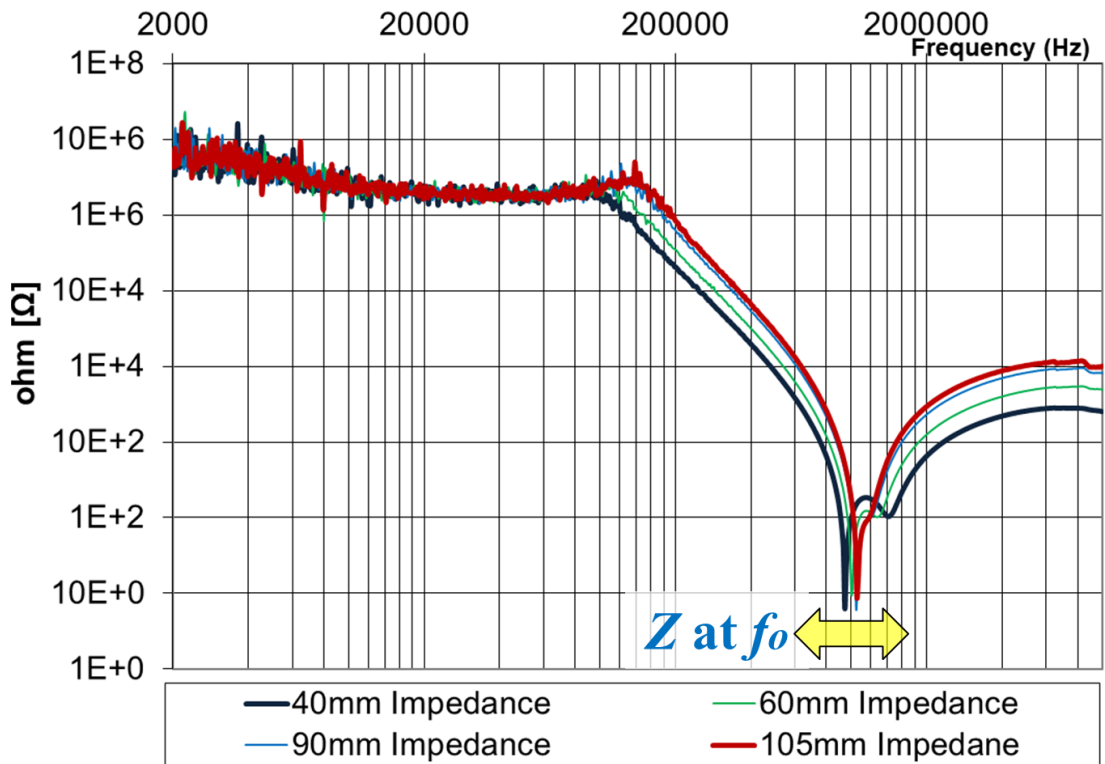


(a)

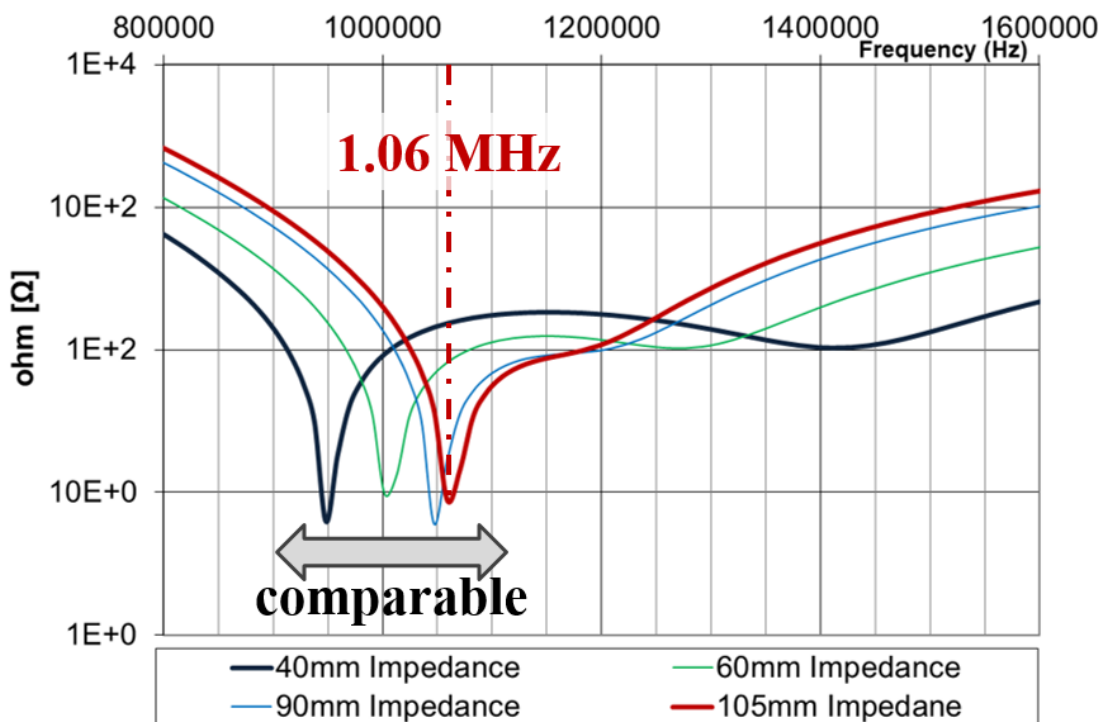


(b)

Figure 3.11. FRA results of VTR magnitude under critical distance: (a) at the wide-range frequencies, and (b) at the resonance frequency

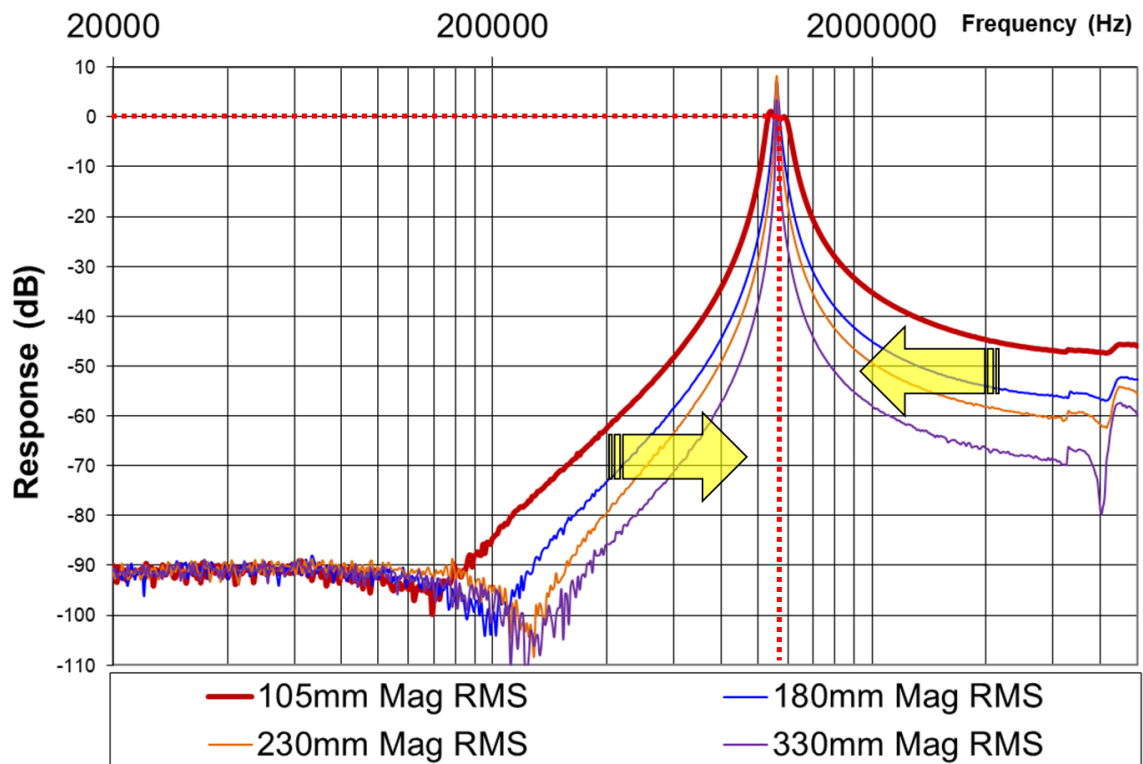


(a)

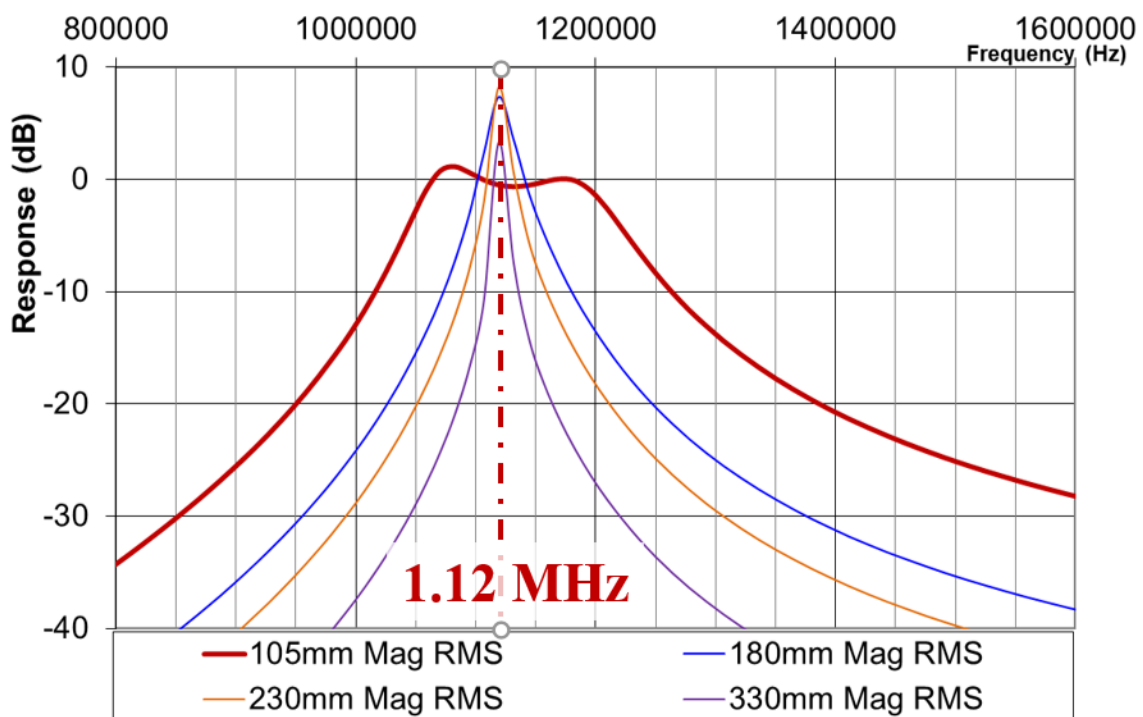


(b)

Figure 3.12. FRA results of impedance value under the critical distance: (a) at the wide-range frequencies, and (b) at the resonance frequency

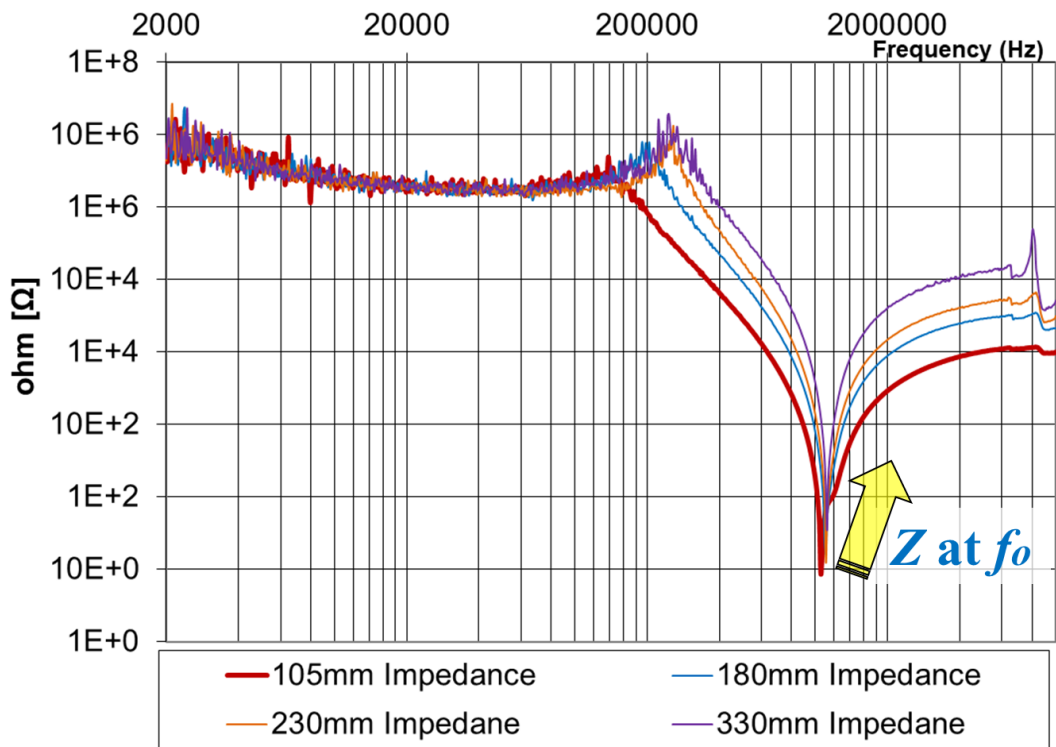


(a)

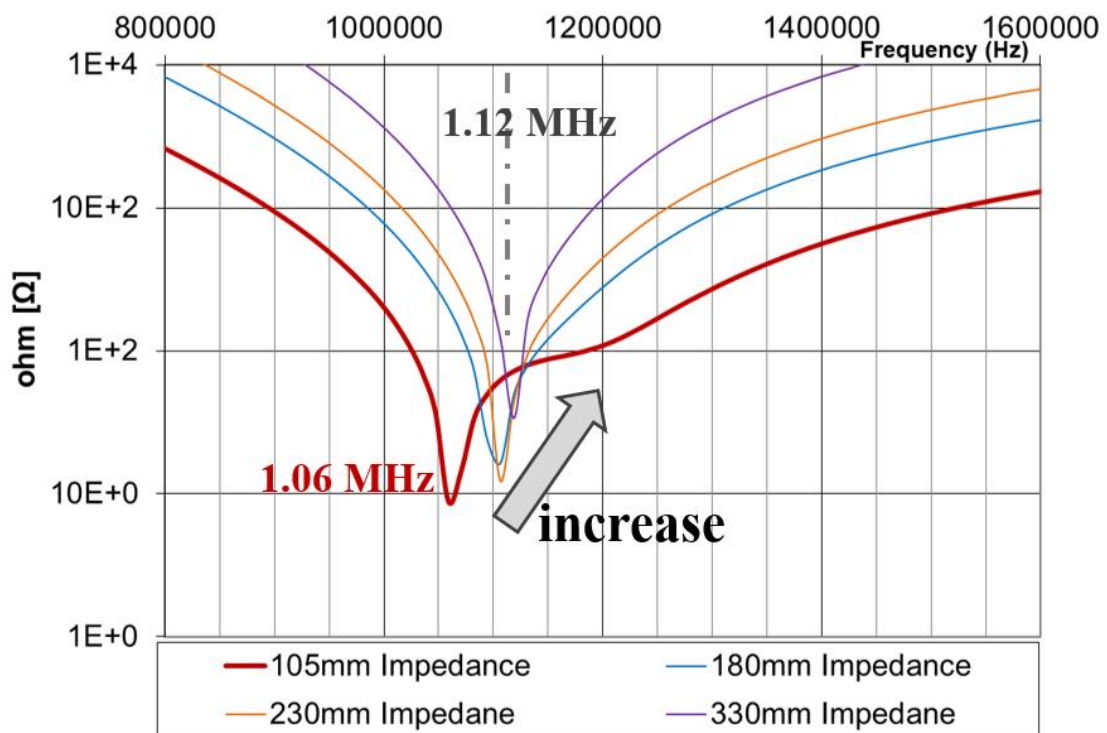


(b)

Figure 3.13. FRA results of VTR magnitude over the critical distance: (a) at the wide-range frequencies, and (b) at the resonance frequency



(a)



(b)

Figure 3.14. FRA results of impedance value over the critical distance: (a) at the wide-range frequencies, and (b) at the resonance frequency

The transfer impedance can be extracted by deducting the load resistance R_L from Z_{in} . The test configuration on the WPT system is similar to the power transformer interwinding measurement, and the ideal WPT two-winding SS system has zero transfer impedance at the resonance frequency, and at the critical distance [147]. The voltage level of V_{in} and V_o becomes V_m when the inductance L_1 and L_2 are eliminated by the compensating capacitors C_1 and C_2 , and the winding resistances R_1 and R_2 are ignorable, as shown in Figure 3.15. In practice, it is difficult to observe the waveform with a single peak at the level of 0 dB and zero transfer impedance, as the WPT system is not perfectly tuned at the expected resonance frequency due to the winding topology and the winding resistance increment at high frequencies.

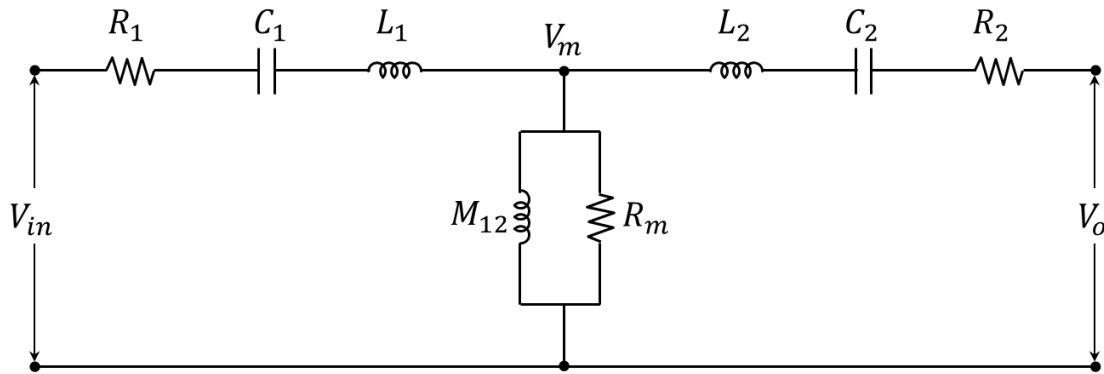


Figure 3.15. Equivalent circuit of WPT interwinding FRA measurement

When the transfer distance is below the critical point, the level of VTR at the resonance frequency declines, as the level of mutual inductance is higher than the critical level. Therefore, the unity VTR or the maximum power transfer occurs at the bifurcated frequencies based on the initial resonance frequency of 1.16 MHz. As shown in Figure 3.11 (b), the unity VTRs at a transfer distance of 40 mm are observed at two different frequencies: 948 kHz and 1.41 MHz. When the Rx winding is closer to the Tx winding, the characteristic of frequency bifurcation is observed. Also, the length between the peak points increases against the proximity of the windings. The efficiency reduction due to the frequency bifurcation can be eliminated by returning the resonance frequency or installing non-identical Tx and Rx windings [93, 94]. The unity VTR can also be accomplished by reducing the level of mutual inductance at the short distance from (3.10).

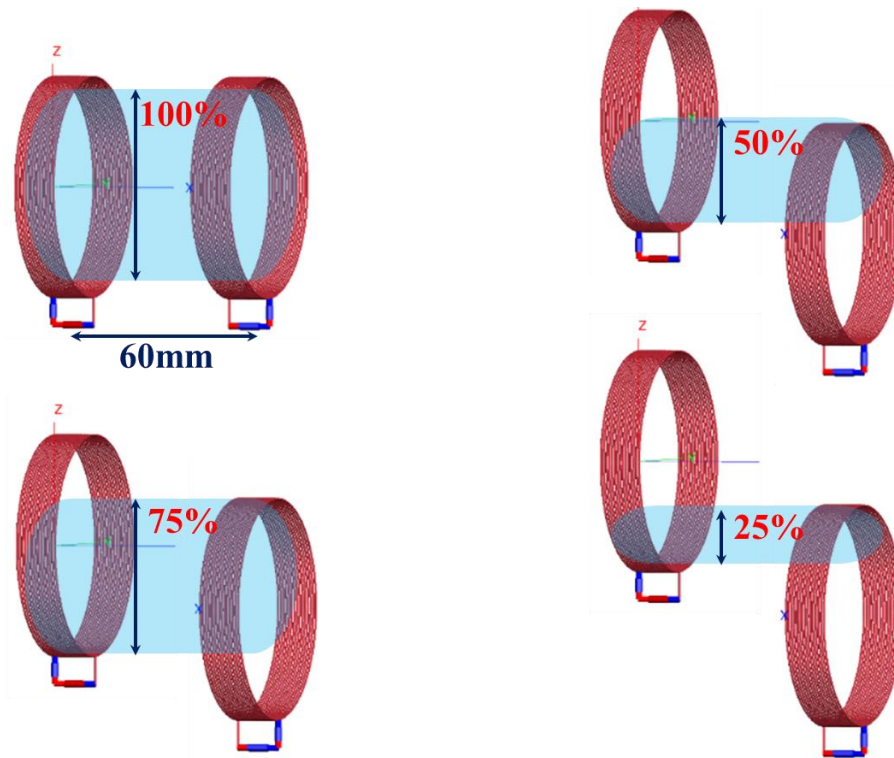


Figure 3.16. Intentional misalignment of Rx winding at 60 mm distance

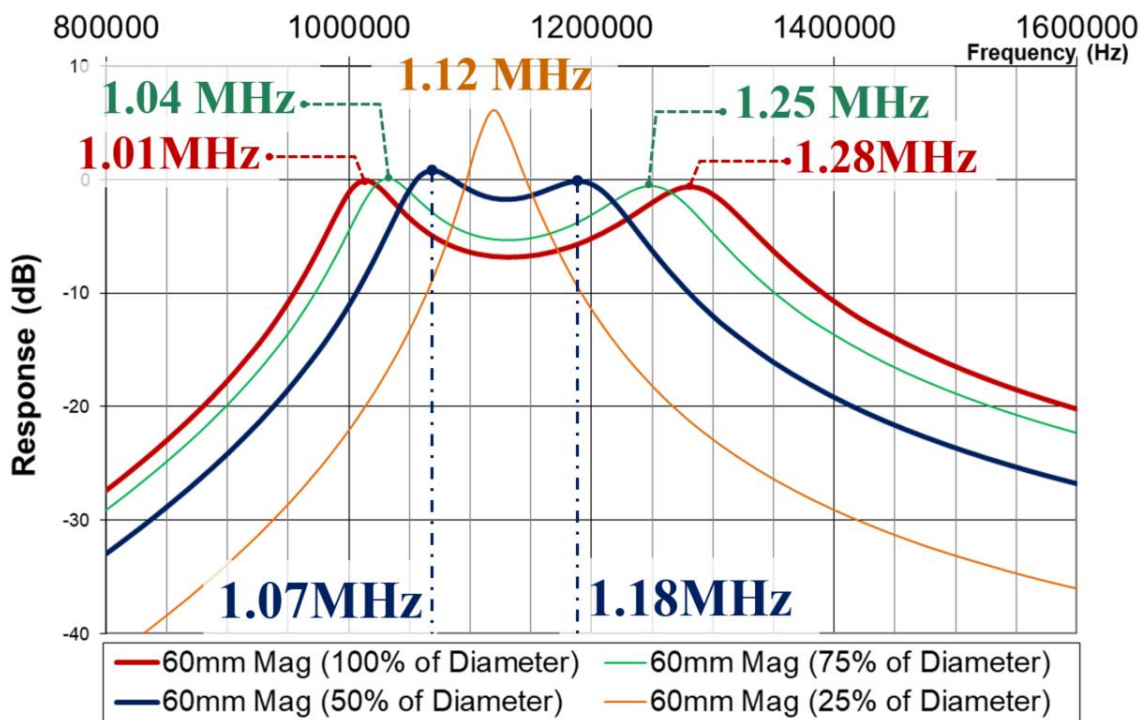


Figure 3.17. FRA measurements under the condition of misalignments

To reduce the level of mutual inductance and to discover the unity VTR at a distance of 60 mm, the Rx winding was misaligned intentionally from the central axis between the windings, as shown in Figure 3.16. It was clarified that a discrepancy in the winding alignment enhances the level of VTR at the near gap. In this demonstration, the unity VTR was detected when half of the Rx winding diameter is magnetically coupled with the Tx winding, as shown in Figure 3.17. The impedance trace at a distance of 60 mm with a 50% misalignment of the diameter corresponds closely to the FRA result at a critical distance 105 mm, as shown in Figure 3.18. Therefore, the appropriate winding alignment at the near gap can be identified using the practical FRA measurements to enhance the efficiency of the WPT system.

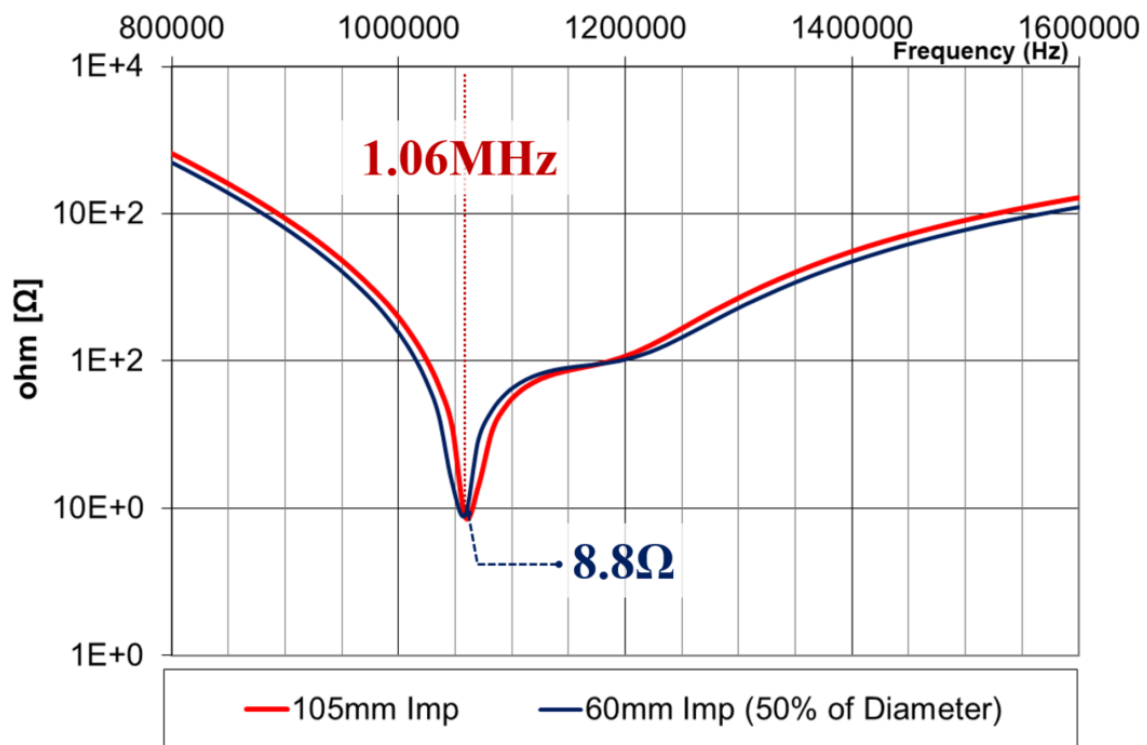


Figure 3.18. Transfer impedance comparison

With increasing the transfer distance, the voltage V_o across the Rx winding is only induced near the resonance frequency of 1.12 MHz. Therefore, the width of the VTR waveforms over the distance at the resonance frequency is narrower than the waveform at the critical distance, as shown in Figure 3.13 (b). The transfer efficiency can be

enhanced by inserting an extra winding between the two windings to bridge the magnetic coupling from Tx to Rx [23, 35]. However, this requires additional space, cost, and precise frequency tuning due to the combination of multiple devices [36].

As stated in chapter 4.1.2, the level of VTR can be greater than the unity level as the FRA measurement in the demonstration provides the relationship between V_o and V_{in} , not V_1 as shown in Figure 3.8. This clarifies that VTR over the critical distance indicates a narrow width with a sharp peak. Furthermore, the value of the transfer impedance becomes significant as the transfer distance is increased, as depicted in Figure 3.14 (b). In contrast, the transfer impedance at the near gap indicates a similar value to the impedance at the critical distance using a different resonance frequency as in Figure 3.12 (b).

3.4. 20 kHz Spiral-coil WPT design

A planar spiral coil is simple, and it can save the installation space; most EV charging systems adopt this shape [148, 149]. This work considered the implantation of a WPT system as a charging device at a frequency of 20 kHz. The various frequency ranges, such as 140 kHz, 85kHz, and 20 kHz, have been adopted in different regions based on the frequency allocation [150-153]. For the electric vehicle wireless charging, the operating frequency of 20 kHz and 85 kHz are mainly considered [154]. The 85 kHz operating frequency was accepted by SAE J2954 standard for light-duty EVs [155], and the 20 kHz frequency is suggested for heavy-duty or railway vehicles wireless charging in International Telecommunication Union (ITU) [156]. To reduce the high-frequency loss and the emission of the electromagnetic field, this study is conducted at a frequency of 20 kHz.

3.4.1. Self and mutual inductance of coils

A planar-circle-spiral coil was built, as shown in Figure 3.19, and the properties of the practical coil are presented in Table 3.3. The loss caused by the skin effect at 20 kHz was ignored in this study. However, the actual coil was built with 1,650 stranded filament of Litz wire to secure the versatility for higher frequency systems. Besides, a WPT system

at a low frequency can be free from the skin effect. However, the system needs more turns on the coils to produce enough magnetic field, and the transferring distance can be decreased at a low frequency because of the low value of the quality factor. For example, the WPT system at a utility frequency of 60 Hz was introduced, and the application was implemented with a coil of 450 turns [8].

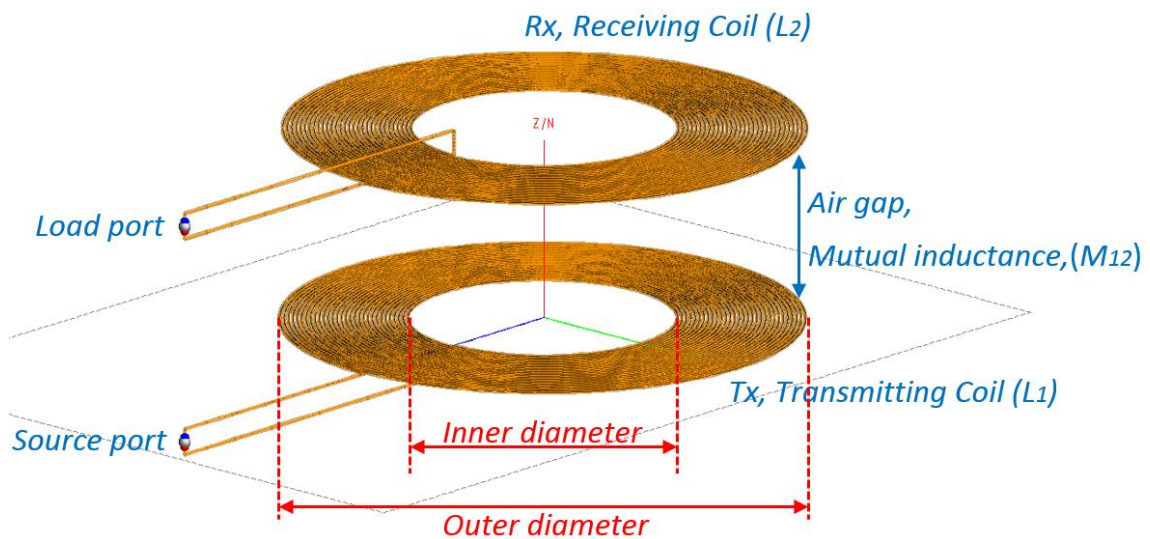
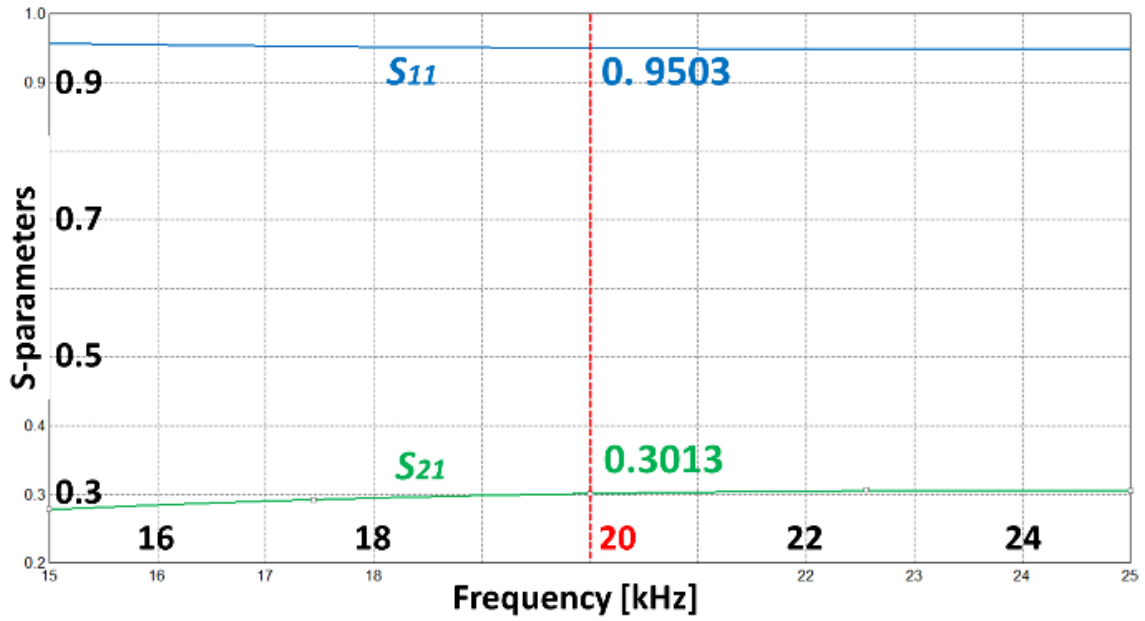


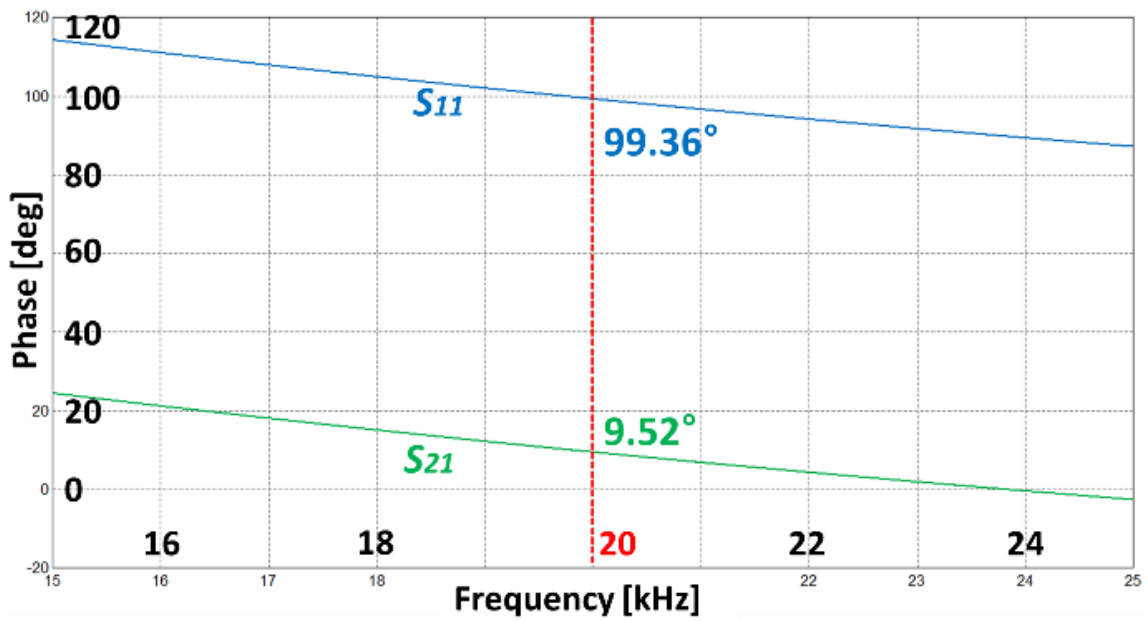
Figure 3.19. WPT system model for calculating the self and mutual inductance of coils

Table 3.3. Properties of the practical coils

Property	Value
Inner diameter of Tx and Rx	210 mm
Outer diameter of Tx and Rx	400 mm
Number of turns	30
Type of wire	Litz wire 1,650 filaments (0.05 mm diameter)
Radius of wire	1.5 mm
Parasitic resistance of wire	5.962 Ω /km up to 850 kHz
Medium of space	Air



(a)



(b)

Figure 3.20. Example of S-parameter result at a 100-mm air gap: (a) absolute, and (b) phase angle

The simulations to obtain the S -parameters were conducted using different transfer distances (10, 55, 100, 150, and 200 mm) over the frequency range from 15 kHz to 25 kHz, as shown in Figure 3.20. The source R_o and load resistance R_L are set at 50Ω respectively during the simulations. The value of self-inductance L_1 and L_2 is constant regardless of the air gap, and the mutual inductance M_{12} , and the coupling coefficient k_{12} are correctly calculated based on (3.11) and (3.12). The coils in the simulation were constructed using copper wire. It was also found that the inductance values present repetitively in the various frequency levels.

$$L_1 = \frac{|Z_{11}|}{\omega}, L_2 = \frac{|Z_{22}|}{\omega} \quad (3.11)$$

$$M_{12} = \frac{|Z_{12}|}{\omega}, k_{12} = \frac{M_{12}}{\sqrt{L_1 L_2}} \quad (3.12)$$

The magnitude and phase angle of S -parameter at a frequency of 20 kHz are shown in Table 3.4. To verify the accuracy of the FEKO results, the actual inductance value of the built coil was measured using FRA (DOBLE SFRA M5300). For reference, the passive electrical parameters RLC in the network can be precisely measured at the various frequencies up to 2 MHz [157].

Table 3.4. S -parameter at 20 kHz

Airgap [mm]	S_{11} at 20 kHz		S_{21} at 20 kHz	
	Magnitude	Phase angle	Magnitude	Phase angle
10	0.6038	114.71 °	0.7929	24.94 °
55	0.8719	103.08 °	0.4831	13.25 °
100	0.9503	99.36 °	0.3013	9.52 °
150	0.9793	97.94 °	0.1870	8.09 °
200	0.9896	97.42 °	0.1214	7.58 °

Table 3.5. Comparison of inductance value between FEKO results and practical measurements

Air gap [mm]	Parameters extracted by FEKO			Practical measurement and accuracy						
	L_1, L_2 [μH]	M_{12} [μH]	k_{12}	L_1 [μH]	$\% \Delta L_1$	L_2 [μH]	$\% \Delta L_2$	M_{12} [μH]	k_{12}	$\% \Delta M_{12}$ or $\% \Delta k_{12}$
10	351.7	308.5	0.877	352.2	-0.14 %	351.1	0.17 %	311.4	0.885	-0.91 %
55	351.7	175.0	0.498	352.2	-0.14 %	351.1	0.17 %	175.7	0.500	-0.40 %
100	351.7	107.7	0.306	352.2	-0.14 %	351.1	0.17 %	111.6	0.317	-3.59 %
150	351.7	66.6	0.189	352.2	-0.14 %	351.1	0.17 %	64.9	0.184	2.65 %
200	351.7	43.2	0.123	352.2	-0.14 %	351.1	0.17 %	41.9	0.119	3.25 %

The results from the computational calculation in Table 3.5 are comparable to the experimental value, and the percentage difference of the self-inductance ($\% \Delta L_1$ and $\% \Delta L_2$) and the coupling coefficient ($\% \Delta M_{12}$ or $\% \Delta k_{12}$) is under 0.17 % and 3.59 %, respectively. Besides, the FEKO result indicated the resistance value of the copper coil by 0.143 Ω , whereas the actual value of the parasitic resistance of L_1 and L_2 are 0.49 Ω and 0.48 Ω at 20 kHz, respectively.

3.4.2. Compensation for resonance

To tune the resonance frequency in the Tx and Rx coils, a compensating capacitor can be implemented in mainly four topologies: SS, SP, PS, and PP, as shown in Figure 3.21. As the SS topology illustrated in Figure 3.21(a) is simple, and the value of the compensating capacitor C_1 at the Tx coil is not a function of the air gap and the load impedance, many devices use this WPT system for wireless charging applications [11, 13, 25]. However, the transfer efficiency of the SS topology decreases significantly when the transfer distance varies [125], and the voltage-source-type SS system can damage the power supply when the Tx does not have a coupling with the Rx unit [100]. Also, the transfer efficiency can be reduced significantly when the two coils are coupled at a nearer

distance than the critical distance. This is defined as a frequency bifurcation [99]. To avoid this phenomenon, it might be necessary to adjust the switching frequency, the value of the compensating capacitance, or the load resistance [158]. The SP, PS, and PP topologies are illustrated in Figure 3.21(b), (c), and (d). They require a precise technique for tuning the resonance frequency [159].

The performance degradation due to the frequency bifurcation in these topologies should also be considered. To supply a sinusoidal HF voltage into the WPT resonant circuit, an additional series inductor is required for the Tx side in the PS and PP systems to filter the harmonics from the square waveform generated by the switching device [160], and the SS and SP topologies are more suitable for high-power WPT applications [19].

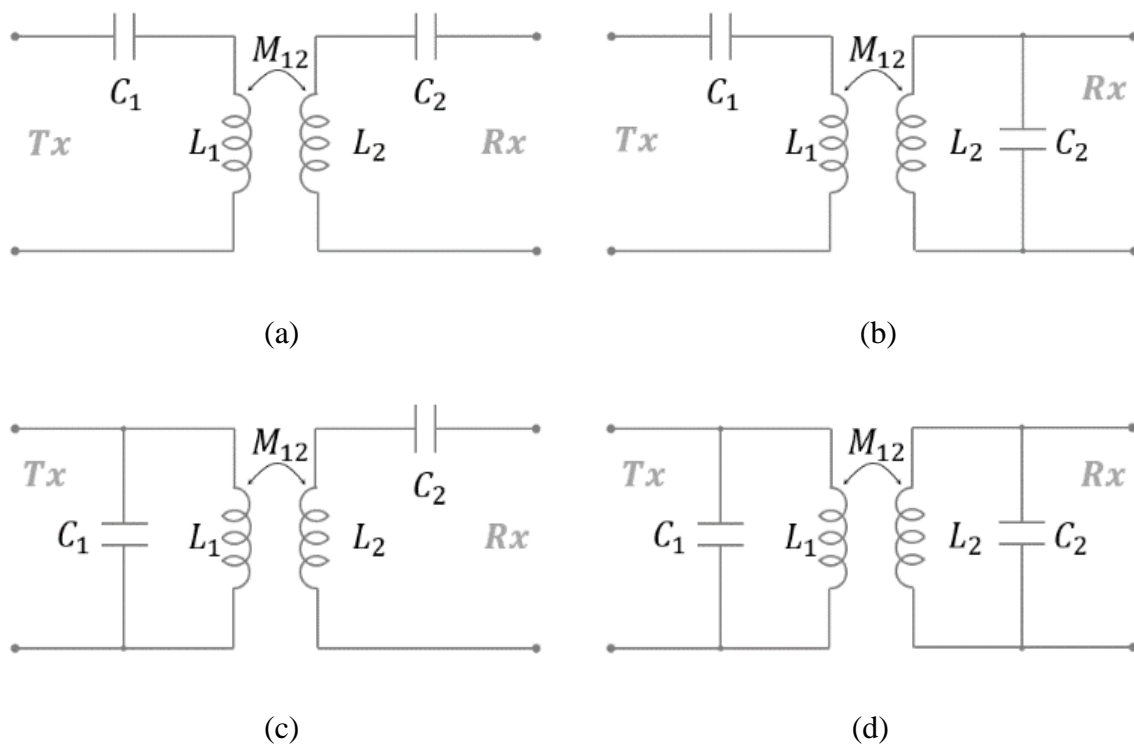


Figure 3.21. Compensating topologies based on C_1 location: (a) SS, (b) SP, (c) PS, and (d) PP

The input voltage V_{in} across the Tx terminals of the SS and SP topology, as shown in Figure 3.21 (a) and (b) is described in the following equations:

$$V_{in,ss} = Z_{in,ss}I_1 = \left(jX_1 + \frac{\omega^2 M_{12}^2}{R_L + r_1 + jX_2} \right) I_1 \quad (3.13)$$

$$V_{in,sp} = Z_{in,sp}I_1 = \left(jX_1 + \frac{\omega^2 M_{12}^2}{j\omega L_2 + r_2 + \frac{R_L}{1 + j\omega C_2 R_L}} \right) I_1 \quad (3.14)$$

Where $X_1 = \omega L_1 - (1/\omega C_1)$, $X_2 = \omega L_2 - (1/\omega C_2)$ and R_L is the load resistance. r_1 and r_2 are the parasitic resistance at Tx and Rx, respectively. Z_{in} is input impedance in the SS and SP compensations, respectively. As this prototype aims to achieve maximum power efficiency, it is assumed that the source impedance is zero [96, 161].

In equations (3.13) and (3.14), the equivalent input impedances are $\omega^2 M_{12}^2 / R_L$ and $M_{12}^2 R_L / L_2^2$, respectively, when the reactive components are eliminated by C_1 and C_2 , and the parasitic resistance is ignored. If the resonance frequency is determined as follows:

$$f_o = \frac{1}{2\pi\sqrt{L_2 C_2}} \quad (3.15)$$

The compensating capacitor C_1 in the SS and SP system, respectively, is as follows:

$$C_{2,sp} = \frac{1}{(2\pi f_o)^2 L_2} \quad (3.16)$$

$$C_{1,sp} = \frac{1}{(2\pi f_o)^2 (L_1 - M_{12}^2 / L_2)} \quad (3.17)$$

It is clarified that the elimination of the imaginary part of the input impedance in the SS topology is not affected by the variation of mutual inductance M_{12} or load resistance R_L . On the other hand, the value of the compensating capacitor $C_{1,sp}$ at the Tx side must be correctly selected due to the variation of M_{12} , which represents the size of the air gap between the coils.

Also, the compensating topology should be selected considering the load resistance value. If the load resistance R_L is smaller than the characteristic impedance at Rx, the SS compensating system is beneficial because the input impedance ($\omega^2 M_{12}^2 / R_L$) at the resonance frequency is inversely proportional to the load resistance. This means that the WPT system can deliver much power to the input impedance, including the load resistance. The characteristic impedance Z_o is determined in (3.18), and Z_o of the prototype is about 44 Ω at 20 kHz.

$$Z_o = \sqrt{L_2 / C_2} \quad (3.18)$$

Besides, if the load resistance R_L is higher than the characteristic impedance Z_o , the SP topology is superior to the SS system. Hence, the SS and SP systems should not be compared with the identical value of the load resistance. In this study, a near-field analysis of the SP compensating topology is conducted here.

3.4.3. Magnetic coupling and field distribution in near field

In the previous chapters, 3.4.2 and 3.4.3, the required electrical parameters: L_1 , L_2 and M_{12} , were obtained precisely, then the value of the compensating capacitors C_1 and C_2 at the Tx and Rx side can be calculated based on (3.16) and (3.17). When the Tx and Rx coil are loosely coupled in the magnetic field at the resonance frequency, the electric energy transfers efficiently through free space [36]. To tune the resonance frequency of 20 kHz in the simulation models, the compensating capacitor C_2 at the Rx side was selected as 180 nF at a self-inductance value of 351 μH on L_2 at 20 kHz.

The compensating capacitor C_1 for the SP topology should be employed from (3.17) with respect to the air gap as the mutual inductance M_{12} varies over the transfer distance. The value of the compensating capacitor is independent of the load resistance in the SP system. However, the low load resistance and near air gap can cause a frequency bifurcation and efficiency reduction [99]. The compensating capacitors at both the Tx and Rx side were implemented on the wire port and the AC voltage of 10 V_{peak} at 20 kHz supplied into the Tx unit during the simulation. As mentioned earlier, the process of the

high-frequency switching is not assessable in FEKO; however, the peak magnitude of the voltage input V_{in} to the Tx unit can be extracted by the Fourier series analysis in (3.19).

$$V_{in} = V_{dc} \frac{4}{\pi} \sum_{k=1}^{\infty} \frac{\sin\{(2n-1)\omega t\}}{(2n-1)} \text{ [V]} \quad (3.19)$$

The input voltage V_{in} is generated in the shape of a square waveform by the DC to AC inverter across the terminal of the Tx coil. Hence, the sinusoidal waveform of the input voltage. It also represents the first harmonic of the square waveform, where V_{dc} is the magnitude of the square waveform, and n is the number of harmonics. In the experiments, a square wave voltage of 7.9 V is to be injected into the Tx unit, an AC voltage of 10 V is applied for the FEKO simulation based on (3.19).

Furthermore, the equivalent load resistance R_{eq} can be determined through (3.20), when the full-bridge rectifier is utilized between the Rx unit and the load resistance R_L [57].

$$R_{eq} = \frac{8}{\pi^2} R_L \text{ [\Omega]} \quad (3.20)$$

In the FEKO analysis, the equivalent resistance R_{eq} was set as 97 Ω at the AC output terminals of the Rx unit. This states that the actual load resistance across the DC output terminal is about 120 Ω .

The magnetic field in the Rx coil induced by the Tx coil, and the strength and distribution of the magnetic field are illustrated in Figure 3.22. The simulation results confirm that the efficiency of the WPT system declines when the air gap is over the limit of the magnetic coupling range discovered by the simulation result. For reference, this electromagnetic analysis of FEKO was conducted using the student edition. The level of the magnetic field at both the Tx and Rx coils indicates about 40 A/m and 100 A/m with a 10 mm and 55 mm air gap, respectively, as shown in Figure 3.22 (a) and (b). At a distance of 100 mm, the amplitude of the magnetic field in the Tx coil is higher than in the Rx coil, but the Rx coil has a similar amount of the magnetic field in the Tx coil as shown in Figure 3.22 (c). The highest level of the 500 A/m magnetic field is recorded at an air gap of 150 mm through the Rx coil has the induced magnetic field of 250 A/m, as shown in Figure 3.22 (d).

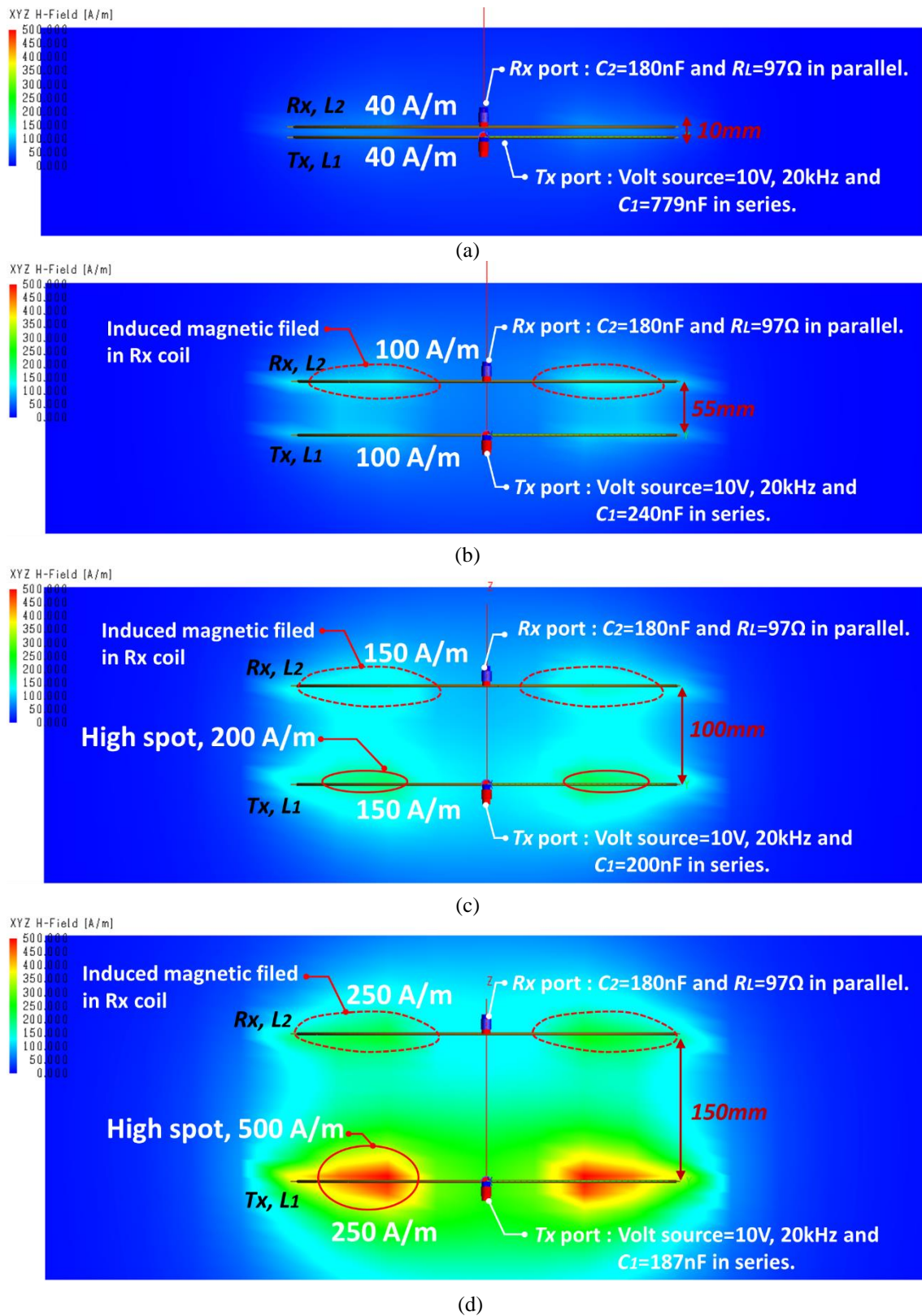
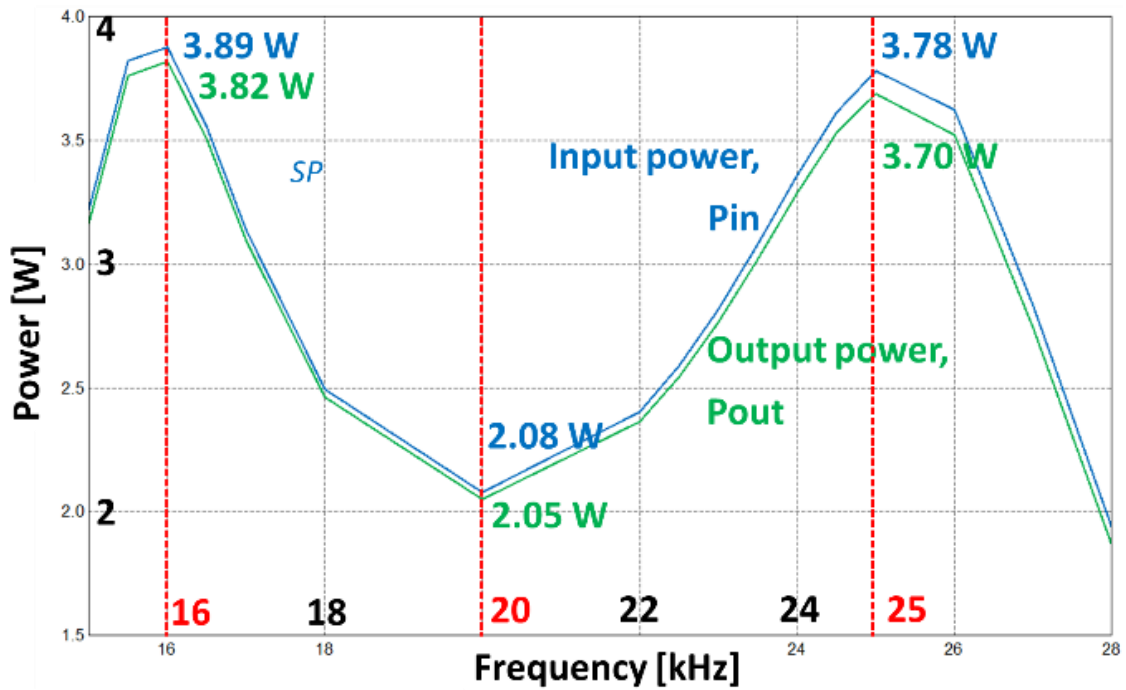
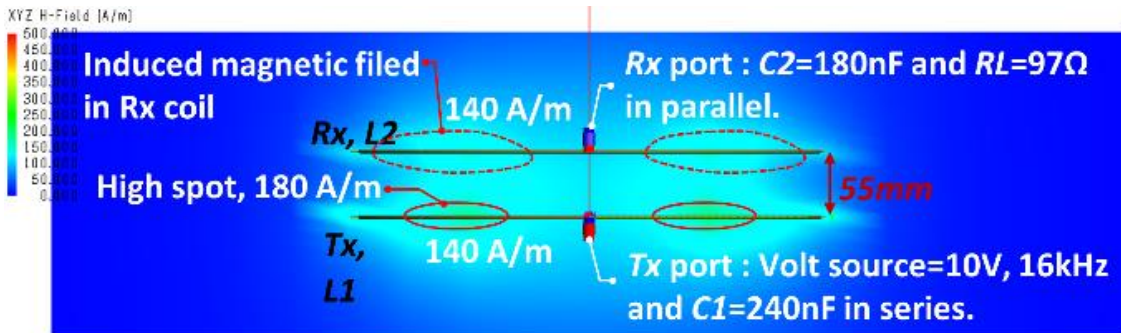


Figure 3.22. Magnetic coupling and field distribution in SP topology using different air gaps ($C_1=180\text{ nF}$) at 20 kHz: (a) 10 mm, $C_1=779\text{ nF}$, (b) 55mm, $C_1=240\text{ nF}$, (c) 100 mm, $C_1=200\text{ nF}$, and (d) 150 mm, $C_1=187\text{ nF}$



(a)



(b)

Figure 3.23. Transferring power and magnetic field distribution in SP topology at 55 mm: (a) supplied power and transferred power across the load, and (b) magnetic coupling at the frequency of 16 kHz

This verifies that a low magnetic field is formed between the Tx and Rx coil at the near gap at 20 kHz; hence, low power is delivered from the Tx unit to the Rx unit. This is caused by the phenomenon of frequency bifurcation, which occurs when two coils are coupled in the over-coupled region. The FEKO simulation can also clarify the frequency bifurcation. For instance, at a distance of 55 mm, the transferring power is only

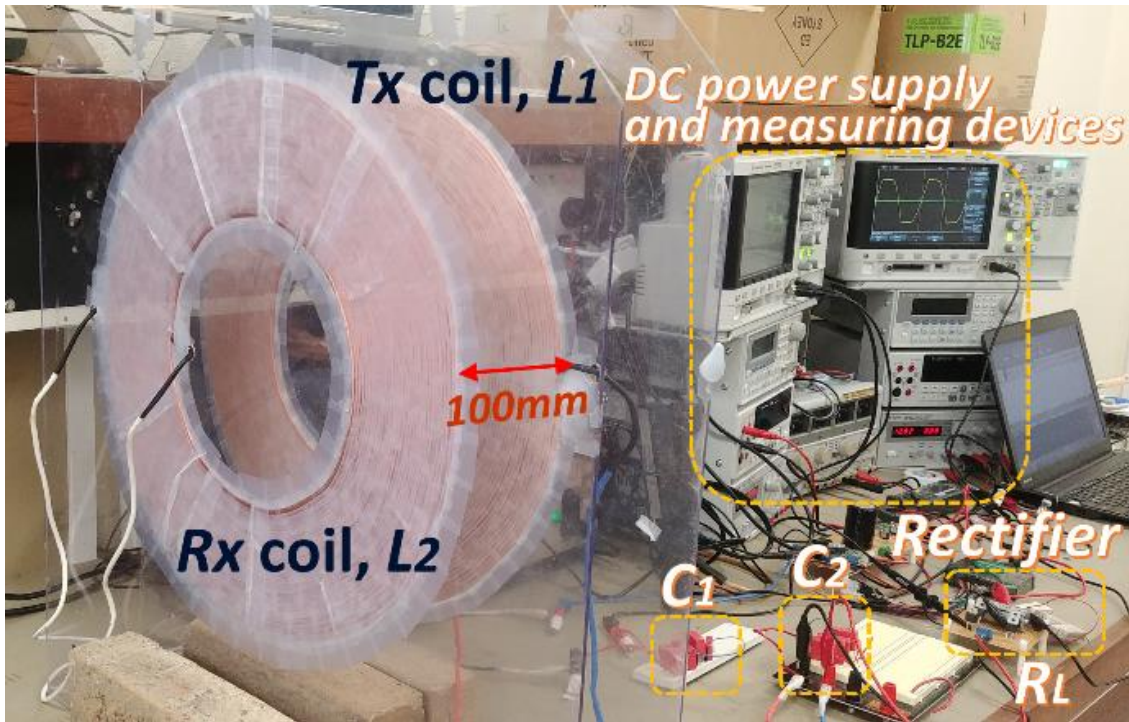
2.05 W at 20 kHz; however, at a frequency of 16 kHz and 25 kHz, power of 3.82 W and 3.70 W is delivered to the Rx unit, respectively, as illustrated in Figure 3.23 (a). Also, the higher magnetic field of 140 A/m is formed at 16 kHz rather than 20 kHz, as shown in Figure 3.23 (b) and Figure 3.22 (b). To achieve improved performance of the WPT system at near distance, it is necessary to shift the switching frequency or utilise the different values of the compensating capacitor to avoid frequency bifurcation.

3.4.4. Power transferred and practical verification

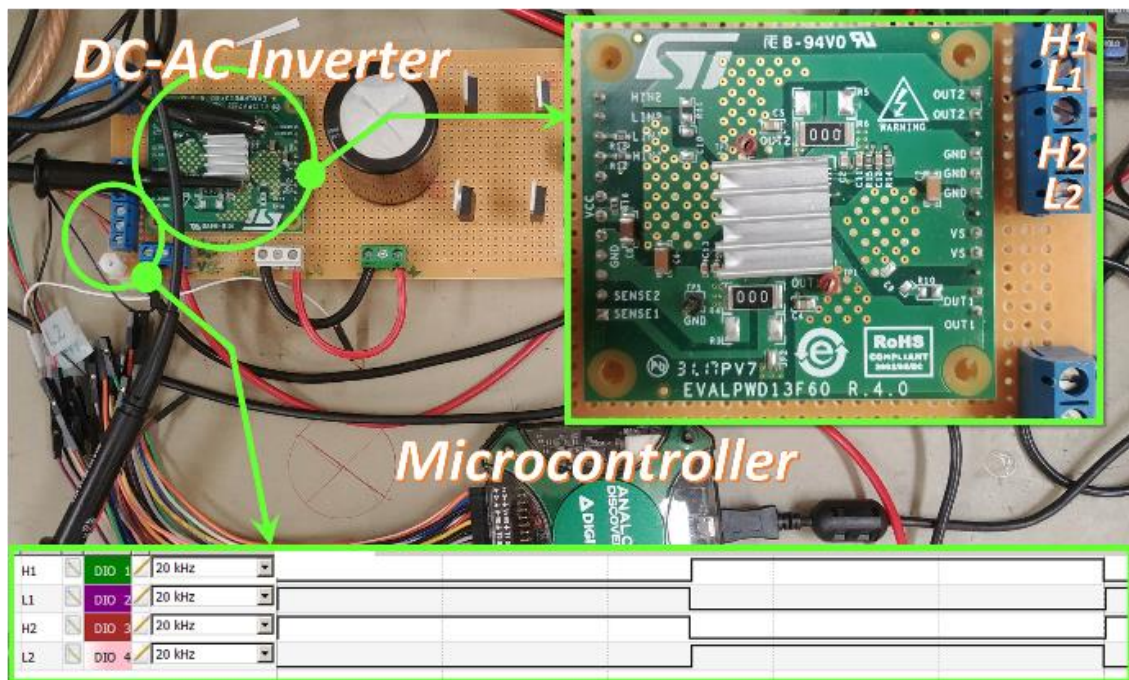
To verify the simulation results, the transferred power and the related parameters were measured in the SP model at an air gap of 100 mm, as shown in Figure 3.24 (a). The WPT model at a distance of 100 mm was selected, as the magnetic coupling between the coils is well maintained, and frequency bifurcation does not occur at that distance. The full-bridge with gate driver (PWD 13F60, STMicroelectronics) was implemented, and the gate signals with a duty cycle of 50% at 20 kHz were given to the switching device from the micro-controller (Analogue discovery 2, Digilent), as shown in Figure 3.24 (b).

In the practical experiment, a low voltage of $10 V_{\text{peak}}$ was supplied to the circuit due to the considerations of high voltage resonance oscillation and electromagnetic interference. As a DC power supply and HF switching devices could not be configured in the simulation tool, the overall efficiency η_o between the DC power supply and the load resistance was not evaluated. However, the transfer efficiency η_T from the Tx unit to the load resistance was correctly identified.

The distribution of the electric and magnetic field between two coils with the wire ports in the SP system at a 100 mm air gap is illustrated, and it indicates that the electric and magnetic fields at the middle of the coil are about 400 V/m and 200 A/m, respectively. In the vicinity of the coils, the values are under 200 V/m and 70 A/m, respectively, as shown in Figure 3.25 (a) and (b). Therefore, the level of the electromagnetic field can be estimated to clarify its safety level in the near-field area based on the following guidelines: IEEE C95.1-2014 or International Commission on Non-Ionising Radiation Protection [162].

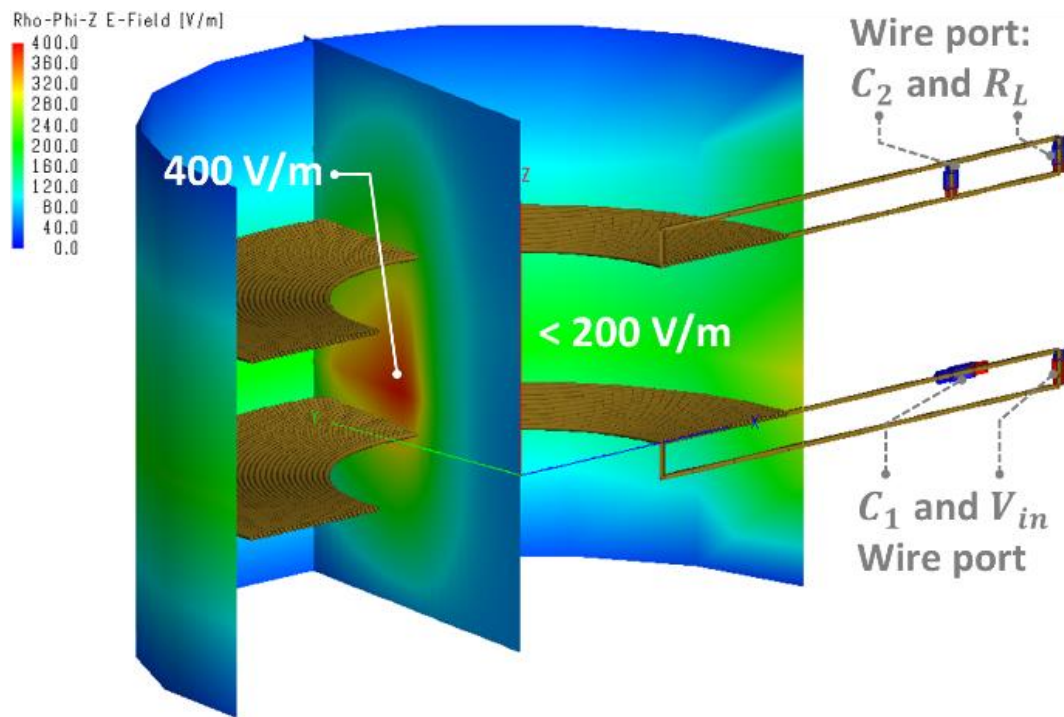


(a)

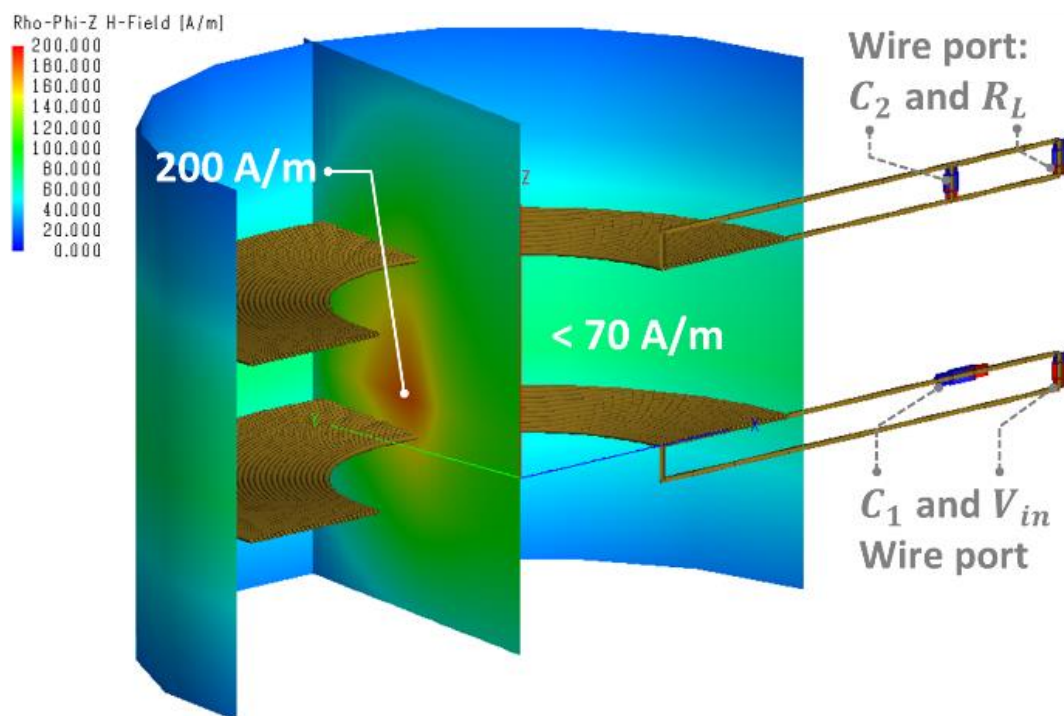


(b)

Figure 3.24. Experimental measurement setup: (a) 1650-filament Litz coils of Tx and Rx with compensating capacitors, and (b) Full-bridge switching device and pulse (gate) signals

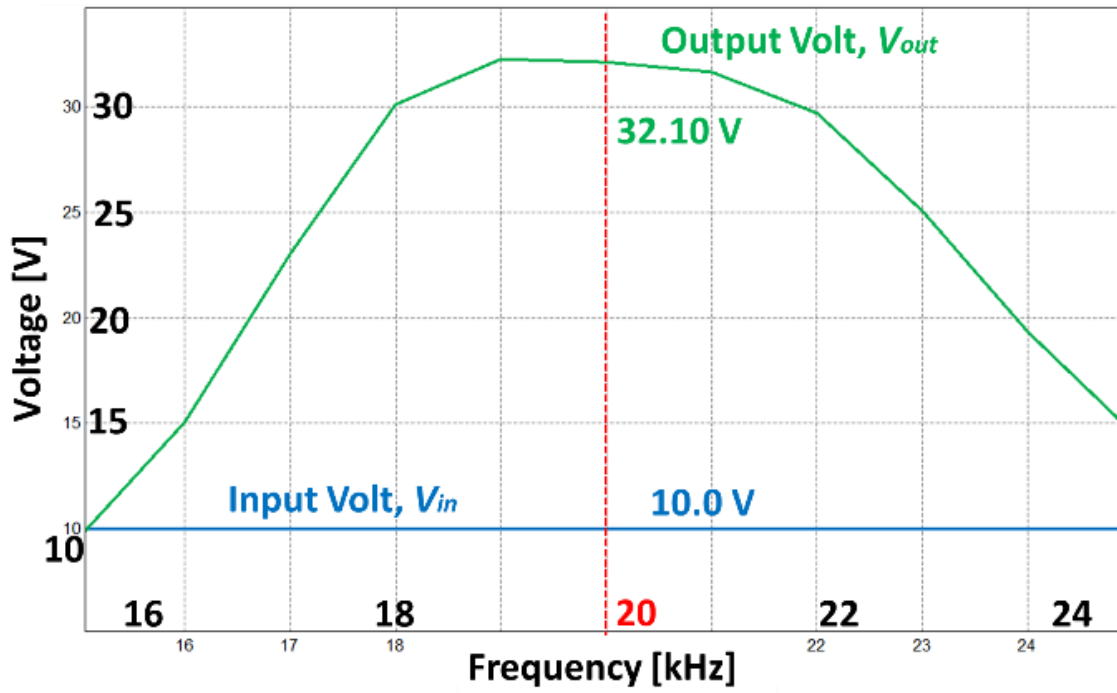


(a)

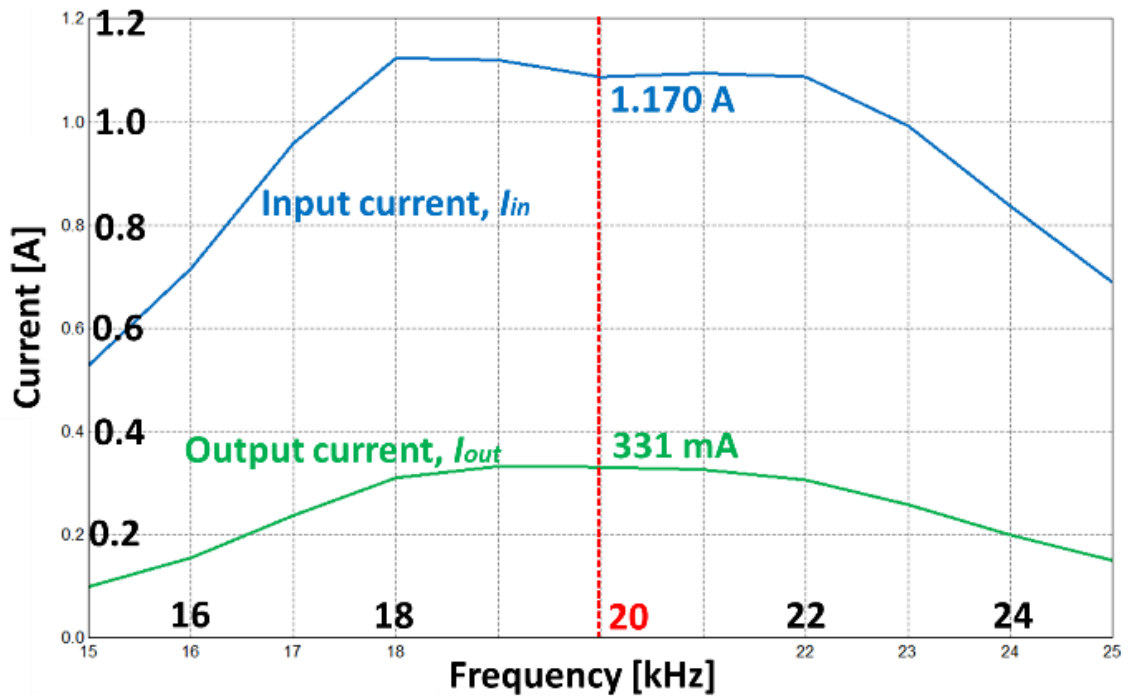


(b)

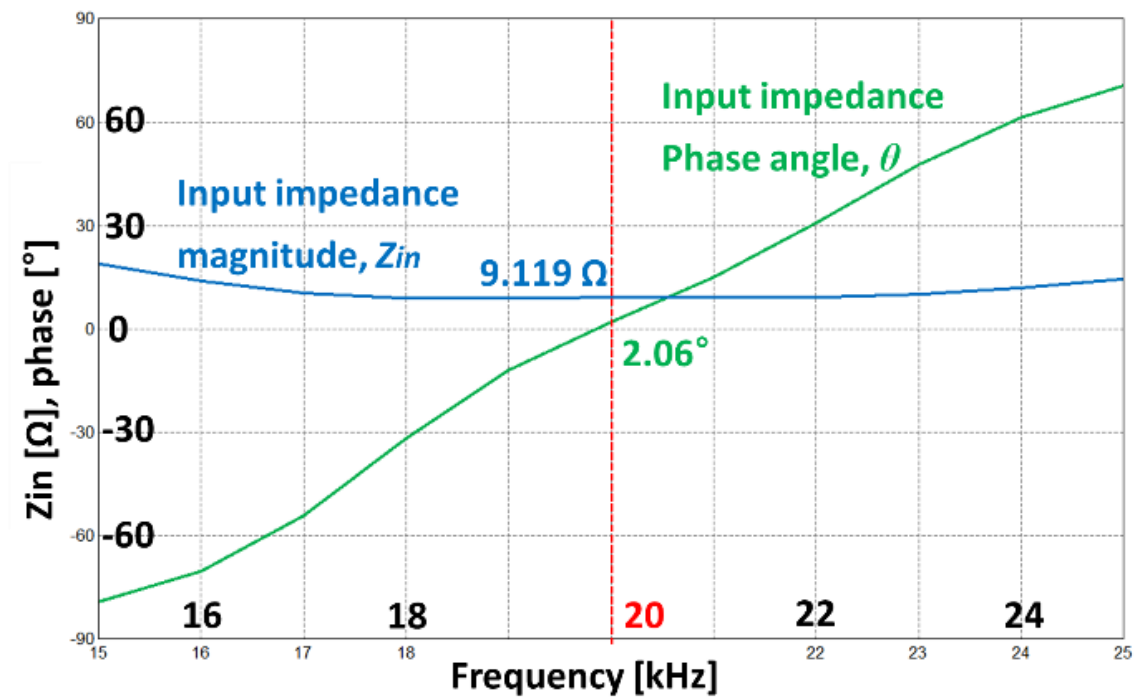
Figure 3.25. FEKO results of the near field in the SP system at a 100 mm air gap at 20 kHz: (a) electric field, and (b) magnetic field



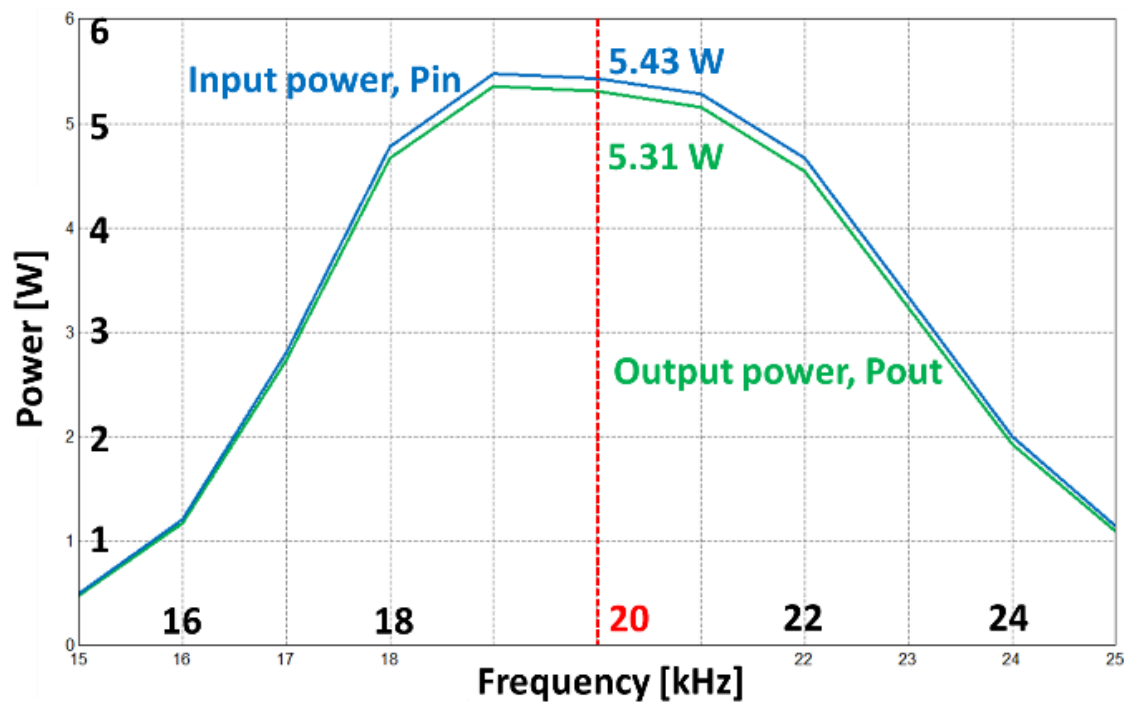
(a)



(b)



(c)



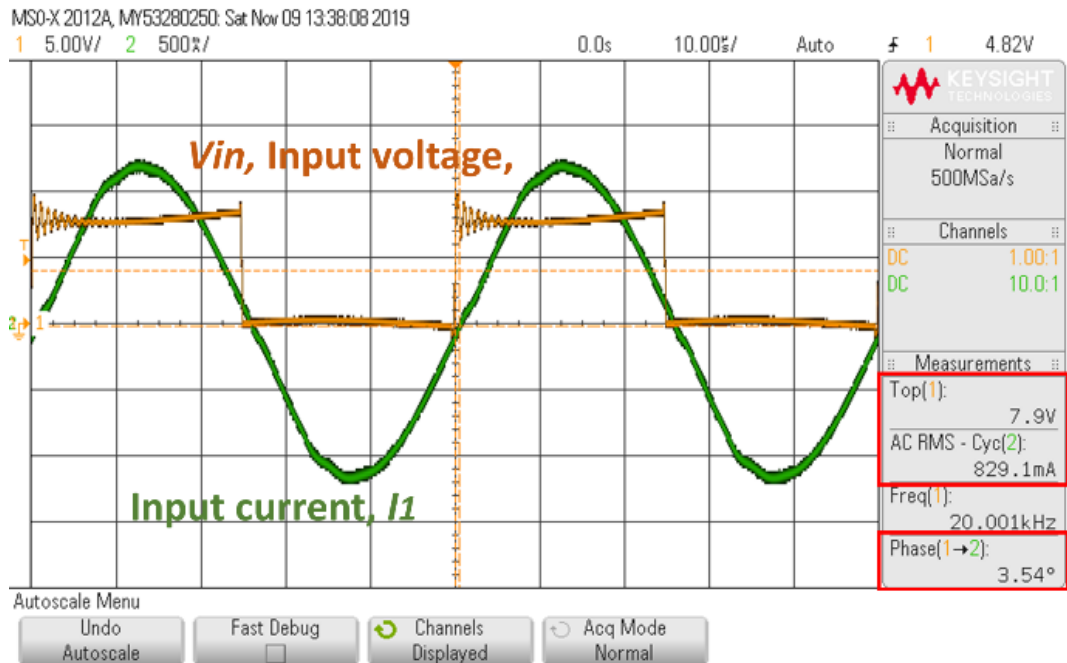
(d)

Figure 3.26. FEKO results for the electrical parameters of an SP WPT system at 100 mm: (a) in/output voltage, (b) in/output current, (c) input impedance, and (d) in/output power

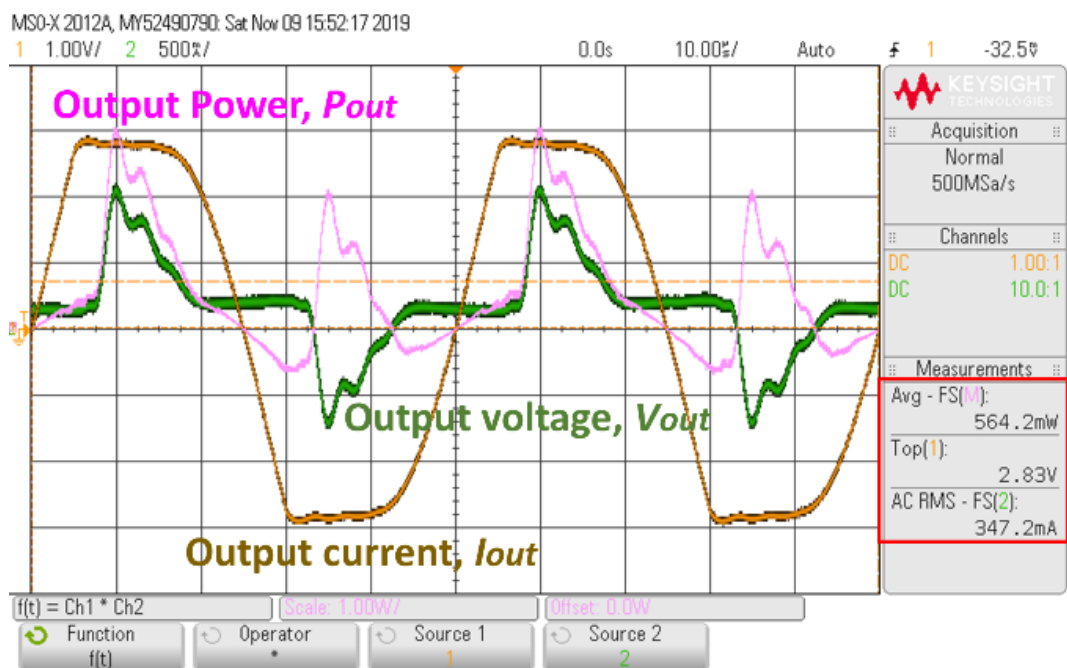
The electrical parameters in the WPT model – V_{in} , V_{out} , Z_{in} , θ , I_{in} , I_{out} , P_{in} and P_{out} can also be determined in the different frequency ranges, as shown in Figure 3.26. When the peak voltage of 10 V is supplied to the Tx unit, an output voltage of 32.1 V is produced across of the load terminal at 20 kHz, and the input and output peak current is recorded as 1.170 A and 0.331 A, respectively, in peak value, as shown in Figure 3.26 (a) and (b).

Table 3.6. Comparison of the FEKO results and the experimental measurement for an SP WPT model at a 100 mm air gap

Parameters	FEKO	Experimental measurement	Δ Difference	% Δ
V_{dc} (DC voltage)	n/a	8.7 V	n/a	n/a
I_{dc} (DC current)	n/a	0.72 A	n/a	n/a
P_{dc_in} (DC power)	n/a	6.264 W	n/a	n/a
P_{in} (Input AC Power)	5.43 W	5.897 W	-0.467 W	-8.600%
V_{in} (Input AC voltage)	n/a 10.00 V_{peak} 7.071 V_{RMS}	7.900 V_{peak} [square wave] 10.06 V_{peak} [1 st harmonic] 7.113 V_{RMS}	n/a n/a -0.042 V_{RMS}	n/a n/a -0.594 %
I_{in} (AC in Tx)	1.170 A_{peak} 0.827 A_{RMS}	n/a 0.829 A_{RMS}	n/a -0.002 A_{RMS}	n/a -0.242 %
Z_{in} (Input impedance)	9.119 Ω	8.580 Ω	0.539 Ω	5.911 %
θ (Phase angle of Z_{in})	2.06 °	3.54 °	-1.480 °	n/a
V_{out} (Voltage across load)	32.10 V_{peak} 22.698 V_{RMS}	n/a 22.543 V_{RMS}	n/a 0.155 V_{RMS}	n/a 0.683 %
I_{out} (Current through load)	0.331 A_{peak} 0.234 A_{RMS}	n/a 0.250 A_{RMS} [Calculated]	n/a -0.016 A_{RMS}	-6.834 %
P_{out} (Output power on Rx)	5.31 W	5.642 W	-0.332 W	-6.252 %
η_T (Transfer efficiency)	97.790 %	95.676 %	2.114 %	2.162 %
P_{dc_out} (Output power on DC Load)	n/a	4.752 W	n/a	n/a
η_o (DC to DC, Overall efficiency)	n/a	75.862 %	n/a	n/a



(a)



(b)

Figure 3.27. Practical measurement of an SP system at 100 mm air gap: (a) Input power, and (b) Output power

The source resistance R_0 was set as 0Ω , and the load resistance of 97Ω was implemented in the wire ports in the FEKO analysis. As the compensating capacitors C_1 and C_2 were correctly utilized, the phase angle of the input impedance $Z_{in,sp}$ in (3.14) was 2.06° ; this presents almost zero degrees, as indicated in Figure 3.26 (c).

Furthermore, the transferred power between the coils was calculated and, the maximum value of 5.31 W of power was delivered at 20 kHz frequency, as presented in Figure 3.26 (d). The actual values of the parameters: V_{in} , I_{in} , V_{out} , I_{out} and the phase angle in the prototype were measured using the oscilloscope (Agilent Technologies: MSO-X 2012A) and the current probe (Tektronix A622), as shown in Figure 3.27. The results of the comparison between the simulation result and practical measurements of the WPT model are presented in Table 3.6. In addition, the input impedance Z_{in} of the experimental measurement in Table 3.6 was calculated based on the voltage and current reading on the oscilloscope. It was observed that the error of the input parameters (input voltage V_{in} , current I_{in} and impedance Z_{in}) is under 6%. The deviation value in the phase angle θ of the input impedance Z_{in} , is only 1.48° . The input and output power (P_{in} and P_{out}) in the practical measurement indicates an error of -8.60% and -6.252%, respectively. The value of the transfer efficiency η_T is recorded as 95.676%, and is comparable to the FEKO result of 97.790%.

This practical measurement was conducted with the implementation of a DC to HF AC inverter on the Tx unit and an HF AC to DC rectifier. Therefore, the square waveform was indicated at the Tx unit, and the distorted waveforms of the output voltage and current were recorded on the load resistance due to the full-bridge rectifier. It clarifies that zero-phase switching in the HF inverter was achieved as the difference of phase angle between the voltage. The current at both ends indicates almost zero, as shown in Figure 3.27 (a) and (b). For reference, the overall efficiency or DC to DC efficiency η_T of 75.862% is presented in the prototype due to heat loss on the switching devices, the full-bridge rectifier, and ohmic loss in the cooper winding. Consequently, the computational electromagnetic field analysis provides acceptable results for the design of the WPT systems. The formation and distribution of electromagnetic coupling between the coils, the self and mutual inductance, the output voltage, and the rate of transferred power can be identified prior to practical WPT implementations.

3.5. Summary

The performance of the inductively-coupled WPT system is sensitive to the structure of the Tx and Rx coil, and the variation of the air gap. In this work, the characteristic of the electromagnetic field and the electrical parameters of the WPT system were correctly identified through the computational analysis (FEKO), frequency response analyser (FRA), and practical experiment.

A 1.16 MHz helical-shaped WPT system was built using FEKO to analyse the variation of the VTR between the Tx and Rx winding over the distance under a wide range of frequencies. It showed that the critical distance that results in unity VTR, or the maximum power transfer, is correctly observed using FRA measurement. Also, the rectified position of the Rx winding below the critical distance was practically determined to enhance the transfer efficiency against the frequency bifurcation. Using the proposed application, critical distance, frequency bifurcation, and impedance variation can be recognised to achieve maximum transfer efficiency on large WPT systems.

The 20 kHz WPT system with spiral-shaped Tx and Rx coil with a radius of 200 mm was also implemented. The *S*-parameter in FEKO results accurately extracted the self and mutual inductance of the coils, and the values of these parameters agreed with the results of the FRA measurements. Subsequently, the characteristic of the magnetic coupling between the two coils in the SP compensating WPT system at the resonance frequency of 20 kHz was observed via near-field analysis. It was also discovered that the prototype of the SP system efficiently delivers electric energy when the air gap is under 100 mm. The electrical parameters (i. e. V_{in} , I_{in} , P_{in} , Z_{in} , V_{out} , I_{out} , and P_{out}) of the WPT system examined by the simulation tool are comparable to the experimental measurements of the prototype. Therefore, this study clarified that the use of FEKO facilitates the comprehensive and accurate analysis of the electromagnetic and electrical behaviour of near-field WPT systems.

Chapter 4

Design and Maintenance of WPT Systems in Different Compensating Topologies Using FRA

This chapter introduces the characteristics of WPT systems using various compensating topologies to mitigate the reactive component of the input impedance. To precisely tune the WPT circuit at the resonance frequency, it is important to correctly identify the compensating capacitors at the Tx and Rx sides. The capacitors can be connected to the Tx and Rx coils either in series or parallel, as shown in Figure 4.1. Consequently, four different compensating topologies: SS, SP, PS, and PP are basically available.

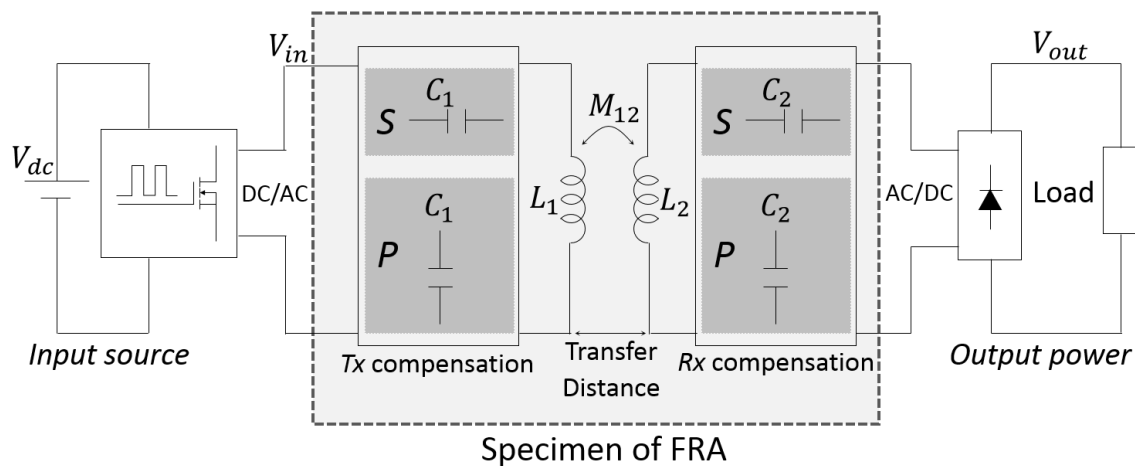


Figure 4.1. Compensating scheme of inductively-coupled WPT system

4.1. Circuit analysis and input impedance

To achieve a resonant state between the Tx and Rx coils, compensating capacitors C_1 at Tx side and C_2 at Rx side should be precisely selected and connected either in series or parallel with the coil. An SS topology is the simplest model, as the resonant frequency can be easily obtained. In this topology, the value of C_1 should be maintained constant regardless of the variation in the coupling coefficient factor k_{12} between the two coils

and the load resistance R_L . On the other hand, the value of C_1 in an SP topology is affected by k_{12} or R_L . In PS and PP topologies, both k_{12} and R_L values should be considered for the precise calculation of C_1 . The value of C_1 as a function of circuit parameters in different topologies is given in Table 4.1. Where $\omega_o = 1/\sqrt{L_2 C_2}$ and $\omega_o' = \sqrt{(1/L_2 C_2) - (1/C_2^2 R_L^2)}$ are the resonance angular frequencies in rad/s [99, 163]. The near-field WPT system is generally applicable in a frequency range from tens of kilohertz to a few megahertz [131]. As the value of the coil inter-turn capacitance, generally in the range of pico-Farads in a high-frequency range, is much smaller than the value of the external compensating capacitor connected to the coil, which is in the range of nano- to micro-Farads, the value of the coil inter-turn capacitance can be ignored [164, 165]. However, if the far-field WPT application in a frequency range from hundreds of megahertz to a few gigahertz is considered, or the inter-turn capacitor level is comparable to the compensating capacitor, the resonance frequency should be correctly tuned with the consideration of the coil self-capacitance value [166].

Table 4.1. Compensating Capacitor Value at the Tx side

Model	ω	C_1 value
SS	ω_o	$C_1 = 1/(\omega_o^2 L_1)$
PS	ω_o	$C_1 = \frac{L_1}{\left(\frac{\omega_o^2 k_{12}^2 L_1 L_2}{R_L}\right)^2 + (\omega_o L_1)^2}$
SP	ω_o	$C_1 = \frac{C_2}{\frac{L_1}{L_2} (1 - k_{12}^2)}$
	ω_o'	$C_1' = \frac{L_2 C_2^2 R_L^2}{(C_2 R_L^2 - L_2) L_1}$
PP	ω_o	$C_1 = \frac{C_2 (1 - k_{12}^2)}{\frac{L_1}{L_2} \left\{ \frac{C_2}{L_2} (R_L k_{12}^2)^2 + (1 - k_{12}^2)^2 \right\}}$
	ω_o'	$C_1' = \frac{L_1 L_2^4 C_2^2}{L_1^2 L_2^3 C_2 - \frac{L_1^2 L_2^4}{R_L^2} + \frac{M^4}{R_L^2} (C_2 R_L^2 - L_2)^2}$

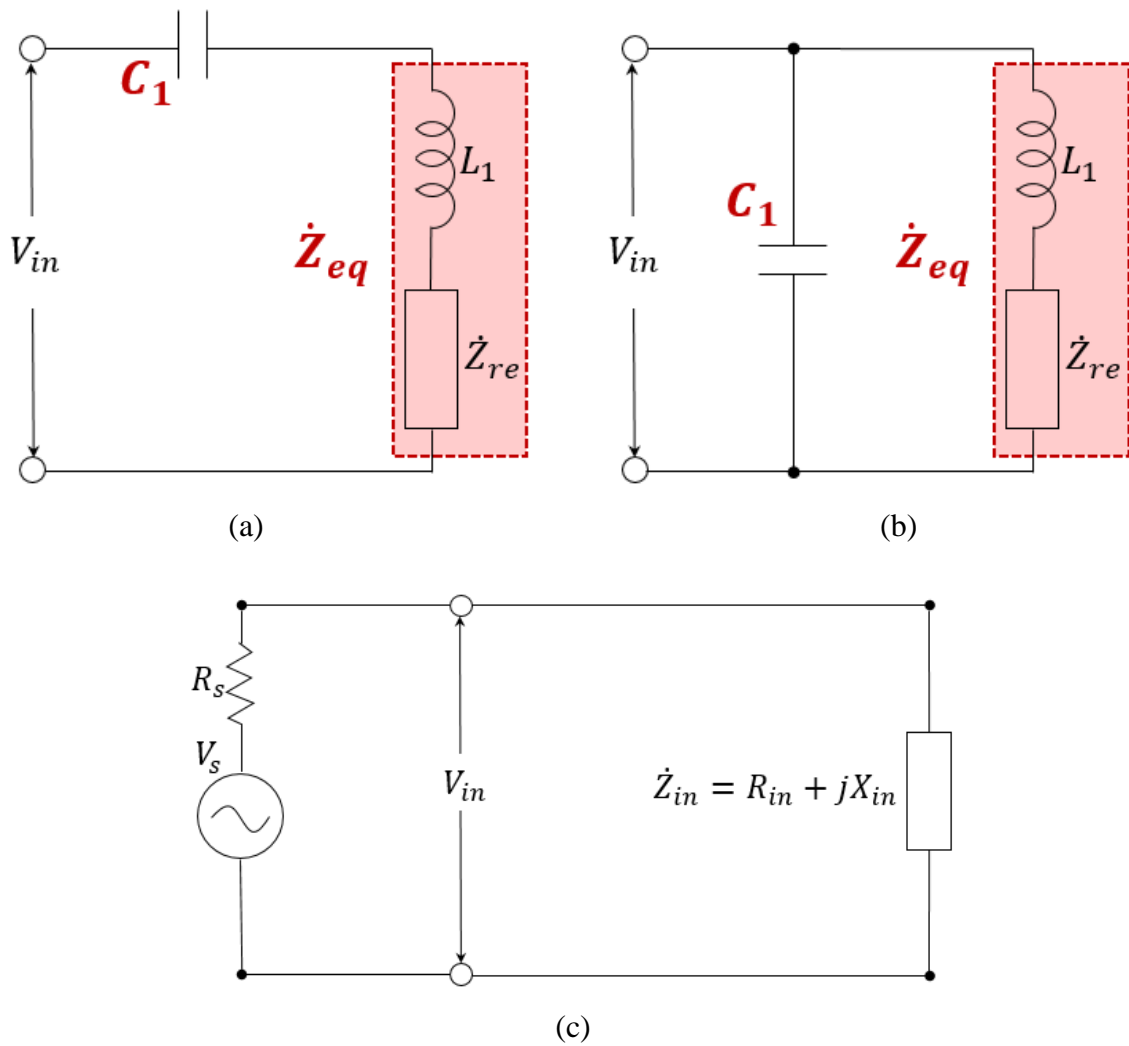


Figure 4.2. Simplified IPT Equivalent Circuit: (a) SS or SP topology, (b) PS or PP topology, and (c) equivalent total input impedance

When the resonance frequency is ω_o' (for SP and PP models), the reflected impedance \dot{Z}_{re} of the equivalent circuit shown in Figure 4.2 (a) and (b) does not include the imaginary component from the parallel-compensated Rx side. On the other hand, both real and imaginary impedance components are reflected when ω_o is implemented as the resonance frequency.

In this study, the circuit analysis and the demonstrations are performed based on ω_o . As each topology has advantages and disadvantages, the compensating circuit should be selected based on the operating frequency, load resistance, and air gap. An SS topology is preferred when the transfer distance and the load are static. PS, SP, and PP topologies

need to consider various parameters to continuously tune the resonance frequency when the air gap and load are changing.

The impedance on the Rx side and the mutual inductance in the series compensated circuit can be simplified as a reflected equivalent impedance \dot{Z}_{eq} . Also, the impedance with the series compensation on the Rx side, as shown in Figure 4.2 (a), can be expressed as

$$\mathcal{R}e(\dot{Z}_{eq,se}) = |R_{eq,se}| = \frac{\omega^2 M_{12}^2}{R_L} \cdot \frac{1}{1 + \gamma^2} \quad (4.1)$$

$$\mathcal{I}m(\dot{Z}_{eq,se}) = |X_{eq,se}| = \omega L_1 + \frac{\omega^2 M_{12}^2}{R_L} \frac{\gamma}{(1 + \gamma)} \quad (4.2)$$

The normalised constant of the reactive component γ is equivalent to $Q_2(\omega/\omega_o - \omega_o/\omega)$. When the operating frequency reaches the resonance frequency, γ vanishes. The operating and resonance angular frequency is denoted as ω and ω_o , respectively. In addition, the load quality factor Q_2 is the ratio between the load resistance and the reactance value on the Rx side. For a parallel compensation topology on the Rx side, as shown in Figure 4.2 (b), the equivalent impedance is

$$\mathcal{R}e(\dot{Z}_{eq,pa}) = |R_{eq,pa}| = \frac{\omega^2 L_1 L_2}{R_L} \frac{\left\{ \tau(k_{12}^2 - 1) + \frac{\omega^2}{\omega_o^2} \left(k_{12}^2 - 1 + \frac{\omega_o^2}{\omega^2} \right) \right\}}{\tau^2 + \frac{\omega^2 L_2^2}{R_L^2}} \quad (4.3)$$

$$\mathcal{I}m(\dot{Z}_{eq,pa}) = |X_{eq,pa}| = \frac{\omega L_1 \left\{ \frac{\omega^2}{\omega_o^2} \tau \left(k_{12}^2 - 1 + \frac{\omega_o^2}{\omega^2} \right) - \frac{\omega^2 L_2^2}{R_L^2} (k_{12}^2 - 1) \right\}}{\tau^2 + \frac{\omega^2 L_2^2}{R_L^2}} \quad (4.4)$$

where τ is the nominalization factor of the resonance frequency and is determined from $\tau = 1 - (\omega^2/\omega_o^2)$.

When the compensation capacitor C_1 is connected to $\dot{Z}_{eq,se}$ or $\dot{Z}_{eq,pa}$ in series for the SS or SP topology, as shown in Figure 4.2 (a), the total input impedance $\dot{Z}_{in,SS}$ and $\dot{Z}_{in,SP}$ can be calculated by adding the capacitive reactance value based on C_1 to (4.2) and

(4.4). On the other hand, to accomplish the PS or PP topology, as depicted in Figure 4.2(b), the compensating reactance influences the resistive and reactive components of the input impedance. The input impedance in the PS and PP topology is expressed as

$$\dot{Z}_{in,PS} = \frac{1}{j\omega C_1} // (R_{eq,Se} + jX_{eq,Se}) \quad (4.5)$$

$$\dot{Z}_{in,PP} = \frac{1}{j\omega C_1} // (R_{eq,Pa} + jX_{eq,Pa}) \quad (4.6)$$

When the resonant circuit is perfectly designed, only the real part of the input impedance is maintained, as shown in Figure 4.2(c). However, if the nominalized factor γ or τ is not zero, a residual value of the imaginary component will exist, and it also affects the resistive part of the equivalent impedance, as shown in (4.1 - 4.4). If not compensated, this residual imaginary component results in the poor performance of the WPT system, and a large capacity power supply must be used.

The resistance value in the different topologies discussed above as a function of the load resistance and mutual inductance between Rx and Tx coils, M_{12} , is given below:

$$\dot{Z}_{in,SS(\omega_o)} = \frac{\omega_o^2 M_{12}^2}{R_L} \quad (4.7)$$

$$\dot{Z}_{in,SP(\omega_o)} = R_L \frac{M_{12}^2}{L_2^2} \quad (4.8)$$

$$\dot{Z}_{in,PS(\omega_o)} = \frac{(\omega_o^2 M_{12}^2)^2 + (\omega_o L_1 R_L)^2}{R_L^2 \omega_o L_1} \quad (4.9)$$

$$\dot{Z}_{in,PP(\omega_o)} = \frac{(R_L M_{12}^2)^2 + \{\omega_o L_2 (L_1 L_2 - M_{12}^2)\}^2}{R_L M_{12}^2 L_2^2} \quad (4.10)$$

The residual imaginary value of the input impedance hinders the perfect performance of WPT. Therefore, it is important to eliminate the residual input reactance. FRA can provide a clear picture of the impedance characteristics in various compensating topologies. As shown in Figure 4.2, \dot{Z}_{re} represents the reflected impedance from Rx. The capacitor compensation on the Rx side can be either in series or parallel with the coil. The equivalent impedance \dot{Z}_{eq} is the vector summation of \dot{Z}_{re} and X_{L_1} of the Tx coil.

4.2. Prototype design for FRA measurement

Planar spiral Tx and Rx coils were built to reduce the installation space, as shown in Figure 4.3. To investigate the variation of the coupling coefficient factor k_{12} between the two coils over a varied separation distance, finite element modelling (FEM) is conducted to calculate the parameters in Table 4.2 based on the physical dimensions provided.

The resistance of the copper wire is increased at high frequencies due to the skin effect, which affects the Q factor of the circuit (ratio of the active and reactive power consumption) and reduces the overall performance of the WPT system [167]. The use of Litz wire, also known as magnet wire or super-conductor, can mitigate the undesirable loss at high operating frequencies [83, 84]. This prototype is considered for demonstrating the wireless charging of EV batteries, which call for electric energy transfers at a relatively high current level. Therefore, the coils in the developed WPT circuit are made of 1,650 stranded Litz wire, which has 0.05mm diameter filament (American wire gauge 44), which are independently insulated to suppress the skin and proximity effects at high frequencies. The ampacity of the implemented Litz wire is 20A in a frequency range of up to 850 kHz [168]. As the resistance value of the wire is 6.4 m Ω /metre, the Tx (or Rx) coil of a 30 m length has 192 m Ω of overall resistance. Therefore, the parasitic resistance of the winding can be ignored for practical circuit analysis.

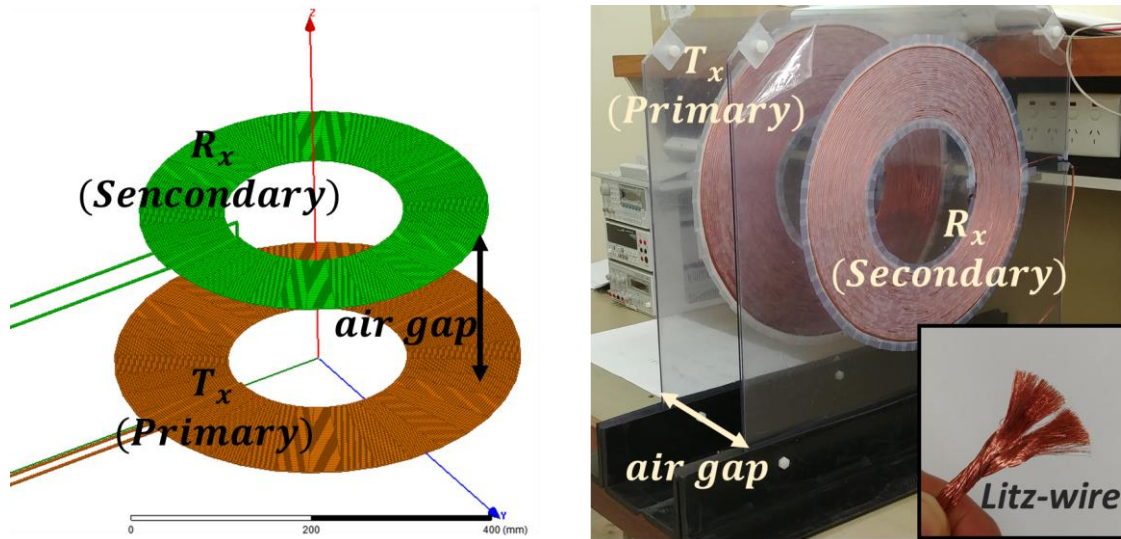


Figure 4.3. Planar Litz-wire spiral coils design and installation

Table 4.2. Parameters of Tx and Rx coils

Winding type	Planar spiral
Wire radius	1.5mm
Inner radius	105 mm
Number of turns	L_1 and L_2 : 30
Spacing between turns	0.1 mm
Self-inductance	L_1 and L_2 : 349.3 μH
Coupling Coefficient k_{12}	10 mm gap: 0.8690 55 mm gap: 0.4868 200 mm gap: 0.1126
Resonance frequency f_0	20 kHz, ($\omega_0 = 2\pi f_0$)
$C_2 = 1/(\omega_0^2 L_2)$	$C_2 = 180$ nF

4.3. Experimental FRA measurement in various topologies

FRA measurement is used to mainly identify three parameters: VTR, the amplitude of the transfer function, and phase angle [143]. From the VTR measurement, the accurate resonant frequency can be identified. The input impedance (magnitude and angle) of the WPT system can be measured using FRA, whereby the characteristics of the WPT system can be correctly identified with respect to the resonance frequency and the

transfer distance between the two coils. A commercial FRA is used to measure the frequency response characteristic of the developed WPT system shown in Figure 4.4, as detailed below.

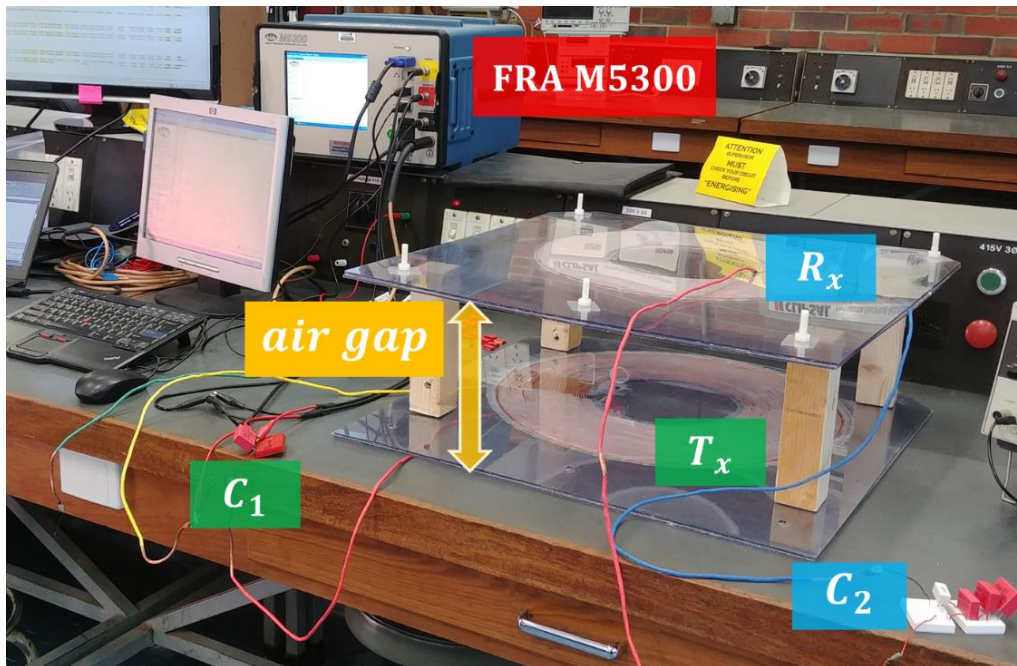


Figure 4.4. Hardware setup along with FRA

The schematic for FRA measurement on the WPT system is depicted in Figure 4.5 in which R_s and R_M are the source and the resistance of the FRA that measures the transfer function $H(j\omega)$ as in (4.11) and (4.12).

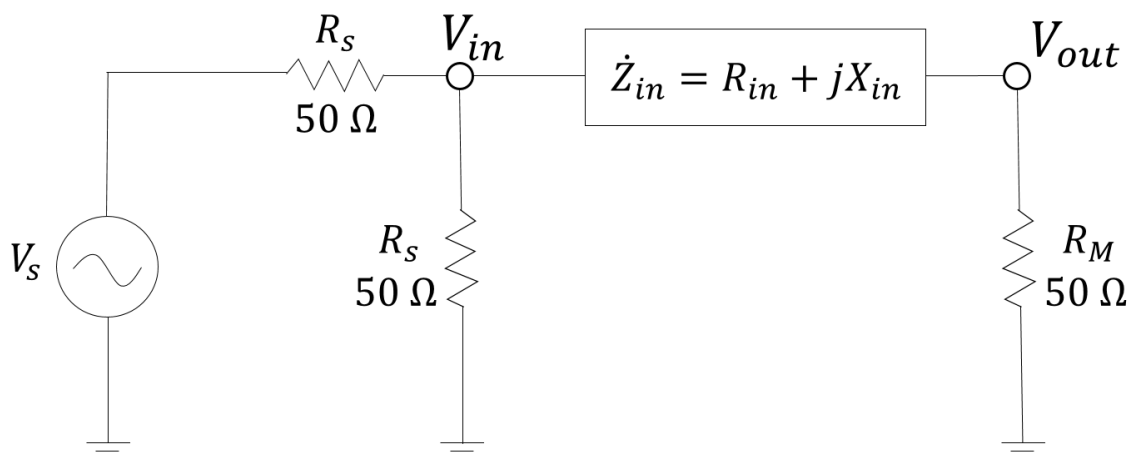


Figure 4.5. FRA measurement schematic

$$VTR = 20 \log H_{(j\omega)} = 20 \log \frac{V_{out}}{V_{in}} \text{ [dB]} \quad (4.11)$$

$$H_{(j\omega)} \angle \delta^\circ = \frac{50}{Z_{in} \angle \theta^\circ + 50} \quad (4.12)$$

The phase angle δ of the transfer function $H_{(j\omega)}$ in (4.12) is a function of the input impedance and the value of R_M . Therefore, the input impedance phase angle θ needs to be extracted from the obtained results to calculate the reactive component of \dot{Z}_{in} . The unknown real and imaginary values of \dot{Z}_{in} can be acquired from (4.11) and (4.12) as follows:

$$\mathcal{R}e(\dot{Z}_{in}) = \left\{ \frac{50}{10^{\left(\frac{VTR}{20}\right)}} \cdot \cos(-\delta) \right\} - 50 \text{ [\Omega]} \quad (4.13)$$

$$\mathcal{J}m(\dot{Z}_{in}) = \frac{50}{10^{\left(\frac{VTR}{20}\right)}} \cdot \sin(-\delta) \text{ [\Omega]} \quad (4.14)$$

Consequently, the absolute value and the phase of \dot{Z}_{in} can be obtained as in (4.15) and (4.16).

$$|\dot{Z}_{in}| = \sqrt{\mathcal{R}e(\dot{Z}_{in})^2 + \mathcal{J}m(\dot{Z}_{in})^2} \text{ [\Omega]} \quad (4.15)$$

$$\theta = \tan^{-1} \frac{\mathcal{J}m(\dot{Z}_{in})}{\mathcal{R}e(\dot{Z}_{in})} \text{ [}^\circ\text{]} \quad (4.16)$$

FRA measurements are performed on different compensation topologies of the developed WPT with various air gaps between the two windings (10 mm, 55 mm, and 200 mm). For these experiments, a load resistor R_L of 50 Ω was connected across the output terminals on the Rx side. The reference and source ports of the FRA are connected to the positive terminal of the Tx coil, while the measurement port is wired to the negative

terminal of the Tx through 50 Ω coaxial cables. This connection is similar to the open-circuit FRA test of a power transformer. The plots of the input impedance phase based on (4.16) for different compensating topologies with various air gaps are shown in Figure 4.6. The phase angle should be nearly zero when the compensating capacitor C_1 on the Tx side, is correctly tuned. The detailed results of the measurements with a comparison to the calculated values are presented in Table 4.3. The results show that the resonance frequency can be tuned precisely at a small air gap of 10 and 55 mm, while a significant error takes place at a distance of 200 mm. The red trace in Figure 4.6 at the air gap of 10 mm shows a smooth characteristic in the proximity of the resonance frequency of 20 kHz. This implies that the WPT system at a small transfer distance allows a wide margin for regulating the resonance condition. On the other hand, the slope of the green colour plot increases significantly at 200 mm transfer distance.

To demonstrate the performance of the untuned circuit, an arbitrary capacitor of 100 nF on the Tx side is implemented for the SS topology. As discussed above, the value of C_1 in this topology is maintained constant regardless of the change in the transfer distance. On the other hand, an arbitrary capacitor C_1 of 180 nF on the Tx side was selected for the SP, PS, and PP topologies at air gap distances of 10 and 55 mm for demonstrating the untuned condition. For both topologies, the self-inductance of the Tx coil L_1 is utilized to extract the resonance frequency ($\omega_o = 1/\sqrt{L_1 C_1}$) without regarding the mutual inductance variation and the load resistance. At an air gap distance of 200 mm in the SP, PS, and PP topologies, an arbitrary capacitor of 100 nF on the Tx side is used to observe the impedance characteristic for untuned circuit conditions. At this distance, the coupling coefficient k_{12} is very low (0.1126). Hence, the Tx and Rx may be considered as two decoupled coils.

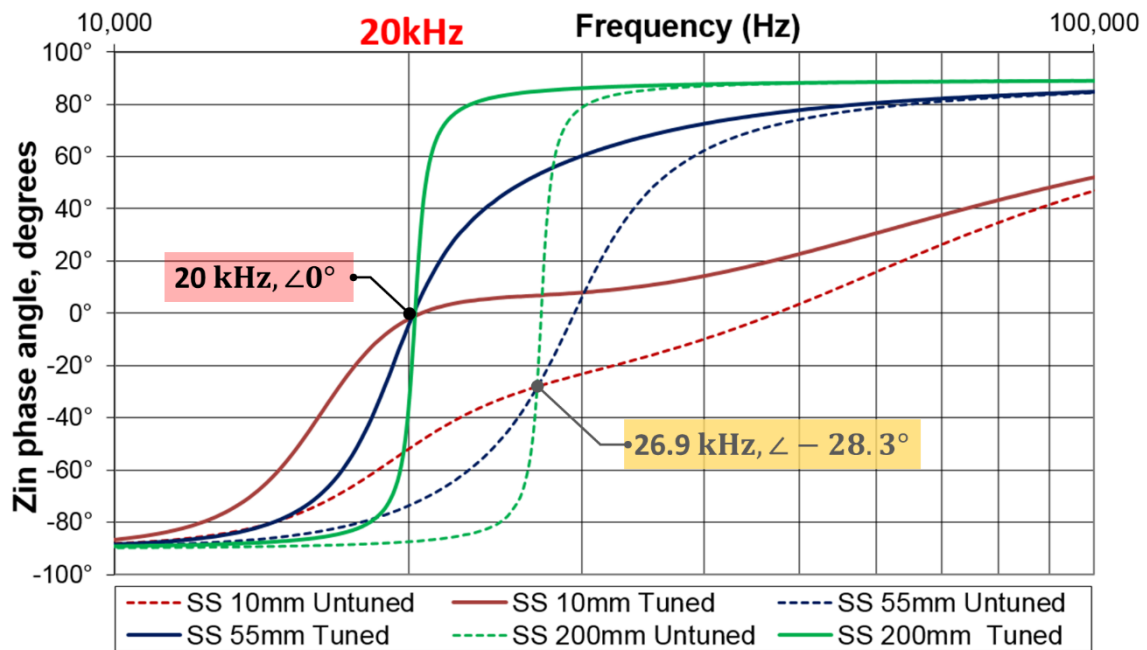
An accurate frequency tuning is required to maintain zero value for the input impedance phase angle at the resonance frequency. The disagreement between the calculated and measured values increases for large air gaps even with the tuning of C_1 due to the rapid increase in the phase angle slope near the resonance frequency. As mentioned above, in the SS topology, a Tx side compensating capacitor C_1 of 100 nF was considered to examine the untuned WPT performance. If the operating frequency is set to 26.9 kHz, the phase angle will be -28.3° regardless of the transfer distance, as shown

in Figure 4.6 (a). Although the electric power can be delivered at the untuned frequency of 26.9 kHz with a non-zero phase angle of the input impedance, it impairs the performance of the system, and it requires a power supply with a large volt-ampere (VA) rating to transfer the load demand power [169, 170]. To transfer the electric power at a frequency of 26.9 kHz efficiently in the SS topology, the compensating capacitance C_2 on the Rx side should be changed from 180 nF to 100 nF, while the value of C_1 is maintained at 100 nF. The amplitude of the input impedance in the PS and PP topologies at air gap distances of 55mm and 200 mm is much higher than the input impedance in the SS and SP topologies, as listed in Table 4.3. From a comprehensive review of the results for the investigated circuits, none of the topologies, as shown in Figure 4.6, is even barely suitable for the WPT system at 200 mm distance.

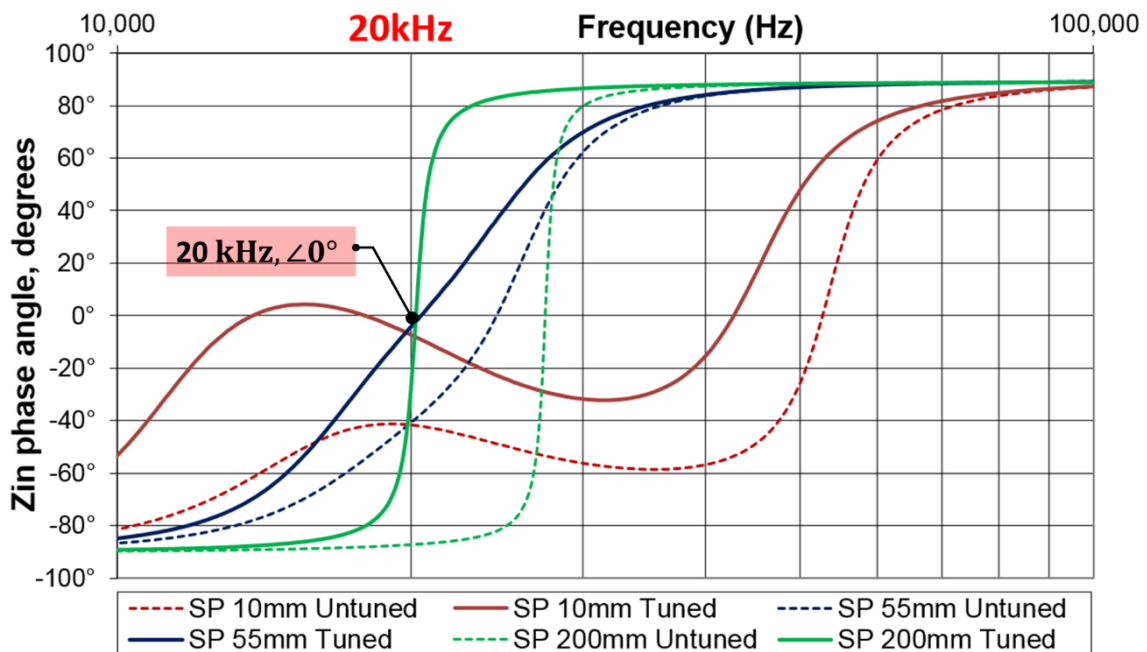
Table 4.3. Input impedance and phase angle results using FRA

Topologies			Amplitude of $Z_{in}[\Omega]$		Phase angle $[\circ]$		Tuned C_1 value
Gap	SS, C_1		Calculated	Measured	Calculated	Measured	
10mm	U	100nF	45.74	47.86	-49.61	-50.89	Independent from k_{12} and load
	T	180nF	29.64	31.59	0.39	-1.15	
55mm	U	100nF	35.86	38.28	-74.96	-73.03	
	T	180nF	9.31	10.69	2.51	-0.23	
200mm	U	100nF	34.55	36.24	-89.17	-87.27	
	T	180nF	<u>0.70</u>	<u>1.86</u>	<u>44.86</u>	<u>-11.59</u>	
Gap	SP, C_1		Calculated	Measured	Calculated	Measured	Tuned C_1 value
10mm	U	180nF	50.44	49.59	-41.54	-41.71	Function of k_{12}
	T	440nF	38.50	38.35	-11.33	-8.02	
55mm	U	180nF	15.60	16.65	-40.59	-39.39	
	T	236nF	11.85	13.08	1.16	-2.84	
200mm	U	100nF	35.12	36.77	-88.97	-87.07	
	T	180nF	<u>0.64</u>	<u>1.96</u>	-6.27	-6.90	
Gap	PS, C_1		Calculated	Measured	Calculated	Measured	Tuned C_1 value
10mm	U	180nF	78.40	76.85	-34.36	-32.29	Function of k_{12} and load
	T	119nF	94.85	91.58	2.29	3.39	
55mm	U	180nF	212.51	189.82	-14.39	-9.83	
	T	164nF	215.59	198.84	10.68	7.00	
200mm	U	100nF	101.09	100.35	88.53	84.85	
	T	180nF	<u>2763.91</u>	<u>1026.33</u>	<u>-45.50</u>	<u>-13.15</u>	
Gap	PP, C_1		Calculated	Measured	Calculated	Measured	Tuned C_1 value
10mm	U	180nF	34.00	34.64	-33.12	-31.10	Function of k_{12} and load
	T	38nF	40.47	39.91	4.50	6.99	
55mm	U	180nF	100.14	94.77	21.19	20.07	
	T	210nF	107.38	102.10	-1.20	-2.52	
200mm	U	100nF	98.20	97.50	88.14	84.68	
	T	180nF	<u>3004.40</u>	<u>994.86</u>	5.44	4.13	

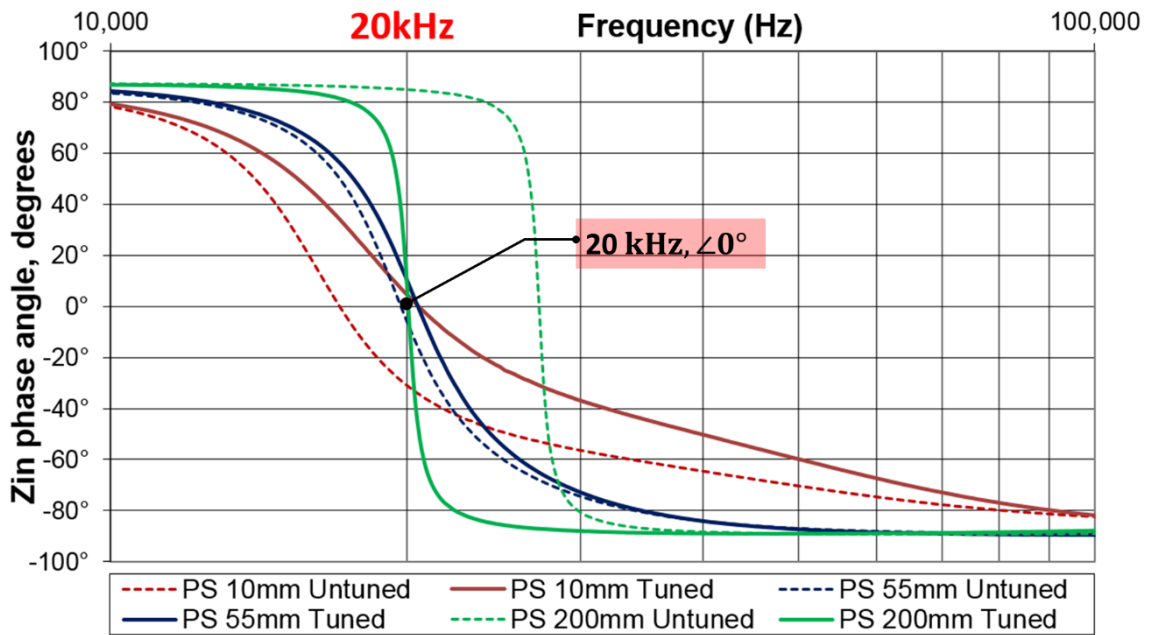
U: Untuned, T: Tuned



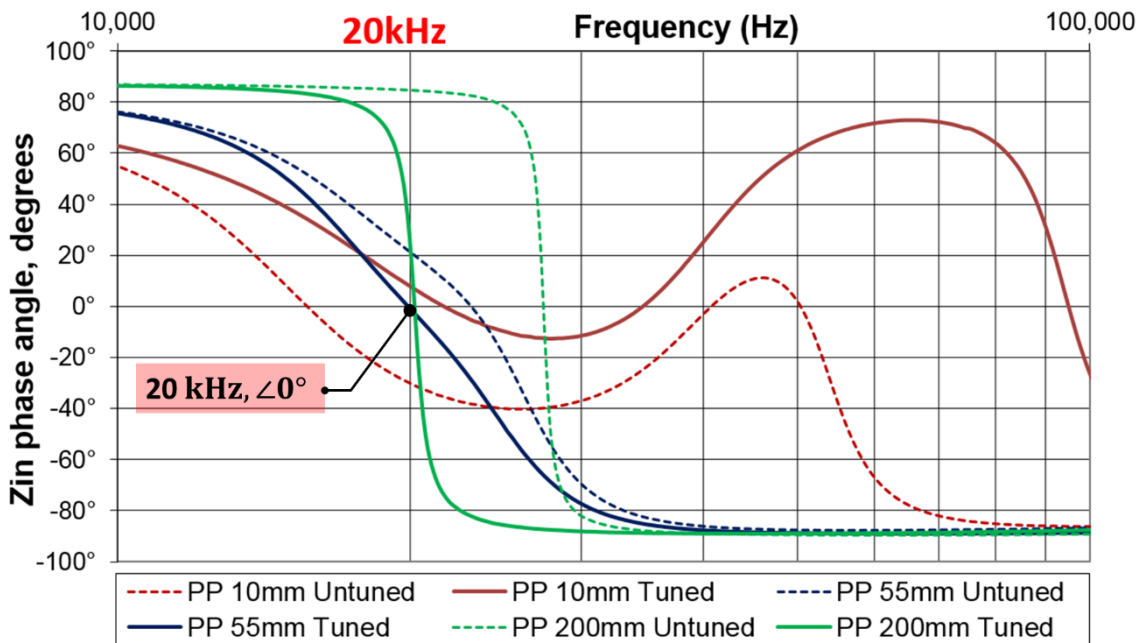
(a)



(b)



(c)



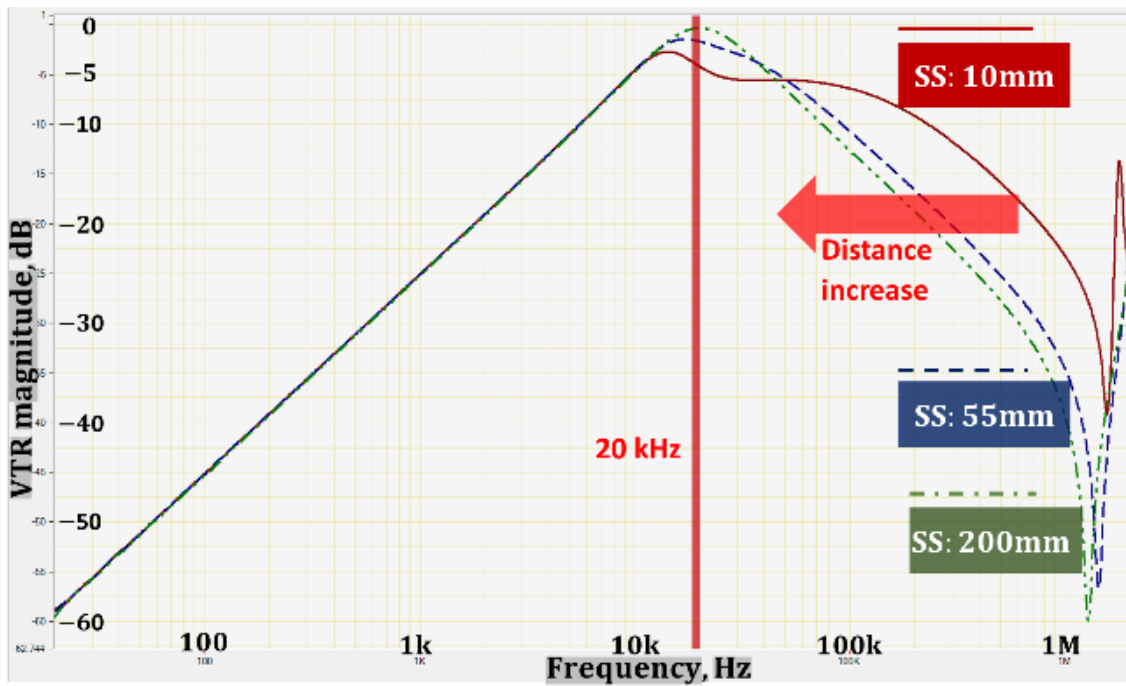
(d)

Figure 4.6. The phase of the input impedance (θ°) using FRA measurement for various compensating topologies: (a) SS, (b) SP, (c) PS, and (d) PP

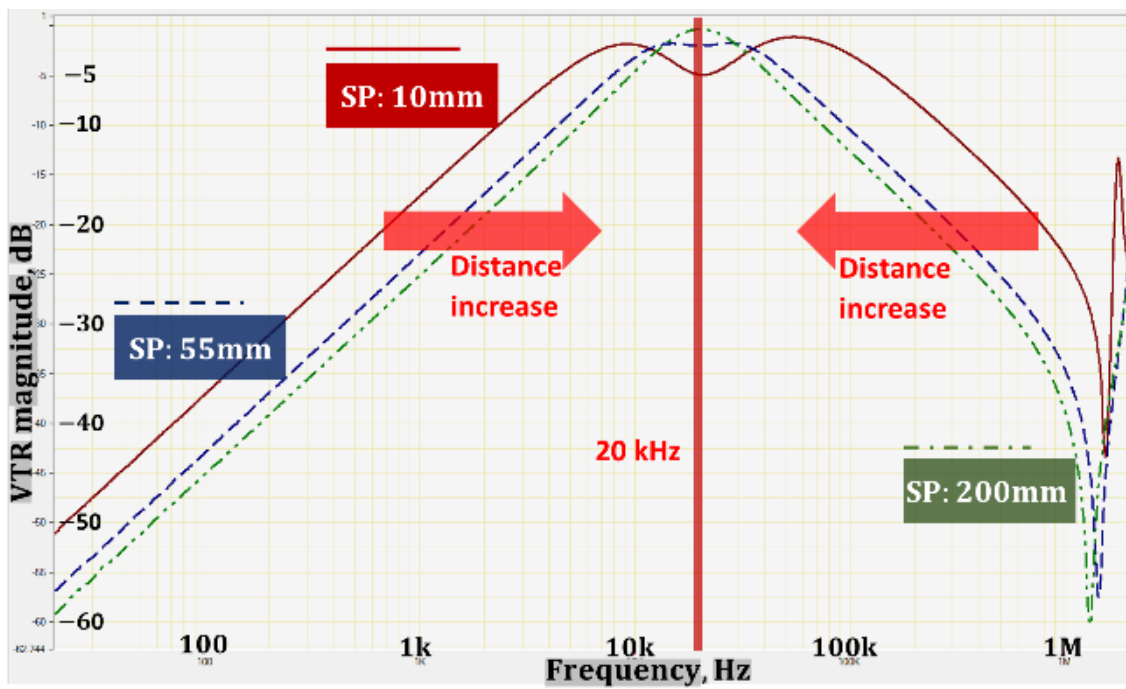
4.4. VTR patterns over different transfer distances

When the distance of the air gap between the Tx and Rx coils varies, the pattern of the VTR is affected due to the change in the mutual inductance between the two coils. In the SS topology, the shape of the VTR waveform in the vicinity of the resonance frequency is narrow and sharp when the transfer distance increases [126]. The VTR for SS and SP topologies gradually increases with the increase of the frequency, and it reaches a maximum level at the resonant frequency (20 kHz), after which the VTR starts to gradually decrease as depicted in Figure 4.7 (a and b). On the other hand, the VTR for the PS and PP topologies will have an opposite trend, as shown in Figure 4.7 (c and d).

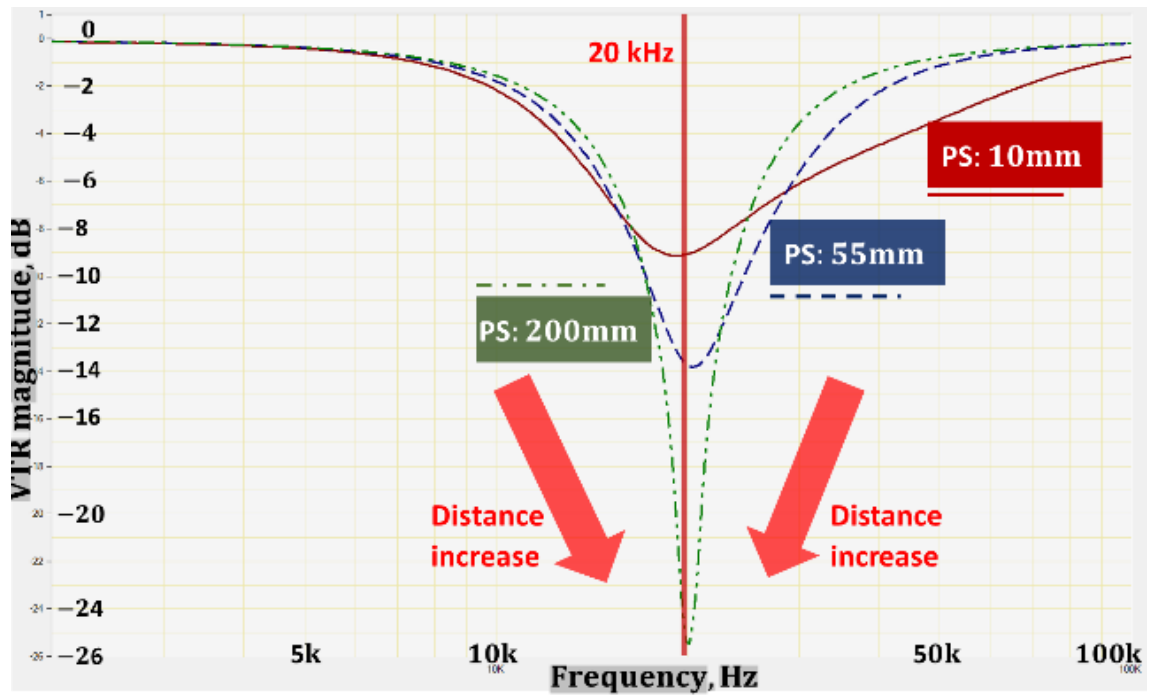
It is worth noting that the accurate maximum or minimum value of VTR is not observed precisely at the frequency of 20 kHz for a 10 mm air gap due to the effect of frequency bifurcation [99]. The frequency bifurcation can be identified by various parameters, including the self and mutual inductance of the coils, load resistance, and resonance frequency [99]. The results also show that the amplitude of the input impedance in the SS and SP topologies decreases when the air gap increases, as shown in Figure 4.8 (a and b). On the contrary, the impedance level of the PS and PP system increases significantly over the distance, as depicted in Figure 4.8 (c and d). The shapes of the VTR signatures shown in Figure 4.7 are opposite in trend to the impedance plots depicted in Figure 4.8 because VTR and impedance levels are inversely proportional, based on (4.11) and (4.12). It is also clear from the VTR and the impedance plots that a 200 mm air gap does not provide appropriate performance regardless of the Rx compensation topology, as stated above in Chapter 4.1.



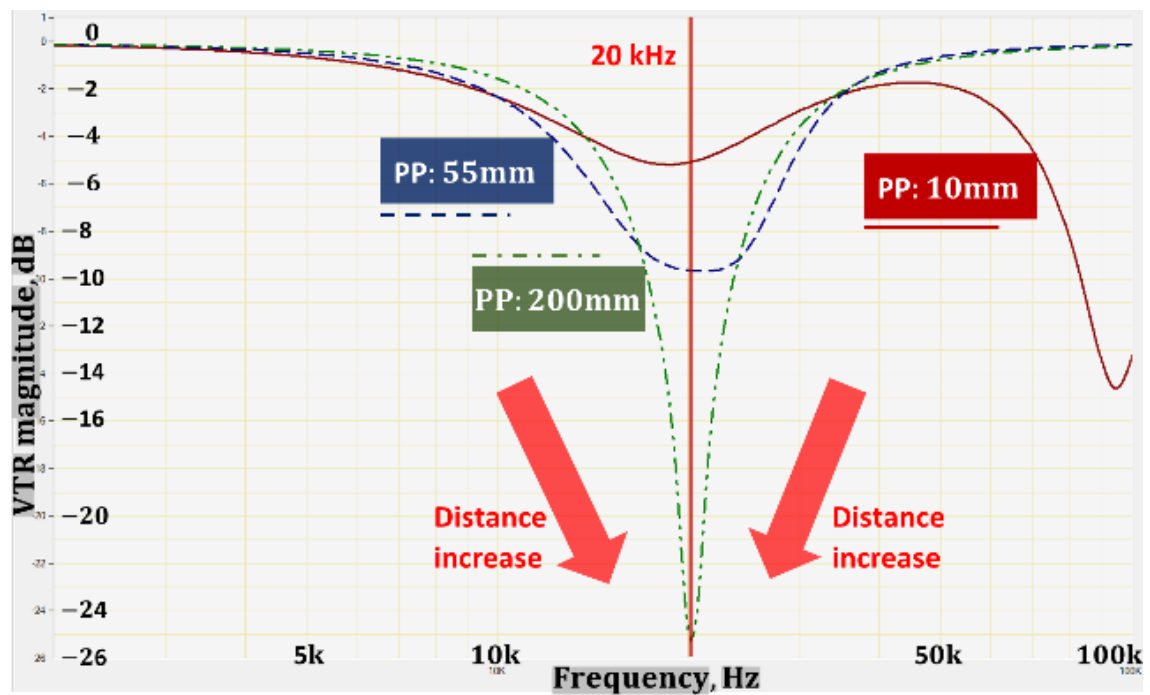
(a)



(b)

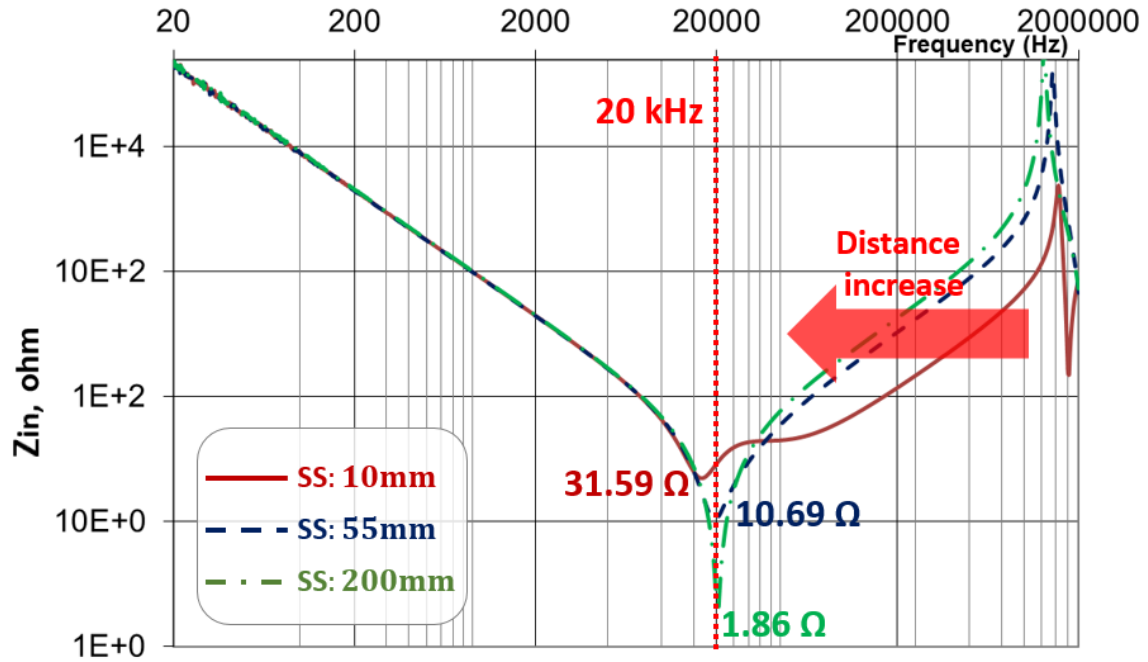


(c)

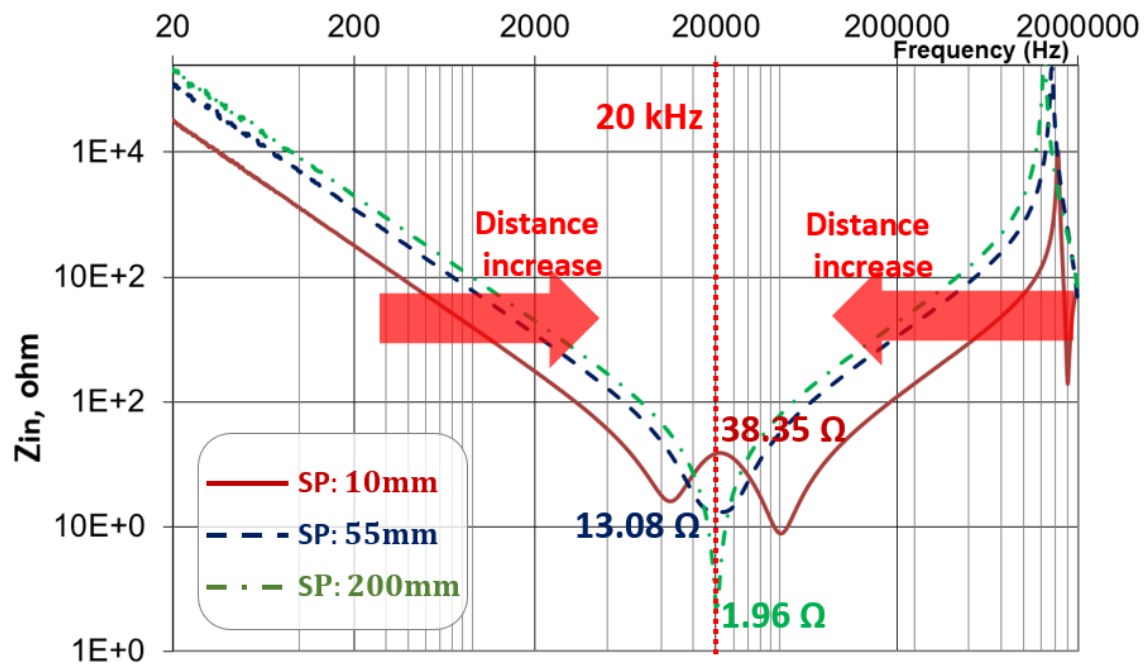


(d)

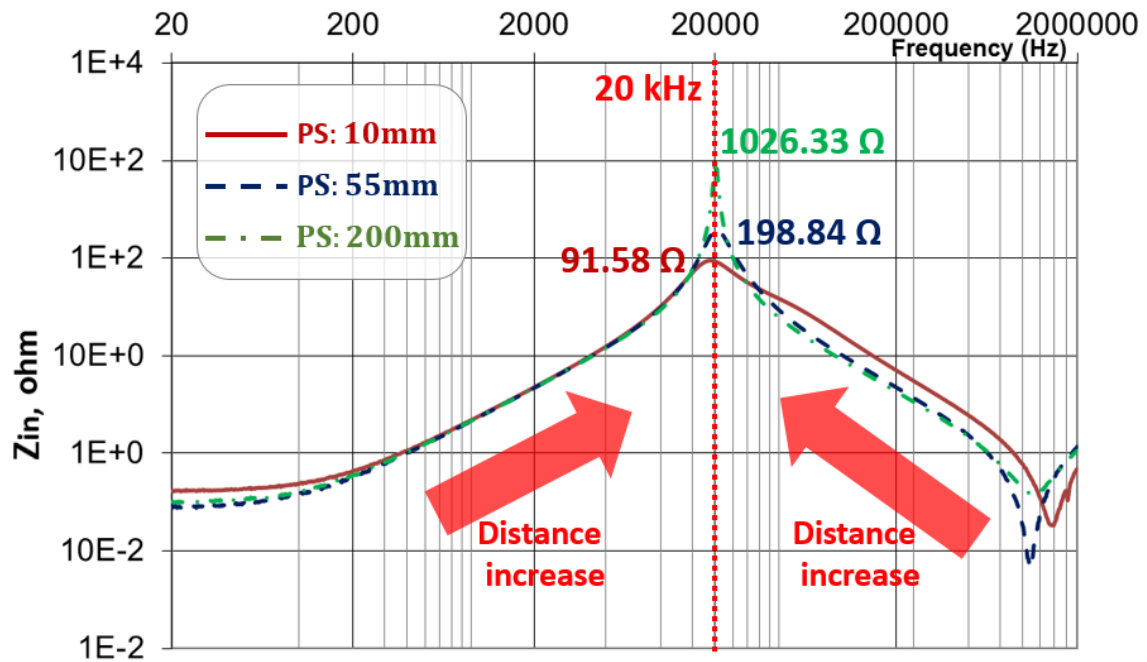
Figure 4.7. VTR patterns at various transfer distances for: (a) SS, (b) SP, (c) PS, and (d) PP topologies



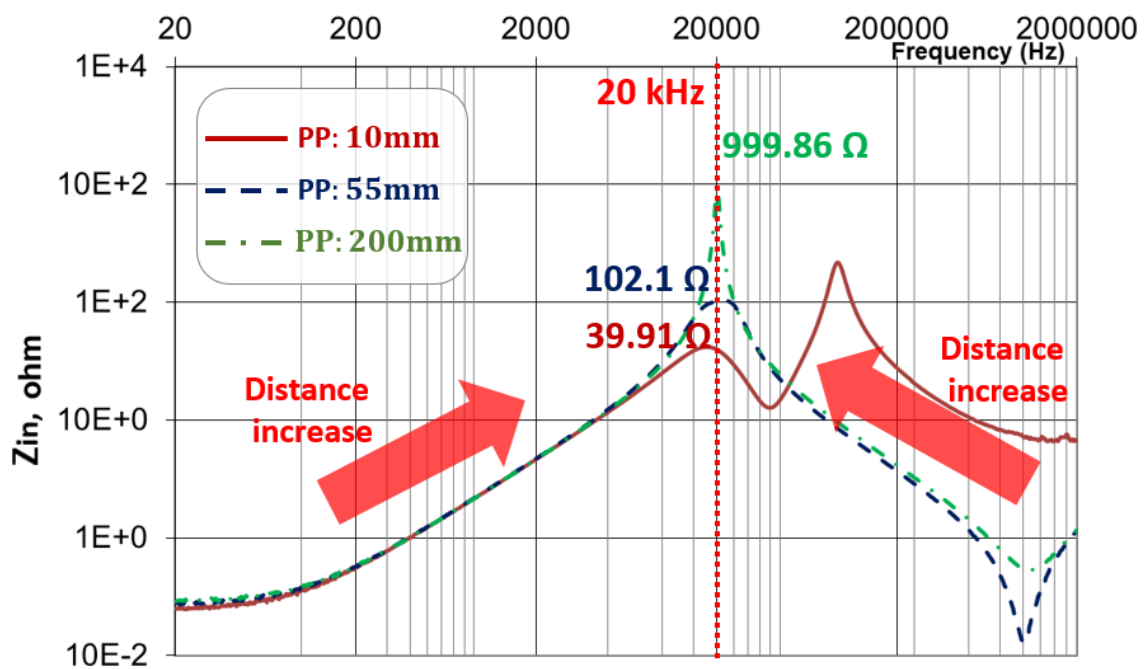
(a)



(b)



(c)



(d)

Figure 4.8. Input impedance patterns at various transfer distances for: (a) SS, (b) SP, (c) PS, and (d) PP topologies

4.5. LCL topology and ferrite material on the coils

To examine the variation of the FRA results with the placement of ferrite material on the coils at a distance of 55 mm, the PP topology was selected. To maintain resonant condition, the PP topology requires more parameters to be considered than others, as presented in Table 4.1. However, it has a high input impedance with a smooth variation in the vicinity of the resonance frequency (20 kHz), as shown in Figure 4.9. Hence, the PP system provides a sufficient level of the input impedance and a broad tolerance to maintain the resonant condition.

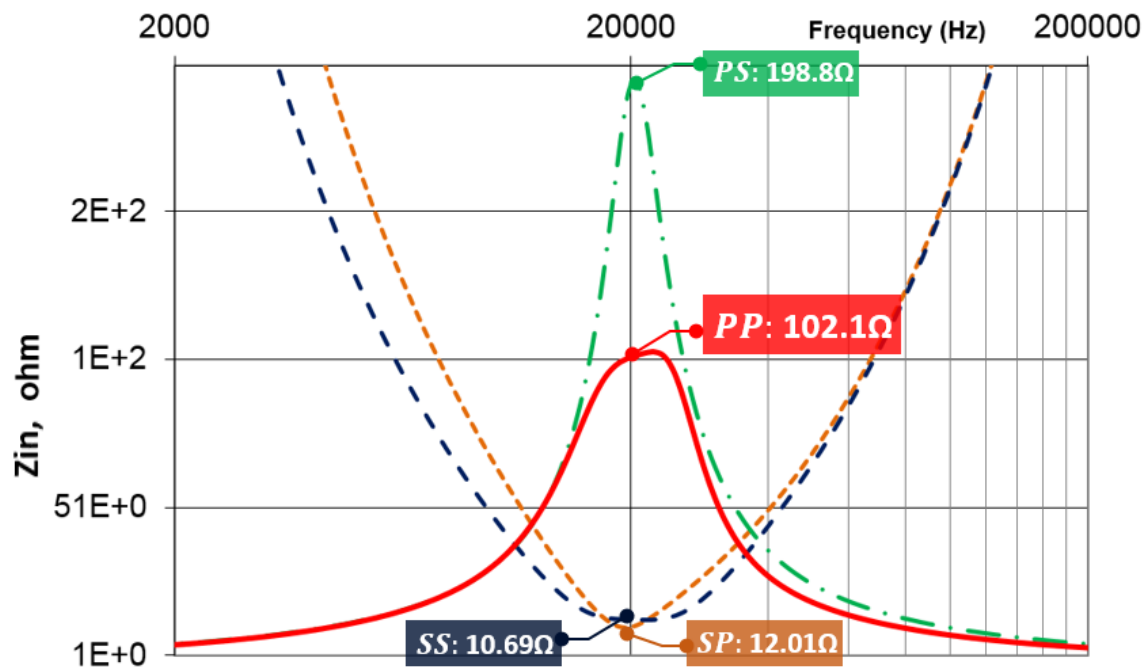


Figure 4.9. Input impedance amplitude of PP topology at an air gap of 55 mm

To enhance the power transfer rate of the WPT system, a ferrite material is implemented with the copper wire to strengthen the magnetic coupling between the coils and reduce the flux leakage path [132, 171]. For the purpose of enhancing the electrical insulation and the mechanical integrity of the system, the Tx and Rx coils are placed between two acrylic boards of 5 mm thickness, and the ferrite bars are positioned on the

lower surface of the Tx winding acrylic board as shown in Figure 4.10. The impact of the non-conductive obstruction in the air gap is insignificant, and the transfer efficiency of the WPT system with the medium between the coils is almost identical to the WPT system in the free space [7, 8].

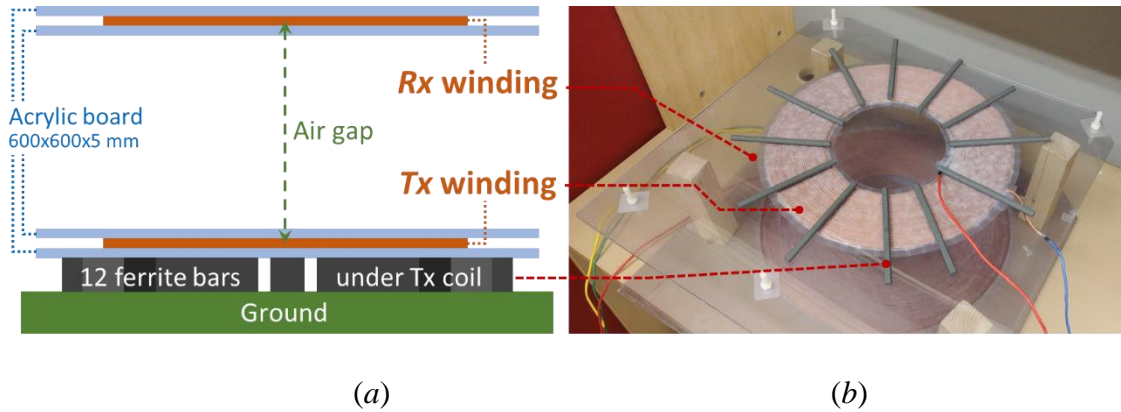


Figure 4.10. The layout of the prototype WPT: (a) cross-sectional diagram, and (b) actual implementation

Table 4.4. Parameters of the WPT system with ferrite material

Gap	k_{12}	$L_1[\mu\text{H}]$	$C_1[\text{nF}]$	$L_2[\mu\text{H}]$	$C_2[\text{nF}]$	$L_r[\mu\text{H}]$
55mm	0.541	493.4	173	353	175	150

The width, height, and length of a single ferrite bar are 10 mm, 10 mm, and 160 mm, respectively. Twelve ferrite rods are positioned at an interval of 300, as shown in Figure 4.11(a). The coupling coefficient and the inductance values at the investigated distance are calculated using FEM, as listed in Table 4.4. An additional inductance L_r is connected to the Tx coil in series to achieve the resonance condition as shown in Figure 4.12. Also, this coil acts as a current filter to provide a pure sinusoidal current signal to the WPT circuit [170]. The system comprising a series inductance L_r and PP topology is known as an LCL resonant inverter. When the ferrite rods are moderately and significantly repositioned as shown in Figure 4.11(b) and (c), respectively, the deviations of the VTR amplitude from the initial position of the rods at the resonance frequency (20 kHz) and 55 mm air gap is measured using FRA as 0.114 dB and 0.132 dB, respectively as shown in Figure 4.13(a).

It can also be observed that the deviation in the VTR amplitude increases in the frequency range around the resonance frequency. Figure 4.13(b) shows that the phase angle δ of the transfer function $H(j\omega)$ at 20 kHz is maintained at zero degree for the initial position of the ferrite rods as the circuit was tuned based on this position. This angle changes to 1.439° and 3.902° when the ferrite bars are moderately and significantly relocated, respectively.

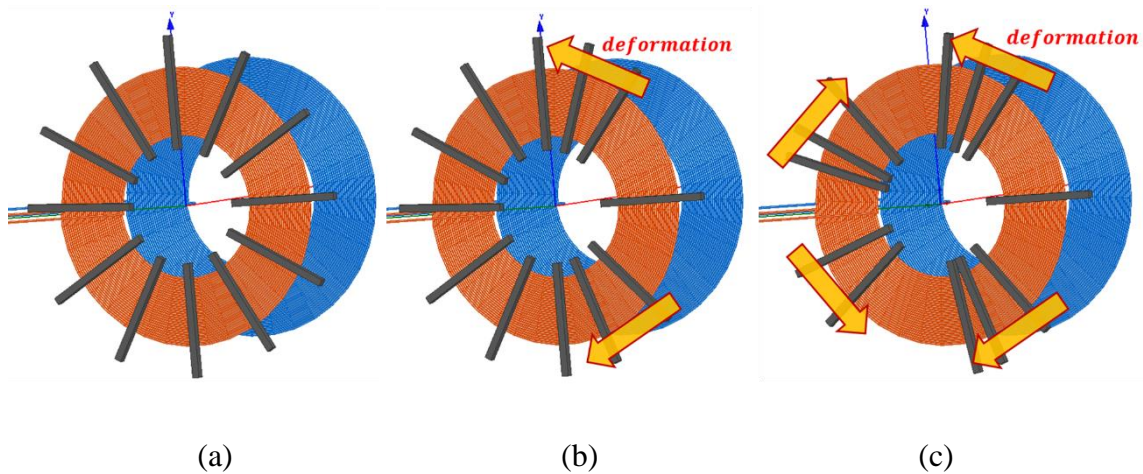


Figure 4.11. Placement of the ferrite bar: (a) initial position, (b) moderate movement, and (c) significant movement

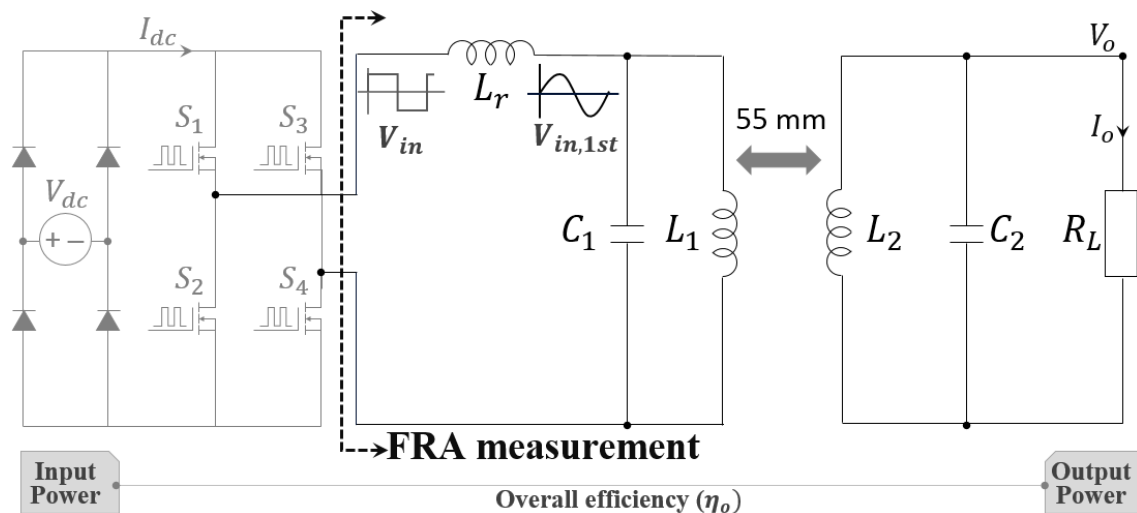
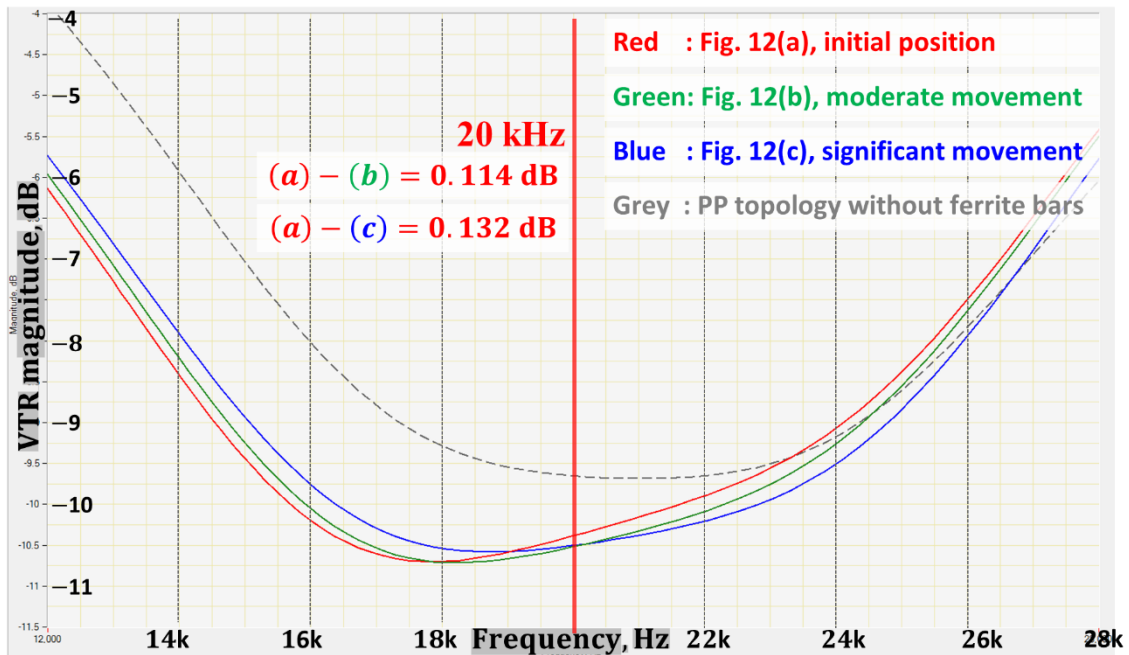
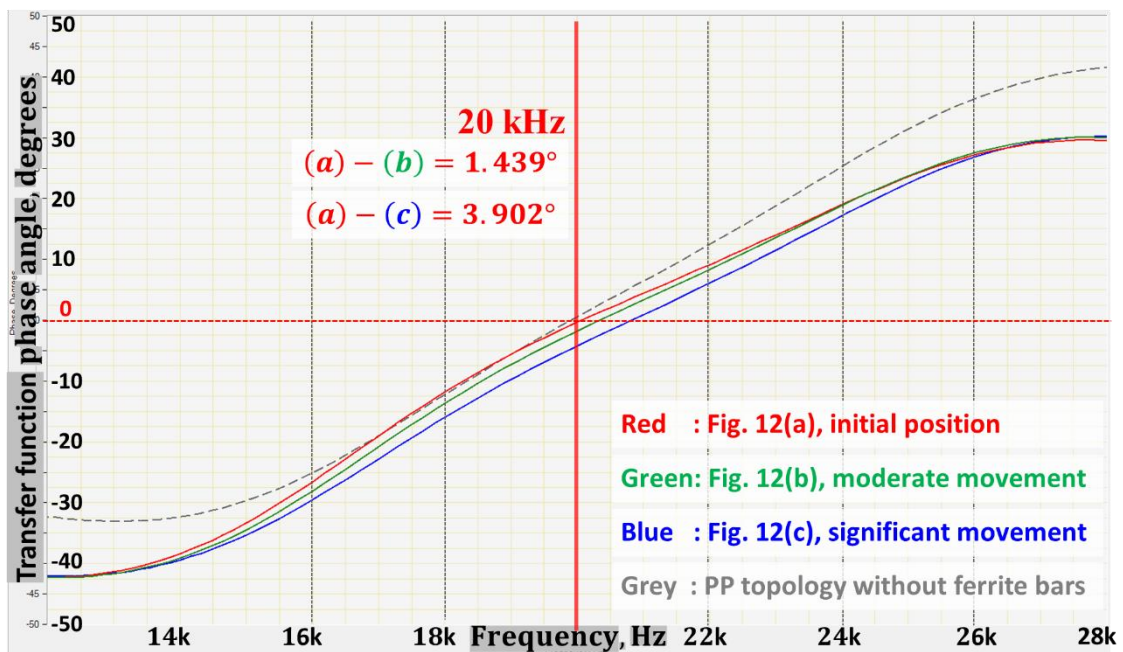


Figure 4.12. Efficiency measurement of the WPT system



(a)



(b)

Figure 4.13. FRA plots at air gap of 55 mm for various placements of the ferrite rods:

(a) VTR, and (b) Phase angle δ° of the transfer function $H_{(j\omega)}$

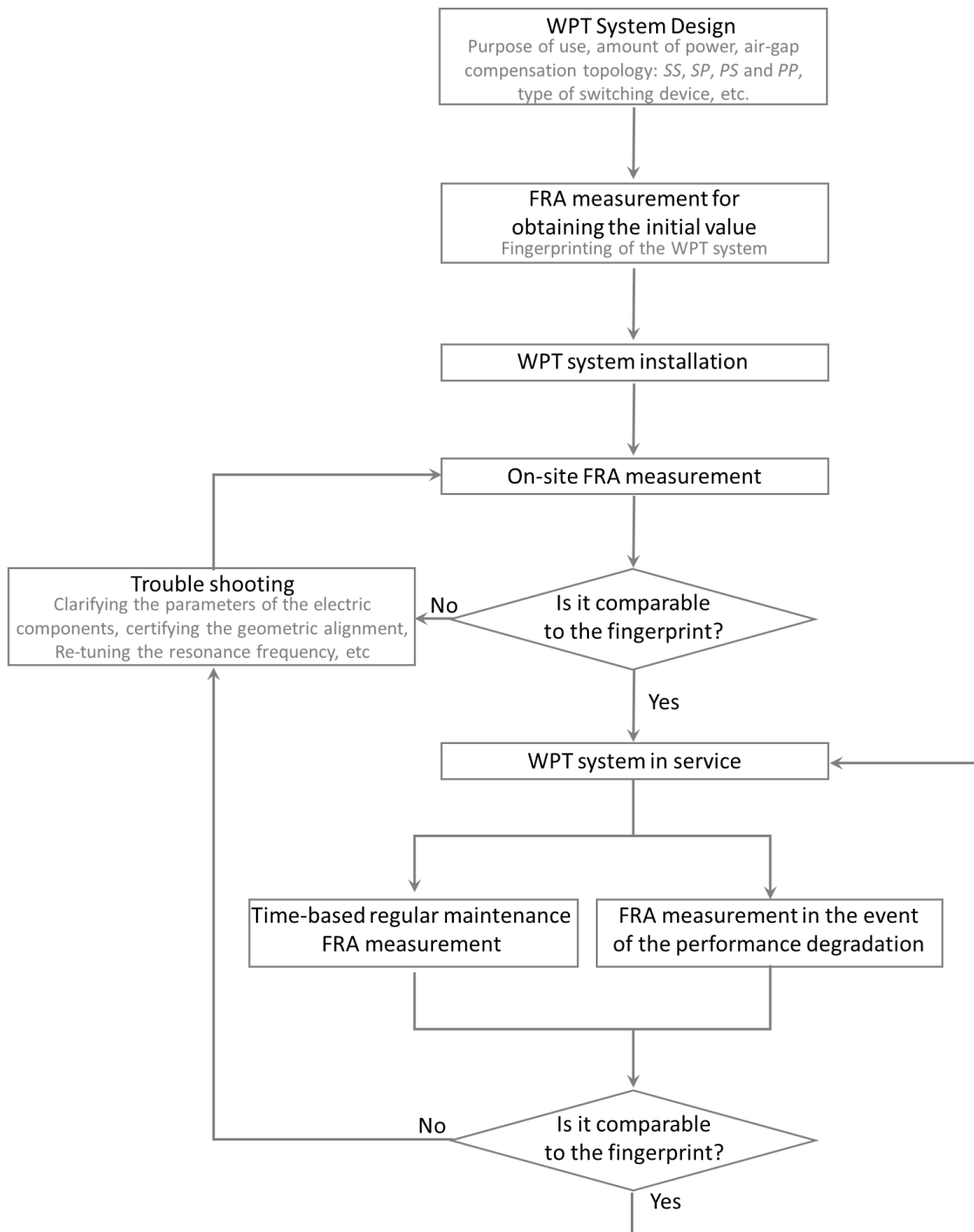


Figure 4.14. Flowchart of FRA application on WPT system

These results validate the feasibility of FRA to precisely detect the deformation of the ferrite material in the WPT system, similar to analysing the magnetizing characteristic of the power transformer within the low-frequency range [172]. The regular FRA results can also indicate the deterioration trends of the resistance, inductance, and capacitance components in WPT systems over time [173]. When the WPT design is completed, the initial FRA measurement of the system can be obtained at the lab or the workshop. Then, the quality of the WPT installation is clarified by comparing the fingerprint to the on-site measurement data. Furthermore, the reliability of the WPT system can be assessed by benchmarking future measurements for regular maintenance, relocation, or investigation of WPT systems, as described in the flowchart in Figure 4.14.

4.6. Practical demonstration of WPT system and discussion

The efficiency of the WPT system in the PP topology with the ferrite material and the series inductance L_r , is examined using the WPT prototype shown schematically in Table 4.4. When the value of the compensating capacitors at both Tx and Rx sides are 173 nF and 175 nF as presented in Table 4.4, the reactive component of the input impedance is not clearly eliminated, and the input impedance of the WPT prototype comprises a capacitive reactance. Therefore, an L_r of 150 μ H can compensate this residual capacitive reactance, and helps provide a sinusoidal current to the circuit [174]. The demonstration in this paper considers that the Tx unit is a stationary device, while the Rx unit is equipped on the mobile device. In the developed system, the overall efficiency η_o achieved is 85.75% as depicted in Table 4.5. When an input DC voltage of 30 V is supplied, an output AC voltage of 16.31 V and a current of 0.324 A with a phase difference of 22.19° are induced across the load resistance at 20 kHz as depicted in Figure 4.15. The switching loss at the power electronic devices (i.e., insulated-gate bipolar transistors (IGBTs) or metal-oxide-semiconductor field-effect transistors (MOSFETs)) is a major cause of the low efficiency in WPT systems [159, 174]. Therefore, recent WPT systems adopt a zero voltage or current switching (ZVS or ZCS, also known as soft-switching) converter with complex gate-driver applications, and their efficiency reaches almost 90% [25, 57].

Table 4.5. Overall efficiency of the developed prototype

V_{dc} [V]	I_{dc} [A]	P_{dc} [W]	V_o [V]	I_o [A]	θ_o [$^\circ$]	P_o [W]	η_o [%]
30.0	0.19	5.71	16.32	0.324	22.2	4.90	85.75

While a two-coil based inductive coupling WPT is demonstrated in this paper, FRA can also analyse the characteristic of the WPT system with multiple repeaters, capacitive coupling WPT systems, and other complex topologies (e.g., double-side LCL, CCL, etc.) [45, 94, 175-178].

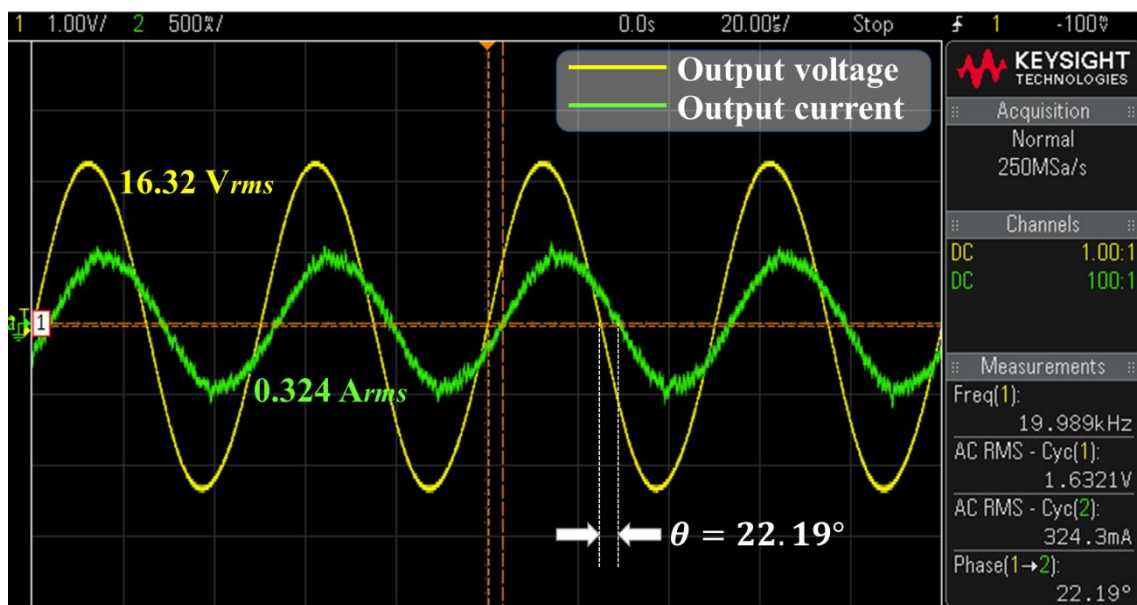


Figure 4.15. The voltage and current waveforms on R_L

Table 4.6. Comparison of compensation topologies

Topology	Power supply requirement	Additional series inductor	Stability when $k_{12}=0$	Compensating capacitor C_1	Input impedance value when the distance increases
SS	Low-voltage rating	Not required	Unstable	Independent from k_{12} and load	Decrease
SP	Low-voltage rating	Not required	Unstable	Function of k_{12} or load	Decrease
PS	Low current rating	Required	Stable	Function of k_{12} and load	Increase
PP	Low current rating	Required	Stable	Function of k_{12} and load	Increase

A brief comparison of various compensation topologies is presented in Table 4.6. As each compensation topology has advantages and disadvantages, it is essential to carefully select the optimal design parameters for the best performance of the WPT system. For instance, the SS topology is widely applicable for high-power applications such as high-speed trains and EV battery charging because the compensating circuit is independent of the load resistance and the air gap [11, 13, 25, 57] and the additional series inductor to provide a sinusoidal current to the parallel resonance circuit is unnecessary [169]. However, the SS topology requires a high current rating power supply that may result in a malfunction when the magnetic coupling between the coils does not exist (e.g. $k_{12} = 0$) [100]. For this reason, the PP topology with an additional series inductor and other supplemented compensation topologies are also adopted. The SP system is applicable for charging a battery in a medical implement device as it supplies a constant voltage regardless of the load resistance [15, 179]. Hence, the correct compensating topology should be selected by considering the purpose of use, the capacity of transfer energy, type of converter, and safety during maximum efficiency or a maximum level of power transfer.

4.7. Summary

FRA is employed to assess various compensating topologies of the inductively-coupled 20 kHz WPT system. The amplitude and the phase angle of the input impedance along with the VTR in the four available topologies (SS, SP, PS, and PP) of the WPT system are examined at various transfer distances (10, 55, and 200 mm). The critical summaries drawn from the FRA measurements can be summarised as follows:

- At air gap distances of 10 and 55 mm, the amplitude and phase angle can be precisely measured. Therefore, the resonance frequency can be precisely tuned.
- As the coupling coefficient is very weak at greater air gap distances (200 mm), a rapid change of the impedance characteristic takes place near the resonance frequency, leading to a significant disagreement between calculated and measured resonance frequency.

- When the transfer distance increases, the width of the VTR traces in the SS, and SP becomes narrow at the vicinity of the resonance frequency. The PS and PP topologies exhibit the opposite trend compared to the SS and SP topologies.
- Experimental results show that the parallel-parallel compensation-based WPT system with ferrite rods and series inductance in the transmitter has an overall efficiency of 85.75%.
- The FRA measurements can detect any displacement in the additional ferrite bars on the winding, and the geometric change of the WPT components.
- When the initial FRA measurement is obtained as a fingerprint, the FRA diagnosis can facilitate a cost-effective condition-based maintenance scheme and re-tuning of system parameters to maintain high operational performance.

Chapter 5

Performance of WPT System Under Various Operating Conditions

When a WPT application is constructed on-site in different environments, the installed device needs to conform to the design. It is also essential to determine the degradation of the electromagnetic parameters in the WPT system over time. The variations of the medium between coils, deformation of the magnetic coupling, and deterioration of electrical components cause different FRA results. This chapter presents practical case studies for assessing the performance of such a WPT system under various operating conditions.

5.1. FRA for an Autonomous Under Water Vehicle

As a WPT application makes direct contact unnecessary between the transmitter on the stationary charging station and the receiver on the mobile device, it can be a safe and reliable battery charging solution for AUVs. This chapter introduces an inductively-coupled WPT system for AUVs, and a circuit based on compensating topologies, and subsequently conducts a 3-D computational simulation to explore electromagnetic phenomena between the transmitter and receiver under seawater. A 2-coil inductively-coupled WPT prototype is employed. The practical experiments and the FRA measurement are carried out to analyse the effectiveness in a different type of medium, the performance using various compensating topologies, and the efficiency of the WPT system.

5.1.1. AUT WPT system design

The design of the prototype WPT system for use in seawater includes two spiral coils built with ferrite bars to enhance the magnetic coupling according to FEKO, as

shown in Figure 5.1. The size of the spiral-shaped coils is identical, and a single filament copper wire was used. To reduce the high-frequency loss because of a skin and proximity effect on the wire, an operational frequency of 20 kHz was adopted. The details of the coil parameters are described in Table 5.1.

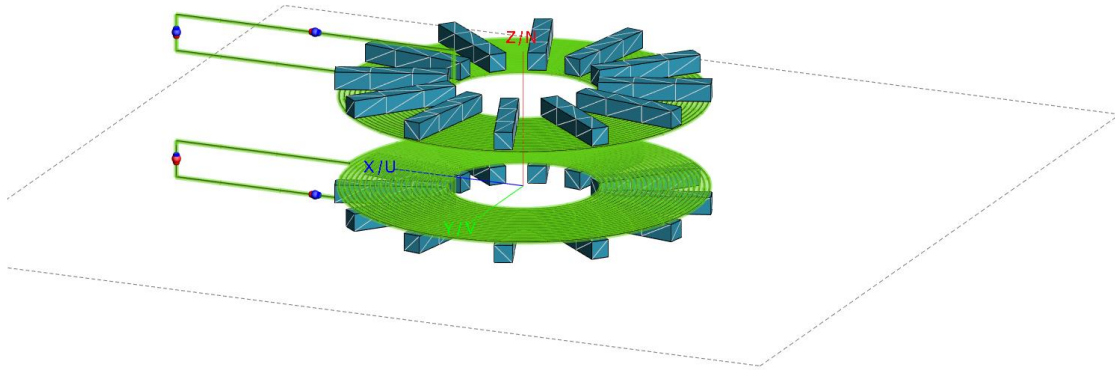
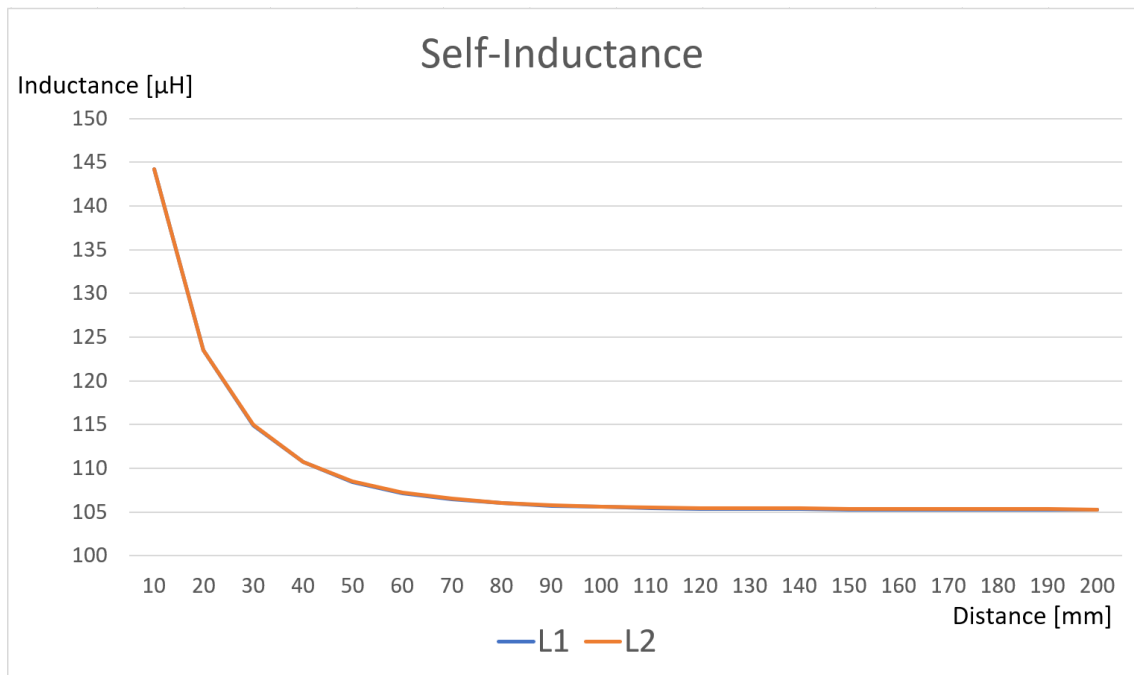


Figure 5.1. Underwater WPT system model

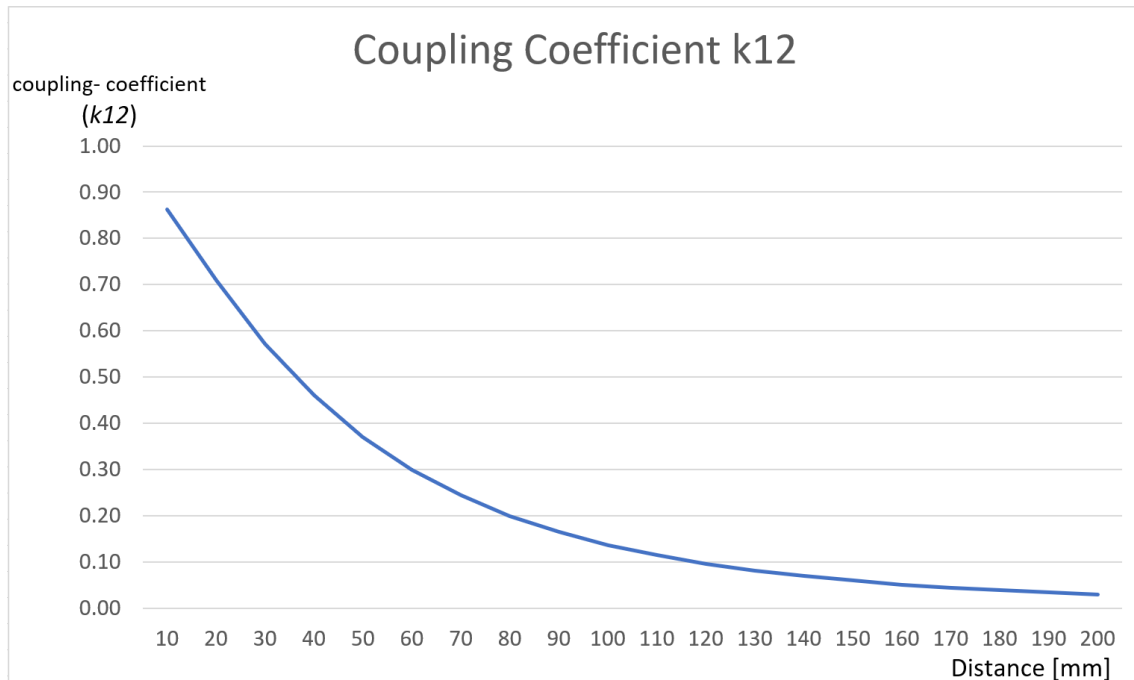
Table 5.1. Underwater WPT system design parameters

Wire Material	Wire Radius	Wire Insulation	Loop Shape	Loop Radius	Loop Turns	Ferrite Rods	Ferrite Rod μ
Copper	0.565mm	PVC single copper 0.8mm	Spiral	40mm (in) 100mm (out)	22	12 (per 30°)	2000

To compensate the inductance of the coil accurately, the self and mutual inductance values were extracted over the distance between the coils. The value of the self-inductance coil without the ferrite material is constant. However, the self-induction of the coil indicated a high value when the two coils are close to each other, as shown in Figure 5.2 (a). At a distance of 10 mm, the value of the self-inductance exceeds 140 μ H, and decreases sharply for the 50 mm gap. The values of the mutual inductance between the coils were also presented, as shown in Figure 5.2 (b). When the Rx unit is placed at a distance that exceeds 80 mm from the Tx unit, the mutual inductance level decreases below 0.2, and the system can be impractical because of the weak magnetic coupling.



(a)



(b)

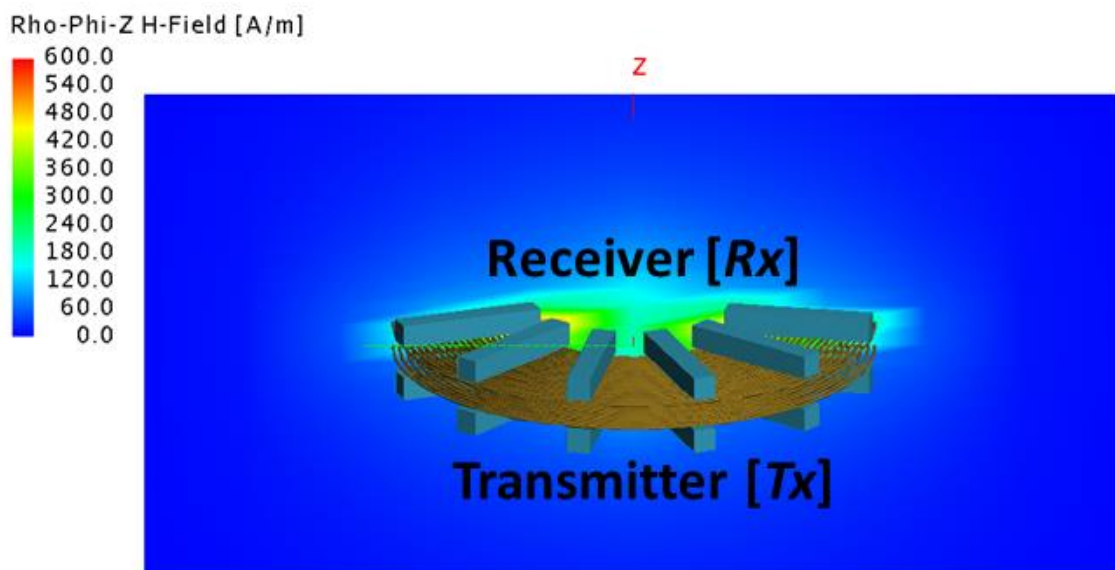
Figure 5.2. Self and mutual inductance of the coils with ferrite materials: (a) self-inductance over the air gap, and (b) coupling coefficient over the air gap.

5.1.2. Magnetic coupling study and practical experiment

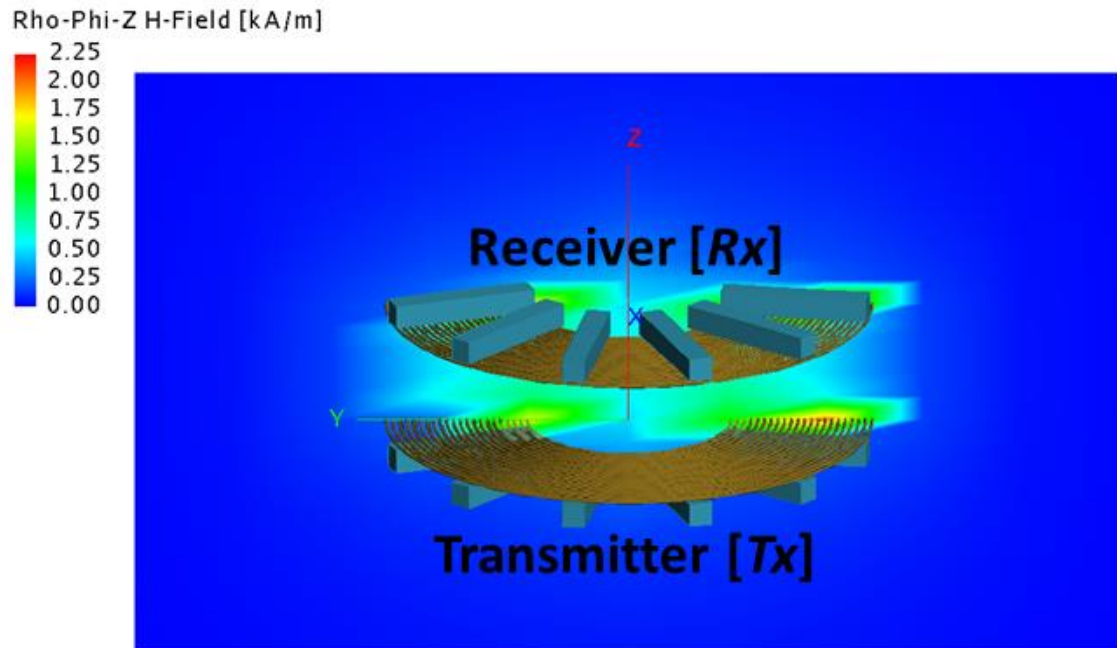
The strength of the magnetic coupling between the coils in seawater was measured over the transfer distance, as shown in Figure 5.3. The WPT model uses SP compensation, and a voltage of 10 V_{rms} at a frequency of 20 kHz was fed into the Tx coil. Magnetic fields of 400 A/m and 1.5 kA/m were evenly distributed at the distances of 10 and 50 mm, respectively, as illustrated in Figure 5.3 (a) and (b). However, the low magnitude of the magnetic field induced on the Rx unit compared to the strength of the magnetic field on the Tx unit is shown in Figure 5.3 (c), presenting this WPT system with a weak magnetic coupling, resulting in poor performance at a distance of 100 mm. The details of the electrical parameters in these WPT models is presented in Table 5.2. In addition, the permeability of seawater around the WPT device was set at 1.0, and is identical to the permeability level [180]. The electromagnetic constant in different mediums is listed in Table 5.3.

Table 5.2. Electrical parameters of the WPT system

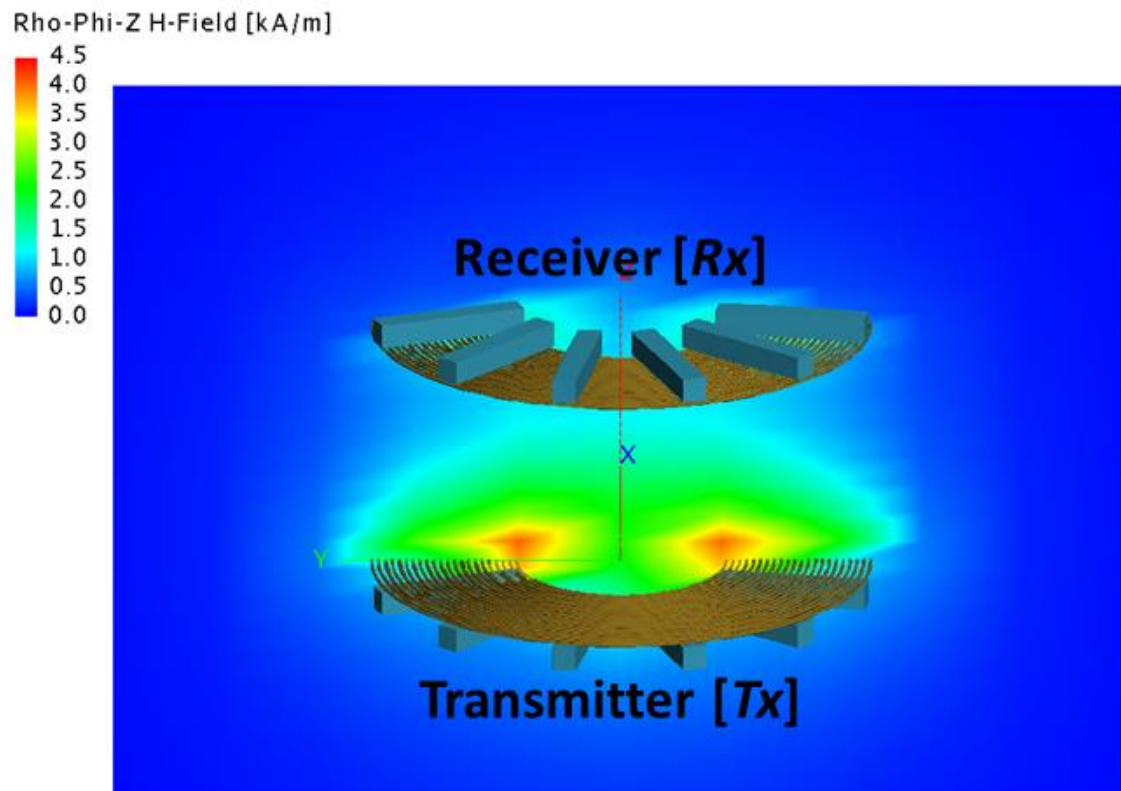
Distance	Inductance L_1 and L_2	Compensation Topology	Parasitic Wire Resistance	Coupling Coefficient k_{12}	Frequency
50 mm	104 μ H	Serial-Parallel	0.3 Ω	0.3703	20 kHz



(a)



(b)



(c)

Figure 5.3. Simulation of the magnetic coupling over the distances of: (a) 10 mm, (b) 50 mm, and (c) 100 mm

Table 5.3. Electromagnetic constant of air and water

Symbol	Appellation	Unit	Air	Springwater	Seawater
σ	conductivity	S/m	$10^{-15} - 10^{-9}$	$5 \cdot 10^{-4} - 5 \cdot 10^{-2}$	4
μ_0	permeability	H/m	$4\pi \cdot 10^{-7}$		
μ_r	relative permeability	-	1	1	1
ϵ_0	permittivity	F/m	$8.854 \cdot 10^{-12}$		
ϵ_r	relative permittivity	-	1	81	81

To demonstrate the WPT model, the prototype was implemented in seawater, as shown in Table 5.5. A full-bridge switching device with a micro-controller was used at the Tx unit to drive the high frequency of 20 kHz. In addition, a full-bridge rectifier and a load resistance of 50 ohms were installed at the Rx unit. The measurement instruments and FRA are set, as shown in Figure 5.5.

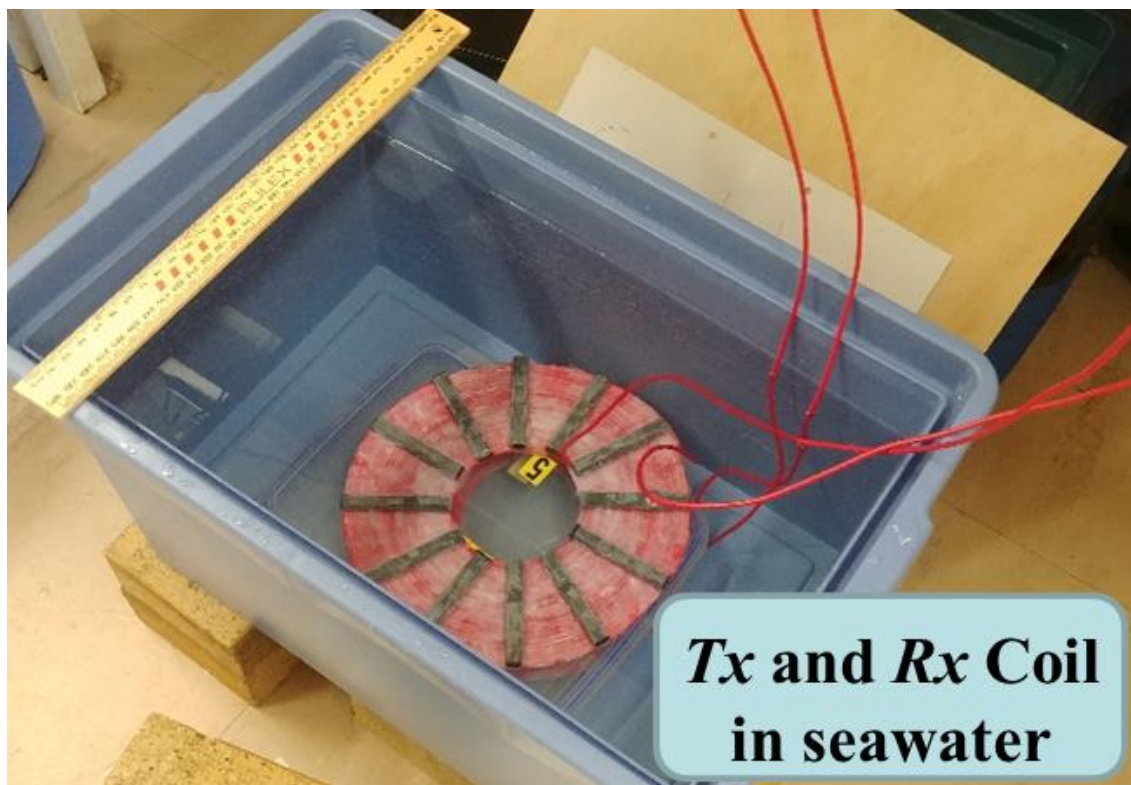
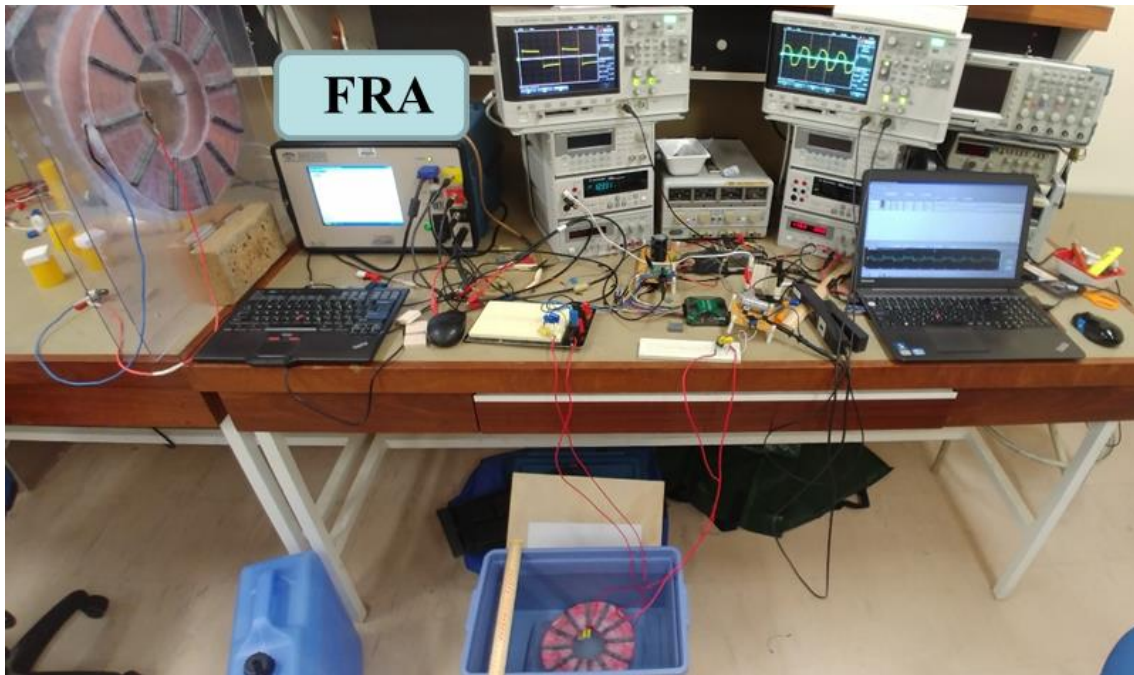
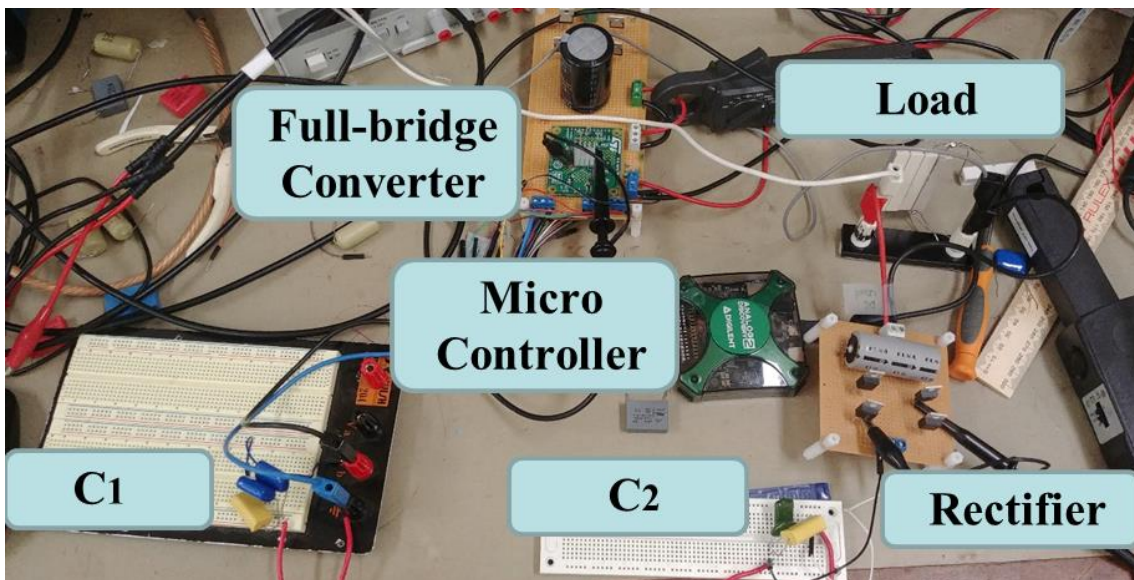


Figure 5.4. Prototype of the AUT WPT system



(a)



(b)

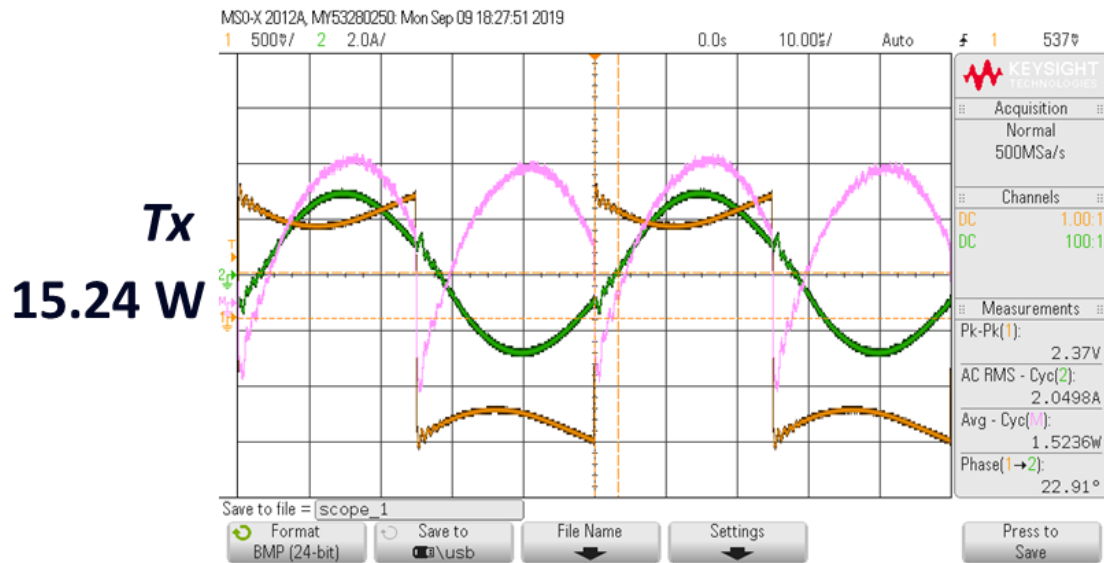
Figure 5.5. Prototype and experiment: (a) hardware setup, and (b) control devices

The experiments were conducted both in the air and in seawater at a gap of 50 mm. The inductive components of the coils in the WTP circuit were compensated, and the zero-angle difference is found in the air and seawater, as shown in Figure 5.6 (a) and Figure 5.7 (a). In addition, the sinusoidal induced voltage, current across the full-bridge rectifier, and the delivered power of 12.79 W and 11.50 W is presented in Figure 5.6 (b) and Figure 5.7 (b), respectively. The transfer efficiency at the distance of 50 mm is 83.95% in air, and 81.33% in seawater, indicating comparable performance.

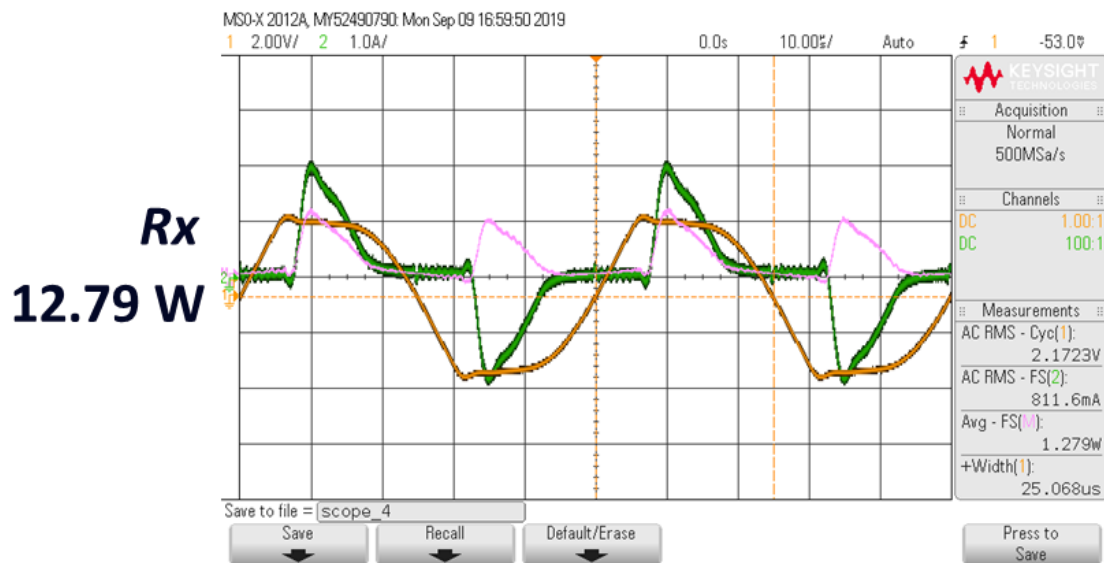
To analyse the performance of the prototype, the transfer efficiency between the two coils and the DC-DC efficiency between the DC power supply and the load resistance was assessed over the distance, as shown in Table 5.4. This indicates that the experiment measurements were in agreement with the simulation results, as shown in Figure 5.8 and Figure 5.9.

Table 5.4. Transfer and DC–DC efficiency over different distances

Distance	DC Input [Watt]		AC Pin [Watt]			AC Pout [Watt]			DC Output [Watt]		Transfer Efficiency			DC–DC Efficiency	
	Air	Seawater	FEKO	Air	Seawater	FEKO	Air	Seawater	Air	Seawater	FEKO	Air	Seawater	Air	Seawater
10mm	5.33	4.60	3.87	4.26	4.24	3.51	3.78	3.89	3.64	3.48	90.70%	88.65%	91.68%	68.20%	69.67%
20mm	6.77	6.77	5.70	5.65	5.89	5.10	5.08	5.05	4.61	4.63	89.47%	89.91%	85.74%	68.07%	68.35%
30mm	8.88	7.88	8.40	7.42	6.81	7.50	6.89	6.12	5.98	5.38	89.29%	92.88%	89.87%	67.29%	68.24%
40mm	14.10	13.32	13.0	11.55	11.42	11.2	9.35	9.18	8.22	7.97	86.15%	80.95%	80.40%	58.27%	59.86%
50mm	20.76	17.21	19.5	15.24	14.14	16.0	12.79	11.5	11.06	10.07	82.05%	83.95%	81.33%	53.28%	58.49%
60mm	23.43	25.65	28.0	17.62	18.47	22.0	12.36	12.89	10.77	11.90	78.57%	70.15%	69.81%	45.98%	46.40%



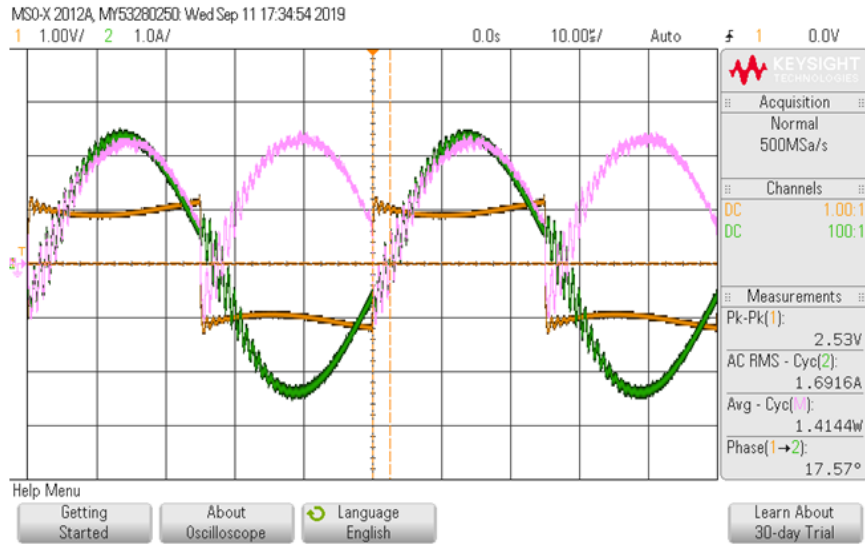
(a)



(b)

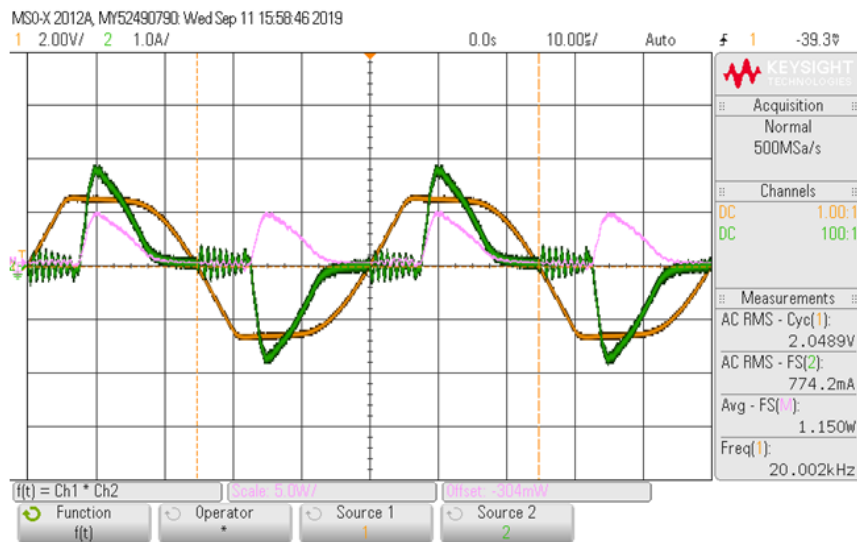
Figure 5.6. Waveform of Tx and Rx in air at 50 mm: (a) Tx measurement, and (b) Rx measurement

T_x
14.41 W



(a)

R_x
11.50 W



(b)

Figure 5.7. Waveform of Tx and Rx in seawater at 50 mm: (a) Tx measurement, and (b) Rx measurement

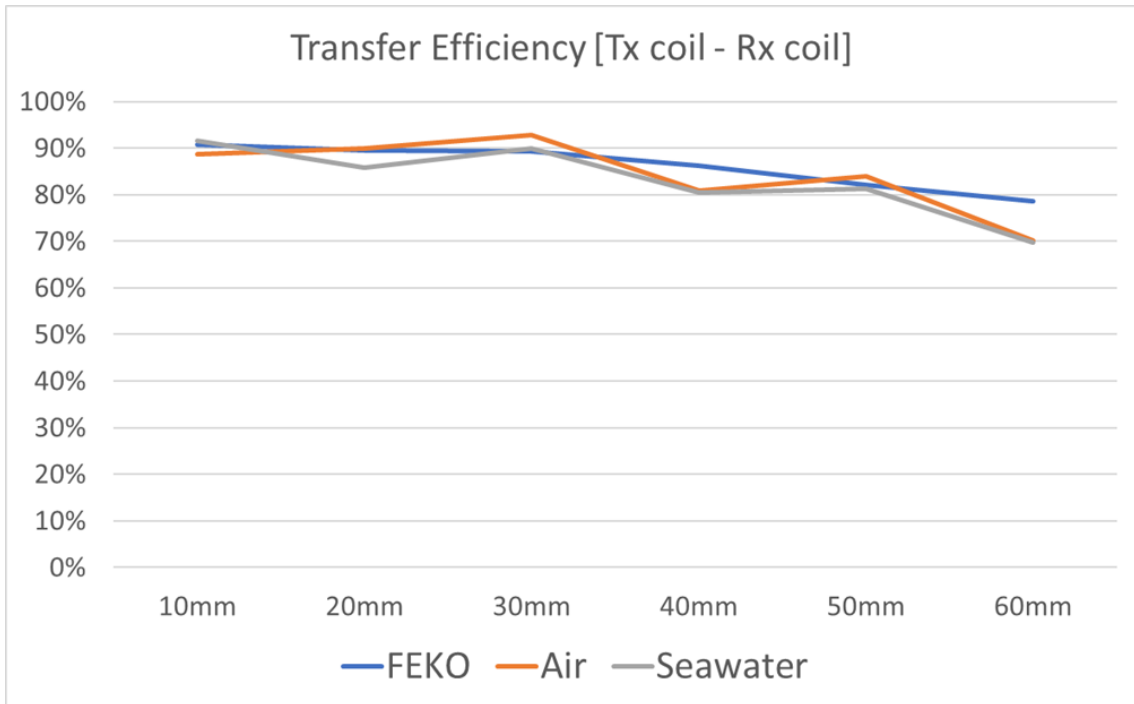


Figure 5.8. Transfer efficiency comparison

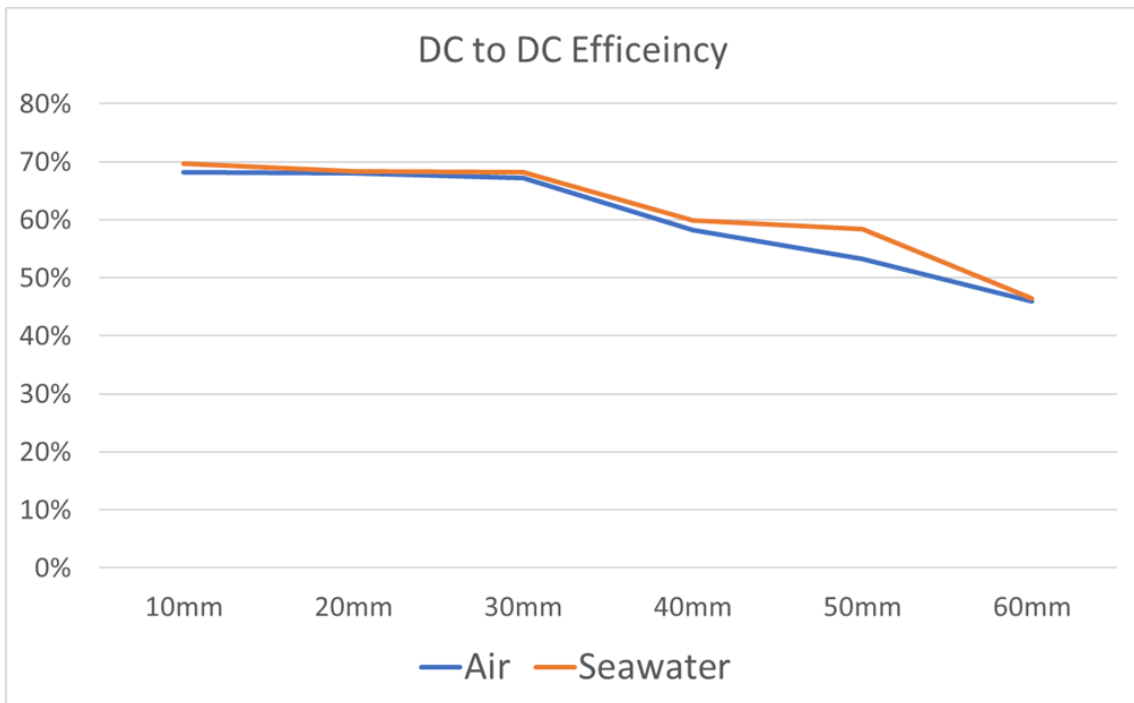


Figure 5.9. DC-DC efficiency comparison

5.1.3. FRA measurement of AUT WPT system

To inspect the resonance characteristics of the WPT system, FRA measurements were carried out over distances of 10 mm and 50 mm, and the plots of the VTR and phase angle of the transfer function $H_{(j\omega)} \angle \delta^\circ$ based on (4.11) and (4.12) are observed, as shown in Figure 5.10. When the transfer distance between the coils is at 10 mm, the VTR indicates the lowest value of -6 dB, whereas -2 dB of VTR was recorded at a gap of 50 mm. The VTR graph over the frequency range becomes narrow when the transfer distance increases, and this represents the difficulty of resonance frequency tuning at the greater distance.

In addition, it was discovered that the FRA result in seawater indicated good agreement with the result in the air up to a frequency of 400 kHz, then a significant difference was observed at higher frequencies, as shown in Figure 5.11. The level and the phase angle of the input impedance in the WPT system were extracted, as shown in Figure 5.12. As the reactive component of the input impedance is much higher than the real component, the large difference of the phase angle between air and seawater was found from the frequency of 800 kHz, as shown in Figure 5.12 (b). The resistance in the AC system consists of DC, AC, and radiation resistance, and the radiation resistance in seawater gradually increases from frequencies of tens of kHz [181]. This also explains that the self and mutual inductance of the coils vary in the high-frequency range. The prototype of the WPT system in seawater showed a similar performance to the system in air at the low frequency of 20 kHz. However, the variation in the electromagnetic parameters should be assessed when a high-frequency underwater WPT system is applied.

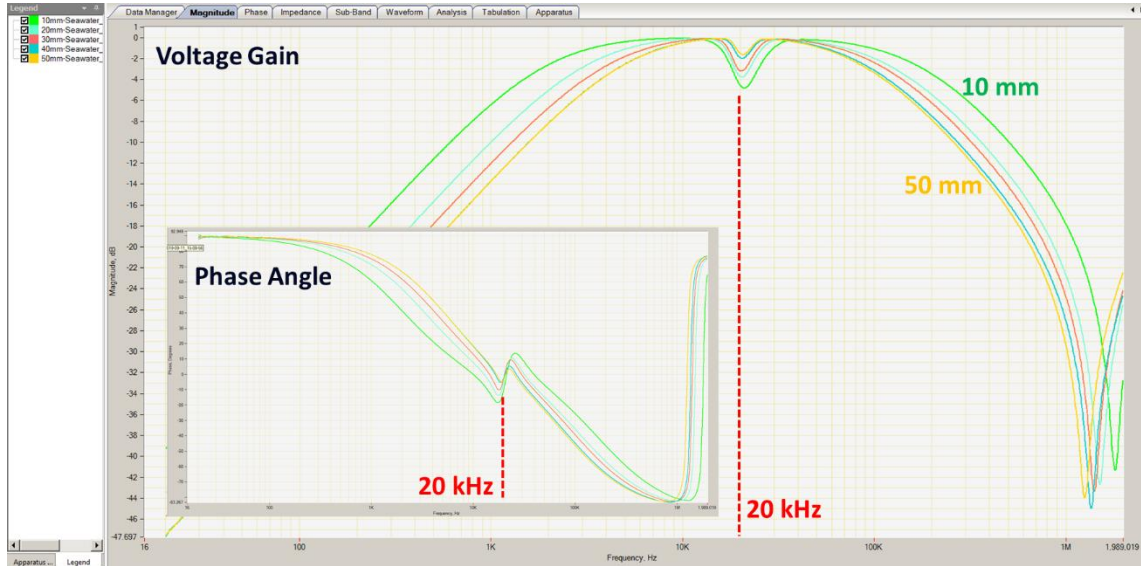


Figure 5.10. FRA measurement of WPT system in seawater

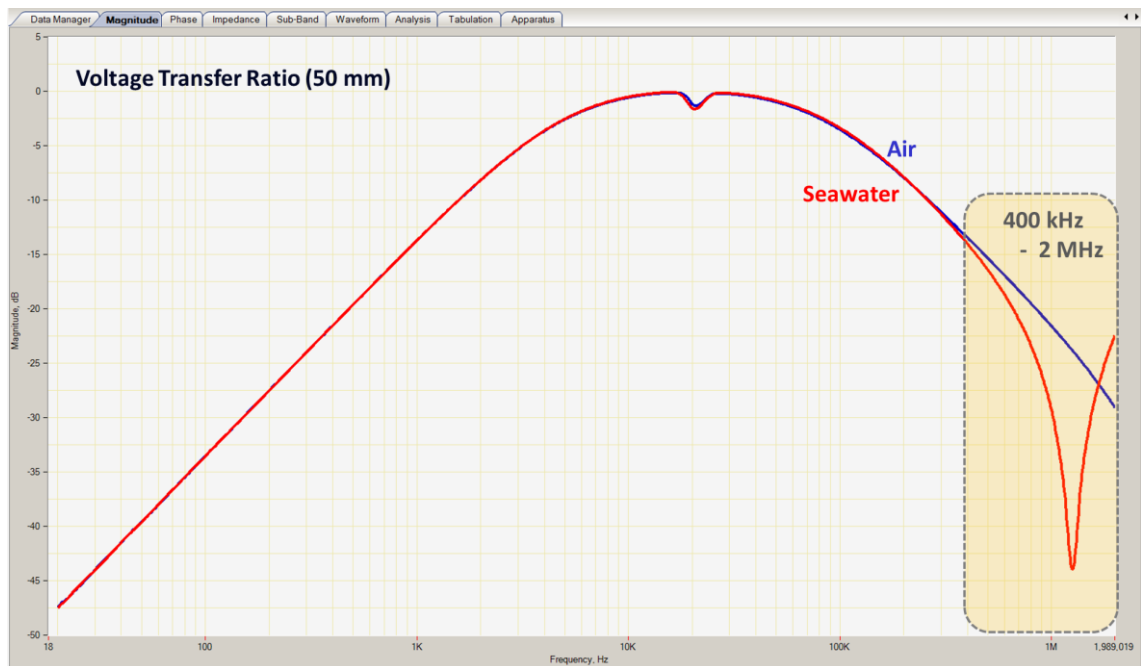
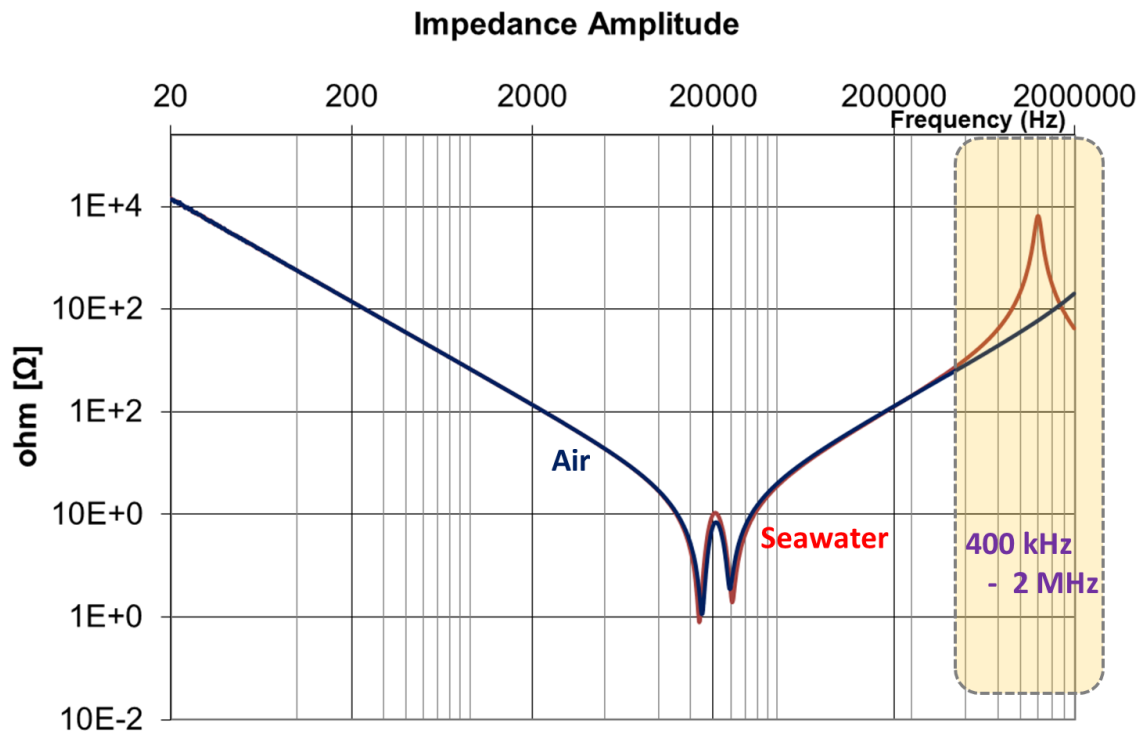
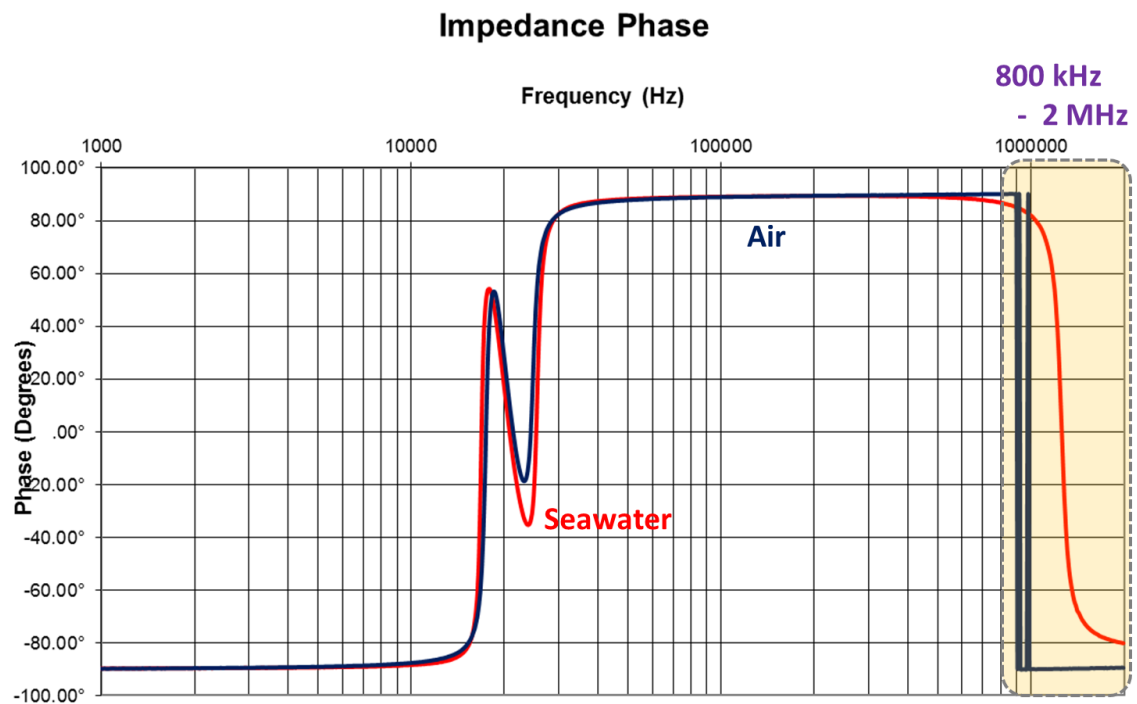


Figure 5.11. Voltage gain results in air and seawater



(a)



(b)

Figure 5.12. Input impedance of AUV WPT system in air and seawater: (a) amplitude, and (b) phase angle

5.2. FRA using Various Misalignments of the Coils

Coil misalignments in different mediums results in a variation in the mutual inductance value and the density of magnetic flux [182]. The geometric variation of the WPT constructions should be identified for the most reliable system for EV charging, based on the SAE J2954 standard [183, 184]. SAE J2954 provides the tolerance of three-dimensional XYZ positioning between the ground assembly and the vehicle assembly [185]. Therefore, it is important to assess the misalignments of two-coil inductively-coupled WPT systems, and the application of FRA on WPT systems specifies both the grade of the coil misalignment and the variation of the electromagnetic parameters. A picture of the practical prototype is shown in Figure 5.13.

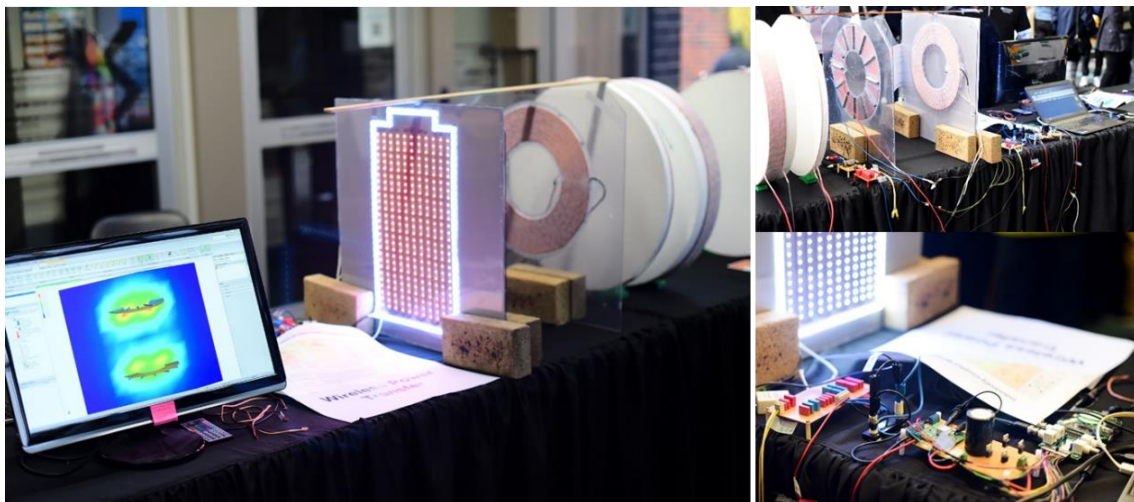


Figure 5.13. Demonstration of the WPT Prototype

The FRA test setup for the WPT system with series/series-parallel (SSP) compensation is shown in Figure 5.14 and Figure 5.15 where C_1 , C_2 and C_m are compensating capacitors, and the ferrite rods are implemented on the 1st and 2nd winding to supplement the magnetic coupling in the WPT model. The signal and reference lead (red lead of the FRA) is connected to the 1st winding [186].

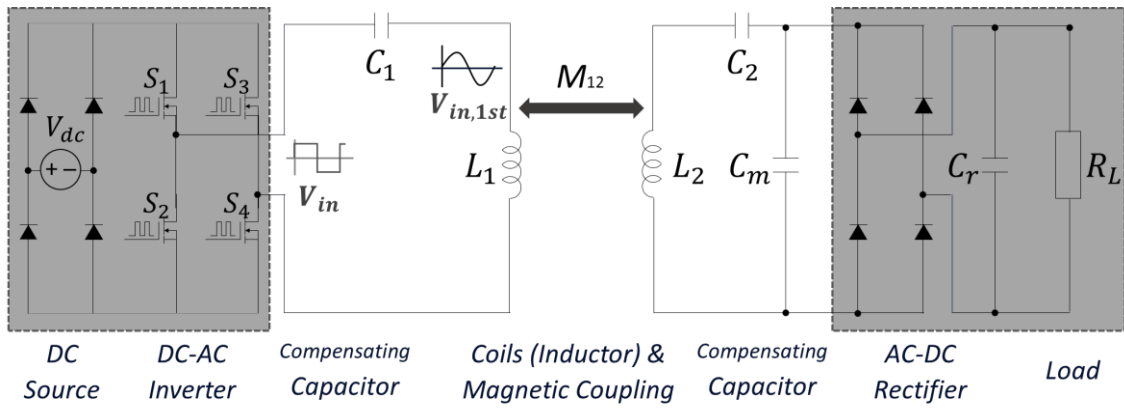


Figure 5.14. Two-Coil inductively-coupled SSP WPT system and FRA application

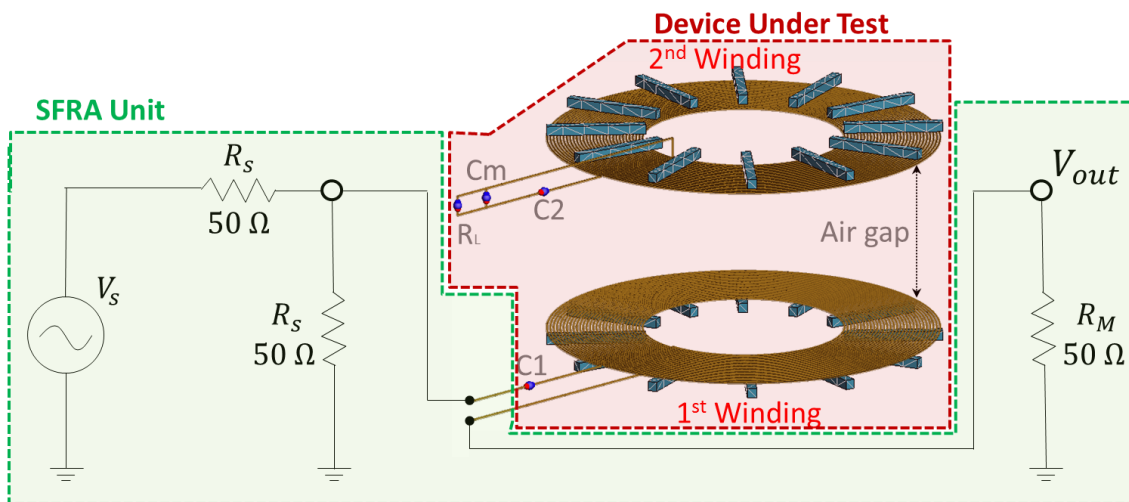


Figure 5.15. Example of FRA connected to WPT system

As SAE J2954 established the EV charging standard with a frequency of 85 kHz for the light vehicles, the developed prototype WPT system was designed to deliver power at a frequency of 85 kHz, and the transfer distance between the coils was extended up to 300 mm, as illustrated in Figure 5.16. As a reference, the electromagnetic field solver called FEKO was employed to construct the windings and simulate the magnetic coupling in the WPT model [119]. The details of the parameters when the distance of the air gap is 200 mm are described in Table 5.5.

Table 5.5. Parameters of WPT System in air

Wire Material	Wire Radius	Compensation	Winding Shape	Loop Radius	Loop Turns	Number of Ferrite Rods	Ferrite Rod μ
Copper	1.5 mm (Litz wire)	Series, Series-Parallel	Spiral	105 mm (in) 200 mm (out)	30	12 ea (per 30°)	2000

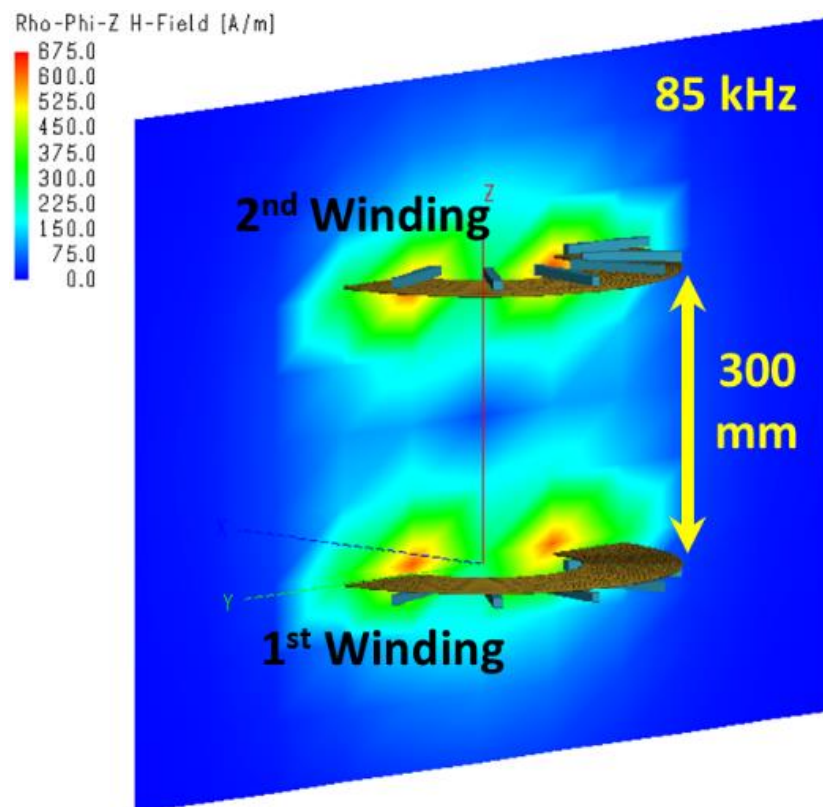


Figure 5.16. Electromagnetic study of two-coil WPT at 85kHz

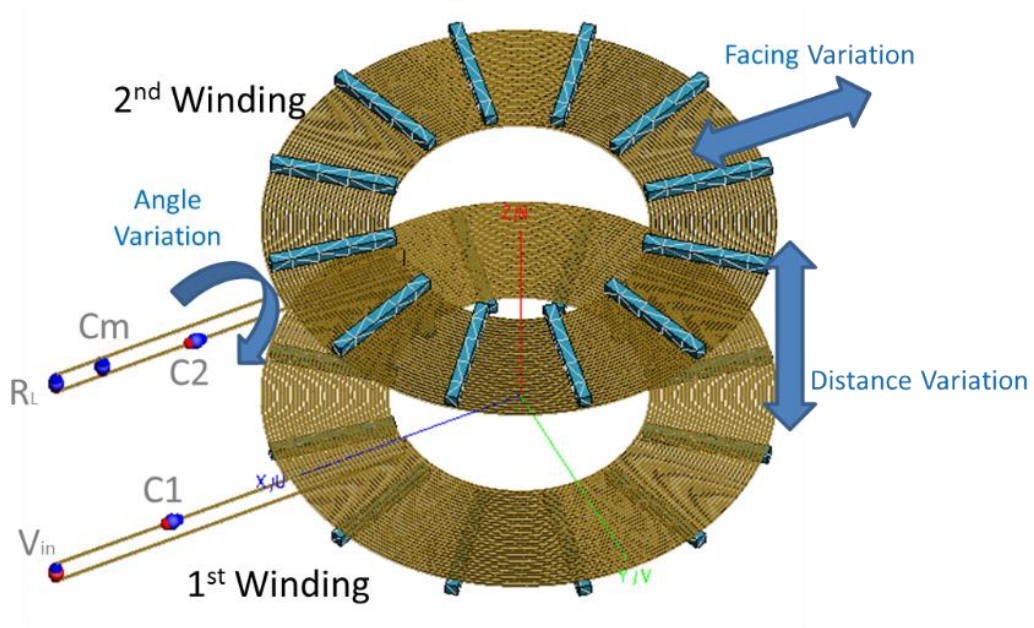


Figure 5.17. Coil misalignments

The measurements using FRA on the WPT system were conducted under distance, angle, and face variations between the two coils, as shown in Figure 5.17; in addition, the difference in the electrical parameters on the WPT system were observed during the case study.

5.2.1. Distance Variation

FRA tests were conducted for various air gap distances from 130 mm to 270 mm, as listed in Table 5.5. At the shortest distance between the windings, the resonance frequency is not found at 85 kHz, as shown in Figure 5.18. When the 2nd winding is placed in the vicinity of the 1st winding, there is more than one resonance point because of the strong magnetic coupling, also referred to as the frequency bifurcation phenomenon. The multiple resonance points are identified clearly by the FRA measurements [125]. A single resonance point at 85 kHz can be found by increasing the transfer distance. The FRA traces also show how narrow and sharp the response is around 85 kHz. This shows how difficult it is to tune the WPT system and how inefficient it is over long transfer

distances. Hence, FRA helps to observe the exact resonance frequency at different distances.

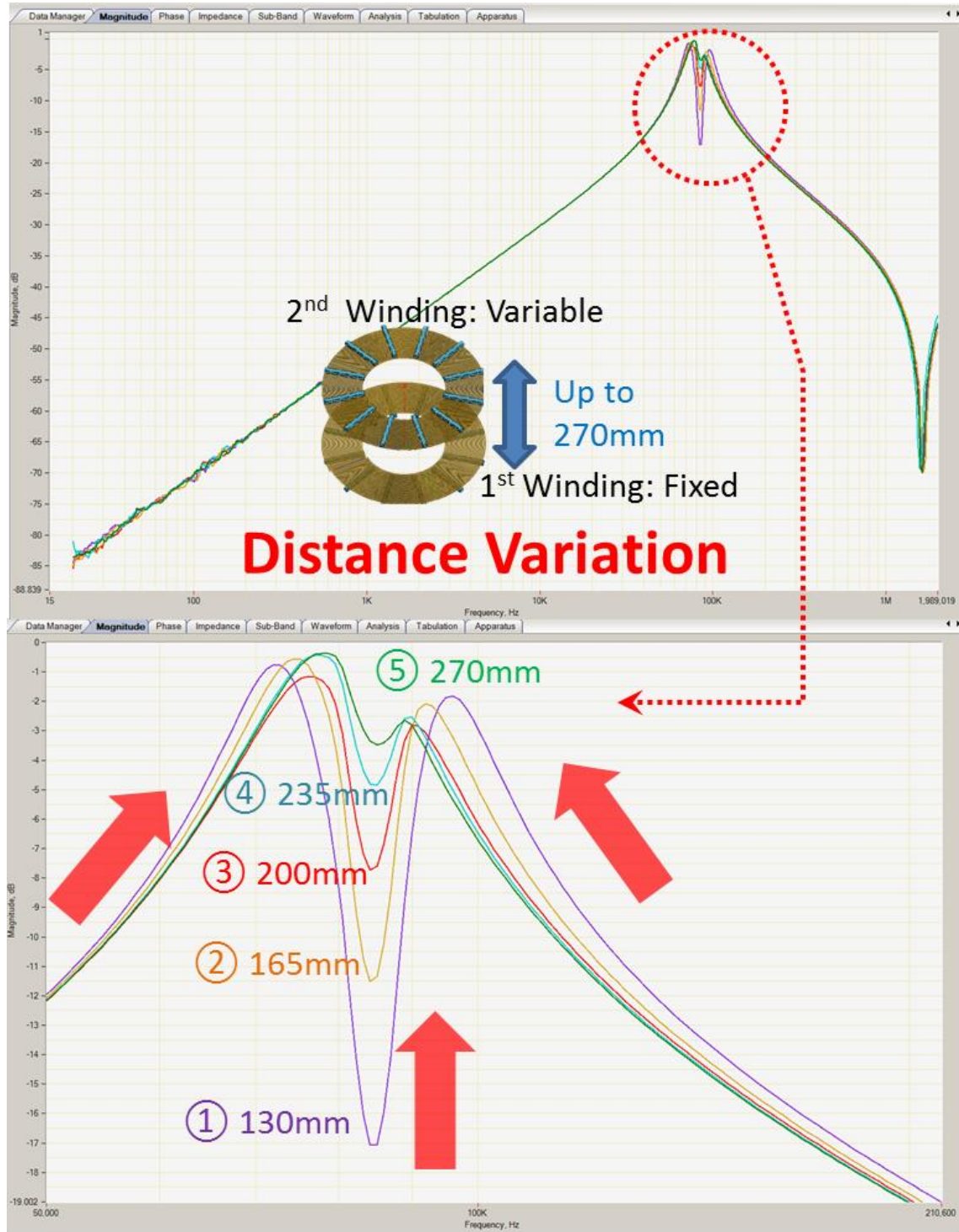


Figure 5.18. FRA measurement at different air gaps

Table 5.6. WPT parameters for various distances

No.	L_1 [uH]	L_1 Ferrite Bars	L_2 [uH]	L_2 Ferrite Bars	Distance	Angle	Facing area Difference	C_1 [nF]	C_2 [nF]	C_m [nF]	R_L [Ω]
①	418.4	12, Well arranged	414.3	12, Well positioned	130mm	0deg	0mm	9.7	9.7	66.6	76
②	418.4	12, Well arranged	414.3	12, Well positioned	165mm	0deg	0mm	9.7	9.7	66.6	76
③	418.4	12, Well arranged	414.3	12, Well positioned	200mm	0deg	0mm	9.7	9.7	66.6	76
④	418.4	12, Well arranged	414.3	12, Well positioned	235mm	0deg	0mm	9.7	9.7	66.6	76
⑤	418.4	12, Well arranged	414.3	12, Well positioned	270mm	0deg	0mm	9.7	9.7	66.6	76

5.2.2. Facing area Variation

When the transportable 2nd winding is not placed in the intended position, the performance of the WPT system can be degraded. The 2nd winding was dragged horizontally from 0 mm to 200 mm, as listed in Table 5.7. As the area of the magnetic coupling between the winding varies over the distance of misalignment, the different signatures were recorded, as illustrated in Figure 5.19. When the two windings are precisely facing each other, two resonance points were detected, as shown by the yellow trace in Figure 5.19. The resonance frequencies converge to the frequency of 85 kHz when the misalignment distance increases in this experiment. If the fingerprint signature is recorded when the WPT is installed on-site, misalignment can be detected sensitively during maintenance work.

Table 5.7. WPT parameters for different facing areas

No.	L_1 [uH]	L_1 Ferrite Bars	L_2 [uH]	L_2 Ferrite Bars	Distance [mm]	Angle	Facing area Difference	C_1 [nF]	C_2 [nF]	C_m [nF]	R_L [Ω]
①	418.4	12, Well arranged	414.3	12, Well positioned	200	0deg	0mm	9.7	9.7	66.6	76
②	418.4	12, Well arranged	414.3	12, Well positioned	200	0deg	50mm	9.7	9.7	66.6	76
③	418.4	12, Well arranged	414.3	12, Well positioned	200	0deg	100mm	9.7	9.7	66.6	76
④	418.4	12, Well arranged	414.3	12, Well positioned	200	0deg	150mm	9.7	9.7	66.6	76
⑤	418.4	12, Well arranged	414.3	12, Well positioned	200	0deg	200mm	9.7	9.7	66.6	76

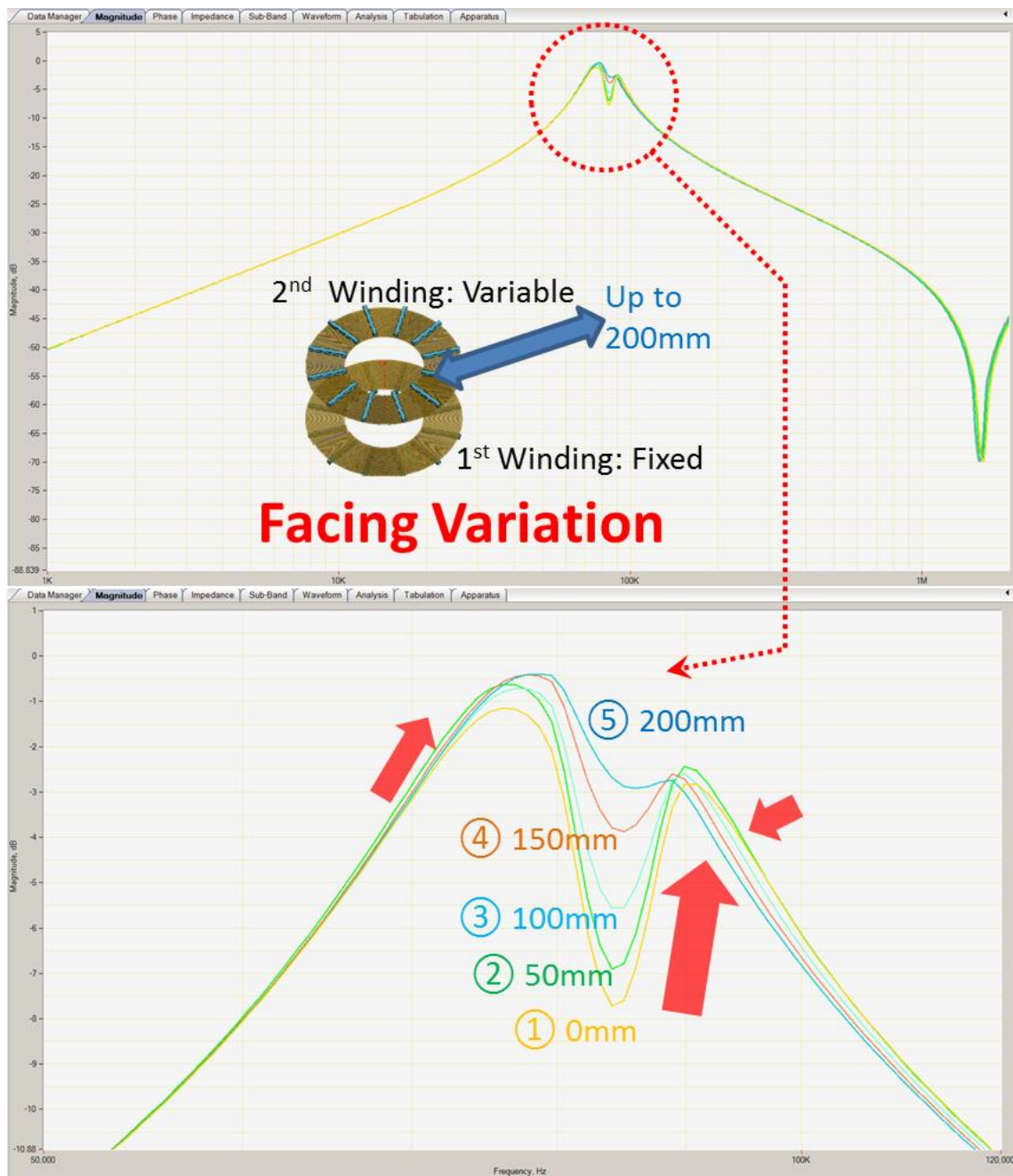


Figure 5.19. FRA measurement under different facing conditions

5.2.3. Angle Variation

In the application of the mobile device charging system, the Tx unit is stationary on or under the ground. The Rx unit is installed under the frame of the mobile device, and it approaches the static Tx unit for magnetic coupling in the right position. This assumes the mobile device is coupled with the charging station aslant at a distance of 200 mm, as shown in Figure 5.20. The FRA tests were carried out for different angles of the Rx unit from 0° to 26°, as listed in Table 5.8. As the transfer distance of 200 mm at the centre of the coupling is fastened, the net coupling surface is unchanged. However, a small difference of approximately 1 dB was observed between the flat Rx and the 28° inclined Rx, as shown in Figure 5.21.

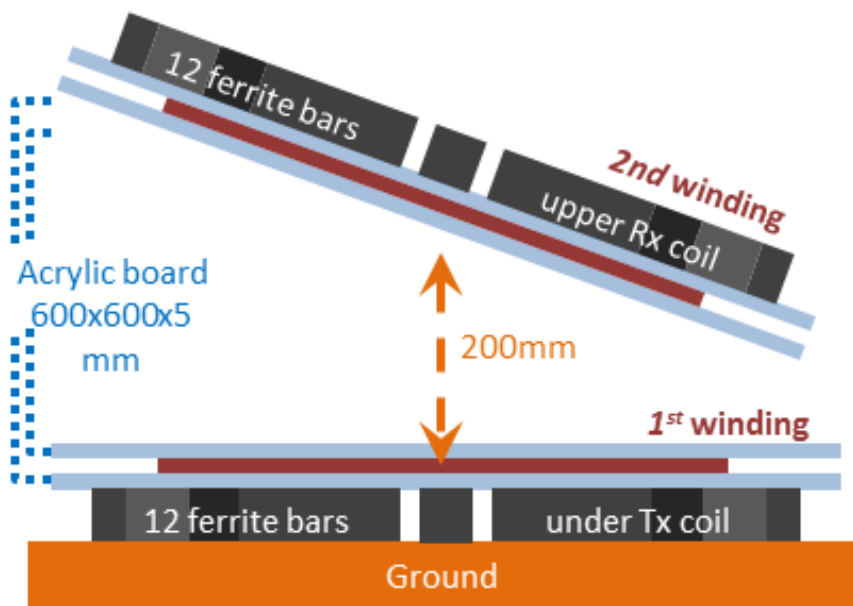


Figure 5.20. Example of a WPT system with tilted Rx unit

Table 5.8. WPT parameters for each angle variation

No.	L_1 [uH]	L_1 Ferrite Bars	L_2 [uH]	L_2 Ferrite Bars	Distance [mm]	Angle	Facing Area Difference	C_1 [nF]	C_2 [nF]	C_m [nF]	R_L [Ω]
①	418.4	12, Well arranged	414.3	12, Well positioned	200mm	0°	0mm	9.7	9.7	66.6	76
②	418.4	12, Well arranged	414.3	12, Well positioned	200mm	8°	0mm	9.7	9.7	66.6	76
③	418.4	12, Well arranged	414.3	12, Well positioned	200mm	19°	0mm	9.7	9.7	66.6	76
④	418.4	12, Well arranged	414.3	12, Well positioned	200mm	26°	0mm	9.7	9.7	66.6	76

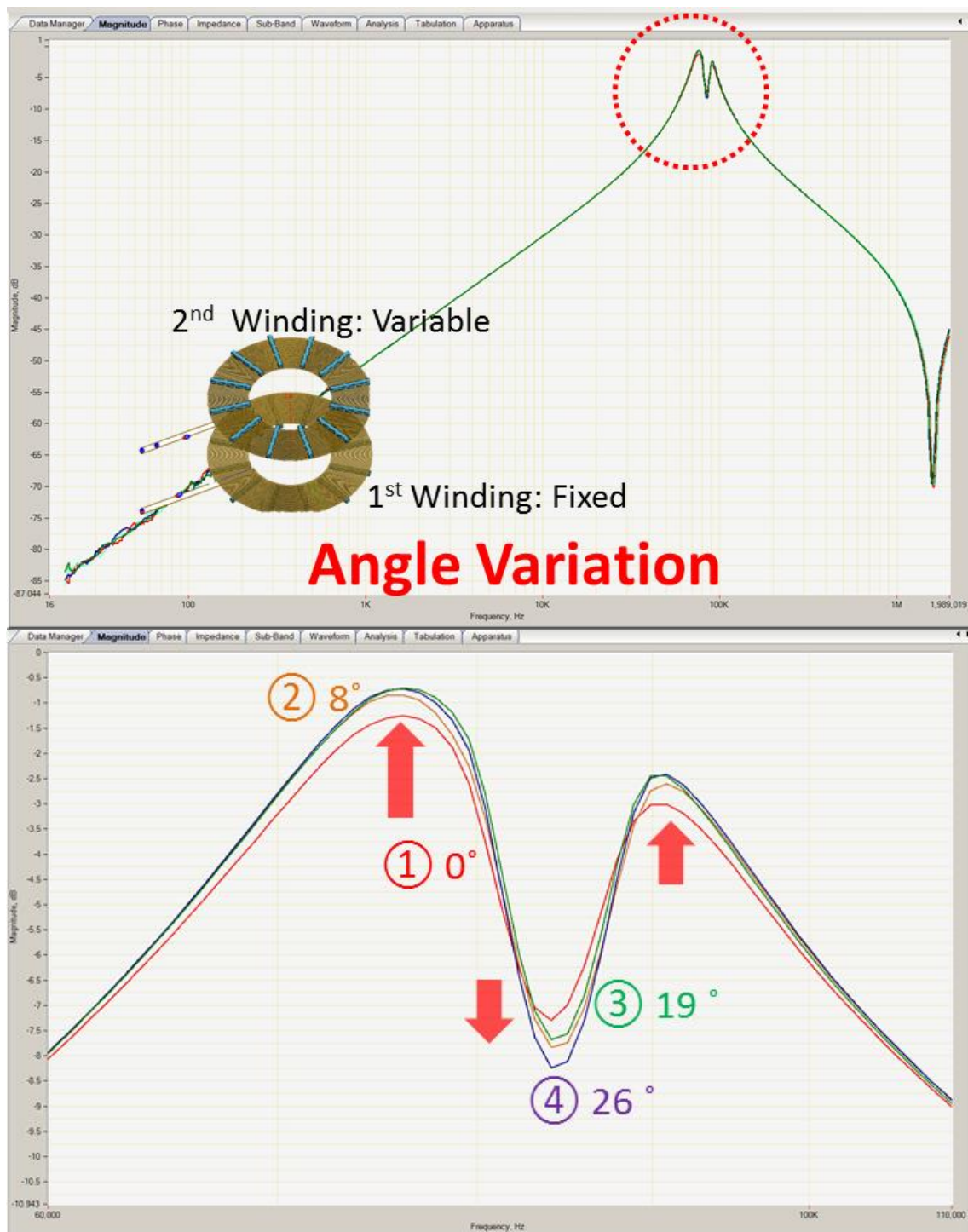


Figure 5.21. FRA measurement for different angles

5.2.4. Electrical parameter C_2 Variation

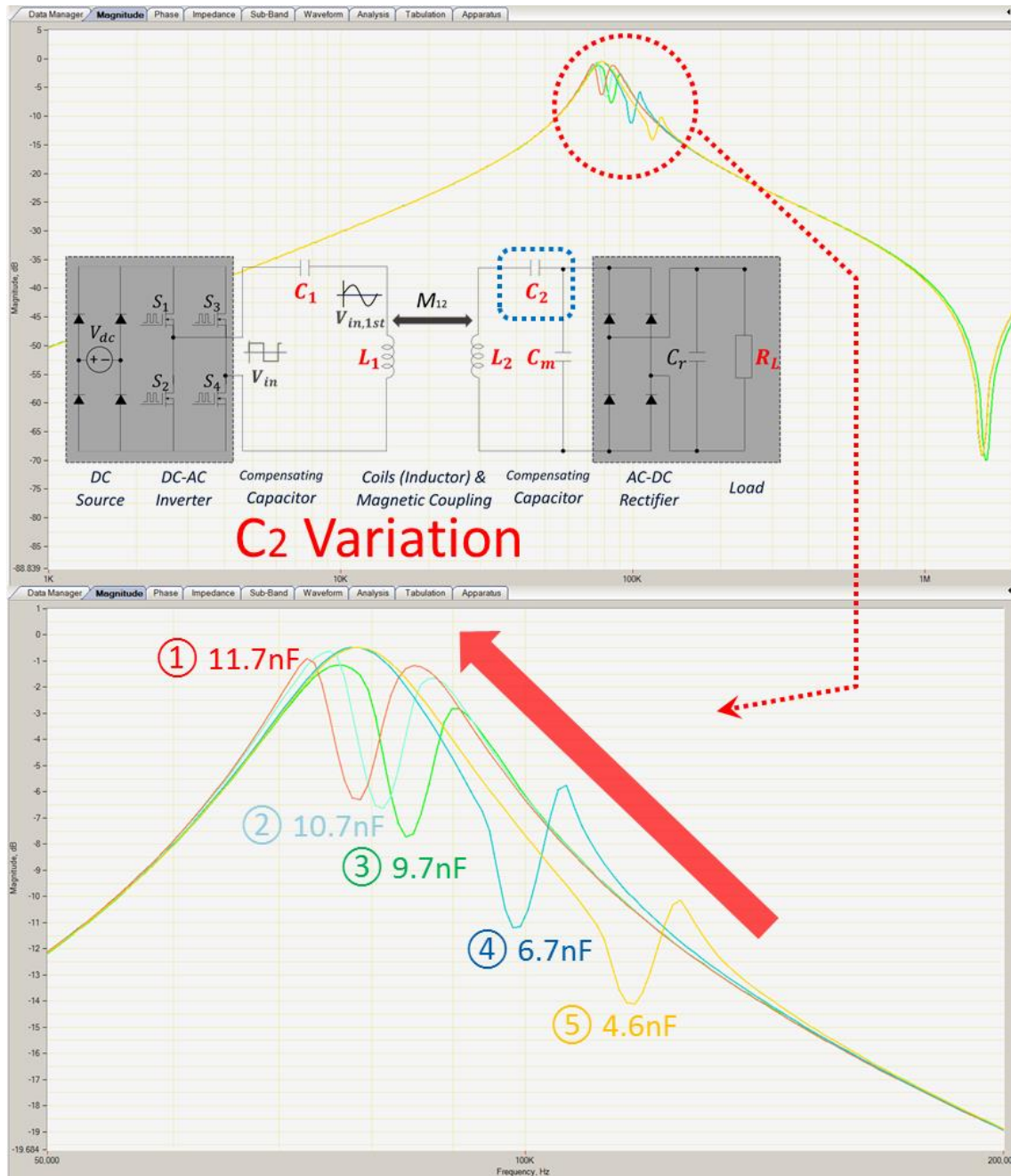
The parameters of electrical components such as inductors, resistors, and capacitors deteriorate or their characteristics vary due to environmental factors. This can also result in performance degradation of the WPT system. The compensating capacitor C_2 and C_m at the 2nd winding of the WPT described was changed from 4.6 nF to 11.7 nF, and from 33 nF to 71.2 nF, respectively, as listed in Table 5.9 and Table 5.10. With the C_2 variation, differences were seen in the frequency range between 70 kHz to 150 kHz, as shown in Figure 5.22. As the C_2 affects the resonance compensation of the Rx coil, a large difference in the resonance frequency was observed. On the other hand, the compensation circuit with the variation of C_m responded less sensitively than the C_2 changes. However, the fine disagreements are recognisable as shown in Figure 5.23. Therefore, the effect of the variation of other parameters such as C_1 , or R_L , can also be determined using FRA.

Table 5.9. WPT parameters of C_2 variations

No.	L_1 [uH]	L_1 Ferrite Bars	L_2 [uH]	L_2 Ferrite Bars	Distance [mm]	Angle	Facing Area Difference	C_1 [nF]	C_2 [nF]	C_m [nF]	R_L [Ω]
①	418.4	12, Well positioned	414.3	12, Well positioned	200mm	0°	0mm	9.7	12.7	66.6	76
②	418.4	12, Well positioned	414.3	12, Well positioned	200mm	0°	0mm	9.7	10.7	66.6	76
③	418.4	12, Well positioned	414.3	12, Well positioned	200mm	0°	0mm	9.7	9.7	66.6	76
④	418.4	12, Well positioned	414.3	12, Well positioned	200mm	0°	0mm	9.7	6.7	66.6	76
⑤	418.4	12, Well positioned	414.3	12, Well positioned	200	0°	0mm	9.7	4.6	66.6	76

Table 5.10. WPT parameters of C_m variations

No.	L_1 [uH]	L_1 Ferrite Bars	L_2 [uH]	L_2 Ferrite Bars	Distance [mm]	Angle	Facing Area Difference	C_1 [nF]	C_2 [nF]	C_m [nF]	R_L [Ω]
①	418.4	12, Well positioned	414.3	12, Well positioned	200mm	0°	0mm	9.7	9.7	71.2	76
②	418.4	12, Well positioned	414.3	12, Well positioned	200mm	0°	0mm	9.7	9.7	70.6	76
③	418.4	12, Well positioned	414.3	12, Well positioned	200mm	0°	0mm	9.7	9.7	66.6	76
④	418.4	12, Well positioned	414.3	12, Well positioned	200mm	0°	0mm	9.7	9.7	55.3	76
⑤	418.4	12, Well positioned	414.3	12, Well positioned	200	0°	0mm	9.7	9.7	33	76

Figure 5.22. FRA measurements under different values for compensating capacitor C_2

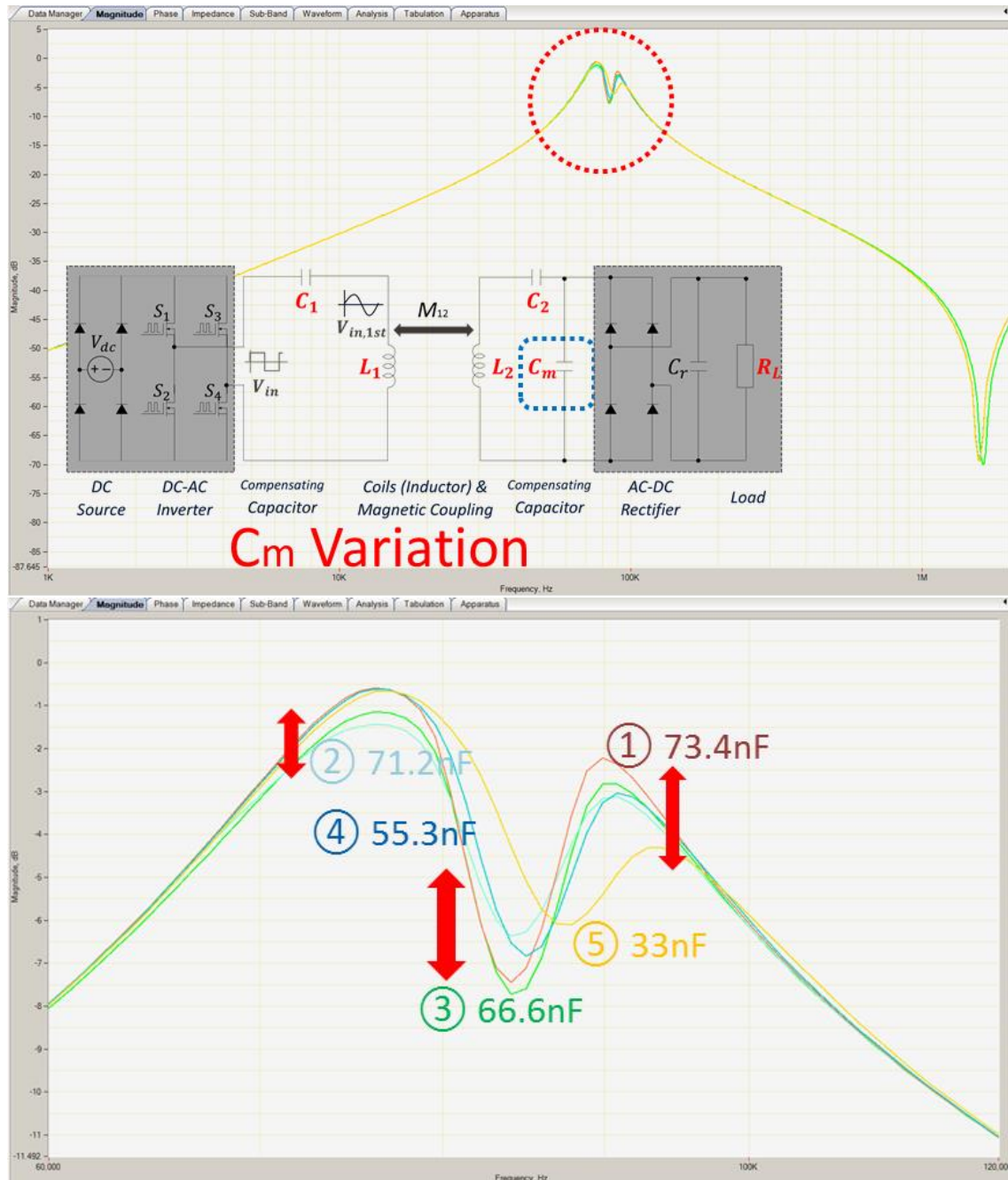


Figure 5.23. FRA measurements under different values for compensating capacitor C_m

5.2.5. Magnetic parameter variation: ferrite bar movements

While the 1st winding is stationary, the 2nd winding is transportable like a wireless charging device. This case study considers the positioning of the ferrite bars on the 2nd winding of the WPT system described in Table 5.5. Three, five, and seven ferrite bars are dispositioned by 10 degrees, respectively, and FRA measurements were conducted. The disagreement of the signatures is not significant, as in the variation of the distance, facing alignment, or electrical parameters. However, the VTR level between the well-positioned condition and the seven dispositioned bars differs by approximately 1.5 dB, as shown in Figure 5.24. Hence, the displacement or the permeability in the ferrite bars can also be observed using FRA.

Table 5.11. WPT parameters from variations in the positioning of L_2 ferrite bars

No.	L_1 [uH]	L_1 Ferrite Bars	L_2 [uH]	L_2 Ferrite Bars	Distance [mm]	Angle	Facing Area Difference	C_1 [nF]	C_2 [nF]	C_m [nF]	R_L [Ω]
①	418.4	12, Well arranged	414.3	12, Well positioned	200	0deg	0mm	9.7	9.7	66.6	76
②	418.4	12, Well arranged	414.3	3 bar 10° dispositioned	200	0deg	0mm	9.7	9.7	66.6	76
③	418.4	12, Well arranged	414.3	5 bar 10° dispositioned	200	0deg	0mm	9.7	9.7	66.6	76
④	418.4	12, Well arranged	414.3	7 bar 10° dispositioned	200	0deg	0mm	9.7	9.7	66.6	76

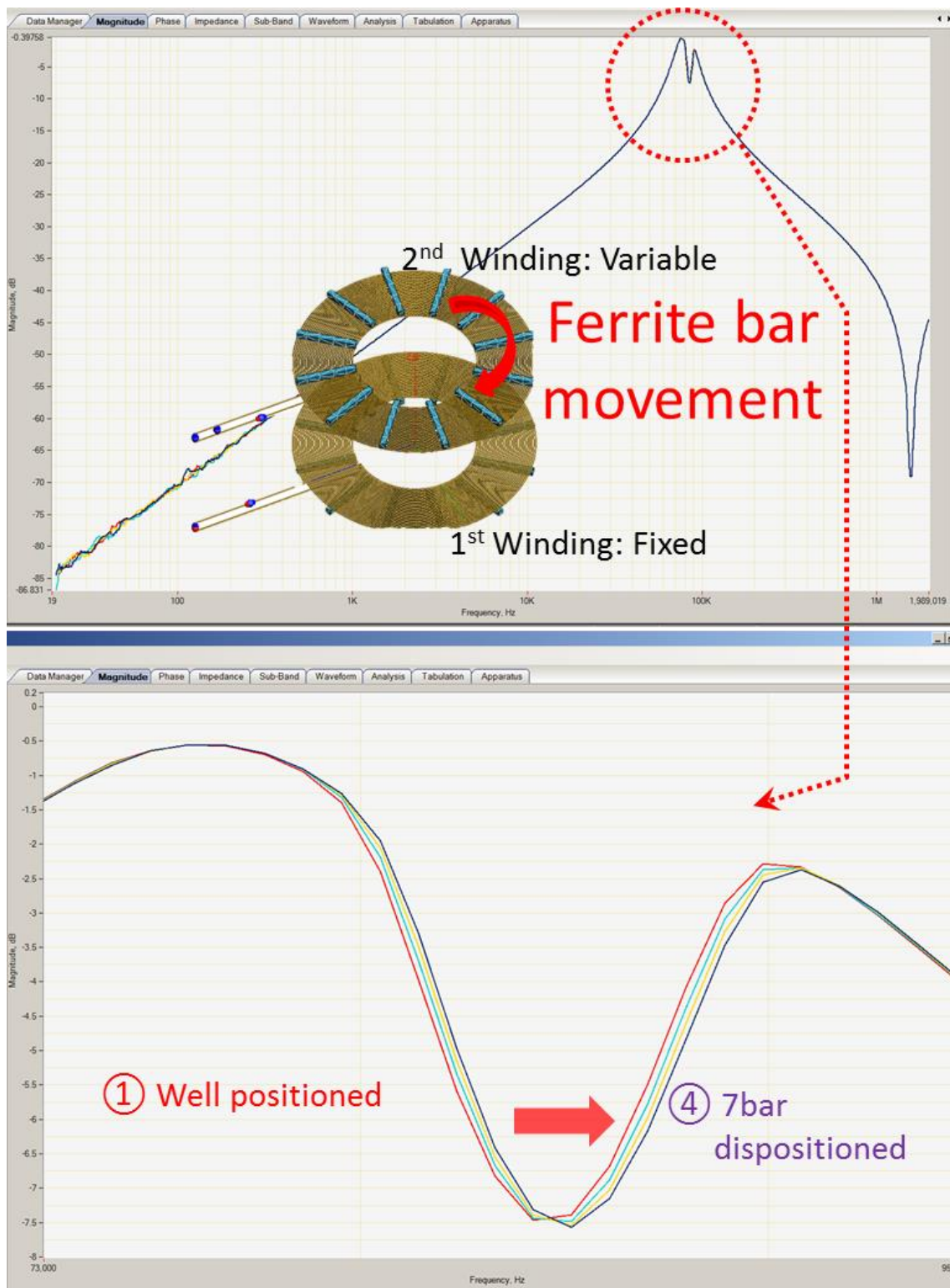
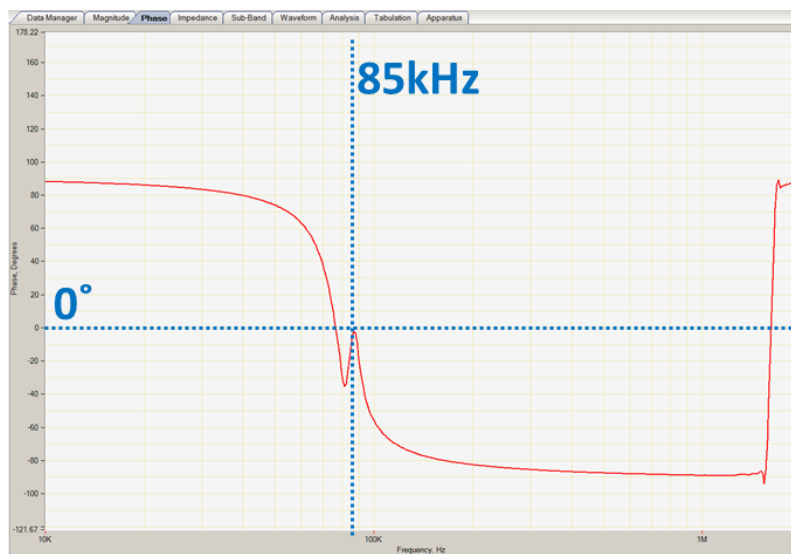


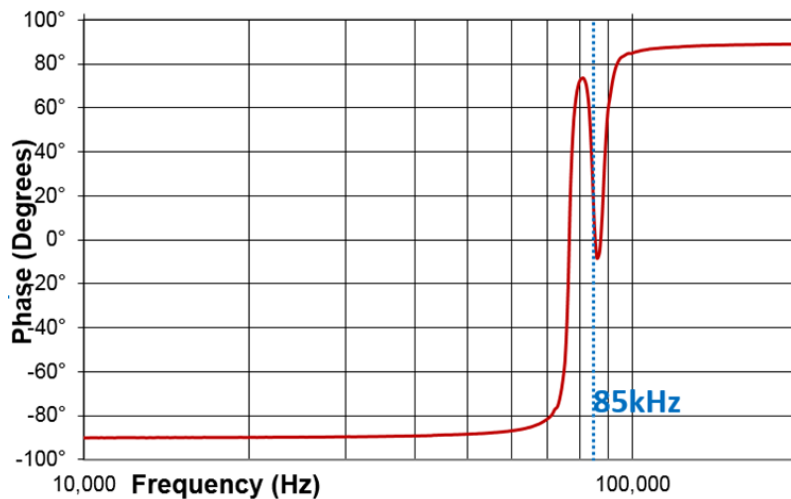
Figure 5.24. FRA measurement under different positioning of ferrite bars

5.3. Discussion

The physical or electrical variations of the WPT system can be determined by interpreting VTR signatures. Furthermore, FRA provides precise values of the impedance and phase angle of the apparatus under test. The Phase and Impedance tabs in the FRA software indicate the value, including the measurement resistance of $50\ \Omega$, as depicted in Figure 5.15. To extract the real and imaginary part of the input impedance, additional calculations are required in (4.13) and (4.14).



(a)



(b)

Figure 5.25. Phase angle graph: (a) FRA measurement, and (b) calculated angle of the WPT system

If the FRA software presents the accurate measurement of the resistance and reactance in the WPT system, the results are useful for analysing the design of the WPT system. For example, the angle of impedance in the WPT system at a distance of 200 mm and 85 kHz is different, as illustrated in Figure 5.25. In Figure 5.25 (b), the phase angle of the WPT input impedance is calculated from the FRA results, while the real and imaginary part of the input impedance can also be computed. Therefore, the short-circuit impedance (or % impedance) of power transformers is theoretically analysable over a range of frequencies with this method.

To obtain a high-frequency power source, WPT systems adopt power electric switching devices such as MOSFETs or IGBTs. Thus, high-frequency square waveforms are fed into the 1st winding of the WPT system, as shown in Figure 5.14. Since the 1st winding of the inductive element and the compensating capacitor are tuned at the resonance frequency, the sinusoidal waveforms at the first harmonic can be extracted using the Fourier analysis in (3-11).

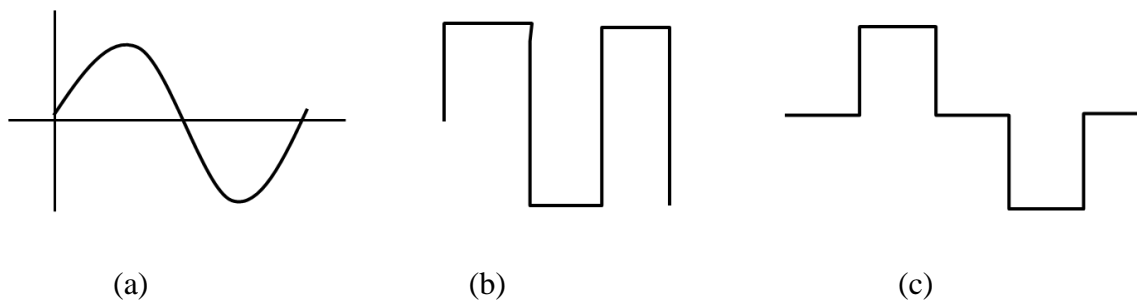


Figure 5.26. Various Waveforms: (a) Sine Wave, (b) Square Wave, and (c) Adjustable Square Wave

If FRA were to supply various waveforms such as sine, square, and adjustable square waveforms, as shown in Figure 5.26, the resonant circuit of the WPT system could also be precisely examined.

5.4. Summary

This chapter has verified that FRA results change when a different medium surrounds the WPT system. Furthermore, different transfer distances, variations in the facing area of magnetic coupling between the windings, and changes in electromagnetic parameters, such as compensating capacitors or ferrite bars on the windings resulted in dissimilarity in the FRA measurements. To enhance the performance of FRA on WPT systems, this study recommends using the input impedance and phase angle tabs in the commercial FRA software, and implementing the source supply with the option for different waveforms such as square and adjustable square wave. When the fingerprint FRA signature of the WPT system is recorded, cost-effective condition monitoring and objective asset assessment become available over time.

Chapter 6

Conclusion and Future Work

The WPT system was already introduced a century ago based on Faraday's law and Tesla's innovative experiments in the twentieth century. As the use of mobile applications and electric vehicles in public transportation (i.e., buses, high-speed trains, and ferries) increase, WPT technology has re-emerged since the 1990s. Hence, it is necessary to develop design and maintenance methods of the WPT system. This chapter describes the overall conclusion of this thesis comprehensively and suggests future works.

6.1. Conclusion

WPT systems are mainly classified into three methods: ITP, CPT, and MPT. The MPT or beam-forming applications can transfer megawatt ranges of electrical energy over a great distance. However, the applications are carefully utilised in limited places due to the HF radiation. Therefore, IPT and CPT applications, where the power transfer occurs in the electromagnetic coupling, also known as near field, have been generally adopted. In addition, ITP topology is broadly used for EV charging and applications in the middle range from a millimetre to a few metres due to its feasibility at low voltages. Hence, this research reviewed recent works and presented novel applications for the enhanced design and maintenance of IPT WPT systems. The comprehensive conclusions of the thesis are described as follows.

- A detailed circuit analysis of the two-coil SS WPT system clarified that the quality factor Q , and the coupling coefficient k_{12} impacts the performance of the WPT system sensitively. To increase the Q factor, it is essential to reduce the winding resistance of the coils. The magnetic supplements, different topologies of the system, and the intermediate coils can also enhance the strength of the magnetic coupling.

- To wirelessly transfer a significant amount of electric energy over a large distance with high efficiency, the main perspectives: design, efficiency, stability, and safety of the WPT system, need to be comprehensively considered.
- The electromagnetic simulation tool called FEKO is mainly employed to analyse the application of high-frequency telecommunication antennas. However, this thesis presented the detailed process of the WPT system design. The self and mutual inductance of the coils using ferrite materials and in different environments can be extracted through the *S*-parameter analysis. The near-field analysis using FEKO offers a precision assessment of the formation and distribution of magnetic coupling in WPT systems.
- In addition, the electrical parameters of the WPT system, input/output voltage, input impedance, phase angle of the input impedance, input/output power and efficiency, are reasonably extracted using the FEKO application.
- When the input voltage of 10 V was supplied to the transmitting unit of the prototype, the power of 5.31 W is delivered with a transfer efficiency of 97.79% according to FEKO. The actual measurements indicated 95.68% transfer efficiency. The electrical parameters indicated fair agreement with the FEKO results, with under 8.4% error.
- To enhance the design and maintenance of high-power WPT applications, this thesis introduced the novel application of FRA. A coupling unit of WPT devices consists of electrical parameters *R*, *L*, and *C*, and is considered an air-core resonance transformer. Hence, FRA can detect the actual resonance frequency, deformation of the magnetic coupling, and the change of the electrical parameters accurately.
- WPT systems perform appropriately when the Tx and Rx units are tuned at the resonance frequency. The single or multiple values of the resonance frequency exist based on the distance between the windings and the condition of the load. FRA can identify the resonance frequency, and the variation or shift of these resonant points.

- If the coils are incorrectly aligned with each other or the transfer distance varies outside of the design, FRA can determine the severity of the deviations. Therefore, the mechanical deformation of the coils or WPT construction changes between Tx and Rx are recognisable.
- The variation of electromagnetic parameters (i.e., R , L , C , and magnetic materials) or a change in the medium surrounding and between the windings will result in a different FRA response compared to the fingerprint record. This offers a cost-effective and reliable method for the maintenance of the WPT system over time.
- The frequency range of industrial FRA is between 20 Hz and 2 MHz. As the operating frequency of most inductive or capacitive power transfer devices is under 2 MHz as shown in Tables 2.2, 2.3, and 2.5, FRA can be utilised to enhance the performance of WPT system design and maintenance.
- In this study, various prototypes of WPT systems were developed and analysed. To reduce the ohmic loss of coils in HF, 1,650-filament Litz wire was used instead of the single copper wire. Also, flat spiral coils with ferrite rods were constructed to demonstrate the charging system used with EVs and AUTs. The design parameters and performance of the developed WPT systems in different topologies and environments were verified through the application of FEKO and FRA.

6.2. Future Work

It is expected that the areas using WPT applications and the size of the devices will consistently increase in parallel with the growth trend in demand for mobile devices and electric-powered transportation. Future research work is recommended as follows.

- To enhance the performance of the WPT system, it is required to conduct a further study about newly-developed materials as this becomes economically feasible.
- Magnetizable concrete can strengthen the coupling between the Tx and Rx unit without using magnetic supplemental materials. A WPT system with

magnetizable concrete is beneficial for maintenance due to its high corrosion resistance and the robust durability [187-189].

- Superconducting material can improve the efficiency of the WPT system [190]. To increase both the quality factor Q and the coupling coefficient k_{12} , the WPT system equipped with a superconductor coil, and ferromagnetic material is presented [191]. In addition, various metamaterial can be used to enhance the electromagnetic coupling [192-196], and supercapacitors can be considered for supplying a constant charging current to the variable load and the high density of power storage [25, 62].
- To analyse the electrical characteristics of the WPT system, this study suggests developing instrument devices and standards. For example, the no-load, also known as open-circuit, test over the transfer distance, and the short-circuit test can provide the characteristics of WPT devices similar to the no-load voltage across the secondary side and the leakage reactance of the transformer.
- It is also recommended to establish the criteria level of VTR and guidelines for FRA measurements of WPT systems to enable precise interpretations, like the power transformer [143, 197].
- The FRA measurements using artificial intelligence (AI) techniques can estimate the reliability or the optimised electromagnetic parameters of power devices [198]. The value of the electrical components (i.e., compensation capacitor or inductance value of the coils) can be accurately estimated when the FRA signatures are interpreted by state-of-the-art AI methods.
- In the future, the wireless power transformer and high-power wireless transmission can be considered with the advanced technology of power electronics. For example, the wireless power transformer can be light due to the absence of an iron core and oil, if the electromagnetic field between the windings is well-isolated. Also, the WPT system can be valuable for the power system interconnections between different frequencies, HVDC systems, or transformers equipped with an electronic tap changer [199-201].

References

- [1] N. Forbes and B. Mahon, *Faraday, Maxwell, and the electromagnetic field: how two men revolutionized physics*. Prometheus Books, 2014.
- [2] T. K. Sarkar, W. Dyab, and M. S. Palma, "What did Maxwell do to prove light was electromagnetic in nature and the concept of his displacement current," in *Wireless Information Technology and Systems (ICWITS), 2012 IEEE International Conference on*, 11-16 Nov. 2012, pp. 1-4, doi: 10.1109/ICWITS.2012.6417753.
- [3] N. Tesla, "System of Transmission of Electrical Energy," US Patent 645576, 20/Mar/1900, 1900.
- [4] T. N, "Apparatus for Transmitting Electrical Energy," US Patent 1,119,732, 01/Dec/1914, 1914.
- [5] N. Shinohara, "History, Present and Future of WPT," in *Wireless Power Transfer via Radiowaves*: John Wiley & Sons, Inc., 2013, pp. 1-20.
- [6] A. S. Marincic, "Nikola Tesla and the Wireless Transmission of Energy," *IEEE Transactions on Power Apparatus and Systems*, vol. PAS-101, no. 10, pp. 4064-4068, 1982, doi: 10.1109/TPAS.1982.317084.
- [7] S. D. Barman, A. W. Reza, N. Kumar, M. E. Karim, and A. B. Munir, "Wireless powering by magnetic resonant coupling: Recent trends in wireless power transfer system and its applications," *Renewable and Sustainable Energy Reviews*, vol. 51, pp. 1525-1552, 2015, doi: <http://dx.doi.org/10.1016/j.rser.2015.07.031>.
- [8] H. Ishida and H. Furukawa, "Wireless Power Transmission Through Concrete Using Circuits Resonating at Utility Frequency of 60 Hz," *IEEE Transactions on Power Electronics*, vol. 30, no. 3, pp. 1220-1229, 2015, doi: 10.1109/TPEL.2014.2322876.
- [9] N. Tesla, "High frequency oscillators for electro-therapeutic and other purposes," *Proceedings of the IEEE*, vol. 87, no. 7, p. 1282, 1898, doi: 10.1109/JPROC.1999.771079.
- [10] MarketsandMarkets. (2020) Wireless Charging for Electric Vehicle Market by Power Supply (3–<11, 11–50, & >50 KW), Application (Home & Commercial), Distribution channel (Aftermarket & OE), Component, Charging System, Propulsion, Vehicle type, & Region - Global Forecast to 2027. Available: <https://www.marketsandmarkets.com/Market-Reports/>
- [11] G. Guidi, J. A. Suul, F. Jensen, and I. Sorfornn, "Wireless Charging for Ships: High-Power Inductive Charging for Battery Electric and Plug-In Hybrid Vessels," *IEEE Electrification Magazine*, vol. 5, no. 3, pp. 22-32, 2017, doi: 10.1109/MELE.2017.2718829.

- [12] Wärtsilä, "Another world's first for Wärtsilä - wireless charging for hybrid coastal ferry successfully tested," ed, 2017.
- [13] J. H. Kim *et al.*, "Development of 1-MW Inductive Power Transfer System for a High-Speed Train," *IEEE Transactions on Industrial Electronics*, vol. 62, no. 10, pp. 6242-6250, 2015, doi: 10.1109/TIE.2015.2417122.
- [14] U. Madawala, D. Thrimawithana, and T. Mouton, "An inductive power tapping (IPT) system for HVDC lines," in *2014 IEEE 5th International Symposium on Power Electronics for Distributed Generation Systems (PEDG)*, 24-27 June 2014 2014, pp. 1-5, doi: 10.1109/PEDG.2014.6878645.
- [15] S. Stoecklin, A. Yousaf, T. Volk, and L. Reindl, "Efficient Wireless Powering of Biomedical Sensor Systems for Multichannel Brain Implants," *IEEE Transactions on Instrumentation and Measurement*, vol. 65, no. 4, pp. 754-764, 2016, doi: 10.1109/TIM.2015.2482278.
- [16] V. J. Brusamarello, Y. B. Blauth, R. d. Azambuja, I. Muller, and F. R. d. Sousa, "Power Transfer With an Inductive Link and Wireless Tuning," *IEEE Transactions on Instrumentation and Measurement*, vol. 62, no. 5, pp. 924-931, 2013, doi: 10.1109/TIM.2013.2245041.
- [17] S. Y. Choi, B. W. Gu, S. Y. Jeong, and C. T. Rim, "Advances in Wireless Power Transfer Systems for Roadway-Powered Electric Vehicles," *IEEE Journal of Emerging and Selected Topics in Power Electronics*, vol. 3, no. 1, pp. 18-36, 2015, doi: 10.1109/JESTPE.2014.2343674.
- [18] J. Dai, S. Hagen, D. C. Ludois, and I. P. Brown, "Synchronous Generator Brushless Field Excitation and Voltage Regulation via Capacitive Coupling Through Journal Bearings," *IEEE Transactions on Industry Applications*, vol. 53, no. 4, pp. 3317-3326, 2017, doi: 10.1109/TIA.2017.2681621.
- [19] Z. Bi, T. Kan, C. C. Mi, Y. Zhang, Z. Zhao, and G. A. Keoleian, "A review of wireless power transfer for electric vehicles: Prospects to enhance sustainable mobility," *Applied Energy*, vol. 179, pp. 413-425, 2016, doi: <https://doi.org/10.1016/j.apenergy.2016.07.003>.
- [20] W. Lumpkins, "Nikola Tesla's Dream Realized: Wireless power energy harvesting," *IEEE Consumer Electronics Magazine*, vol. 3, no. 1, pp. 39-42, 2014, doi: 10.1109/MCE.2013.2284940.
- [21] G. R. M. Garratt, *The Early History of Radio: from Faraday to Marconi* (IET History of Technology Series 20). London: The Institution of Engineering and Technology in association with The Science Museum, 1994.
- [22] A. W. Green and J. T. Boys, "10 kHz inductively coupled power transfer-concept and control," in *1994 Fifth International Conference on Power Electronics and Variable-Speed Drives*, 26-28 Oct 1994 1994, pp. 694-699, doi: 10.1049/cp:19941049.

- [23] A. Kurs, A. Karalis, R. Moffatt, J. D. Joannopoulos, P. Fisher, and M. Soljačić, "Wireless Power Transfer via Strongly Coupled Magnetic Resonances," *Science*, vol. 317, no. 5834, pp. 83-86, 2007, doi: 10.1126/science.1143254.
- [24] C. Park, S. Lee, G. H. Cho, and C. T. Rim, "Innovative 5-m-Off-Distance Inductive Power Transfer Systems With Optimally Shaped Dipole Coils," *IEEE Transactions on Power Electronics*, vol. 30, no. 2, pp. 817-827, 2015, doi: 10.1109/TPEL.2014.2310232.
- [25] Z. Li, C. Zhu, J. Jiang, K. Song, and G. Wei, "A 3-kW Wireless Power Transfer System for Sightseeing Car Supercapacitor Charge," *IEEE Transactions on Power Electronics*, vol. 32, no. 5, pp. 3301-3316, 2017, doi: 10.1109/TPEL.2016.2584701.
- [26] J. Dai and D. C. Ludois, "A Survey of Wireless Power Transfer and a Critical Comparison of Inductive and Capacitive Coupling for Small Gap Applications," *IEEE Transactions on Power Electronics*, vol. 30, no. 11, pp. 6017-6029, 2015, doi: 10.1109/TPEL.2015.2415253.
- [27] H. Zhang, F. Lu, H. Hofmann, and C. Mi, "An LC compensated electric field repeater for long distance capacitive power transfer," in *2016 IEEE Energy Conversion Congress and Exposition (ECCE)*, 18-22 Sept. 2016 2016, pp. 1-5, doi: 10.1109/ECCE.2016.7854858.
- [28] F. Lu, H. Zhang, H. Hofmann, and C. C. Mi, "An Inductive and Capacitive Combined Wireless Power Transfer System With LC Compensated Topology," *IEEE Transactions on Power Electronics*, vol. 31, no. 12, pp. 8471-8482, 2016, doi: 10.1109/TPEL.2016.2519903.
- [29] B. Luo, T. Long, L. Guo, R. Mai, and Z. He, "Analysis and Design of Hybrid Inductive and Capacitive Wireless Power Transfer System," in *2019 IEEE Applied Power Electronics Conference and Exposition (APEC)*, 17-21 March 2019 2019, pp. 3107-3110, doi: 10.1109/APEC.2019.8722140.
- [30] N. Tesla, "High frequency oscillators for electro-therapeutic and other purposes," *Proceedings of the IEEE*, vol. 87, no. 7, p. 1282, 1999, doi: 10.1109/JPROC.1999.771079.
- [31] J. W. Fuller, "Apparatus for Efficient Power Transfer Through a Tissue Barrier," *IEEE Transactions on Biomedical Engineering*, vol. BME-15, no. 1, pp. 63-65, 1968, doi: 10.1109/TBME.1968.4502534.
- [32] J. C. Schuder, J. H. Gold, and H. E. Stephenson, "An Inductively Coupled RF System for the Transmission of 1 kW of Power Through the Skin," *IEEE Transactions on Biomedical Engineering*, vol. BME-18, no. 4, pp. 265-273, 1971, doi: 10.1109/TBME.1971.4502849.
- [33] A. Ghahary and B. H. Cho, "Design of transcutaneous energy transmission system using a series resonant converter," *IEEE Transactions on Power Electronics*, vol. 7, no. 2, pp. 261-269, 1992, doi: 10.1109/63.136242.
- [34] J. Boys and A. Green, "Inductively Coupled Power Transmission: - Concept, Design and Application," in *Papers presented in the technical programme of the IPENZ Annual Conference*, Nelson, February 18-21 1994, vol. 2, pp. 254-259.

- [35] J. T. Boys, "Inductive power transfer across an extended gap," New Zealand Patent WO1998050993 A1 Patent Appl. PCT/NZ1998/000053, 1998.
- [36] S. Y. R. Hui, "Magnetic Resonance for Wireless Power Transfer [A Look Back]," *IEEE Power Electronics Magazine*, vol. 3, no. 1, pp. 14-31, 2016, doi: 10.1109/MPEL.2015.2510441.
- [37] D. Lee, D. Lim, and S. Jeon, "Technological and theoretical relationship between wireless power transfer technologies," *The Transactions of the Korean Institute of Electrical Engineers*, vol. 63, no. 2, pp. 245-249, 2014. [Online]. Available: <http://www.dbpia.co.kr/Article/NODE02356149>.
- [38] S. L. Ho, J. Wang, W. N. Fu, and M. Sun, "A Comparative Study Between Novel Witricity and Traditional Inductive Magnetic Coupling in Wireless Charging," *IEEE Transactions on Magnetics*, vol. 47, no. 5, pp. 1522-1525, 2011, doi: 10.1109/TMAG.2010.2091495.
- [39] A. Kamineni, G. A. Covic, and J. T. Boys, "Analysis of Coplanar Intermediate Coil Structures in Inductive Power Transfer Systems," *IEEE Transactions on Power Electronics*, vol. 30, no. 11, pp. 6141-6154, 2015, doi: 10.1109/TPEL.2014.2378733.
- [40] J. Dai and D. C. Ludois, "Capacitive Power Transfer Through a Conformal Bumper for Electric Vehicle Charging," *IEEE Journal of Emerging and Selected Topics in Power Electronics*, vol. 4, no. 3, pp. 1015-1025, 2016, doi: 10.1109/JESTPE.2015.2505622.
- [41] F. Musavi and W. Eberle, "Overview of wireless power transfer technologies for electric vehicle battery charging," *IET Power Electronics*, vol. 7, no. 1, pp. 60-66, 2014, doi: 10.1049/iet-pel.2013.0047.
- [42] T. W. Ching and Y. S. Wong, "Review of wireless charging technologies for electric vehicles," in *2013 5th International Conference on Power Electronics Systems and Applications (PESA)*, 11-13 Dec. 2013 2013, pp. 1-4, doi: 10.1109/PESA.2013.6828235.
- [43] K. V. T. Piipponen, R. Sepponen, and P. Eskelinen, "A Biosignal Instrumentation System Using Capacitive Coupling for Power and Signal Isolation," *IEEE Transactions on Biomedical Engineering*, vol. 54, no. 10, pp. 1822-1828, 2007, doi: 10.1109/TBME.2007.894830.
- [44] S. Li, Z. Liu, H. Zhao, L. Zhu, C. Shuai, and Z. Chen, "Wireless Power Transfer by Electric Field Resonance and Its Application in Dynamic Charging," *IEEE Transactions on Industrial Electronics*, vol. 63, no. 10, pp. 6602-6612, 2016, doi: 10.1109/TIE.2016.2577625.
- [45] H. Zhang, F. Lu, H. Hofmann, W. Liu, and C. Mi, "A Six-Plate Capacitive Coupler to Reduce Electric Field Emission in Large Air-Gap Capacitive Power Transfer," *IEEE Transactions on Power Electronics*, 2017, doi: 10.1109/TPEL.2017.2662583.
- [46] H. Zhang, F. Lu, H. Hofmann, W. Liu, and C. C. Mi, "An LC-Compensated Electric Field Repeater for Long-Distance Capacitive Power Transfer," *IEEE Transactions on Industry Applications*, vol. 53, no. 5, pp. 4914-4922, 2017, doi: 10.1109/TIA.2017.2697846.

- [47] J. Dai and D. C. Ludois, "Single Active Switch Power Electronics for Kilowatt Scale Capacitive Power Transfer," *IEEE Journal of Emerging and Selected Topics in Power Electronics*, vol. 3, no. 1, pp. 315-323, 2015, doi: 10.1109/JESTPE.2014.2334621.
- [48] R. H. Nansen, "Wireless power transmission: the key to solar power satellites," *IEEE Aerospace and Electronic Systems Magazine*, vol. 11, no. 1, pp. 33-39, 1996, doi: 10.1109/62.484148.
- [49] P. Jaffe and J. McSpadden, "Energy Conversion and Transmission Modules for Space Solar Power," *Proceedings of the IEEE*, vol. 101, no. 6, pp. 1424-1437, 2013, doi: 10.1109/JPROC.2013.2252591.
- [50] X. Lu, P. Wang, D. Niyato, D. I. Kim, and Z. Han, "Wireless Networks With RF Energy Harvesting: A Contemporary Survey," *IEEE Communications Surveys & Tutorials*, vol. 17, no. 2, pp. 757-789, 2015, doi: 10.1109/COMST.2014.2368999.
- [51] X. Lu, D. Niyato, P. Wang, and D. I. Kim, "Wireless charger networking for mobile devices: fundamentals, standards, and applications," *IEEE Wireless Communications*, vol. 22, no. 2, pp. 126-135, 2015, doi: 10.1109/MWC.2015.7096295.
- [52] IEA, *Global EV Outlook 2017*. IEA, 2017.
- [53] A. Bindra, "Wireless Power Transfer Is Fueling the Electric Vehicles Market [From the Editor]," *IEEE Power Electronics Magazine*, vol. 4, no. 2, pp. 4-8, 2017, doi: 10.1109/MPEL.2017.2692382.
- [54] W. C. Brown, "Experiments Involving a Microwave Beam to Power and Position a Helicopter," *IEEE Transactions on Aerospace and Electronic Systems*, vol. AES-5, no. 5, pp. 692-702, 1969, doi: 10.1109/TAES.1969.309867.
- [55] M. Budhia, J. T. Boys, G. A. Covic, and C. Y. Huang, "Development of a Single-Sided Flux Magnetic Coupler for Electric Vehicle IPT Charging Systems," *IEEE Transactions on Industrial Electronics*, vol. 60, no. 1, pp. 318-328, 2013, doi: 10.1109/TIE.2011.2179274.
- [56] U. Foresight, *50 Big Ideas Shaping the Future of Electric Mobility*. Urban Foresight, 2014.
- [57] Z. Huang, S. C. Wong, and C. K. Tse, "Design of a Single-Stage Inductive-Power-Transfer Converter for Efficient EV Battery Charging," *IEEE Transactions on Vehicular Technology*, vol. 66, no. 7, pp. 5808-5821, 2017, doi: 10.1109/TVT.2016.2631596.
- [58] T. Kan, F. Lu, T. Nguyen, P. P. Mercier, and C. C. Mi, "Integrated Coil Design for EV Wireless Charging Systems Using LCC Compensation Topology," *IEEE Transactions on Power Electronics*, vol. 33, no. 11, pp. 9231-9241, 2018, doi: 10.1109/TPEL.2018.2794448.
- [59] A. Tejada, S. Kim, F. Y. Lin, G. A. Covic, and J. T. Boys, "A Hybrid Solenoid Coupler for Wireless Charging Applications," *IEEE Transactions on Power Electronics*, vol. 34, no. 6, pp. 5632-5645, 2019, doi: 10.1109/TPEL.2018.2867430.

- [60] Y. Song, U. K. Madawala, D. J. Thrimawithana, and M. Vilathgamuwa, "Three-phase bi-directional wireless EV charging system with high tolerance to pad misalignment," *IET Power Electronics*, vol. 12, no. 10, pp. 2697-2705, 2019, doi: 10.1049/iet-pe.2018.6279.
- [61] N. Khan, H. Matsumoto, and O. Trescases, "Wireless Electric Vehicle Charger With Electromagnetic Coil-Based Position Correction Using Impedance and Resonant Frequency Detection," *IEEE Transactions on Power Electronics*, vol. 35, no. 8, pp. 7873-7883, 2020, doi: 10.1109/TPEL.2020.2965476.
- [62] Y. Geng, Z. Yang, and F. Lin, "Design and Control for Catenary Charged Light Rail Vehicle Based on Wireless Power Transfer and Hybrid Energy Storage System," *IEEE Transactions on Power Electronics*, vol. 35, no. 8, pp. 7894-7903, 2020, doi: 10.1109/TPEL.2020.2966218.
- [63] F. Lu, H. Zhang, H. Hofmann, and C. Mi, "A Double-Sided LCLC Compensated Capacitive Power Transfer System for Electric Vehicle Charging," *IEEE Transactions on Power Electronics*, vol. 30, no. 11, pp. 6011-6014, 2015, doi: 10.1109/TPEL.2015.2446891.
- [64] V. Vu, M. Dahidah, V. Pickert, and V. Phan, "An Improved LCL-L Compensation Topology for Capacitive Power Transfer in Electric Vehicle Charging," *IEEE Access*, vol. 8, pp. 27757-27768, 2020, doi: 10.1109/ACCESS.2020.2971961.
- [65] F. Lu, H. Zhang, H. Hofmann, and C. C. Mi, "An Inductive and Capacitive Integrated Coupler and Its LCL Compensation Circuit Design for Wireless Power Transfer," *IEEE Transactions on Industry Applications*, vol. 53, no. 5, pp. 4903-4913, 2017, doi: 10.1109/TIA.2017.2697838.
- [66] B. Luo, T. Long, L. Guo, R. Dai, R. Mai, and Z. He, "Analysis and Design of Inductive and Capacitive Hybrid Wireless Power Transfer System for Railway Application," *IEEE Transactions on Industry Applications*, vol. 56, no. 3, pp. 3034-3042, 2020, doi: 10.1109/TIA.2020.2979110.
- [67] N. Shinohara and N. Shinohara, "Applications of WPT," in *Wireless Power Transfer via Radiowaves*: John Wiley & Sons, Inc., 2013, pp. 143-211.
- [68] N. Shinohara, Y. Kubo, and H. Tonomura, "Wireless charging for electric vehicle with microwaves," in *2013 3rd International Electric Drives Production Conference (EDPC)*, 29-30 Oct. 2013 2013, pp. 1-4, doi: 10.1109/EDPC.2013.6689750.
- [69] H. Tonomura, J. Miyakoshi, and N. Shinohara, "Researches of microwave safety issue of wireless power transfer technology for commercial vehicles," in *2015 9th European Conference on Antennas and Propagation (EuCAP)*, 13-17 May 2015 2015, pp. 1-4.
- [70] J. Jung and W. Han, "A study on the trends and standards of WPT charging for EVs," (in 한국어), *The Korean Institute of Electrical Engineers*, vol. 64, no. 4, pp. 18-23, 4 2015. [Online]. Available: <http://www.dbpia.co.kr/Article/NODE06263594>.

- [71] R. S. McEwen, B. W. Hobson, L. McBride, and J. G. Bellingham, "Docking Control System for a 54-cm-Diameter (21-in) AUV," *IEEE Journal of Oceanic Engineering*, vol. 33, no. 4, pp. 550-562, 2008, doi: 10.1109/JOE.2008.2005348.
- [72] J.-g. Shi, D.-j. Li, and C.-j. Yang, "Design and analysis of an underwater inductive coupling power transfer system for autonomous underwater vehicle docking applications," *Computers & Electronics*, vol. 15, no. 1, pp. 51-62, 2014, doi: 10.1631/jzus.C1300171.
- [73] T. McGinnis, C. P. Henze, and K. Conroy, "Inductive Power System for Autonomous Underwater Vehicles," ed, 2007, pp. 1-5.
- [74] Z.-s. Li, D.-j. Li, L. Lin, and Y. Chen, "Design considerations for electromagnetic couplers in contactless power transmission systems for deep-sea applications," *Computers & Electronics*, vol. 11, no. 10, pp. 824-834, 2010, doi: 10.1631/jzus.C0910711.
- [75] S. Yoshida *et al.*, "Underwater wireless power transfer for non-fixed unmanned underwater vehicle in the ocean," in *2016 IEEE/OES Autonomous Underwater Vehicles (AUV)*, 6-9 Nov. 2016 2016, pp. 177-180, doi: 10.1109/AUV.2016.7778668.
- [76] W. Niu, W. Gu, and J. Chu, "Analysis and experimental results of frequency splitting of underwater wireless power transfer," *The Journal of Engineering*, vol. 2017, no. 7, pp. 385-390, 2017, doi: 10.1049/joe.2017.0194.
- [77] T. Kan, R. Mai, P. P. Mercier, and C. Mi, "Design and Analysis of a Three-Phase Wireless Charging System for Lightweight Autonomous Underwater Vehicles," *IEEE Trans. Power Electron.*, vol. 33, no. 8, pp. 6622-6632, 2018, doi: 10.1109/TPEL.2017.2757015.
- [78] Z. Yan *et al.*, "Frequency Optimization of a Loosely Coupled Underwater Wireless Power Transfer System Considering Eddy Current Loss," *IEEE Transactions on Industrial Electronics*, vol. 66, no. 5, pp. 3468-3476, 2019, doi: 10.1109/TIE.2018.2851947.
- [79] C. Cai, Y. Zhang, S. Wu, J. Liu, Z. Zhang, and L. Jiang, "A Circumferential Coupled Dipole-Coil Magnetic Coupler for Autonomous Underwater Vehicles Wireless Charging Applications," *IEEE Access*, vol. 8, pp. 65432-65442, 2020, doi: 10.1109/ACCESS.2020.2984530.
- [80] T. a. Orekan, *Underwater wireless power transfer : smart ocean energy converters / Taofeek Orekan, Peng Zhang*. Cham, Switserzland : Springer International Publishing : Imprint: Springer, 2019.
- [81] Y. Kawamura and M. Shoyama, "Wireless power transmission using LC cancellation," in *ECCE Asia Downunder (ECCE Asia), 2013 IEEE*, 3-6 June 2013 2013, pp. 1041-1045, doi: 10.1109/ECCE-Asia.2013.6579236.
- [82] R. Narayanan, "Advances in Wireless Power Coils: The key element in a wireless power charging system," *IEEE Power Electronics Magazine*, vol. 2, no. 4, pp. 40-46, 2015, doi: 10.1109/MPEL.2015.2485358.

- [83] Q. Deng *et al.*, "Frequency-Dependent Resistance of Litz-Wire Square Solenoid Coils and Quality Factor Optimization for Wireless Power Transfer," *IEEE Transactions on Industrial Electronics*, vol. 63, no. 5, pp. 2825-2837, 2016, doi: 10.1109/TIE.2016.2518126.
- [84] I. S. Jeong, B. I. Jung, D. S. You, and H. S. Choi, "Analysis of S-Parameters in Magnetic Resonance WPT Using Superconducting Coils," *IEEE Transactions on Applied Superconductivity*, vol. 26, no. 3, pp. 1-4, 2016, doi: 10.1109/TASC.2016.2544139.
- [85] J. F. Zhao, X. L. Huang, and W. Wang, "Efficiency analysis of magnetic resonance wireless power transfer with three-dimensional transmitters," *Journal of Applied Physics*, vol. 117, no. 17, p. 17B516, 2015, doi: <http://dx.doi.org/10.1063/1.4914360>.
- [86] W. X. Zhong, C. K. Lee, and S. Y. Hui, "Wireless power domino-resonator systems with noncoaxial axes and circular structures," *IEEE Transactions on Power Electronics*, vol. 27, no. 11, pp. 4750-4762, 2012, doi: 10.1109/TPEL.2011.2174655.
- [87] Z. N. Low, R. A. Chinga, R. Tseng, and J. Lin, "Design and Test of a High-Power High-Efficiency Loosely Coupled Planar Wireless Power Transfer System," *IEEE Transactions on Industrial Electronics*, vol. 56, no. 5, pp. 1801-1812, 2009, doi: 10.1109/TIE.2008.2010110.
- [88] S. Liu, M. Liu, S. Yang, C. Ma, and X. Zhu, "A Novel Design Methodology for High-Efficiency Current-Mode and Voltage-Mode Class-E Power Amplifiers in Wireless Power Transfer systems," *IEEE Transactions on Power Electronics*, vol. 32, no. 6, pp. 4514-4523, 2017, doi: 10.1109/TPEL.2016.2600268.
- [89] J. Kim, D. H. Kim, and Y. J. Park, "Analysis of Capacitive Impedance Matching Networks for Simultaneous Wireless Power Transfer to Multiple Devices," *IEEE Transactions on Industrial Electronics*, vol. 62, no. 5, pp. 2807-2813, 2015, doi: 10.1109/TIE.2014.2365751.
- [90] J. C. McLaughlin and K. L. Kaiser, "Deglorifying the Maximum Power Transfer Theorem and Factors in Impedance Selection," *IEEE Transactions on Education*, vol. 50, no. 3, pp. 251-255, 2007, doi: 10.1109/TE.2007.900030.
- [91] K. E. Koh, T. C. Beh, T. Imura, and Y. Hori, "Impedance Matching and Power Division Using Impedance Inverter for Wireless Power Transfer via Magnetic Resonant Coupling," *IEEE Transactions on Industry Applications*, vol. 50, no. 3, pp. 2061-2070, 2014, doi: 10.1109/TIA.2013.2287310.
- [92] A. P. Sample, D. T. Meyer, and J. R. Smith, "Analysis, Experimental Results, and Range Adaptation of Magnetically Coupled Resonators for Wireless Power Transfer," *IEEE Transactions on Industrial Electronics*, vol. 58, no. 2, pp. 544-554, 2011, doi: 10.1109/TIE.2010.2046002.
- [93] Y. L. Lyu *et al.*, "A Method of Using Nonidentical Resonant Coils for Frequency Splitting Elimination in Wireless Power Transfer," *IEEE Transactions on Power Electronics*, vol. 30, no. 11, pp. 6097-6107, 2015, doi: 10.1109/TPEL.2014.2387835.

- [94] D. Ahn and S. Hong, "A Study on Magnetic Field Repeater in Wireless Power Transfer," *IEEE Transactions on Industrial Electronics*, vol. 60, no. 1, pp. 360-371, 2013, doi: 10.1109/TIE.2012.2188254.
- [95] S. Huang, Z. Li, and K. Lu, "Frequency splitting suppression method for four-coil wireless power transfer system," *IET Power Electronics*, vol. 9, no. 15, pp. 2859-2864, 2016, doi: 10.1049/iet-pel.2015.0376.
- [96] W. X. Zhong, C. Zhang, X. Liu, and S. Y. R. Hui, "A Methodology for Making a Three-Coil Wireless Power Transfer System More Energy Efficient Than a Two-Coil Counterpart for Extended Transfer Distance," *IEEE Transactions on Power Electronics*, vol. 30, no. 2, pp. 933-942, 2015, doi: 10.1109/TPEL.2014.2312020.
- [97] B. L. Cannon, J. F. Hoburg, D. D. Stancil, and S. C. Goldstein, "Magnetic Resonant Coupling As a Potential Means for Wireless Power Transfer to Multiple Small Receivers," *IEEE Transactions on Power Electronics*, vol. 24, no. 7, pp. 1819-1825, 2009, doi: 10.1109/TPEL.2009.2017195.
- [98] Z. N. Low, J. J. Casanova, P. H. Maier, J. A. Taylor, R. A. Chinga, and J. Lin, "Method of Load/Fault Detection for Loosely Coupled Planar Wireless Power Transfer System With Power Delivery Tracking," *IEEE Transactions on Industrial Electronics*, vol. 57, no. 4, pp. 1478-1486, 2010, doi: 10.1109/TIE.2009.2030821.
- [99] W. Chwei-Sen, G. A. Covic, and O. H. Stielau, "Power transfer capability and bifurcation phenomena of loosely coupled inductive power transfer systems," *IEEE Transactions on Industrial Electronics*, vol. 51, no. 1, pp. 148-157, 2004, doi: 10.1109/TIE.2003.822038.
- [100] Y. H. Sohn, B. H. Choi, E. S. Lee, G. C. Lim, G. H. Cho, and C. T. Rim, "General Unified Analyses of Two-Capacitor Inductive Power Transfer Systems: Equivalence of Current-Source SS and SP Compensations," *IEEE Transactions on Power Electronics*, vol. 30, no. 11, pp. 6030-6045, 2015, doi: 10.1109/TPEL.2015.2409734.
- [101] V. Shevchenko, O. Husev, R. Strzelecki, B. Pakhaliuk, N. Poliakov, and N. Strzelecka, "Compensation Topologies in IPT Systems: Standards, Requirements, Classification, Analysis, Comparison and Application," *IEEE Access*, vol. 7, pp. 120559-120580, 2019, doi: 10.1109/ACCESS.2019.2937891.
- [102] K. N. Mude and K. Aditya, "Comprehensive review and analysis of two-element resonant compensation topologies for wireless inductive power transfer systems," *Chinese Journal of Electrical Engineering*, vol. 5, no. 2, pp. 14-31, 2019, doi: 10.23919/CJEE.2019.000008.
- [103] G. Monti *et al.*, "Wireless power transfer between one transmitter and two receivers: optimal analytical solution," *Wireless Power Transfer*, vol. 3, no. 1, pp. 63-73, 2016, doi: 10.1017/wpt.2016.3.
- [104] M. Koohestani, M. Zhadobov, and M. Ettore, "Design Methodology of a Printed WPT System for HF-Band Mid-Range Applications Considering Human Safety Regulations,"

- IEEE Transactions on Microwave Theory and Techniques*, vol. 65, no. 1, pp. 270-279, 2017, doi: 10.1109/TMTT.2016.2609931.
- [105] J. C. Lin, "Wireless Power Transfer for Mobile Applications, and Health Effects [Telecommunications Health and Safety]," *IEEE Antennas and Propagation Magazine*, vol. 55, no. 2, pp. 250-253, 2013, doi: 10.1109/MAP.2013.6529362.
- [106] Y. Jung, J. Choi, H. Gu, H. Son, and J. Yun, *Wireless Power Transmission Theory and Practice*. Korean: Hongrung (in Korean), 2014, p. 297.
- [107] S. Park, "Evaluation of Electromagnetic Exposure During 85 kHz Wireless Power Transfer for Electric Vehicles," *IEEE Transactions on Magnetics*, vol. 54, no. 1, pp. 1-8, 2018, doi: 10.1109/TMAG.2017.2748498.
- [108] R. Huang, B. Zhang, D. Qiu, and Y. Zhang, "Frequency Splitting Phenomena of Magnetic Resonant Coupling Wireless Power Transfer," *IEEE Transactions on Magnetics*, vol. 50, no. 11, pp. 1-4, 2014, doi: 10.1109/TMAG.2014.2331143.
- [109] W. Niu, W. Gu, J. Chu, and A. Shen, "Frequency splitting patterns in wireless power relay transfer," *IET Circuits, Devices & Systems*, vol. 8, no. 6, pp. 561-567, 2014, doi: 10.1049/iet-cds.2013.0440.
- [110] International Commission on Non-Ionizing Radiation Protection, "Guidelines for Limiting Exposure to Time-varying Electric and Magnetic Fields (1 Hz to 100 kHz)," *Health Physics*, vol. 99, no. 6, pp. 818-836, 2010. [Online]. Available: <http://link.lis.curtin.edu.au/cgi-bin/ezproxy/ezpgateway.cgi?url=http://ovidsp.ovid.com/ovidweb.cgi?T=JS&CSC=Y&NEWS=N&PAGE=fulltext&D=ovftl&AN=00004032-201012000-00026>.
- [111] S. Park, "Market Prospect of Wireless Power Transfer Market," (in Korean), *Korea Telecommunications Technology Association*, vol. 138, pp. 40-44, 2011.
- [112] M. Young-Jin and Y. Changsik, "Development of Wireless Power Transceiver with Bi-directional DC-DC Converter," (in Korean), *Journal of the Institute of Electronics and Information Engineers*, vol. 51, no. 7, pp. 111-121, 7 2014. [Online]. Available: <http://www.dbpia.co.kr/Article/NODE02450061>.
- [113] International Commission on Non-Ionizing Radiation Protection, "Guidelines for Limiting Exposure to Time-varying Electric and Magnetic Fields (up to 300 GHz)," *Health Physics*, vol. 74, no. 4, pp. 494-522, 1998.
- [114] C. B. Park, B. S. Lee, and S. G. Lee, "Analysis of Technology Trend on High Capability of WPT for Railway," (in 한국어), *The Korean Institute of Electrical Engineers*, vol. 63, pp. 35-42, 2014. [Online]. Available: <http://www.dbpia.co.kr/Article/NODE02482282>.
- [115] X. Li, C. Y. Tsui, and W. H. Ki, "A 13.56 MHz Wireless Power Transfer System With Reconfigurable Resonant Regulating Rectifier and Wireless Power Control for Implantable Medical Devices," *IEEE Journal of Solid-State Circuits*, vol. 50, no. 4, pp. 978-989, 2015, doi: 10.1109/JSSC.2014.2387832.

- [116] J. Moon, H. Hwang, B. Jo, H. A. Shin, and S. W. Kim, "Design of a 5-W power receiver for 6.78 MHz resonant wireless power transfer system with power supply switching circuit," *IEEE Transactions on Consumer Electronics*, vol. 62, no. 4, pp. 349-354, 2016, doi: 10.1109/TCE.2016.7838086.
- [117] Y. Yan, W. Shi, and X. Zhang, "Design of UAV wireless power transmission system based on coupling coil structure optimization," *EURASIP Journal on Wireless Communications and Networking*, vol. 2020, no. 1, 2020, doi: 10.1186/s13638-020-01679-4.
- [118] L. Wang, J. Li, H. Nie, J. Liu, and S. Ke, "Coaxial Nested Couplers-Based Offset-Tolerance Rotary Wireless Power Transfer Systems for Electric Excitation Motors," *IEEE Access*, vol. 8, pp. 44913-44923, 2020, doi: 10.1109/ACCESS.2020.2978130.
- [119] *FEKO Computational Electromagnetics Software*. [Online]. Available: <http://www.altairhyperworks.com/product/FEKO>
- [120] U. Jakobus, M. Bingle, M. Schoeman, J. J. V. Tonder, and F. Illenseer, "Tailoring FEKO for microwave problems," *IEEE Microwave Magazine*, vol. 9, no. 6, pp. 76-85, 2008, doi: 10.1109/MMM.2008.929557.
- [121] S. Clarke and U. Jakobus, "Dielectric material modeling in the MoM-based code FEKO," *IEEE Antennas and Propagation Magazine*, vol. 47, no. 5, pp. 140-147, 2005, doi: 10.1109/MAP.2005.1599186.
- [122] S. Chai, L. Guo, K. Li, and L. Li, "Combining CS With FEKO for Fast Target Characteristic Acquisition," *IEEE Transactions on Antennas and Propagation*, vol. 66, no. 5, pp. 2494-2504, 2018, doi: 10.1109/TAP.2018.2816599.
- [123] I. Yoon and H. Ling, "Investigation of Near-Field Wireless Power Transfer in the Presence of Lossy Dielectric Materials," *IEEE Transactions on Antennas and Propagation*, vol. 61, no. 1, pp. 482-488, 2013, doi: 10.1109/TAP.2012.2215296.
- [124] J. Moshfegh, M. Shahabadi, and J. Rashed-Mohassel, "Conditions of maximum efficiency for wireless power transfer between two helical wires," *IET Microwaves, Antennas & Propagation*, vol. 5, no. 5, pp. 545-550, 2011, doi: 10.1049/iet-map.2010.0134.
- [125] D. Kim, A. Abu-Siada, and A. Sutinjo, "State-of-the-art literature review of WPT: Current limitations and solutions on IPT," *Electric Power Systems Research*, vol. 154, pp. 493-502, 2018, doi: <https://doi.org/10.1016/j.epsr.2017.09.018>.
- [126] D. Kim, A. Abu-Siada, and A. Sutinjo, "A novel application of frequency response analysis for wireless power transfer system," in *2017 Australasian Universities Power Engineering Conference (AUPEC)*, 19-22 Nov. 2017 2017, pp. 1-6, doi: 10.1109/AUPEC.2017.8282474.
- [127] A. Capozzoli, O. Kilic, C. Curcio, and A. Liseno, "The Success of GPU Computing in Applied Electromagnetics," *The Applied Computational Electromagnetics Society*, vol. 33, 2018.

- [128] A. Z. a. Elsherbeni, *Antenna analysis and design using FEKO electromagnetic simulation software* / Atef Z. Elsherbeni, Payam Nayeri and C. J. Reddy. Edison, New Jersey : Scitech Publishing, 2014.
- [129] M. Márton, L. Ovseník, and M. Spes, "DESIGN OF ANTENNA IN PROGRAM ENVIRONMENT FEKO," (in English), *Annals of the Faculty of Engineering Hunedoara*, vol. 15, no. 1, pp. 169-174, Feb 2017
- [130] S. Y. R. Hui, W. Zhong, and C. K. Lee, "A Critical Review of Recent Progress in Mid-Range Wireless Power Transfer," *IEEE Transactions on Power Electronics*, vol. 29, no. 9, pp. 4500-4511, 2014, doi: 10.1109/TPEL.2013.2249670.
- [131] X. Lu, P. Wang, D. Niyato, D. I. Kim, and Z. Han, "Wireless Charging Technologies: Fundamentals, Standards, and Network Applications," *IEEE Communications Surveys & Tutorials*, vol. 18, no. 2, pp. 1413-1452, 2016, doi: 10.1109/COMST.2015.2499783.
- [132] G. A. Covic and J. T. Boys, "Modern Trends in Inductive Power Transfer for Transportation Applications," *IEEE Journal of Emerging and Selected Topics in Power Electronics*, vol. 1, no. 1, pp. 28-41, 2013, doi: 10.1109/JESTPE.2013.2264473.
- [133] N. Hashemnia, A. Abu-Siada, and S. Islam, "Improved power transformer winding fault detection using FRA diagnostics part 1: axial displacement simulation," *IEEE Transactions on Dielectrics and Electrical Insulation*, vol. 22, no. 1, pp. 556-563, 2015, doi: 10.1109/TDEI.2014.004591.
- [134] N. Hashemnia, A. Abu-Siada, and S. Islam, "Improved power transformer winding fault detection using FRA diagnostics part 2: radial deformation simulation," *IEEE Transactions on Dielectrics and Electrical Insulation*, vol. 22, no. 1, pp. 564-570, 2015, doi: 10.1109/TDEI.2014.004592.
- [135] H. Akcay, S. M. Islam, and B. Ninness, "Subspace-based identification of power transformer models from frequency response data," *IEEE Transactions on Instrumentation and Measurement*, vol. 48, no. 3, pp. 700-704, 1999, doi: 10.1109/19.772199.
- [136] P. T. M. Vaessen and E. Hanique, "A new frequency response analysis method for power transformers," *IEEE Transactions on Power Delivery*, vol. 7, no. 1, pp. 384-391, 1992, doi: 10.1109/61.108932.
- [137] E. P. Dick and C. C. Erven, "Transformer Diagnostic Testing by Frequency Response Analysis," *IEEE Transactions on Power Apparatus and Systems*, vol. PAS-97, no. 6, pp. 2144-2153, 1978, doi: 10.1109/TPAS.1978.354718.
- [138] R. Malewski and B. Poulin, "Impulse testing of power transformers using the transfer function method," *IEEE Transactions on Power Delivery*, vol. 3, no. 2, pp. 476-489, 1988, doi: 10.1109/61.4283.
- [139] N. Hashemnia, A. Abu-Siada, and S. Islam, "Detection of power transformer bushing faults and oil degradation using frequency response analysis," *IEEE Transactions on*

- Dielectrics and Electrical Insulation*, vol. 23, no. 1, pp. 222-229, 2016, doi: 10.1109/TDEI.2015.005032.
- [140] O. Aljohani and A. Abu-Siada, "Application of digital image processing to detect transformer bushing faults and oil degradation using FRA polar plot signature," *IEEE Transactions on Dielectrics and Electrical Insulation*, vol. 24, no. 1, pp. 428-436, 2017, doi: 10.1109/TDEI.2016.006088.
- [141] M. A. Abou-Khousa, M. A. Baumgartner, S. Kharkovsky, and R. Zoughi, "Novel and Simple High-Frequency Single-Port Vector Network Analyzer," *IEEE Transactions on Instrumentation and Measurement*, vol. 59, no. 3, pp. 534-542, 2010, doi: 10.1109/TIM.2009.2024701.
- [142] A. Holdyk, B. Gustavsen, I. Arana, and J. Holboell, "Wideband Modeling of Power Transformers Using Commercial sFRA Equipment," *IEEE Transactions on Power Delivery*, vol. 29, no. 3, pp. 1446-1453, 2014, doi: 10.1109/TPWRD.2014.2303174.
- [143] "IEEE Guide for the Application and Interpretation of Frequency Response Analysis for Oil-Immersed Transformers," *IEEE Std C57.149-2012*, pp. 1-72, 2013, doi: 10.1109/IEEESTD.2013.6475950.
- [144] D. Engineering. *Sweep Frequency Response Analyzer User Guide*, 72A-2570-01 ed., 2015.
- [145] "2_1_Lumped_Element_Circuit_Distributed_Model_package."
- [146] D. A. Frickey, "Conversions between S, Z, Y, H, ABCD, and T parameters which are valid for complex source and load impedances," *IEEE Transactions on Microwave Theory and Techniques*, vol. 42, no. 2, pp. 205-211, 1994, doi: 10.1109/22.275248.
- [147] M. F. M. Yousof, C. Ekanayake, and T. K. Saha, "Examining the ageing of transformer insulation using FRA and FDS techniques," *IEEE Transactions on Dielectrics and Electrical Insulation*, vol. 22, no. 2, pp. 1258-1265, 2015, doi: 10.1109/TDEI.2015.7076829.
- [148] M. Abou Houran, X. Yang, and W. Chen, "Magnetically Coupled Resonance WPT: Review of Compensation Topologies, Resonator Structures with Misalignment, and EMI Diagnostics," *Electronics*, vol. 7, no. 11, p. 296, 2018. [Online]. Available: <https://www.mdpi.com/2079-9292/7/11/296>.
- [149] X. Liu, C. Xia, and X. Yuan, "Study of the Circular Flat Spiral Coil Structure Effect on Wireless Power Transfer System Performance," *Energies*, vol. 11, no. 11, p. 2875, 2018. [Online]. Available: <http://www.mdpi.com/1996-1073/11/11/2875>.
- [150] S. Park, "Evaluation of Electromagnetic Exposure During 85 kHz Wireless Power Transfer for Electric Vehicles," *IEEE Transactions on Magnetics*, vol. PP, no. 99, pp. 1-1, 2017, doi: 10.1109/TMAG.2017.2748498.

- [151] C. Zheng *et al.*, "High-Efficiency Contactless Power Transfer System for Electric Vehicle Battery Charging Application," *IEEE Journal of Emerging and Selected Topics in Power Electronics*, vol. 3, no. 1, pp. 65-74, 2015, doi: 10.1109/JESTPE.2014.2339279.
- [152] P. Machura and Q. Li, "A critical review on wireless charging for electric vehicles," *Renewable and Sustainable Energy Reviews*, vol. 104, pp. 209-234, 2019/04/01/ 2019, doi: <https://doi.org/10.1016/j.rser.2019.01.027>.
- [153] *IEC 61980-1:2015 Electric vehicle wireless power transfer (WPT) systems*, 2015.
- [154] J. T. Boys and G. A. Covic, "The Inductive Power Transfer Story at the University of Auckland," *IEEE Circuits and Systems Magazine*, vol. 15, no. 2, pp. 6-27, 2015, doi: 10.1109/MCAS.2015.2418972.
- [155] J. Hu *et al.*, "Hybrid Energy Storage System of an Electric Scooter Based on Wireless Power Transfer," *IEEE Transactions on Industrial Informatics*, vol. 14, no. 9, pp. 4169-4178, 2018, doi: 10.1109/TII.2018.2806917.
- [156] Y. B. Jeon, "Trend of Operating Frequency for EV Wireless Charging," *Telecommunications Technology Association ICT Standard Weekly (Korean)*, no. 24, 2020. [Online]. Available: http://www.tta.or.kr/data/weekly_view.jsp?news_id=6709.
- [157] D. Kim, A. Abu-Siada, and A. T. Sutinjo, "Application of FRA to Improve the Design and Maintenance of Wireless Power Transfer Systems," *IEEE Transactions on Instrumentation and Measurement*, vol. 68, no. 11, pp. 4313-4325, 2019, doi: 10.1109/TIM.2018.2889360.
- [158] M. Kim, J. W. Lee, and B. Lee, "Practical Bifurcation Criteria considering Inductive Power Pad Losses in Wireless Power Transfer Systems," *J. Electr. Eng. Technol.*, vol. 12, no. 1, pp. 173-181, 2017, doi: 10.5370/JEET.2017.12.1.173.
- [159] C. Jiang, K. Chau, C. Liu, and C. Lee, "An Overview of Resonant Circuits for Wireless Power Transfer," *Energies*, vol. 10, no. 7, p. 894, 2017, doi: 10.3390/en10070894.
- [160] A. J. Moradewicz and M. P. Kazmierkowski, "Contactless Energy Transfer System With FPGA-Controlled Resonant Converter," *IEEE Transactions on Industrial Electronics*, vol. 57, no. 9, pp. 3181-3190, 2010, doi: 10.1109/TIE.2010.2051395.
- [161] C. S. Kong, "A general maximum power transfer theorem," *IEEE Transactions on Education*, vol. 38, no. 3, pp. 296-298, 1995, doi: 10.1109/13.406510.
- [162] V. Marché. "Contactless Energy Transfer Systems Finite Elements Modeling with Flux." <https://insider.altairhyperworks.com/flux-finite-elements-modeling-optimize-contactless-energy-transfer-systems-efficiency/> (accessed).
- [163] H. Hong, D. Yang, and S. Won, "The Analysis for Selecting Compensating Capacitances of Two-Coil Resonant Wireless Power Transfer System," in *2017 IEEE International Conference on Energy Internet (ICEI)*, 17-21 April 2017 2017, pp. 220-225, doi: 10.1109/ICEI.2017.46.

- [164] S. C. Tang, S. Y. Hui, and C. Henry Shu-Hung, "Coreless planar printed-circuit-board (PCB) transformers-a fundamental concept for signal and energy transfer," *IEEE Transactions on Power Electronics*, vol. 15, no. 5, pp. 931-941, 2000, doi: 10.1109/63.867683.
- [165] D. Kim, J. Kim, and Y. Park, "Optimization and Design of Small Circular Coils in a Magnetically Coupled Wireless Power Transfer System in the Megahertz Frequency," *IEEE Transactions on Microwave Theory and Techniques*, vol. 64, no. 8, pp. 2652-2663, 2016, doi: 10.1109/TMTT.2016.2582874.
- [166] M. Borage, K. V. Nagesh, M. S. Bhatia, and S. Tiwari, "Design of LCL-T Resonant Converter Including the Effect of Transformer Winding Capacitance," *IEEE Transactions on Industrial Electronics*, vol. 56, no. 5, pp. 1420-1427, 2009, doi: 10.1109/TIE.2009.2012417.
- [167] C. Carretero, "Coupling Power Losses in Inductive Power Transfer Systems With Litz-Wire Coils," *IEEE Transactions on Industrial Electronics*, vol. 64, no. 6, pp. 4474-4482, 2017, doi: 10.1109/TIE.2017.2668988.
- [168] N. E. W. Technologies. "Round Litz-wire data table." http://www.litzwire.com/nepdfs/Round_Litz_Catalog.pdf (accessed).
- [169] J. Hou, Q. Chen, S. C. Wong, C. K. Tse, and X. Ruan, "Analysis and Control of Series/Series-Parallel Compensated Resonant Converter for Contactless Power Transfer," *IEEE Journal of Emerging and Selected Topics in Power Electronics*, vol. 3, no. 1, pp. 124-136, 2015, doi: 10.1109/JESTPE.2014.2336811.
- [170] W. Chwei-Sen, G. A. Covic, and O. H. Stielau, "Investigating an LCL load resonant inverter for inductive power transfer applications," *IEEE Transactions on Power Electronics*, vol. 19, no. 4, pp. 995-1002, 2004, doi: 10.1109/TPEL.2004.830098.
- [171] N. A. Keeling, G. A. Covic, and J. T. Boys, "A Unity-Power-Factor IPT Pickup for High-Power Applications," *IEEE Transactions on Industrial Electronics*, vol. 57, no. 2, pp. 744-751, 2010, doi: 10.1109/TIE.2009.2027255.
- [172] S. A. Ryder, "Diagnosing transformer faults using frequency response analysis," *IEEE Electrical Insulation Magazine*, vol. 19, no. 2, pp. 16-22, 2003, doi: 10.1109/MEI.2003.1192032.
- [173] H. M. Hashemian, "State-of-the-Art Predictive Maintenance Techniques," *IEEE Transactions on Instrumentation and Measurement*, vol. 60, no. 1, pp. 226-236, 2011, doi: 10.1109/TIM.2010.2047662.
- [174] Y. Su, C. Tang, S. Wu, and Y. Sun, "Research of LCL Resonant Inverter in Wireless Power Transfer System," in *2006 International Conference on Power System Technology*, 22-26 Oct. 2006 2006, pp. 1-6, doi: 10.1109/ICPST.2006.321550.
- [175] Y. Yao, Y. Wang, X. Liu, F. Lin, and D. G. Xu, "A Novel Parameter Tuning Method for Double-sided LCL Compensated WPT System with Better Comprehensive

- Performance," *IEEE Transactions on Power Electronics*, vol. PP, no. 99, pp. 1-1, 2017, doi: 10.1109/TPEL.2017.2778255.
- [176] S. Samanta, A. K. Rathore, and S. K. Sahoo, "Current-fed full-bridge and half-bridge topologies with CCL transmitter and LC receiver tanks for wireless inductive power transfer application," in *2016 IEEE Region 10 Conference (TENCON)*, 22-25 Nov. 2016 2016, pp. 756-761, doi: 10.1109/TENCON.2016.7848105.
- [177] H. Hao, G. A. Covic, and J. T. Boys, "A Parallel Topology for Inductive Power Transfer Power Supplies," *IEEE Transactions on Power Electronics*, vol. 29, no. 3, pp. 1140-1151, 2014, doi: 10.1109/TPEL.2013.2262714.
- [178] S. Cheon, Y. H. Kim, S. Y. Kang, M. L. Lee, J. M. Lee, and T. Zyung, "Circuit-Model-Based Analysis of a Wireless Energy-Transfer System via Coupled Magnetic Resonances," *IEEE Transactions on Industrial Electronics*, vol. 58, no. 7, pp. 2906-2914, 2011, doi: 10.1109/TIE.2010.2072893.
- [179] M. Saad, A. H. Mahammad, A. S. Salina, and H. Aini, "Analysis and Optimization of Spiral Circular Inductive Coupling Link for Bio-Implanted Applications on Air and within Human Tissue," *Sensors*, vol. 14, no. 7, pp. 11522-11541, 2014, doi: 10.3390/s140711522.
- [180] C. Uribe and W. Grote, "Radio Communication Model for Underwater WSN," in *2009 3rd International Conference on New Technologies, Mobility and Security*, 20-23 Dec. 2009 2009, pp. 1-5, doi: 10.1109/NTMS.2009.5384789.
- [181] V. Bana, G. Anderson, L. Xu, D. Rodriguez, A. Phipps, and J. D. Rockway, "Characterization of Coupled Coil in Seawater for Wireless Power Transfer," *Space and C. Naval Warfare Systems Center Pacific San Diego*, Eds., ed, 2013.
- [182] J. M. González-González, A. Triviño-Cabrera, and J. A. Aguado, "Design and validation of a control algorithm for a SAE J2954-compliant wireless charger to guarantee the operational electrical constraints," *Energies*, vol. 11, no. 3, 2018, doi: 10.3390/en11030604.
- [183] D. Kim *et al.*, "Analysis and introduction of effective permeability with additional air-gaps on wireless power transfer coils for electric vehicle based on SAE J2954 recommended practice," *Energies*, vol. 12, no. 24, 2019, doi: 10.3390/en12244797.
- [184] T. Campi, S. Cruciani, F. Maradei, and M. Feliziani, "Magnetic field during wireless charging in an electric vehicle according to standard SAE J2954," *Energies*, vol. 12, no. 9, 2019, doi: 10.3390/en12091795.
- [185] X. Mou, D. T. Gladwin, R. Zhao, and H. Sun, "Survey on magnetic resonant coupling wireless power transfer technology for electric vehicle charging," *IET Power Electronics*, vol. 12, no. 12, pp. 3005-3020, 2019, doi: 10.1049/iet-pel.2019.0529.
- [186] D. E. Company, *Sweep Frequency Response Analyzer (SFRA) User Guide*: Doble Engineering Company, 2008.

- [187] R. Tavakoli *et al.*, "Magnetizable concrete composite materials for road-embedded wireless power transfer pads," in *2017 IEEE Energy Conversion Congress and Exposition (ECCE)*, 1-5 Oct. 2017 2017, pp. 4041-4048, doi: 10.1109/ECCE.2017.8096705.
- [188] C. Carretero, I. Lope, and J. Acero, "Magnetizable Concrete Flux Concentrators for Wireless Inductive Power Transfer Applications," *IEEE Journal of Emerging and Selected Topics in Power Electronics*, pp. 1-1, 2019, doi: 10.1109/JESTPE.2019.2935226.
- [189] L. Hutchinson, B. Waterson, B. Anvari, and D. Naberezhnykh, "Potential of wireless power transfer for dynamic charging of electric vehicles," *IET Intelligent Transport Systems*, vol. 13, no. 1, pp. 3-12, 2019, doi: 10.1049/iet-its.2018.5221.
- [190] X. Wang, Y. Wang, Y. Hu, Y. He, and Z. Yan, "Analysis of Wireless Power Transfer Using Superconducting Metamaterials," *IEEE Transactions on Applied Superconductivity*, vol. 29, no. 2, pp. 1-5, 2019, doi: 10.1109/TASC.2018.2882234.
- [191] X. Wang, Y. Wang, G. Fan, Y. Hu, X. Nie, and Z. Yan, "Experimental and Numerical Study of a Magnetic Resonance Wireless Power Transfer System Using Superconductor and Ferromagnetic Metamaterials," *IEEE Transactions on Applied Superconductivity*, vol. 28, no. 5, pp. 1-6, 2018, doi: 10.1109/TASC.2018.2825305.
- [192] A. Grbic, R. Merlin, E. M. Thomas, and M. F. Imani, "Near-Field Plates: Metamaterial Surfaces/Arrays for Subwavelength Focusing and Probing," *Proceedings of the IEEE*, vol. 99, no. 10, pp. 1806-1815, 2011, doi: 10.1109/JPROC.2011.2106191.
- [193] B. Wang, W. Yerazunis, and K. H. Teo, "Wireless Power Transfer: Metamaterials and Array of Coupled Resonators," *Proceedings of the IEEE*, vol. 101, no. 6, pp. 1359-1368, 2013, doi: 10.1109/JPROC.2013.2245611.
- [194] T. Shaw and D. Mitra, "Wireless Power Transfer System Based on Magnetic Dipole Coupling With High Permittivity Metamaterials," *IEEE Antennas and Wireless Propagation Letters*, vol. 18, no. 9, pp. 1823-1827, 2019, doi: 10.1109/LAWP.2019.2930769.
- [195] H. Wang, W. Wang, X. Chen, Q. Li, and Z. Zhang, "Analysis and Design of kHz-Metamaterial for Wireless Power Transfer," *IEEE Transactions on Magnetics*, pp. 1-1, 2020, doi: 10.1109/TMAG.2020.3001360.
- [196] W. Yang, S. Ho, and W. Fu, "Numerical and Experimental Study on Design Optimization of Hybrid Metamaterial Slab for Wireless Power Transmission," *IEEE Access*, vol. 8, pp. 82700-82708, 2020, doi: 10.1109/ACCESS.2020.2990964.
- [197] "IEEE Guide for the Transportation of Transformers and Reactors Rated 10 000 kVA or Higher," *IEEE Std C57.150-2012*, pp. 1-52, 2013.
- [198] A. Abu-Siada, M. I. Mosaad, D. Kim, and M. F. El-Naggar, "Estimating Power Transformer High Frequency Model Parameters Using Frequency Response Analysis," *IEEE Transactions on Power Delivery*, vol. 35, no. 3, pp. 1267-1277, 2020, doi: 10.1109/TPWRD.2019.2938020.

- [199] S. M. Fernández, S. M. García, C. C. Olay, J. C. C. Rodríguez, R. V. García, and J. V. López, "Electronic Tap Changer for Very High-Power Medium-Voltage Lines With No Series-Parallel Thyristors," *IEEE Transactions on Industrial Electronics*, vol. 65, no. 7, pp. 5237-5249, 2018, doi: 10.1109/TIE.2017.2777380.
- [200] A. S. Meyer and J. V. Coller, "Electronic tap changers for use with ultra-light rural distribution lines," in *1999 IEEE Africon. 5th Africon Conference in Africa (Cat. No.99CH36342)*, 28 Sept.-1 Oct. 1999 1999, vol. 2, pp. 909-912 vol.2, doi: 10.1109/AFRCON.1999.821890.
- [201] J. Faiz and B. Siahkollah, "New Controller for an Electronic Tap Changer—Part I: Design Procedure and Simulation Results," *IEEE Transactions on Power Delivery*, vol. 22, no. 1, pp. 223-229, 2007, doi: 10.1109/TPWRD.2006.881424.

Every reasonable effort has been made to acknowledge the owners of copyright material. I would be pleased to hear from any copyright owner who has been omitted or incorrectly acknowledged.

AUTHORSHIP STATEMENT of

"State-of-the-art literature review of WPT: Current limitations and solutions on IPT,"
Electric Power Systems Research, vol. 154, pp. 493-502, 2018, doi:
<https://doi.org/10.1016/j.epsr.2017.09.018>.

Accepted by ELSEVIER Electric Power Systems Research

Authors: Dowon Kim, Ahmed Abu-Siada, and Adrian Sutinjo.

Dowon Kim

I, Dowon Kim, a Ph.D. student at Curtin University, conducted an in-depth literature survey, wrote the manuscript, and responded to the reviewers. I performed the 3-D simulations of the developed WPT system with the detailed circuit analysis and conducted the practical experiments. I analysed the results and provided future perspectives to overcome current WPT limitations in four main areas: design, efficiency, stability, and safety.

Signature:

Date: 25 / 9 / 2020

Ahmed Abu-Siada

I, Ahmed Abu-Siada, encouraged and supported the research. I clarified the aim of the article and its contributions. Also, I reviewed the process and results of the theoretical derivations and practical experiments and corrected academic writing. I believe my contribution to this publication has been 20 % of the work.

Signature:

Date: 25 / 09 / 2020

Adrian Sutinjo

I, Adrian Sutinjo, I reviewed the manuscript and investigated the contribution of the article. I also provided technical advice in high-frequency (HF) engineering. I believe my contribution to this publication has been 10 % of the work.

Signature:

Date: 05 Oct. 2020

AUTHORSHIP STATEMENT of

"Application of FRA to Improve the Design and Maintenance of Wireless Power Transfer Systems," *IEEE Transactions on Instrumentation and Measurement*, pp. 1-13, 2019, doi: [10.1109/TIM.2018.2889360](https://doi.org/10.1109/TIM.2018.2889360).

Accepted by IEEE Transactions on Instrumentation and Measurement

Authors: Dowon Kim, Ahmed Abu-Siada, and Adrian Sutinjo.

Dowon Kim

I, Dowon Kim, a Ph.D. student at Curtin University, suggested a novel idea of frequency response analyzer application and developed the theoretical circuit model in different compensations. I wrote the manuscript and replied to the reviewers. I conducted the simulations for investigating the magnetic coupling and performance of a two-coil WPT system. Also, I built the hardware and carried out practical experiments. I suggested a new procedure for the WPT maintenance and WPT reliability diagnosis using FRA.

Signature:

Date: 25/9/2020

Ahmed Abu-Siada

I, Ahmed Abu-Siada, reviewed the novel idea and encouraged the research. I investigated circuit models, experiment results, and the necessity of the contribution. Also, I reviewed the FRA measurement results and provided feedback on the interpretation of FRA results. I corrected academic writing and advised about the structure of the article. I believe my contribution to this publication has been 20 % of the work.

Signature:

Date: 25/09/2020

Adrian Sutinjo

I, Adrian Sutinjo, I reviewed the manuscript and verified the simulation process and results. I provided consultation about the magnetic coupling and the relationship between S -parameter and Z -parameter. I believe my contribution to this publication has been 10 % of the work.

Signature:

Date: 05 Oct. 2020

AUTHORSHIP STATEMENT of

"Near-Field Analysis and Design of Inductively-Coupled Wireless Power Transfer System in FEKO," *Applied Computational Electromagnetics Society*, vol. 35, pp. 82-93, 2020.

Accepted by Applied Computational Electromagnetics Society

Authors: Dowon Kim, Adrian Sutinjo, and Ahmed Abu-Siada.

Dowon Kim

I, Dowon Kim, a Ph.D. student at Curtin University, presented a new application of the electromagnetic solver software known as FEldberechnung für Körper mit beliebiger Oberfläche (FEKO) for the WPT system design. I verified the effectiveness of FEKO and analysed the performance of the developed inductively-coupled WPT system through a practical experiment. I wrote the manuscript, replied to the reviewers, built the hardware, and conducted the practical experiments.

Signature:

Date: 25/9/2020

Adrian Sutinjo

I, Adrian Sutinjo, introduced FEKO in high-frequency applications and encourage Dowon to use it for the WPT system design. I reviewed the topologies of the WPT model and verified the simulation results. I corrected academic writing and clarified the aim of the article. I believe my contribution to this publication has been 20 % of the work.

Signature:

Date: 05 Oct. 2020

Ahmed Abu-Siada

I, Ahmed Abu-Siada, I reviewed the manuscript and investigated the practical experiments on the prototype. Also, I provided consultation on the frequency tuning of the inductively coupled WPT system. I believe my contribution to this publication has been 10 % of the work.

Signature:

Date: 25/09/2020

AUTHORSHIP STATEMENT of

"A novel application of frequency response analysis for wireless power transfer system,"
in 2017 Australasian Universities Power Engineering Conference (AUPEC), 19-22 Nov. 2017,
pp. 1-6, doi: 10.1109/AUPEC.2017.8282474.

Accepted by 2017 Australasian Universities Power Engineering Conference

Authors: Dowon Kim, Ahmed Abu-Siada, and Adrian Sutinjo.

Dowon Kim

I, Dowon Kim, a Ph.D. student at Curtin University, conceived the new application of frequency response analyser to WPT systems. I conducted wrote the manuscript and responded to the reviewer, and presented it during the conference. I performed the 3-D simulation and the circuit analysis of the two-winding WPT system, built the prototype, and conducted the practical experiments. I presented the usability of FRA for WPT design.

Signature:

Date: 25/9/2020

Ahmed Abu-Siada

I, Ahmed Abu-Siada, encouraged the research and verified Dowon's idea. I advised the structure of the manuscript and investigated the necessity of the contribution. Also, I reviewed the procedure and interpretations of the FRA measurements on the developed WPT system. I believe my contribution to this publication has been 20 % of the work.

Signature:

Date: 25/09/2020

Adrian Sutinjo

I, Adrian Sutinjo, I verified the electromagnetic coupling result of the simulation and reviewed the manuscript. I believe my contribution to this publication has been 10 % of the work.

Signature:

Date: 05 Oct. 2020

AUTHORSHIP STATEMENT of

“Literature Review of Wireless Power Transfer Technology for Electric Vehicle Battery Charging,” in *2017 One Curtin International Postgraduate Conference*, 10-12 Dec. 2017.

Accepted by Curtin University

Authors: Dowon Kim.

Dowon Kim

I, Dowon Kim, a Ph.D. student at Curtin University, conducted an in-depth survey on the wireless charging electric vehicles (EVs). I provided state-of-the-art EVs wireless charging technologies in different methods: inductive, capacitive, and microwave power transfer (IPT, CPT, and MPT) systems. Also, I provided considerations for enhancing the WPT charging system. I wrote the manuscript and presented it during the conference.

Signature:

Date: 25/9/2020

AUTHORSHIP STATEMENT of

“An Inductively-coupled Wireless Power Transfer Application for Autonomous Underwater Vehicles,” in *2019 11th Autonomous Underwater Technology, technical conference & exhibition*, 23 Oct. 2019.

Accepted by Society of Underwater Technology

Authors: Dowon Kim, Ahmed Abu-Siada and Stuart Higgins.

Dowon Kim

I, Dowon Kim, a Ph.D. student at Curtin University, conducted a literature survey, and wrote the manuscript. I performed the software simulations with the detailed circuit analysis, built the prototype, and carried out the practical experiments. I analysed the results and suggested the future perspective for the enhancing WTP application for charging AUTs.

Signature: _____ Date: 25/9/2020

Ahmed Abu-Siada

I, Ahmed Abu-Siada, encouraged and supported the research. I reviewed Dowon’s idea, hypothesis, and the results of practical experiments. Also, I revised the presentation slides and corrected them in academic writing. I believe my contribution to this publication has been 10 % of the work.

Signature: _____ Date: 25/09/2020

Stuart Higgins

I, Stuart Higgins, reviewed the presentations slides. I contributed to the corrections of the underwater technology part in the presentation. I also corrected the order and format of the presentation. I believe my contribution to this publication has been 10 % of the work.

Signature: _____ Date: 25/9/2020

AUTHORSHIP STATEMENT of

“A new role of SFRA for reliable performance in wireless power transfer system,” in *2020 International Conference of Doble Clients*, 8-13 Mar. 2020.

Accepted by DOBLE Engineering

Authors: Dowon Kim, and Ahmed Abu-Siada.

Dowon Kim

I, Dowon Kim, a Ph.D. student at Curtin University, wrote the manuscript, created presentation slides, and responded to the reviewer. I introduced the effectiveness of FRA for the WPT system design and maintenance and conducted FRA measurements in different environments. Also, I suggested improving the FRA software and implementing the different types of high-frequency source for strengthening the FRA application on WPT systems.

Signature:

Date: 25/9/2020

Ahmed Abu-Siada

I, Ahmed Abu-Siada, reviewed the manuscript and corrected academic writing. I also verified the circuit model of the developed WPT system and procedures of FRA measurements. I believe my contribution to this publication has been 10 % of the work.

Signature:

Date: 25/09/2020